AD_________________

Award Number: W81XWH-05-1-0278

TITLE: Image Processing and Computer Aided Diagnosis in Computed Tomography of the Breast

PRINCIPAL INVESTIGATOR: Jessie Qing Xia, Ph.D.

CONTRACTING ORGANIZATION: Duke University
Durham, NC 27710

REPORT DATE: October 2007

TYPE OF REPORT: Annual Summary

PREPARED FOR: U.S. Army Medical Research and Materiel Command
Fort Detrick, Maryland 21702-5012

DISTRIBUTION STATEMENT: Approved for Public Release;
Distribution Unlimited

The views, opinions and/or findings contained in this report are those of the author(s) and should not be construed as an official Department of the Army position, policy or decision unless so designated by other documentation.

REPORT DOCUMENTATION PAGE

Form Approved
OMB No. 0704-0188

Public reporting burden for this collection of information is estimated to average 1 hour per response, including the time for reviewing instructions, searching existing data sources, gathering and maintaining the data needed, and completing and reviewing this collection of information. Send comments regarding this burden estimate or any other aspect of this collection of information, including suggestions for reducing this burden to Department of Defense, Washington Headquarters Services, Directorate for Information Operations and Reports (0704-0188), 1215 Jefferson Davis Highway, Suite 1204, Arlington, VA 22202-4302. Respondents should be aware that notwithstanding any other provision of law, no person shall be subject to any penalty for failing to comply with a collection of information if it does not display a currently valid OMB control number. **PLEASE DO NOT RETURN YOUR FORM TO THE ABOVE ADDRESS.**

1. REPORT DATE
01-10-2007

2. REPORT TYPE
Annual Summary

3. DATES COVERED
1 MAR 2005 - 4 SEP 2007

4. TITLE AND SUBTITLE
Image Processing and Computer Aided Diagnosis in Computed Tomography of the Breast

5a. CONTRACT NUMBER

5b. GRANT NUMBER
W81XWH-05-1-0278

5c. PROGRAM ELEMENT NUMBER

6. AUTHOR(S)
Jessie Qing Xia, Ph.D.

E-Mail: qing.xia@duke.edu

5d. PROJECT NUMBER

5e. TASK NUMBER

5f. WORK UNIT NUMBER

7. PERFORMING ORGANIZATION NAME(S) AND ADDRESS(ES)

Duke University
Durham, NC 27710

8. PERFORMING ORGANIZATION REPORT NUMBER

9. SPONSORING / MONITORING AGENCY NAME(S) AND ADDRESS(ES)
U.S. Army Medical Research and Materiel Command
Fort Detrick, Maryland 21702-5012

10. SPONSOR/MONITOR'S ACRONYM(S)

11. SPONSOR/MONITOR'S REPORT NUMBER(S)

12. DISTRIBUTION / AVAILABILITY STATEMENT
Approved for Public Release; Distribution Unlimited

13. SUPPLEMENTARY NOTES

14. ABSTRACT

Dedicated breast CT imaging is a novel breast imaging modality, which may improve lesion detection with a comparable radiation dose to conventional mammography. However, due to its cone beam geometry, breast CT suffers from image degradation due to scatter radiation. Moreover, the breast CT images divide the dose of mammography among hundreds of projection views, resulting in considerable quantum noise. It is therefore desirable to reduce scatter and noise in the reconstructed breast volume without loss of spatial resolution. Several new image-processing techniques were developed based on the unique physical properties of this modality. Using images obtained on a full field digital mammography system, the Gaussian noise model demonstrated effective scatter removal. A PDE technique taking into the account the non-uniform distribution of the noise in the projection image after the preprocessing step provides excellent denoised data with sharp edges. Applying a denoising technique before reconstruction provides better images than after reconstruction. The preliminary ROC study showed that with a fixed size lesion in real anatomical backgrounds, PDE-denoised images had higher detectability, higher CNR and better qualitative appearance. These promising new techniques for noise and scatter compensation pave the way for future implementations of dedicated breast CT.

15. SUBJECT TERMS
Breast Imaging, Breast CT, Scatter Compensation, Denoising, CAD, Cone-Beam CT

16. SECURITY CLASSIFICATION OF:			17. LIMITATION OF ABSTRACT	18. NUMBER OF PAGES	19a. NAME OF RESPONSIBLE PERSON
					USAMRMC
a. REPORT	b. ABSTRACT	c. THIS PAGE			19b. TELEPHONE NUMBER *(include area code)*
U	U	U	UU	235	

Standard Form 298 (Rev. 8-98)
Prescribed by ANSI Std. Z39.18

Table of Contents

Introduction…………………………………………………………………..……….... 1

Body……………………………………………………………………………….….. 2

Key Research Accomplishments………………………………………….……..…. 14

Conclusions……………………………………………………………………..…. 15

Reportable Outcomes……………………………………………………………….. 16

References………………………………………………………………………….. 16

Appendices…………………………………………………………………………. 19

Introduction

Breast cancer is the most common cancer type that affects women globally [1]. In the United States, due to the long life spans, the incidence is even higher: every one woman over eight will develop breast cancer in her lifetime. It was estimated that approximately 178,480 new invasive breast cancer cases would be found in American women in 2007 [2]. Moreover, breast cancer is one of the leading causes of cancer-related women mortality, secondary only to lung cancer. It is predicted that the disease will kill about 40,460 US women in 2007 [2].

Presently there is no effective way of preventing the disease. However, detection of the cancer at its early stage has been found to significantly improve survival rates [3-6]. For example, when breast cancer is detected at the localized stage, the five-year relative survival rate is 98% [2]. By contrast, when it is not found until metastasized, the five-year survival rate drops dramatically. In addition, when the cancer is found earlier, more viable treatment options are also available [7-9].

X-ray mammography is presently the primary tool for early detection of breast cancer. The standard screening procedure is to acquire a pair of two-dimensional projection images: mediolateral oblique (MLO) view and cranial-caudal (CC) view. The abnormalities can manifest themselves on a mammogram as either masses, clusters of microcalcifications, or architectural distortions even before any symptom shows up. An annual screening program based on mammography is recommended for women older than forty years or younger women with high risk by National Cancer Institute, American Cancer Society and American College of Radiology.

While x-ray mammography has been proven to be effective, it is not perfect in its detection sensitivity of breast lesions due to several limitations such as two-dimensional projection data acquisition and restricted range of linear optical response of the detector. Overall, it has a sensitivity within the range of 63% to 88% depending on the patient's age group, family history [10] and breast density [11]. For women with dense breasts, the sensitivity is lower since in their mammograms the dense appearance of the breast tissue is more likely to obscure any abnormalities and makes the detection of breast cancer even more challenging [12]. In addition, the situation gets complicated by the fact that breast density is also a risk factor by itself, which means that women with dense breasts tend to be more likely to get breast cancer.

With the advent of high-resolution flat-panel detectors at the end of the 1990s, dedicated breast CT technology is emerging, which offers the potential to detect breast lesions among women with dense breasts.

Unlike a conventional CT system, where the x-ray tube/ detector move around the torso of a patient, a dedicated breast CT system has a joint x-ray tube/detector movement just around a breast. It is set up as shown in Figure 1: a woman patient lies prone on a lead-shielded table with one breast hanging freely through a hole on the table. The x-ray tube and the flat panel detector are installed vertically underneath the table. The tube-detector assembly rotates around the exposed breast of the patient. By this design of the dedicated system, the field of view (FOV) of the detector can be fully employed for breast imaging. What's more, since other tissues do not attenuate the x-ray beam, the effective glandular dose delivered to the patient can be lowered to match the two-view screening mammogram for the same breast, as is demonstrated by Boone et al in 2001 [13].

There are five research groups investigating dedicated breast CT. They are: Dr. Boone *et al* in University of California, Davis [14-17], Glick *et al* in University of Massachusetts [18-20], Ning *et al* in University of Rochester [21-24], Shaw *et al* in University of Texas M.D. Anderson Cancer Center [25-27], and Tornai *et al* in Duke University [28-32]. In addition, they all have fabricated their own dedicated breast CT systems. These breast CT systems differ in their detailed technical aspects: the choice of x-ray beam, the x-ray source orbit, and the peak voltage and tube current values used.

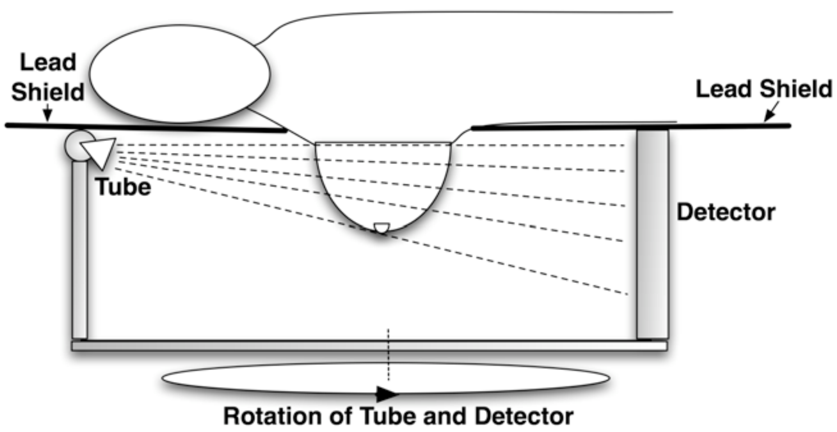

Figure 1: Illustration of a dedicated breast CT system. The x-ray tube and flat-panel detector rotate together around the breast, which is the only region to be illuminated.

This dissertation has been conducted in close collaboration with Boone's breast CT research group, which provided raw human subject datasets and corresponding geometric calibration results. Based on the raw data provided by them, we developed the techniques for image improvement via the scatter compensation and/or denoising. Finally, a pilot computer aided detection (CAD) study was conducted to compare the original datasets to the datasets with image processing.

Report Body

Task 1: Develop and test a unique two-dimensional Bayesian image processing technique on the projection data of cone-beam breast Computed Tomography (breast CT) obtained without a grid. (Months 1-4)

This task has been completed and the results are incorporated into the papers listed under the category of reportable outcomes. This task is split into two subtasks. The first subtask is to develop an algorithm for scattered radiation removal. The second subtask is to reduce the quantum noise from breast CT data.

For the first subtask, a model-based algorithm was designed and implemented for scatter reduction. To account for the energy-integrating characteristic of the flat-panel digital detector, Gaussian distributions were employed to approximate the signals recorded at individual pixels of the detector. For the task of removing scattered radiation, a Gaussian noise model was proposed. The Maximum Likelihood Estimator (MLE) was obtained via an Expectation Maximization algorithm in an iterative manner. With more iteration steps, the high frequency noise in the image would also be amplified. In order to suppress this side effect, the Maximum *a Posteriori* (MAP) estimator was obtained by combining the Gaussian noise model with a Gibbs prior via Bayes rule. The technical details can be found in the paper corresponding to reportable outcome #2.

Figure 2 shows the comparison between the radiographs of an anthropomorphic breast phantom with and without an anti-scatter grid, and MAP processed radiograph on the one without the grid. Table 1 is the residual scatter fraction (RSF) and contrast to noise ratio (CNR) measurements on these three images. It is shown that with our algorithm, the scattered radiation on the images acquired without a grid can be reduced down to the level achieved by using a grid. Meanwhile, the CNR of the processed image is twice that of the image acquired with a grid.

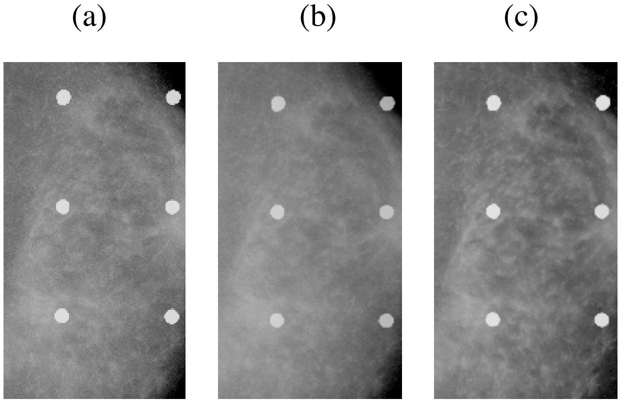

Figure 2: Radiographs of an anthropomorphic breast phantom acquired on Siemens prototype FFDM system (a) with and (b) without an anti-scatter grid; (b) the MAP algorithm processed image based on (b). The white disks are the beam stop (made of lead) array for scatter radiation measurement.

Table 1: Corresponding residual scatter fraction (RSF) and contrast to noise ratio (CNR) results for the three images shown in Figure 1.

	With grid	**Without grid**	**Without grid; scatter reduction**
RSF	11%	45%	10%
CNR	7.04	6.99	15.29

For the second subtask, a partial-diffusion-equation (PDE) based denoising technique was developed for noise removal in breast CT. It was observed that the line integral images (converted from the raw images by logarithmic operation) had the following property: line integrals through the breast close to chest wall have much higher variance than those through the breast close to nipple.

We derived a theoretical formula between the line integral variance and the number of photons hitting the detector at a specific pixel region:

$$\mathrm{var}(l_{ij}) \cong \frac{1}{\lambda_{ij}}. \qquad \textit{Equation 1}$$

The details of the derivation can be found in the paper corresponding to reportable outcome #3. Based on this formalism, we proposed a $\mathrm{PDE}_{\mathrm{tomo}}$ (abbreviation for: PDE for tomography/tomosynthesis) algorithm for breast CT data noise removal.

Task 2: Reconstruct the three-dimensional breast image based on the processed projection data from Task 1. (Months 5-8)

This task has already been completed and some results are shown in the reportable outcome #3. A Feldkamp-type filtered back projection (FBP) algorithm [33] was custom-written and used for the cone-beam reconstruction of the breast CT data.

For the results shown in Figure 3, the $\mathrm{PDE}_{\mathrm{tomo}}$ technique was applied to the line integral images converted from raw projections. The processed projection images were then fed into the FBP core for reconstruction. The reconstructed breast CT volume provided unique anatomic information of the breast. In addition, the $\mathrm{PDE}_{\mathrm{tomo}}$ technique was very effective in removing the noise while maintaining the details.

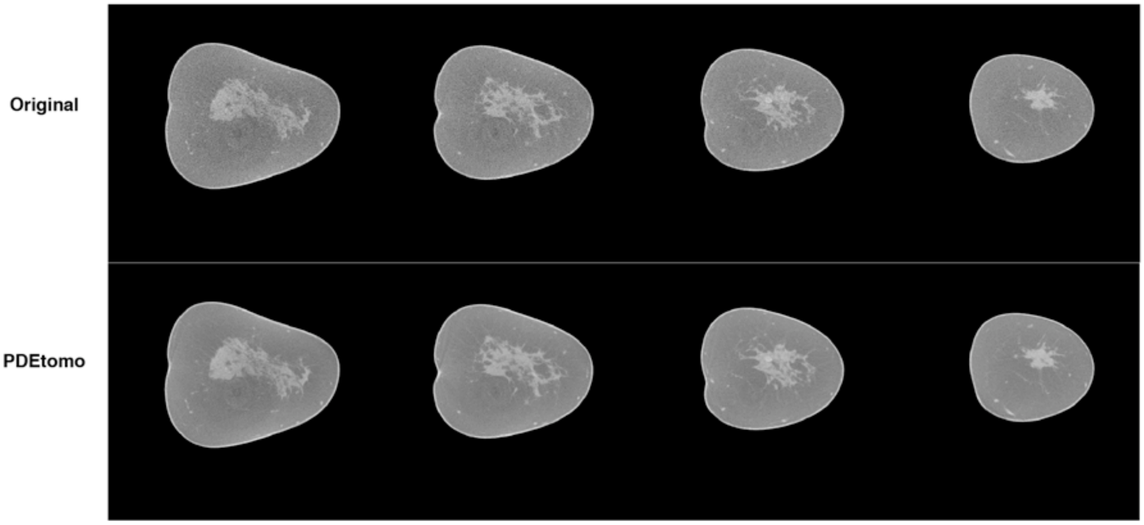

Figure 3: Reconstructed coronal sections of a breast of a human subject. The section thickness is 0.5 mm. The top row is derived with the original dataset. The bottom row is derived with the PDE_{tomo} processed

dataset. It is manifest that PDE_{tomo} processed volume has remarkable less noise than the original volume while maintaining the details.

Task 3: Apply the algorithm in Task 1 to the two-dimensional slices of the reconstructed three-dimensional breast image from the unprocessed projection data. (Months 9-12)

This task and Task 4 were aimed at developing variants of PDE denoising techniques that could be used at different steps in the reconstruction process, which was illustrated in Figure 4.

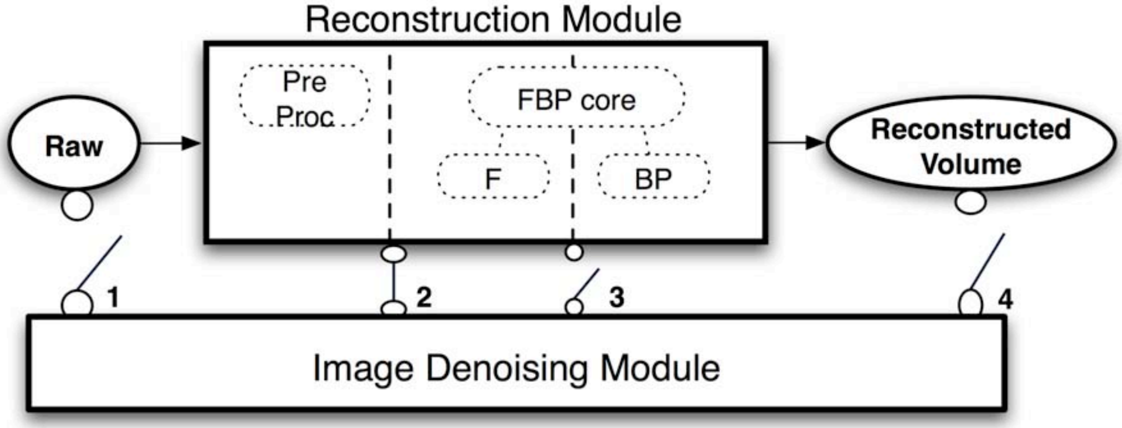

Figure 4: Illustration of possible steps in the reconstruction process that an image denoising module can be applied to in dedicated breast CT.

However, applying a denoising technique in step 1 would not be very effective due to the nonlinear operation of the preprocessing step. Only step 2, 3 and 4 were considered. All together three variants of the Partial Diffusion Equation based denoising techniques were implemented for this study, corresponding to the three steps considered. Firstly, the PDE_{tomo} technique described in Task 1 was applied at step 2. Secondly, the standard two-dimensional PDE technique (denoted by PDE_{2D}) was applied at step 3, for the completion of Task 2. Finally, a three-dimensional PDE technique (denoted by PDE_{3Dpost}) was used at step 4, for the completion of Task 3. The comparison between PDE_{tomo} and PDE_{2D} were shown in Figure 7, which indicated that PDE_{tomo} outperformed PDE_{2D}.

Task 4: Develop and test three-dimensional Bayesian image-processing technique on the reconstructed image based on the unprocessed projection data acquired without a grid. (Months 12-20)

This task has been completed. Extending the neighborhood system expands to six neighbors along x, y and z directions, a three-dimensional PDE technique denoted as PDE_{3Dpost} was developed and applied to the reconstructed breast CT dataset for noise removal.

To compare $\text{PDE}_{3\text{Dpost}}$ with PDE_{tomo}, a simulated breast was generated with embedded contrast-detail phantoms. The reconstructed coronal slice containing the center of contrast detail phantoms without noise was shown in Figure 5 and Figure 6.

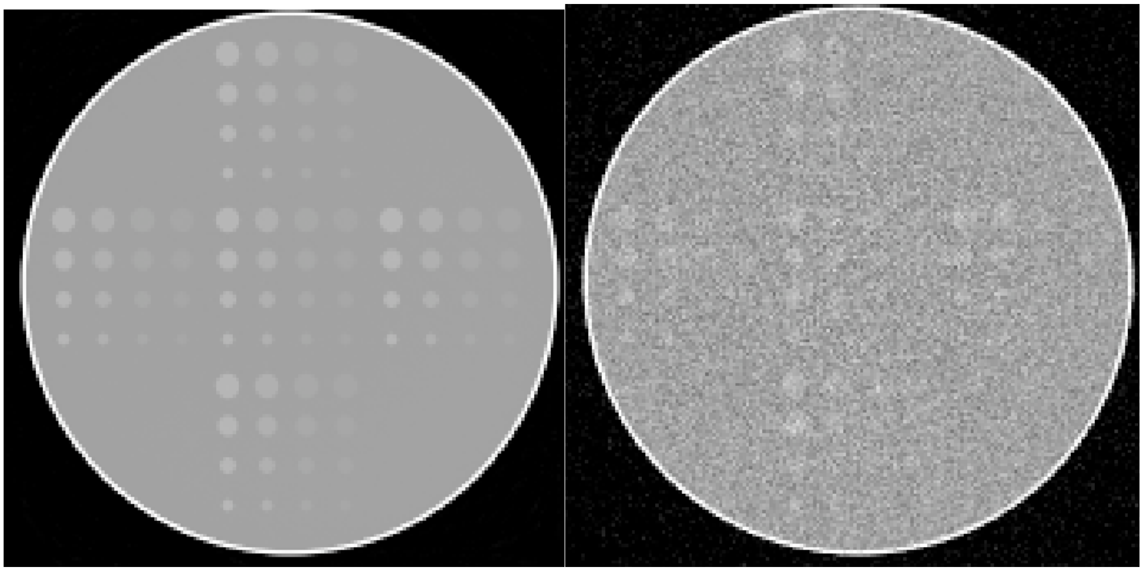

(a) Ideal

(b) With Noise: I_0=2.5e4

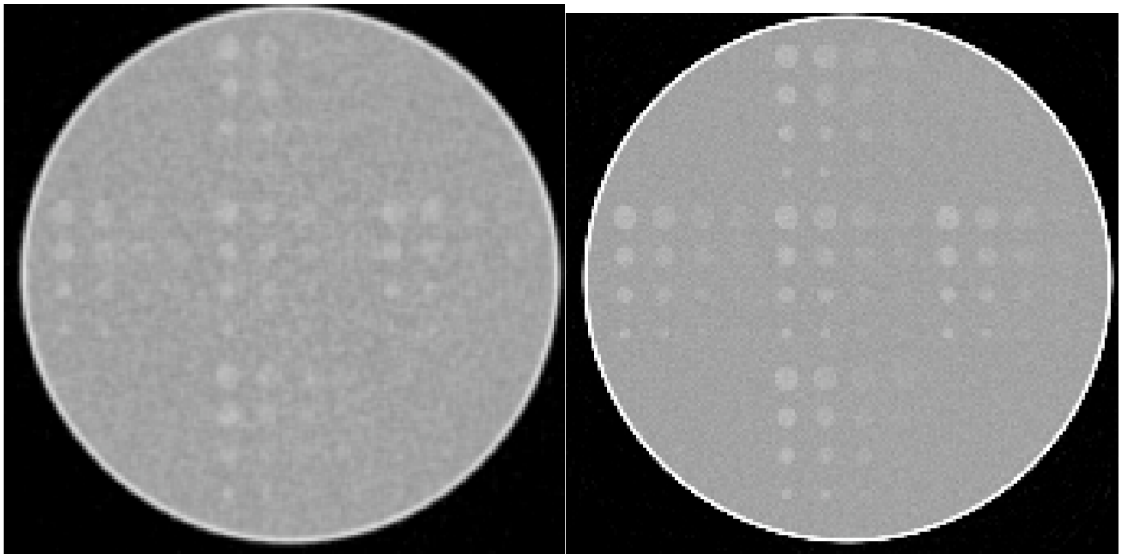

(c) $\text{PDE}_{3\text{Dpost}}$

(d) PDE_{tomo}

Figure 5: Step comparison at I_0=2.5e4. To (a) an ideal contrast detail phantom, noise is added to yield (b) the initial image without any denoising. (d) PDE_{tomo} noise removal before the FBP reconstruction is better than (c) after reconstruction.

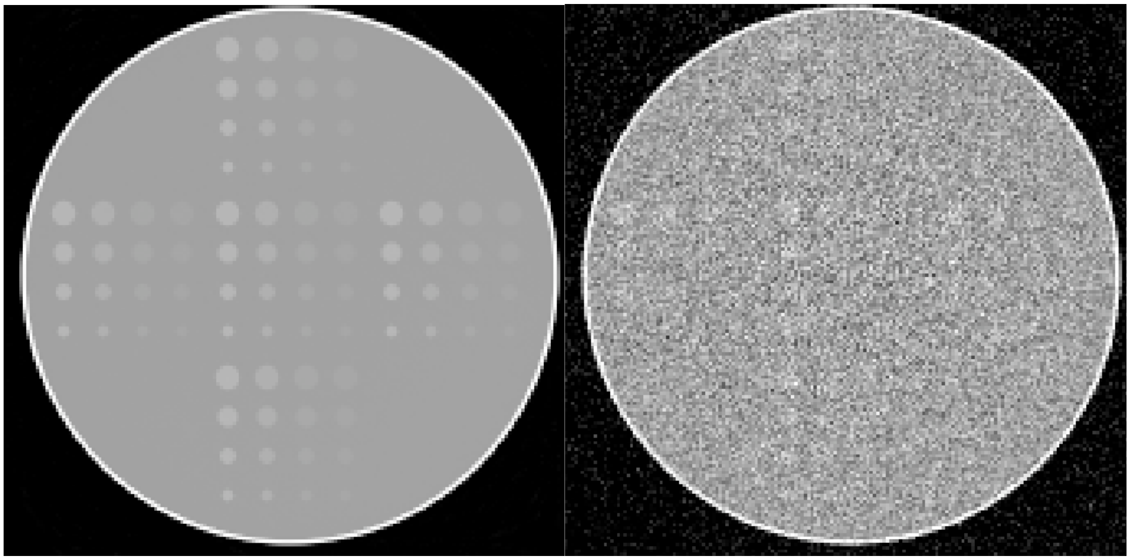

(a) Ideal

(b) With Noise: I_0=2.5e4

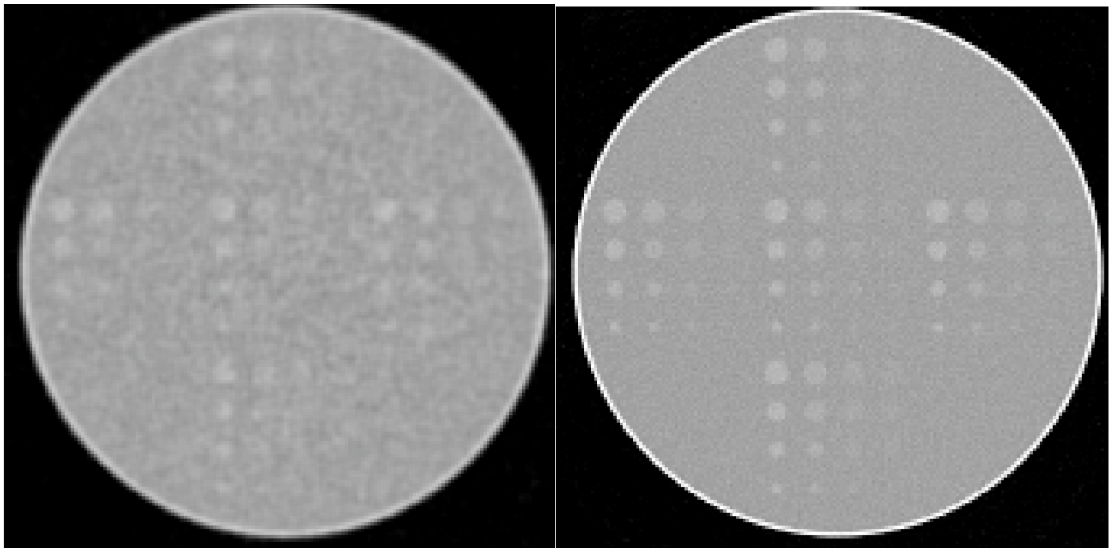

(c) $\text{PDE}_{3\text{Dpost}}$

(d) PDE_{tomo}

Figure 6: Step comparison at I_0=1e4. Figure 5(b) is noisier than Figure 6(b). For subfigures (c) and (d), they come to the same conclusion: (d) PDE_{tomo} applied at step 2 is better than (c) PDE_{3Dpost} applied at step4.

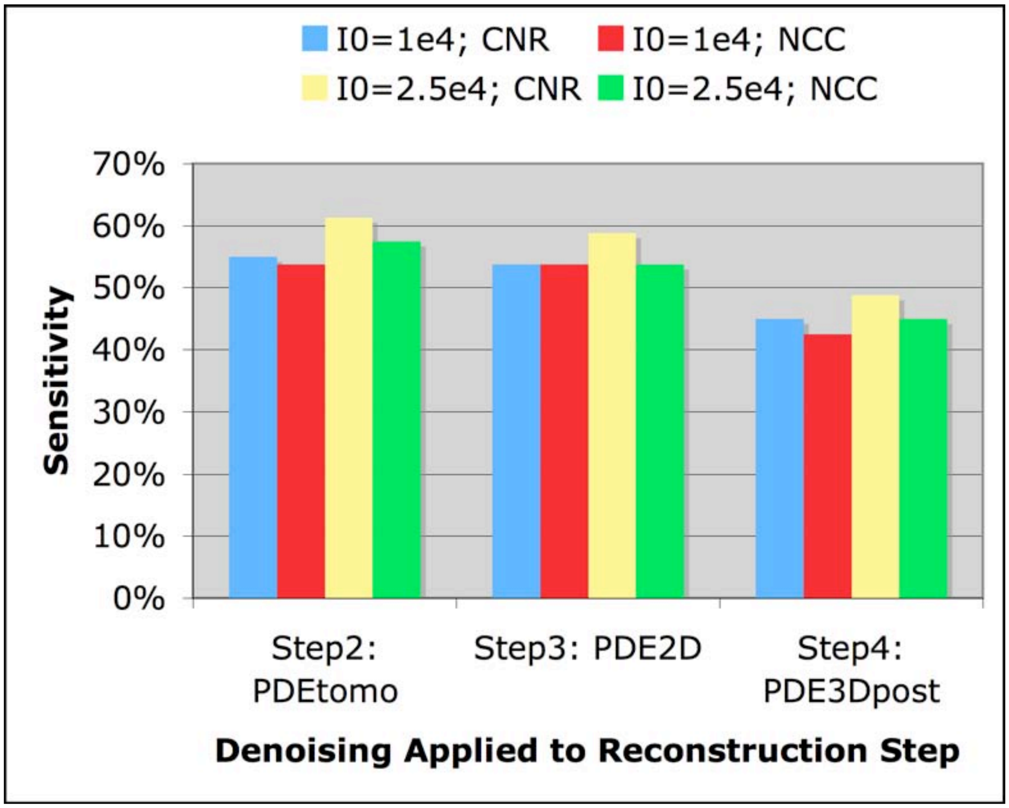

Figure 7: Comparison between denoising applied to reconstruction steps 2, 3 and 4, using CNR and NCC as the criteria. Denoising at step 2 before reconstruction consistently provides higher number of detectable lesions or sensitivity, as does increasing the exposure level.

Visual comparison between PDE_{tomo} and PDE_{3Dpost} processed volumes showed that PDE_{tomo} resulted in superior denoised volume than PDE_{3Dpost}. Even though the background noise were matched for two volumes, as was shown in Figure 5 and Figure 6, PDE_{3Dpost} processed volume exhibited some unpleasant mottle, which was especially true in Figure 6 (c). The noise mottle was due to the FBP reconstruction process, which correlated the independent quantum noise in the projection views. By contrast, PDE_{tomo} processed volumes were exempt from this effect.

Quantitative results based on the lesion detection sensitivity of the contrast detail phantom (shown in Figure 7) agreed with the qualitative evaluation. While the CNR and NCC criteria didn't give the same number, they were very close to each other and provided the same trend: PDE_{tomo} processed volumes (step 2) have more detectable lesions than processed ones by PDE_{2D} (step 3) and PDE_{3Dpost} (step 4). Moreover, given that the background noise was matched, when the exposure level was higher, the lesion detection sensitivity was higher for all three variants of PDE technique according to the CNR criterion.

By optimizing each of them independently, it was found that denoising before reconstruction provided better images than after reconstruction. This is understandable, since some fine details in the volumes can be overwhelmed by the abundant noise during the reconstruction step. Applying denoising afterwards cannot recover that information. By contrast, if a denoising technique is applied before reconstruction, it is possible for the fine details to be preserved. As far as we know, this is the first time that anybody has studied the effect of where to apply denoising in dedicated breast CT.

Task 5: Develop a Computer Aided Diagnosis tool for detecting breast mass lesions based on the projection data. (Months 21-32)

At this time, very few groups are conducting clinical trials with dedicated breast CT. We were very fortunate to have secured from Boone *et al* at University of California Davis 20 human subject datasets to be used for the breast mass detectability study. As these are prospectively collected cases, the ground truth of these 20 volumes is unknown. In present study, we will assume that there is no lesion in the volumes. And all the lesions of interest will be simulated.

The procedure of simulating a mass is as follows:

1. For a given human subject dataset, the reconstructed volume was used as the reference. The location of 10 masses that would be embedded into the volume was randomly chosen.
2. Spherical masses with fixed size and contrast were put at the locations selected in step 1, and projected onto a virtual 100% DQE detector using a virtual monochromatic cone-beam projector, which had the same system geometry, projection angles and reconstruction parameters as the individual human subject dataset. These projection images of masses would then be added to the original projection images of human subjects to get the synthetic projection sets.
3. The synthetic projection sets either went through the afore-mentioned PDE_{tomo} denoising technique followed by FBP reconstruction or directly went for FBP reconstruction.
4. The three-dimensional region of interest (ROIs) could then be retrieved from the reconstructed volumes. In the present study, instead of using 3D ROIs, only the x-y plane section containing the mass (i.e., 2D ROIs) was retrieved for numerical observer study.

The human subject ROI dataset was comprised of the total of 400 ROIs: 200 with and 200 without simulated masses. A sample ROI was shown in Figure 8.

(a) Orig; nomass (b) Orig; mass

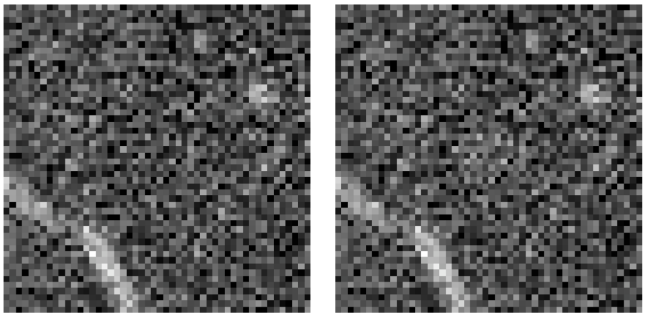

(c) PDE; nomass (d) PDE; mass

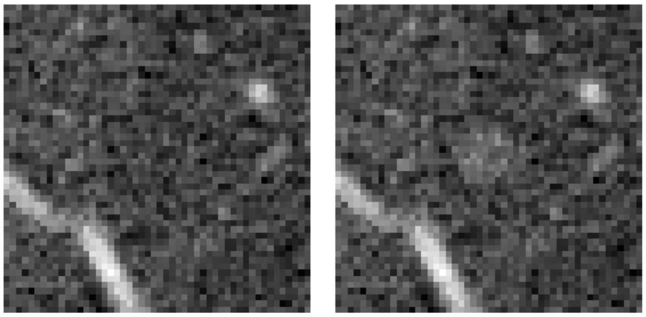

Figure 8: Sample ROIs for simulated lesion with a diameter of 4 mm and contrast of 2%: Original ROIs (a) without mass and (b) with a mass, and, PDE denoised ROIs (c) without mass and (d) with a mass.

Three numerical CAD tools are used: SKE/BKE observer, LG-CHO observer and the SNR-based observer.

Ideal Observer for SKE/BKE

The task of an observer is to detect these masses from background tissues. It can also be formulated as the following hypothesis testing:

$$\begin{aligned} &H_0 : x = n \\ &H_1 : x = n + s \end{aligned} \quad . \qquad \textit{Equation 2}$$

The null hypothesis represents the mass absent case, whereas the alternative hypothesis represents the mass present case. If treated as signal known exactly (SKE) case, according to signal detection theory [34], the optimal detector is a likelihood ratio detector. Assuming the background noise *n* follows a Gaussian distribution with a covariance matrix of Σ, the log likelihood ratio has the following form:

$$\ln(\lambda(x)) = s^T \Sigma^{-1} x \, . \qquad \textit{Equation 3}$$

If the background noise follows independent and identical distributed (i.i.d.) Gaussian, i.e., the covariance matrix Σ is an identity matrix, then Equation 3 can be further simplified to:

$$\ln(\lambda(x)) = s^T x / \sigma^2. \qquad \text{Equation 4}$$

Usually real breast tissue background does not satisfy the i.i.d. condition, so the ideal observer shown in Equation 4 will perform sub-optimally on the real breast tissue background case.

Laguerre-Gauss Channelized Hotelling Observer (LG-CHO)

When the covariance matrix *Σ* is not an identity matrix, the likelihood ratio observer shown in Equation 3 is equivalent to a Hotelling observer [35]. The estimation of the covariance matrix *Σ* requires a large number of training cases, which is presently not available in breast CT. Alternatively, Laguerre-Gauss channelized hotelling observer (LG-CHO) [35, 36] can be used for this purpose.

The nth order Laguerre function has the following form:

$$L_n(x) = \sum_{m=0}^{n} (-1)^m \binom{n}{m} \frac{x^m}{m!}. \qquad \text{Equation 5}$$

The LG-CHO has nth order template with the form of:

$$LG_n(r) = \exp(-\frac{\pi r^2}{a^2}) \cdot L_m(\frac{2\pi r^2}{a^2}), \qquad \text{Equation 6}$$

where a is a free parameter proportional to the standard deviation of the Gaussian kernel through

$$a = \sqrt{2\pi}\sigma. \qquad \text{Equation 7}$$

CNR Observer

Traditionally, one would like to use Rose model of statistical detection for a simple lesion detectability study based on x-ray projection images. However Rose model does not directly apply to the breast CT reconstructed slices in this study since the physical measurement on these reconstructed slices is linear attenuation coefficients. Instead, the contrast to noise ratio for each ROI is calculated and used as the decision variable. Given the uncertainties associated with any model observer study, it is desirable to be able to compare all results against such a simple, well-understood technique.

ROC Analysis

The receiver operating characteristic (ROC) analysis is a comprehensive tool for performance measure of the numerical observers. The horizontal axis represents False Positive Fraction (FPF), which equals to (1- specificity), and the vertical axis represents True Positive Fraction (TPF), which equals to sensitivity. They both range from 0 to 1. A ROC curve can be summarized by its area under the curve (AUC). The larger AUC value, the better the performance is, while AUC of 0.5 corresponds to random guessing. The area can also be calculated via semi-parametric fitting resulting in an area index denoted as Az [37].

Task 6: Test and compare the performances of the CAD developed in Task 5 applied to processed projection data from Task 1 with the CAD performance on the projection data without Bayesian processing. (Months 33-36)

This task has been completed. The three numerical CAD tools in Task 5 were applied to the clinical data.

The human subject background ROC analysis based on CNR observer is shown in Figure 9 for simulated mass with a diameter of 4 mm and contrast of 2%. The histograms of CNR for original and PDE processed datasets with and without simulated masses were shown in Figure 9 (a). The corresponding ROC curves were plotted in Figure 9 (b). The Az value of the PDE processed dataset (0.770 ± 0.023) was higher than the Az value of the original dataset (0.801 ± 0.022). The p value was less than 0.009, indicating that the difference was statistically significant. AUC values of the three types of numerical observers using real anatomical background from breast CT were shown in Table 2 for lesions of 5 mm and 10%, 5 mm and 3%, and 4 mm and 2%, respectively. For all the cases, the CNR observer gave the highest AUC values, followed by 1st order LG template, and the ideal observer gave the lowest AUC values. For masses with 4 mm diameter and 2% contrast, the ROC performance of ideal observer reduced to the chance curve.

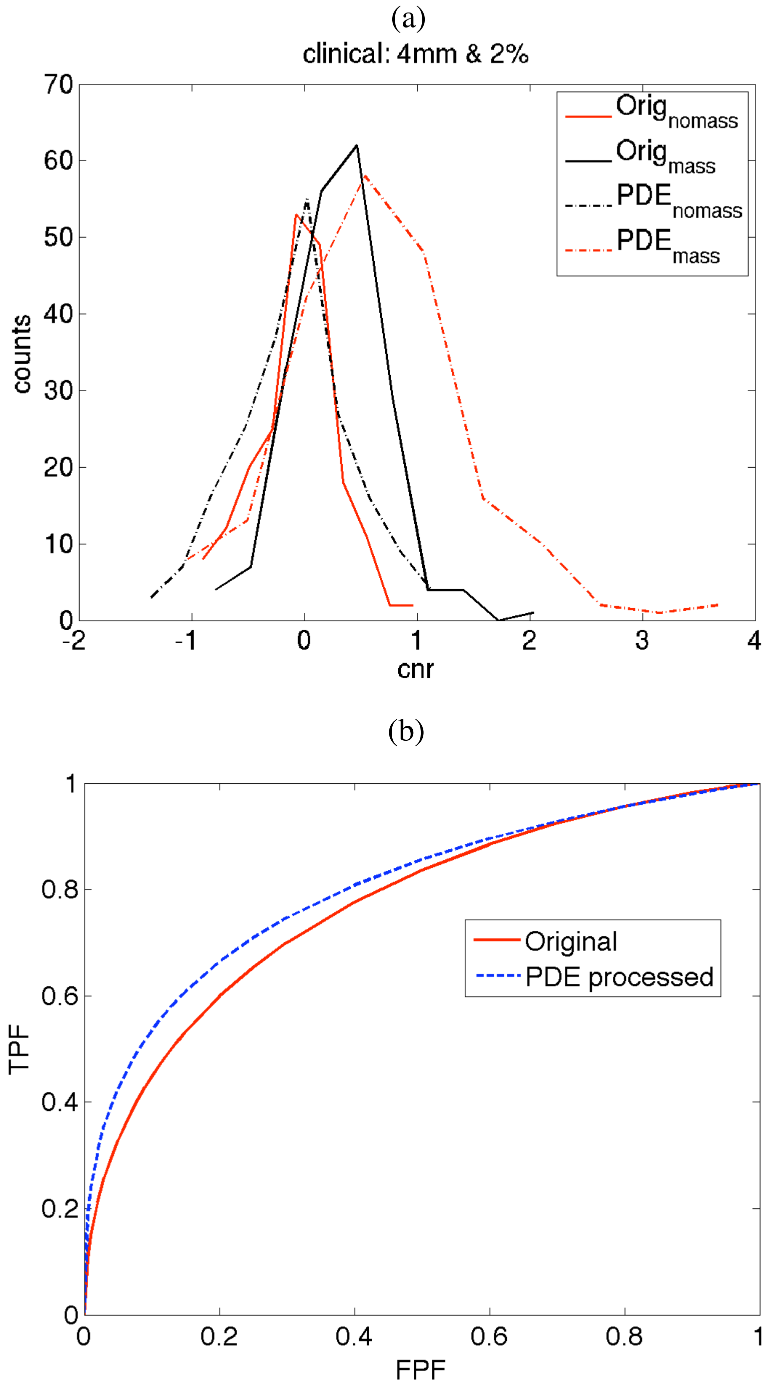

Figure 9: CNR observer results for simulated lesions of 4mm and 2% embedded in real anatomical backgrounds. CNR histograms for original and PDE processed ROI databases are shown in (a) and the corresponding ROC curves are shown in (b). The Az value of the PDE processed dataset (0.770 ± 0.023) is statistically higher than the Az value of the original dataset (0.801 ± 0.022). The p value is less than 0.01.

Table 2: AUC values for the three types of numerical observers using real anatomical background from breast CT.

Lesion	**CNR observer**		**LG-CHO observer**		**Ideal observer**	
	Original	**PDE processed**	**Original**	**PDE processed**	**Original**	**PDE processed**
5mm & 10%	0.999	0.997	0.999	0.999	0.896	0.904
5mm & 3%	0.877	0.883	0.850	0.853	0.690	0.700
4mm & 2%	0.770	0.801	0.703	0.702	0.446	0.443

For the ROIs with real anatomical backgrounds, the ROC curves vary with respect to the mass size and contrast. For masses with 5 mm and 10%, it is very easy to detect them, whereas for masses with 4 mm and 2%, the detection task is extremely challenging. Even in such conditions, $\mathrm{PDE}_{\mathrm{tomo}}$ denoising always provided statistically significant improvements in performance, as well as higher CNR values and better visual appearance.

A common problem shared by all the observers is the tendency to perform too well due to the fixed, single type of lesion. Even for the subtlest lesions that were virtually impossible to see by the human eye, the observers routinely performed quite well with ROC areas approaching 0.8. As such, such model observer performances should not be construed as what would be typical of clinical performance by radiologists. Instead, these studies offer valuable insight in terms of comparing one technique against another in a fair (or equally unfair) fashion.

In summary, several numerical observers were used to analyze the mass detectability in breast CT. With real anatomical background with fixed size lesion, $\mathrm{PDE}_{\mathrm{tomo}}$ denoised images have higher detectability, higher CNR and better qualitative appearance.

Key Research Accomplishments

- Proposed and developed the Gaussian noise model, and showed its effectiveness in removing the scattered radiation based on Full Field Digital Mammography data;

- Proposed and developed three variants of PDE techniques to be used at different steps in FBP reconstruction process for volume denoising in breast CT: PDE_{tomo} algorithm, PDE_{2D} algorithm, and PDE_{3Dpost} algorithm;
- Developed a complete simulation routine of breast CT data and masses;
- Comparison between the three variants of PDE techniques showed that denoising before reconstruction resulted in better images than denoising after reconstruction;
- Clinical breast CT data have been reconstructed;
- Application of the PDE_{tomo} algorithm on simulation data and clinical data has shown improvement of image quality using CNR and resolution as figures of merit;
- Three numerical observers were custom-written;
- Application of CAD tools on the clinical breast CT data with simulated masses showed that PDE_{tomo} processed volumes resulted in higher detectability than the original volumes.

Conclusions

Dedicated breast CT imaging is a novel breast imaging modality. Compared to conventional mammography, breast CT may improve lesion detection while using a comparable radiation dose. Since it can totally remove the overlapping of tissues, it will be even more beneficial for women with dense breasts.

Still, there is a lot to be done for advancing the breast CT technology. As a result of its cone beam geometry, however, breast CT suffers from image degradation due to scatter radiation. Moreover, the breast CT images divide the dose of mammography among hundreds of projection views, resulting in considerable quantum noise. It is therefore desirable to reduce scatter and noise in the reconstructed breast volume without loss of spatial resolution.

Several new image-processing techniques were developed based on the unique physical properties of this modality. Firstly, a Gaussian noise model was proposed for scatter removal, which was a statistical model based post-acquisition scatter compensation technique. Algorithms using maximum likelihood estimation and maximum *a posterior* estimation of scatter-free images were evaluated.

Secondly, several partial diffusion equation (PDE) based denoising technique were developed for dedicated breast CT. The techniques were thoroughly evaluated based on simulation. Specifically two issues were considered: (1) where in the reconstruction process to apply a denoising technique and (2) which of the spatially adaptive techniques is a better choice. The technique was then applied to human subject data.

Finally, the project was concluded with computer aided detection tools for the assessment of mass detectability based on the original breast CT volumes and those with image processing. The previously described image processing tools were analyzed for the clinically relevant task of lesion detectability in human subjects, using numerical observers and ROC analysis methodology.

Using images obtained on a full field digital mammography system, the Gaussian noise model demonstrated effective scatter removal. The denoising techniques were also promising. Applying a denoising technique before reconstruction provides better images than after reconstruction. A PDE technique taking into the account the non-uniform distribution of the noise in the projection image after the preprocessing step provides excellent denoised data with sharp edges. It outperforms two other spatially adaptive techniques (Wiener and 2D ATM filters). The preliminary ROC study showed that with a fixed size lesion in real anatomical backgrounds, PDE_{tomo} denoised images had higher detectability, higher CNR and better qualitative appearance. These are the first steps towards the eventual goal of optimizing image quality and thus diagnostic utility for the novel modality of dedicated breast CT imaging.

Reportable Outcomes

The following is the list of papers resulted from this project, which are attached to the end of the report as appendices.

1. **Qing Xia,** Gaussian Noise Model for Scatter Compensation in Digital Mammography *(M.S. thesis, Duke University, December 2005)*.
2. **Jessie Q. Xia**, Georgia D. Tourassi, Joseph Y. Lo, Carey E. Floyd Jr., On the Development of a Gaussian Noise Model for Scatter Compensation. *Proceedings of SPIE 6510-93:1-10, 2007.*
3. **Jessie Q. Xia,** Joseph Y. Lo, Kai Yang, Carey E. Floyd Jr., John M. Boone, Dedicated Breast CT: Volume Image Denoising via a Partial Diffusion Equation Based Technique. *Medical Physics 35(5):1950-1958, 2008.*
4. **Qing Xia,** Dedicated Computed Tomography of the Breast: Image Processing and its Impact on Breast Mass Detectability *(Ph.D. dissertation, Duke University, August 2007)*.
5. **Jessie Q. Xia,** Anuj Kapadia, Joseph Lo, Improved Mass Detectability in Dedicated Breast CT by Applying Novel Volume Noise Removal Techniques, *DOD BCRP 5th Era of Hope Meeting, 2008.*
6. **Jessie Q. Xia** and Joseph Y. Lo, Simulation Study on Mass Detectability in Dedicated Breast CT: Application of PDE Volume Noise Removal. *8th IEEE International Conference on Bioinformatics and Bioengineering (BIBE) 2008, Athens, Greece. (Submitted)*

References

[1] "Breast cancer," Encyclopedia Britannica (2007).

[2] ACS, "American cancer society: Cancer facts and figures 2007," Atlanta, GA: American Cancer Society (2007).

[3] I. Reiser, R.M. Nishikawa, M.L. Giger, *et al.*, "Computerized detection of mass lesions in digital breast tomosynthesis images using two- and three dimensional radial gradient index segmentation," Technology in Cancer Research & Treatment 3, 437-441 (2004).

[4] C.E. Floyd, Jr, J.Y. Lo and G.D. Tourassi, "Cased-based reasoning computer algorithm that uses mammographic findings for breast biopsy decisions," American Journal of Roentgenology 175, 1347-1352 (2000).

[5] H.P. Chan, J. Wei, B. Sahiner, *et al.*, "Computer-aided detection system for breast masses on digital tomosynthesis mammograms: Preliminary experience," Radiology 238, 1075-1080 (2006).

[6] V.L. Ernster, J. Barclay, K. Kerlikowske, *et al.*, "Mortality among women with ductal carcinoma in situ of the breast in the population-based surveillance, epidemiology and end results program," Archives of Internal Medicine 160, 953-958 (2000).

[7] G. Dave, H. Cosmatos, T. Do, *et al.*, "Metaplastic carcinoma of the breast: A retrospective review," International Journal of Radiation Oncology Biology Physics 64, 771-775 (2006).

[8] S. Sahoo, W.M. Recant, N. Jacskowiak, *et al.*, "Defining negative margins in DCIS patients treated with breast conservation therapy: The university of Chicago experience," Breast Journal 11, 242-247 (2005).

[9] S.A. Joslyn, "Ductal carcinoma in situ: Trends in geographic, temporal, and demographic patterns of care and survival," Breast Journal 12, 20-27 (2006).

[10] K. Kerlikowske, P.A. Carney, B. Geller, *et al.*, "Performance of screening mammography among women with and without a first-degree relative with breast cancer," Annals of Internal Medicine 133, 855-863 (2000).

[11] T.M. Kolb, J. Lichy and J.H. Newhouse, "Comparison of the performance of screening mammography, physical examination, and breast US and evaluation of factors that influence them: An analysis of 27,825 patient evaluations," Radiology 225, 165-175 (2002).

[12] V.P. Jackson, R.E. Hendrick, S.A. Feig, *et al.*, "Imaging of the radiographically dense breast," Radiology 188, 297-301 (1993).

[13] J.M. Boone, T.R. Nelson, K.K. Lindfors, *et al.*, "Dedicated breast CT: Radiation dose and image quality evaluation," Radiology 221, 657-667 (2001).

[14] A.L.C. Kwan, J.A. Seibert and J.M. Boone, "An improved method for flat-field correction of flat panel x-ray detector," Medical Physics 33, 391-393 (2006).

[15] A.L.C. Kwan, J.M. Boone, K. Yang, *et al.*, "Evaluation of the spatial resolution characteristics of a cone-beam breast CT scanner," Medical Physics 34, 275-281 (2007).

[16] K. Yang, A.L.C. Kwan, D.F. Miller, *et al.*, "A geometric calibration method for cone beam CT systems," Medical Physics 33, 1695-1706 (2006).

[17] K. Yang, A.L.C. Kwan and J.M. Boone, "Computer modeling of the spatial resolution properties of a dedicated breast CT system," Medical Physics 34, 2059-2069 (2007).

[18] X. Gong, A.A. Vedula and S.J. Glick, "Microcalcification detection using cone-beam CT mammography with a flat-panel imager," Physics in Medicine and Biology 49, 2183-2195 (2004).

[19] S.C. Thacker and S.J. Glick, "Normalized glandular dose (DgN) coefficients for flat-panel CT breast imaging," Physics in Medicine and Biology 49, 5433-5444 (2004).

[20] X. Gong, S.J. Glick, B. Liu, *et al.*, "A computer simulation study comparing lesion detection accuracy with digital mammography, breast tomosynthesis, and cone-beam CT breast imaging," Medical Physics 33, 1041-1052 (2006).

[21] B. Chen and R.L. Ning, "Cone-beam volume CT breast imaging: Feasibility study," Medical Physics 29, 755-770 (2002).

[22] R.L. Ning, D. Conover, B. Chen, *et al.*, "Flat panel detector-based cone beam volume CT breast imaging: Phantom and specimen study," Proceedings of SPIE 4682, 218–27 (2002).

[23] R. Ning, "Flat panel detector-based cone beam volume CT imaging," Medical Physics 30, 1370-1370 (2003).

[24] R.L. Ning, X.Y. Tang and D. Conover, "X-ray scatter correction algorithm for cone beam CT imaging," Medical Physics 31, 1195-1202 (2004).

[25] C.J. Lai, C.C. Shaw, M.C. Altunbas, *et al.*, "Effects of radiation dose level on calcification visibility in cone beam breast CT: A preliminary study," Proceedings of SPIE 6142, 614233-1:8 (2006).

[26] L.Y. Chen, C.C. Shaw, C.J. Lai, *et al.*, "Comparison of full-scan and half-scan for cone beam breast CT imaging," Proceedings of SPIE 6142, 16424M-1:7 (2006).

[27] S.J. Tu, C.C. Shaw and L.Y. Chen, "Noise simulation in cone beam ct imaging with parallel computing," Physics In Medicine and Biology 51, 1283-1297 (2006).

[28] R.L. McKinley, M.P. Tornai, E. Samei, *et al.*, "Initial study of quasi-monochromatic x-ray beam performance for x-ray computed mammotomography," IEEE Transactions on Nuclear Science 52, 1243-1250 (2005).

[29] M.P. Tornai, J.E. Bowsher and C.N. Archer, "Feasibility of application specific emission & transmission tomography (ASETT) of the breast," Journal of Nuclear Medicine 43, 39 (2002).

[30] R.L. McKinley, M.P. Tornai, E. Samei, *et al.*, "Simulation study of a quasi-monochromatic beam for x-ray computed mammotomography," Medical Physics 31, 800-813 (2004).

[31] R.L. McKinley, M.P. Tornai, E. Samei, *et al.*, "Development of an optimal x-ray beam for dual-mode emission and transmission mammotomography," Nuclear Instruments and Methods in Physics Research A 527, 102-109 (2004).

[32] D.J. Crotty, R.L. McKinley and M.P. Tornai, "Experimental spectral measurements of heavy k-edge filtered beams for x-ray computed mammotomography," Physics in Medicine and Biology 52, 603-616 (2007).

[33] L.A. Feldcamp, L.C. Davis and J.W. Kress, "Pratical cone-beam algorithm," Journal of Optical Society of America A 1, 612-619 (1984).

[34] S.M. Kay, Fundamentals of statistical signal processing: Detection theory (Prentice Hall, 1998).

[35] H.H. Barrett, C.K. Abbey and B. Gallas, "Stabilized estimates of hotelling-observer detection performance in patient-structured noise," Proceedings of SPIE 3340, 27-43 (1998).

[36] A.H. Baydush, D.M. Catarious and C.E. Floyd, Jr, "Computer aided detection of masses in mammography using a laguerre-gauss channelized hotelling observer," Proceedings of SPIE 5034, 71-76 (2003).

[37] C.E. Metz, B.A. Herman and J.H. Shen, "Maximum likelihood estimation of receiver operating characteristic (roc) curves from continuously-distributed data," Statistics in Medicine 17, 1033-1053 (1998).

Appendices

1. M.S. thesis (2006)
2. SPIE Proceedings (2007)
3. Medical Physics paper (2008)
4. PhD dissertation (2007)
5. DOD 5th Era of Hope Meeting Abstract (2008)
6. 8th IEEE BIBE meeting paper (2008)

GAUSSIAN NOISE MODEL FOR SCATTER COMPENSATION IN DIGITAL MAMMOGRAPHY

by

Qing Xia

Institute of Statistics and Decision Science
Duke University

Date:________________________

Approved:

____
Michael L. Lavine, Ph.D, Supervisor

____
Feng Liang, Ph.D

____
Leslie M. Collins, Ph.D

A thesis submitted in partial fulfillment of
the requirements for the degree of Master of Science
in the Institute of Statistics and Decision Science
in the Graduate School
of Duke University

2006

Abstract

Breast cancer is the most common cancer type that affects women worldwide. In the United States, every one woman over eight will develop breast cancer in her lifetime. Although no effective way of preventing the disease has been found, early detection of the cancer through noninvasive breast imaging is desirable because it warrants more choices of viable treatments and higher survival rates. Digital Mammography is among such imaging techniques.

Compton scattering of x-ray photons is one mechanism of attenuating the x-ray beam, which in turn forms the contrast in a projection image. However, its detection in the projection image is a cause of image quality degradation since it will add noise to the image and reduce the contrast. Therefore many efforts are made to reduce the detected scatter radiation in the projection image either by applying some hardware during acquisition or by using post-acquisition software compensation. The method presented in this thesis belongs to the latter category. A Gaussian noise model for scatter is proposed and its EM ML estimation is derived. In addition, Bayesian MAP estimation is obtained by applying a Gibbs prior with a discontinuity adaptive potential function.

The previously proposed Poisson noise model is flawed in that the radiation does not directly follow a Poisson distribution. Instead, a Gaussian distribution can reasonably describe the radiation data. When a computation method like Gibbs sampling is used, Poisson noise model will give erroneous results due to the incorrect modeling. The conversion factor between radiation and the number of photons is energy dependent. If it is approximated by a constant independent of energy, then the Poisson noise model can be justified through a latent data augmentation scheme when EM algorithm is used.

The reason we pursue the EM computation in this thesis is that it has a nice analytic formula. Due to the large number of pixels in an image and the existence of a convolution operation, the computation can be greatly reduced with this analytic formula.

The digital mammography image of a uniform breast phantom is processed by the MLE and MAP algorithms of Poisson model and Gaussian model. The results are compared through the image quality metrics like the residual scatter radiation, the contrast-to-noise ratio and the spatial resolution.

From the results we get, it is shown that Gaussian noise model can be used to reduce the scatter radiation in the digital mammography images. Its performance is improved by incorporating Gibbs priors without loss of resolution. In addition, Gaussian noise model works slightly better in improving the contrast-to-noise ratio than the Poisson noise model.

Table of Contents

Abstract ii

List of Tables vi

List of Figures vii

List of Abbreviations x

Acknowledgments xi

Chapter 1 Introduction 1

1.1 Digital Mammography. 1

1.2 Scatter Radiation and Its Degrading Effect on the Quality of Medical Images 3

1.3 Scatter Compensation 6

1.4 Overview of the Thesis 9

Chapter 2 Materials and Methods 11

2.1 Scatter Kernel 11

2.2 Poisson Noise Model 12

2.3 Gaussian Noise Model 13

2.4 Incorporation of Gibbs prior 18

2.5 Image Acquisition 19

2.6 Image Analysis Metrics 20

  2.6.1 RSF 21

2.6.2 Contrast, Noise and CNR 21

2.6.3 Resolution 22

Chapter 3 Results and Discussion **24**

3.1 Normality Check of the Data 24

3.2 Latent Data Augmentation Scheme for Poisson Model 28

3.3 Comparison between the Two Models 29

3.4 Further Evaluation of Gaussian Noise Model 34

3.4.1 Effect of the Magnitude of the Scatter Kernel 34

3.4.2 Effect of the Delta in the Gibbs prior 38

Chapter 4 Conclusion **43**

References **45**

List of Tables

3.1: The resolution results for Poisson model and Gaussian model when delta=0.1. 33

3.2: The resolution results for the Gaussian noise model with different magnitudes of scatter kernel. 38

3.3: The resolution results for Poisson model and Gaussian model when delta=0.2. 40

3.4: The resolution results for Poisson model and Gaussian model when delta=0.05. 42

List of Figures

1.1: Typical energy spectrum of an x-ray beam. 3

1.2: Illustration of possible interactions between x-ray photons and the object to be imaged within the diagnostic x-ray energy range. 5

1.3: A simple example to see the adverse effect of detected scatter radiation on image quality. 6

1.4: An anti-scatter grid can be added on top of the detector to remove scatter radiation. 7

2.1: The three-dimensional surface plot of a scatter kernel with magnitude of 1 and FWHM of 80 pixels. 12

2.2: A sample breast phantom image taken with the beam stop array superimposed. 20

3.1: The histogram of data from a uniform region-of-interest with total of 201x201 pixels in an image acquired with an anti-scatter grid. 25

3.2: The quantile-quantile plot of the same data as in Figure 3.1 with respect to the standard Gaussian distribution with mean of 0 and standard deviation of 1. 26

3.3: One-dimensional profile through the center of a beam stop(or lead disc). 26

3.4: The histogram of data from a region-of-interest with total of 441 pixels behind a beam stop in an image acquired without an anti-scatter grid. 27

3.5: The quantile-quantile plot of the same data as in Figure3.4 with respect to the standard Gaussian distribution with mean of 0 and standard deviation of 1. 27

3.6: RSF vs. iteration plots for MLE and MAP estimator of b from both the Poisson noise model and the Gaussian noise model. 30

3.7: The noise vs. iteration plots for MLE and MAP estimator of b from both the Poisson noise model and the Gaussian noise model. 32

3.8: The contrast noise vs. iteration plots for MLE and MAP estimator of b from both the Poisson noise model and the Gaussian noise model. 32

3.9: The CNR vs. iteration plots for MLE and MAP estimator of b from both the Poisson noise model and the Gaussian noise model. 33

3.10: The RSF vs. iteration curves for the magnitude (M) of the scatter kernel ranging from 0.0 to 0.65. 35

3.11: The noise vs. iteration curves for M ranging from 0.0 to 0.65. 36

3.12: The contrast vs. iteration curves for M ranging from 0.0 to 0.65. . . 37

3.13: The CNR vs. iteration curves for M ranging from 0.0 to 0.65. 37

3.14: The noise vs. iteration plots for MLE and MAP estimators based on delta of 0.2. 39

3.15: The CNR vs. iteration plots for MLE and MAP estimators based on delta of 0.2. 40

3.16: The noise vs. iteration plots for MLE and MAP estimators based on delta of 0.05. 41

3.17: The CNR vs. iteration plots for MLE and MAP estimators based on delta of 0.05 42

List of Abbreviations

Abbreviation	Expansion
CIF	Contrast Improvement Factor
CNR	Contrast-to-Noise Ratio
MAP	Maximum ***a posteriori*** Estimate
MLE	Maximum Likelihood Estimate
ROI	Region of Interest
RSF	Residual Scatter Fraction
SF	Scatter Fraction
SPR	Scatter to Primary Ratio

Acknowledgments

I would like to thank my thesis advisor, Professor Michael L. Lavine, for his great guidance, support and encouragement.

My gratitude also goes to Professor Feng Liang and Professor Leslie Collins for serving on my thesis committee.

My PhD advisor Professor Carey E. Floyd, Jr has offered me the opportunity to work on this project as well as the freedom to explore the new method, for which I am very grateful.

Lastly, I am thankful for the support from my family including my lovely five-month old son. Their love and trust make the experience during the writing of this thesis a memorable one.

Chapter 1

Introduction

1.1 Digital Mammography

Breast cancer is the most common cancer type that affects women worldwide [1]. In the United States, every one woman over eight will develop breast cancer in her lifetime. And it was estimated that approximately 211,240 new cases of invasive breast cancer would be found in American women and the disease would kill 40,410 women in 2005 [2]. Although there is no effective way of preventing the disease, it is desirable to find early signs of the cancer (e.g., impalpable masses and/or micro-calcifications) through noninvasive breast imaging techniques such as x-ray mammography. The detection of the cancer at its early stage warrants more choices of viable treatments and higher survival rates[3-5].

An x-ray mammography system is typically comprised of two major parts: the x-ray source and the detector. Depending on the type of the detector, the mammography system can be either analog or digital. The analog system utilizes a screen-film as the detector, and is the only FDA approved screening tool aiming at the early detection of the breast cancer for women more than 40 years old. While it has been proven to be effective, it has several shortcomings: 1) the analog film has narrow latitude. Overexposure or underexposure of the film will result in a poor image which will be unacceptable for breast cancer detection and diagnosis. 2) The film development is critical for the quality of the mammogram as well as time-consuming. 3) The radiology department needs a lot of space and personnel to keep the films. And 4) the transfer of the films between departments or hospitals not only is a lot of hassle, but also causes the wear and tear of films, which is inevitable since they are often the only copies of the case. Due to these limitations of using films as the recording media, many radiology departments are trying to go film-less. It is realized by the digital mammography technique.

A digital mammography system utilizes a flat-panel detector instead of a screen-film detector. Recent studies show that the diagnostic accuracy based on digital mammograms is comparable to those based on conventional film mammograms [6, 7]. In some situations, the digital mammography works even better [6]. In addition, a digital mammography system enjoys the following merits. After x-ray exposure, a digital image of the breast can be readily read out from the flat-panel detector within seconds. There is no overexposure or underexposure issue related with this type of image since the flat-panel detectors have a wide latitude and excellent linear relationship between pixel values and exposure levels. The image can be saved into different media. The transfer and copy of the images are easy, fast and reliable. A very recent study [8] shows that the digital mammography images can be accurately transferred via the broadband internet, which will greatly alleviate the problem related to the shortage of mammographers as well as improve the accuracy of the diagnosis. Moreover, the digital format of images makes advanced imaging (e.g., breast tomosynthesis [9, 10]) and image processing techniques (such as the technique presented in the thesis) feasible.

1.2 Scatter Radiation and Its Degrading Effect on the Quality of Medical Images

X-ray source emits x-ray photons with different energies. Figure 1.1 shows a typical energy spectrum of an x-ray beam. When the beam passes through the object to be imaged such as a breast, it interacts with the matter and gets attenuated. At the

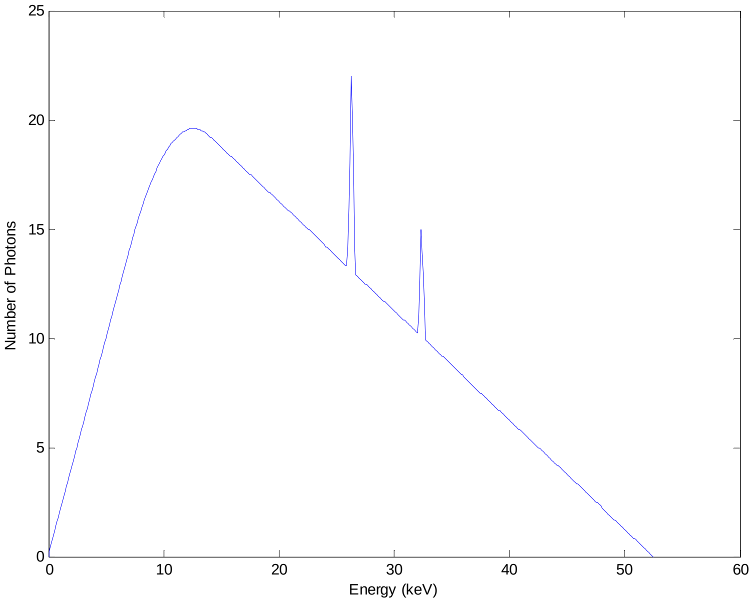

Figure 1.1: Typical energy spectrum of an x-ray beam. The abscissa represents the energy levels that a photon can possibly take on, and ordinate represents the number of photons having the corresponding energy level. The peak voltage (in the unit of kVp) corresponds to maximal energy level. The spectrum shown here has a peak voltage of 52.5 kVp.

diagnostic energy level, there are three basic mechanisms for x-ray attenuation: photoelectric effect, Compton scattering and Raleigh scattering [11]. Raleigh scattering, also called coherent scattering, accounts for less than 5% of the total interactions between x-rays and the matter. Therefore it is often omitted for consideration. Photoelectric effect occurs when x-ray photons are totally absorbed by the atoms within the tissue, as illustrated by ray 1 in Figure 1.2. Compton scattering occurs when the photons are deflected from their incident path with partial energy loss. These photons are called scattered photons or scatter radiation, as shown by ray 2 in Figure 1.2. The rest will survive the attenuation and are called the primary photons or primary radiation (ray 3 in Figure 1.2). The primary radiation differs from location to location, which forms the contrast of various tissues in the final image.

The scatter radiation escaped from the imaged object can either miss the detector or impinge on it. The latter will be inevitably detected due to the fact that the detector typically has broad energy sensitivity and does not effectively reject photons that have lost energy by scattering. The total radiation detected is thus the sum of the primary radiation and the scatter radiation. The detection of scattered photons in locations that are different from their original path will add a component of noise and cause the blurring of the image.

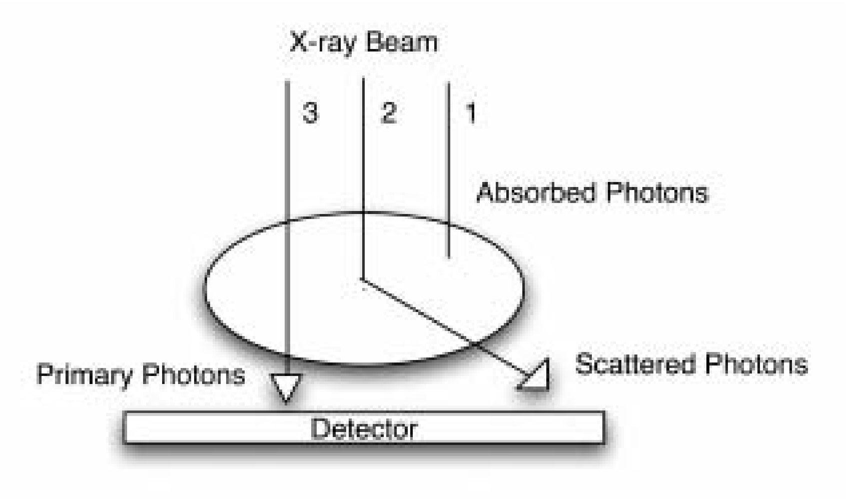

Figure 1.2: Illustration of possible interactions between x-ray photons and the matter within the diagnostic x-ray energy range. The ellipsoid represents the object to be imaged. Photons can be totally absorbed by the photoelectric effect (ray 1), or be scattered through Compton scattering (ray 2) and Raleigh scattering (a very small portion, thus neglected). The rest will survive the attenuation and are called the primary photons or primary radiation (ray 3).

To see how detected scatter radiation adversely affect the quality of a medical image, let's take a look at the simple example shown in Figure 1.3. An ellipsoid lesion is embedded in a uniform background. In the ideal case where no scatter radiation is detected, the total radiation is equal to the primary radiation. In Figure 1.3 (a), assume radiation in the background is P_0 and radiation in the lesion is P_1, then the contrast of the lesion is $C_1 = (P_1-P_0)/P_0$. If in practice, a constant scatter radiation S is added all over the image (shown in Figure 1.3(b)), then the radiation in the background becomes $T_0 = P_0+S$ and radiation in the lesion becomes $T_1 = P_1+S$. The contrast of the lesion in this image will be $C_2 = (T_1-T_0)/T_0 = (P_1-P_0) / (P_0+S) = C_1 *[P_0 / (P_0+S)]$, which is smaller than C_1. That is, the detection of scatter radiation reduces the contrast of the lesion. In cases where scatter is large, lesions can even be obscured.

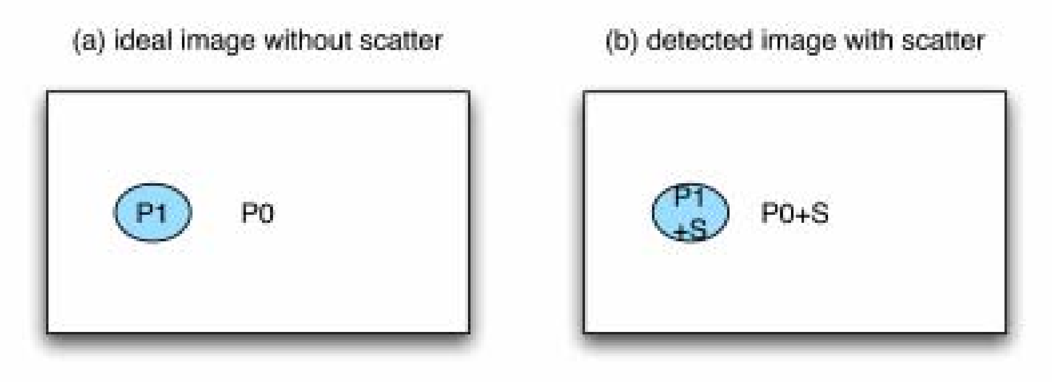
(a) ideal image without scatter
P1
P0
(b) detected image with scatter
P1
+S
P0+S

Figure 1.3: A simple example to demonstrate the adverse effect of detected scatter radiation on image quality. An ellipsoid lesion is embedded in a uniform background. (a) The ideal image without scatter radiation is shown. (b) The actual image is shown, which is the sum of primary radiation and scatter radiation. The contrast of the lesion is decreased.

1.3 Scatter Compensation

In summary, the scatter radiation is a physical phenomenon, which together with photoelectric effect causes the attenuation of the x-ray beam. The detection of scatter radiation on the detector will degrade the quality of the image and thus adversely affect the medical diagnosis. This issue exists widely in many imaging techniques such as Single Photon Emission Computed Tomography (SPECT) [12], Positron Emission Tomography (PET) [13], and projection radiographies like chest radiography [14] and mammography [15]. Therefore, it is important to reduce the scatter radiation that is detected. Or in other words, scatter radiation needs to be compensated.

There are two general categories of scatter radiation compensation methods: one is hardware compensation such as the application of anti-scatter grids [16], slot scanning systems [17], or air gaps [18]; the other is software compensation via post-acquisition image processing, such as simple estimation-subtraction [19], convolution-subtraction [20], de-convolution [21], artificial neural networks [22], maximum likelihood expectation maximization (EM-MLE) [23], or Bayesian image estimation [24, 25].

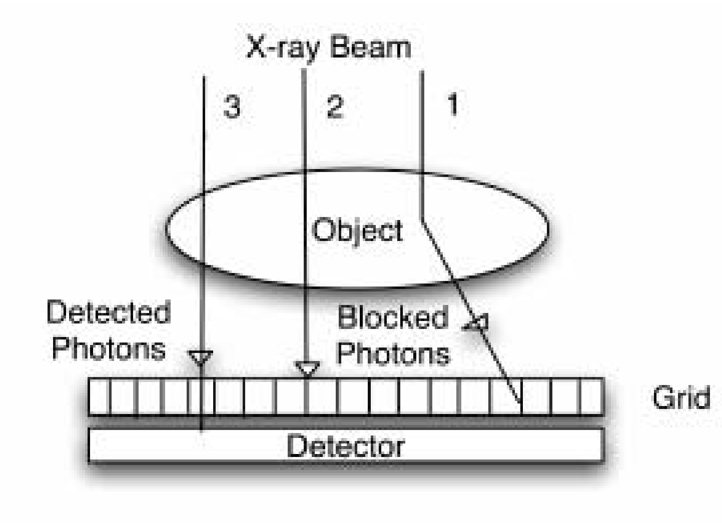

Figure1.4: An anti-scatter grid can be added on top of the detector to remove scatter radiation. However, as shown by the middle ray, some primary radiation will be blocked as well. To maintain the image quality, the patient dose has to be increased.

An anti-scatter grid is routinely used on a clinical screen-film mammography system. Figure 1.4 illustrates how an anti-scatter grid can be used to reduce the scatter radiation. The orientation of the grid slots is parallel to the primary radiation. Most primary radiation will pass through the slots and reach the detector. Scatter radiation, by contrast, will mostly hit on the metal slits and be absorbed by them.

Thus an anti-scatter grid effectively removes many scatter radiation. Its major drawback is that it also removes some primary radiation, as shown by the middle ray of Figure 1.4. To maintain the same image quality, the magnitude of the x-ray beam needs to be increased, which will also increase the total absorbed dose of the patient.

By contrast, post-acquisition image processing techniques won't change the dose that a patient receives. In addition, some studies [15, 24] show that they can be more effective than an anti-scatter grid in scatter compensation.

A fundamental assumption behind the image processing techniques is that the scatter radiation can be approximated by the convolution of the primary radiation and a scatter kernel. It is verified both theoretically [26] and empirically [27, 28]. In the two-dimensional case, if Y is used to represent the matrix of detected total radiation at each pixel, D for the matrix of the primary radiation, S for the matrix of the scatter radiation, and P for the matrix of the scatter kernel, then the following equation is true:

$$Y = D + S = D + D ** P = D ** (\delta + P), \tag{1.1}$$

where ** is the two-dimensional convolution operator and δ is the Dirac delta function in a matrix form. The task of scatter compensation is equivalent to estimating the unknown D from the measured Y.

One solution is to de-convolve the Equation (1.1) [21, 29, 30]. If this is done through the Fourier Transform (FT), then

$$D = FT^{-1}\left(\frac{FT(Y)}{FT(\delta + P)}\right). \tag{1.2}$$

Or, statistical models can be formulated to solve the problem. In the past Poisson noise model was used, which assumed that both primary radiation and scatter radiation follow Poisson distributions. The maximum likelihood estimate (MLE) of D in two-dimensional projection radiography was obtained by borrowing the iterative equation originally derived for SPECT reconstruction [23], and it was combined with a Gibbs prior to form the maximum ***a posteriori*** (MAP) estimator of D [24]. Later a revision was made on the iterative equation [26]. Although promising, the Poisson noise model presents some problems: 1) the primary radiation and scatter radiation can not be directly modeled to follow Poisson distribution; 2) due to the polychromatic characteristic of x-ray beam, the radiation is not only related to the number of photons but to the energies of the photons as well. Therefore, in this thesis, a new explanation is given that justifies the Poisson noise model, and a new model is proposed, implemented and tested on the digital mammography data for the reduction of detected scatter radiation.

1.4 Overview of the Thesis

The thesis is organized as follows. In Chapter 2, the old Poisson noise model is briefly introduced. The Gaussian noise model is then proposed and its analytical EM algorithm is derived. Moreover, the Gibbs prior is incorporated into the algorithm to constrain the noise in the processed image. Chapter 3 presents the latent data augmentation scheme to justify the Poisson noise model, the image processing results obtained from both the Poisson model and the Gaussian model, their comparison as well as the some further evaluation of the Gaussian noise model. The thesis is concluded in chapter 5.

Chapter 2

Materials and Methods

2.1 Scatter Kernel

Towards the end of the previous chapter, we mentioned that scatter radiation is often modeled as the convolution of the primary radiation and a scatter kernel. The scatter kernel is also called scatter point spread function (PSF). Experiments [31, 32] and Monte-Carlo simulation models [33, 34] showed that the scatter kernel can be represented by a circularly symmetric exponential decay curve. The curve can be uniquely determined by two parameters: the magnitude (M) and full width at half maximum (FWHM). The two parameters are illustrated in Figure 2.1 (a). Figure 2.1(b) shows the three-dimensional representation of such a scatter kernel with M of 1 and FWHM of 80 pixels. Throughout the thesis, matrix P is used to represent the scatter kernel and it is known ***a priori***.

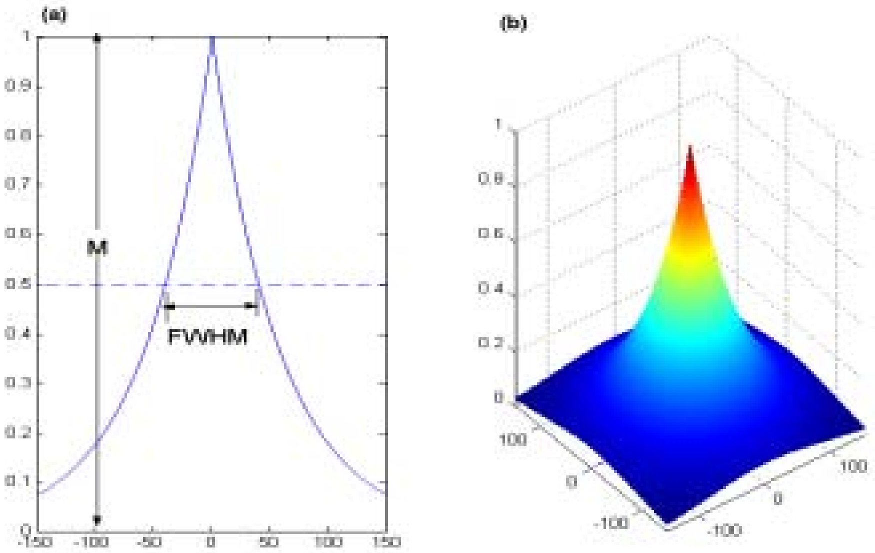

Figure 2.1: A sample scatter kernel with magnitude of 1 and FWHM of 80 pixels. (a) One-dimensional profile of the kernel. (b) Its three-dimensional surface plot.

2.2 Poisson Noise Model

When put in a statistical framework, equation (1.1) becomes:

$$E(Y) = E(D+S) = B + B**P \quad , \qquad (2.1)$$

where $B = E(D)$. If we use d_i, s_i, and y_i (i=1,…,N; N is the total number of pixels in the image) to represent the elements in the matrices D, S and Y, then Poisson noise model is as follows:

$$\boxed{\begin{array}{l} d_i \mid B \sim Poisson(b_i) \\ s_i \mid B \sim Poisson((B**P)_i) \\ y_i = d_i + s_i \mid B \sim Poisson(b_i + (B**P)_i) \end{array}} \, , \qquad (2.2)$$

where d_i and s_i (i=1,…,N) given B are mutually independent. The purpose of using

(B**P)$_i$ to represent $\sum_{j=1}^{N} b_j p_{ij}$ is two-folds: 1) (B**P)$_i$ is more straightforward than $\sum_{j=1}^{N} b_j p_{ij}$ and 2) it is a reminder to us that two-dimensional convolution has a fast implementation in Fourier domain. We are interested in estimating B = {b$_i$; i=1,…,N}.

In [26], a detailed derivation of MLE estimators of B through Expectation Maximization was provided. For conciseness, only the final iterative equation is shown here:

$$b_k^{(n+1)} = b_k^{(n)} \cdot \frac{y_k}{b_k^{(n)} + (B^{(n)} **P)_k} \tag{2.3}$$

2.3 Gaussian Noise Model

The radiation is intrinsically related to the number of photons via a conversion factor, which is a function of the photon energy. Even if an ideal monochromatic x-ray beam is available, i.e. all the photons from the x-ray source carry the same energy, the detected primary photons have the same energy but the detected scatter photons vary in their energy levels, thus causing different radiation or exposure conversion efficiency. This issue will be even more apparent when in practice a polychromatic x-ray beam as what’s shown in Figure 1.1 is usually used. In this case even the primary photons will take on different energy levels. The radiation or exposure will be related not only to the number of photons, but also to their individual energies and the energy-dependent conversion factors.

As will be discussed in the next chapter, our experimental data show that primary d_i and scatter radiation s_i can not be directly modeled as Poisson distribution. By contrast, the data approximately follow Gaussian distribution. Thus, a Gaussian noise model is proposed as follows:

$$\boxed{\begin{aligned} & d_i \mid B, {\sigma_{i1}}^2 \sim Gaussian(b_i, {\sigma_{i1}}^2) \\ & s_i \mid B, {\sigma_{i2}}^2 \sim Gaussian((B**P)_i, {\sigma_{i2}}^2) \\ & y_i = d_i + s_i \mid B, {\sigma_{i1}}^2, {\sigma_{i2}}^2 \sim Gaussian(b_i + (B**P)_i, {\sigma_{i1}}^2 + {\sigma_{i2}}^2) \end{aligned}} \tag{2.4}$$

where d_i, s_i, y_i and b_i have the same meaning as those in Poisson noise model (in block (2.2)). In addition, ${\sigma_{i1}}^2$ and ${\sigma_{i2}}^2$ represent the variance of the primary radiation and the variance of the scatter radiation in each pixel i.

Due to the convolution operation, the estimation of B = {b_i; i=1,…,N} directly from Y does not have a simple analytic form. The MLE of B is thus derived through the EM algorithm as follows.

Treat the measured Y = {y_i, i=1,…,N} as an incomplete dataset, and unobserved (D,S) = {(d_i,s_i), i=1,…,N} as a complete dataset. The d_i ’s and s_i ’s given B are mutually independent, therefore the complete data likelihood is:

$$p_c(D,S \mid B, \{{\sigma_{i1}}^2, {\sigma_{i2}}^2; i=1,...,N\}) = \prod_{j=1}^{N} [\frac{1}{\sqrt{2\pi{\sigma_{j1}}^2}} e^{-(d_j-b_j)^2/2{\sigma_{j1}}^2} \cdot \frac{1}{\sqrt{2\pi{\sigma_{j2}}^2}} e^{-(s_j-(b**p)_j)^2/2{\sigma_{j2}}^2}]. \tag{2.5}$$

Assuming {${\sigma_{i1}}^2$, ${\sigma_{i2}}^2$; i=1,…,N} are known, we will get the complete data log likelihood by taking the logarithm on both sides,

$$L_c(B\,|\,D,S)=\sum_{j=1}^{N}[-(d_j-b_j)^2/2\sigma_{j1}{}^2-(s_j-(b**p)_j)^2/2\sigma_{j2}{}^2-\log\sqrt{2\pi\sigma_{j1}{}^2}-\log\sqrt{2\pi\sigma_{j2}{}^2}]\cdot \tag{2.6}$$

The EM algorithm is comprised of two steps: one is the E-step where the expectation of the complete data log likelihood with respect to the present estimate of B is computed; and the other is the M-step where a new estimate of B is obtained which will maximize the computed expectation in the E-step.

Firstly, let us consider the E-step:

$$\begin{aligned}&Q(B\,|\,B^{(n)})\\&=E[L_c(B\,|\,D,S)\,|\,Y,B^{(n)}]\\&=\sum_{j=1}^{N}\{-(b_j{}^2-2d_j{}^{(n)}b_j)/2\sigma_{j1}{}^2-[((B**P)_j)^2-2s_j{}^{(n)}(B**P)_j]/2\sigma_{j2}{}^2\\&+terms\cdot independent\cdot of\ \cdot B\},\end{aligned} \tag{2.7}$$

where $$\begin{aligned}d_j{}^{(n)}&=E[d_j\,|\,Y,B^{(n)}]\\ s_j{}^{(n)}&=E[s_j\,|\,Y,B^{(n)}]\end{aligned}\ . \tag{2.8}$$

Secondly, consider the M-step to find $B^{(n+1)}$ that will maximize $Q(B|B^{(n)})$:

$$\frac{\partial Q(B\,|\,B^{(n)})}{\partial b_k}=0=-(2b_k-2d_k{}^{(n)})/2\sigma_{k1}{}^2-\sum_{j=1}^{N}[2(B**P)_j\,p_{jk}-2s_j{}^{(n)}p_{jk}]/2\sigma_{j2}{}^2\,.$$

Solving the above equation for b_k gives

$$b_k{}^{(n+1)}=d_k{}^{(n)}-\sigma_{k1}{}^2\sum_{j=1}^{N}p_{jk}\cdot[(B^{(n+1)}**P)_j-s_j{}^{(n)}]/\sigma_{j2}{}^2. \tag{2.9}$$

Using $B^{(n)}$ to approximate $B^{(n+1)}$ in the right hand side, we get:

$$b_k^{(n+1)} = d_k^{(n)} - \sigma_{k1}^{2} \sum_{j=1}^{N} p_{jk} \cdot [(B^{(n)} ** P)_j - s_j^{(n)}] / \sigma_{j2}^{2}. \qquad (2.10)$$

As a good estimate of the primary image is formed, $(B^{(n)} ** P)_j - s_j^{(n)} \approx 0$, then,

$$b_k^{(n+1)} \cong d_k^{(n)}. \qquad (2.11)$$

The same apparent form was obtained for Poisson noise model in [26]. But due to the different statistical models, the actual forms of $d_k^{(n)}$ are different and so do the iterative formula of b_k. We will get the iterative formula of b_k for the Gaussian noise model through the following theorem.

Theorem 2.1 Let X ~ Gaussian(μ_x,σ_x^2), Y ~ Gaussian(μ_y,σ_y^2), independent. Let Z=X+Y be the third random variable. We know that Z follows a Gaussian distribution with mean of μ_z =(μ_x+μ_y) and variance of σ_z^2 =(σ_x^2+σ_y^2). It can be proved that the conditional distribution of X|X+Y i.e. X|Z is

$$Gaussian\left(\left(\frac{\sigma_x^2}{\sigma_z^2} Z + \frac{\sigma_y^2}{\sigma_z^2} \mu_x - \frac{\sigma_x^2}{\sigma_z^2} \mu_y\right), \frac{\sigma_x^2 \sigma_y^2}{\sigma_z^2}\right).$$

Proof: According to the definition of conditional distribution:

$$p(X \mid Z) = \frac{p(X,Z)}{p(Z)} = \frac{p(Z \mid X) p(X)}{p(Z)}. \qquad (2.12)$$

Note that

$$p(Z \mid X) = p(X+Y \mid X) = p(Y) = p(Z - X). \qquad (2.13)$$

Therefore, equation (2.12) becomes:

$$p(X \mid Z) = \frac{p(Z-X) p(X)}{p(Z)}$$

$$= \frac{\frac{1}{\sqrt{2\pi\sigma_y^{\,2}}} e^{-\frac{(y-\mu_y)^2}{2\sigma_y^{\,2}}} \frac{1}{\sqrt{2\pi\sigma_x^{\,2}}} e^{-\frac{(x-\mu_x)^2}{2\sigma_x^{\,2}}}}{\frac{1}{\sqrt{2\pi\sigma_z^{\,2}}} e^{-\frac{(z-\mu_z)^2}{2\sigma_z^{\,2}}}}$$

$$= \frac{1}{\sqrt{2\pi \frac{\sigma_x^{\,2}\sigma_y^{\,2}}{\sigma_z^{\,2}}}} e^{-\frac{[x-(\frac{\sigma_x^{\,2}}{\sigma_z^{\,2}}Z+\frac{\sigma_y^{\,2}}{\sigma_z^{\,2}}\mu_x-\frac{\sigma_x^{\,2}}{\sigma_z^{\,2}}\mu_y)]^2}{2(\frac{\sigma_x^{\,2}\sigma_y^{\,2}}{\sigma_z^{\,2}})}}$$

$$\sim Gaussian((\frac{\sigma_x^{\,2}}{\sigma_z^{\,2}} Z + \frac{\sigma_y^{\,2}}{\sigma_z^{\,2}} \mu_x - \frac{\sigma_x^{\,2}}{\sigma_z^{\,2}} \mu_y), \frac{\sigma_x^{\,2}\sigma_y^{\,2}}{\sigma_z^{\,2}}) .$$

□

Because the primary and scatter radiation of each pixel given B is independent of those of other pixels, $d_k^{(n)} = E[d_k \mid Y, B^{(n)}] = E[d_k \mid y_k = d_k + s_k, B^{(n)}]$. Consider random variables in Theorem 2.1 to be X=d$_k$, Y=s$_k$ and Z=y$_k$, therefore,

$$d_k^{(n)} = (\sigma_{k1}^{\,2} y_k + \sigma_{k2}^{\,2} b_k^{(n)} - \sigma_{k1}^{\,2}(B^{(n)} **P)_k]/(\sigma_{k1}^{\,2} + \sigma_{k2}^{\,2}) . \tag{2.14}$$

Then equation (2.11) combines with equation (2.14) to give the following updating equation:

$$b_k^{(n+1)} = b_k^{(n)} + W_k \cdot [y_k - (b_k^{(n)} + (B^{(n)} **P)_k)], \tag{2.15}$$

where

$$W_k = \sigma_{k1}^{\,2} /(\sigma_{k1}^{\,2} + \sigma_{k2}^{\,2}) . \tag{2.16}$$

2.4 Incorporation of Gibbs Prior

MLEM is known to have adverse effect on high frequency image noise. To overcome this, some constraints can be put on the noise level within the estimated B, or in other words, the prior information about B is provided. By Bayes's Rule,

$$p(B|Y) \propto p(Y|B)p(B), \tag{2.17}$$

where p(B) is the prior joint distribution of B={b_i; i=1,…,N}, p(Y|B) is equal to the likelihood of B, and p(B|Y) is the posterior joint distribution of B given measured pixel values Y={y_i; i=1,…,N}.

We assume B is a Markov random process; it therefore follows a Gibbs distribution:

$$p(B) = \frac{1}{K} e^{-U(B)/\beta}, \tag{2.18}$$

where K is a normalizing factor which is independent of B, U(B) is the energy function, and β is a free parameter adjusting the relative weight of this prior on the maximum ***a posteriori*** (MAP) estimator of B. When β is approaching infinity, the MAP of B approaches MLE of B.

The energy function is the sum of the potential function, i.e.,

$$U(B) = \sum_{c \in C} V_c(B), \tag{2.19}$$

where C is the set comprised of all cliques in the image. One clique is defined as a set of pixels where each one is a neighbor of all the others in the same clique. In the thesis, the Gibbs prior is defined over a 2nd –order neighborhood system (for each pixel its north, south, east, west neighboring pixels plus its four diagonal neighboring pixels) with each clique comprising of two neighboring pixels. There are many forms of the potential function Vc(b). The one we pick up is adaptive to discontinuity [35-37]:

$$V(\{b_i : b_j\}) = \frac{(b_i - b_j)^2}{\delta_c{}^2 + (b_i - b_j)^2}, \qquad (2.20)$$

where i and j are the neighboring pixels within the clique i~j. The b_i and b_j represent their intensities. δ_c is an adjustable parameter to regulate the cut-off frequency of the noise in the image.

2.5 Image Acquisition

A Siemens prototype digital mammography system (Mammomat Novation ^{DR}) with 70 μm isotropic resolution was used for image acquisition. Uniform breast phantoms (CIRS, Inc., Norfolk, VA) were imaged with the x-ray beam generated by 28kVp and Mo/Mo target/filter combination. The phantoms are radiographically equivalent to a compressed breast of 4cm in thickness and 50% in glandular tissue density. At the center of the phantom there is a square dent, which mimics a high-contrast lesion in the digital mammography images. The images used in this thesis were acquired without an anti-scatter grid. Some of them have a beam stop (i.e., lead discs with 3mm diameter) array superimposed on the breast phantoms. The beam stop method is a standard technique to measure the scatter radiation. Because lead discs absorb all the primary radiation, only scatter radiation can arrive behind them. Figure 2.2 shows one such image.

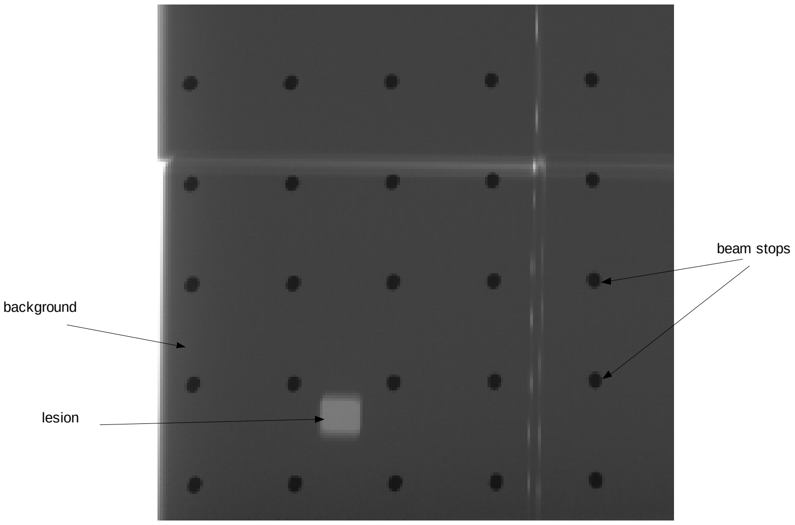

Figure 2.2: A sample breast phantom image taken with the beam stop array superimposed. The bright square mimics a high density lesion, based on which the contrast and CNR values are obtained.

The image can then be fed into the algorithms for processing. The effect of processing is evaluated through various metrics, which will be discussed in the following subsection.

2.6 Image Analysis Metrics

The primary purpose of the algorithms is to estimate the expectation of primary radiation. Its effect is measured by the residual scatter fraction (RSF). At the same time, it is desirable that the contrast-to-noise ratio (CNR) will be constrained or even improved after image processing. In addition, the effect of the algorithms on spatial resolution of the image has to be carefully monitored. In the following, we will give the definition of each of these metrics and how they are measured in this thesis.

2.6.1 Residual Scatter Fraction

Scatter fraction (SF) is defined as the ratio of the scatter radiation to the total radiation. Residual scatter fraction (RSF) is a quantity used to indicate how much of the scatter radiation remains after applying the scatter compensation algorithm.

For the given imaging technique, two sets of images of the phantom were obtained. One is taken without a beam stop array, and the other is taken with the beam stop array. The signals behind beam stops (lead discs) are the scatter radiation. The total radiation, which is the sum of primary radiation and the scatter radiation, will reach the region without the beam stops. Thus the measured primary radiation ($P_{measured}$) is calculated by subtracting the mean radiation of a region-of-interest (ROI) behind a beam stop from the mean of the same ROI location without a beam stop. In the image processed for scatter compensation, the mean of total radiation (T) in the same ROI location ($T_{estimated}$) is the sum of the residual scatter radiation and the primary radiation. Then

$$RSF = \frac{T_{estimated} - P_{measured}}{T_{estimated}} . \qquad (2.21)$$

2.6.2 Contrast, Noise and CNR

The contrast is defined as the ratio of the difference between the mean value of the lesion (T_{lesion}) and that of the background ($T_{background}$) to the mean of the background. That is,

$$Contrast = \frac{T_{lesion} - T_{background}}{T_{background}} . \tag{2.22}$$

The noise is derived by dividing the standard deviation ($STD_{background}$) to the mean ($T_{background}$) of the background:

$$Noise = \frac{STD_{background}}{T_{background}} . \tag{2.23}$$

Contrast-to-noise ratio is the ratio of the contrast to the noise. i.e.,

$$CNR = \frac{Contrast}{Noise} = \frac{T_{lesion} - T_{background}}{STD_{background}} . \tag{2.24}$$

2.6.3 Resolution

Due to the nonlinearity of the algorithm, the metric like modulation transfer function (MTF) which is designed for a linear system can not be used here. Instead, a test bar comprised of alternating bright and dark lines with size corresponding to Nyquist frequency are embedded in the phantom image.

The contrast improvement factor (CIF), defined as the ratio of the contrast after image processing to the initial contrast, is obtained for the test bar with various initial contrast. If CIF is not less than 1, no resolution is lost. Otherwise, resolution is degraded. The minimal initial contrast that the test bar can take on with CIF no less than 1 is recorded as an indication of the effect of the image processing on resolution.

Chapter 3

Results and Discussion

3.1 Normality Check of the Data

In our new model, primary, scatter and total radiations of each pixel in the projection mammography images are assumed to follow Gaussian distributions. To check whether Gaussian distribution is a good approximation to the real data, we analyze a uniform ROI outside of a beam stop (ROI1) and a uniform ROI behind a beam stop (ROI2) in an image acquired without an anti-scatter grid.

ROI1 is a square region with 201x201 pixels, and its histogram is plotted in Figure 3.1. Visually, it follows approximately a Gaussian distribution. For further evaluation, the empirical quantile-quantile plot of the data with respect to a standard Gaussian distribution is drawn in Figure 3.2. The quantile of the data has a nice linear relationship with the quantile of the standard Gaussian distribution, indicating that the total radiation can be well represented by a Gaussian distribution.

As stated before, the exposure of the area behind a beam stop is due to the scattered radiation from the neighboring regions. Figure 3.3 shows the profile of radiation along a line through the center of a beam stop. It has a nice flat profile for the scatter radiation. The circular ROI2 is selected which has a total number of 441 pixels. Its histogram and quantile-quantile plot with respect to the standard Gaussian distribution are shown in Figure 3.4 and Figure 3.5 respectively. Figure 3.5 shows that scatter radiation is also approximately Gaussian distribution.

It is obvious that both total radiation shown in Figure 3.1 and scatter radiation shown in Figure 3.4 can not be directly modeled as Poisson distributions, since 1) the radiation does not take on discrete integer values only; and 2) the variance is much smaller than the mean, whereas a Poisson distribution has an equal variance and mean. Therefore, from the modeling perspective, the Poisson noise model (shown in block (2.2)) is problematic especially when a computation method other than EM algorithm is used. Luckily, if the model is modified by adding a latent data, then the iterative equation (equation (2.3)) derived from EM algorithm can be approximately true under certain assumptions.

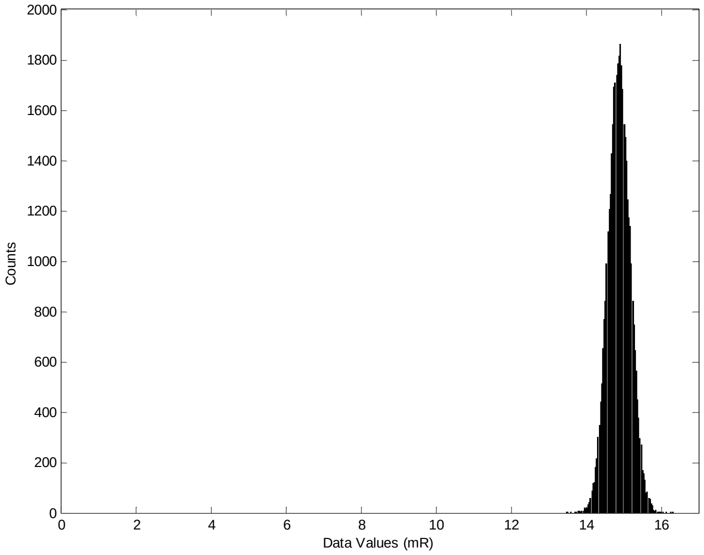

Figure 3.1: The histogram of data from a uniform region-of-interest with total of 201x201 pixels in an image acquired without an anti-scatter grid. The data is seen to be approximately Gaussian distribution.

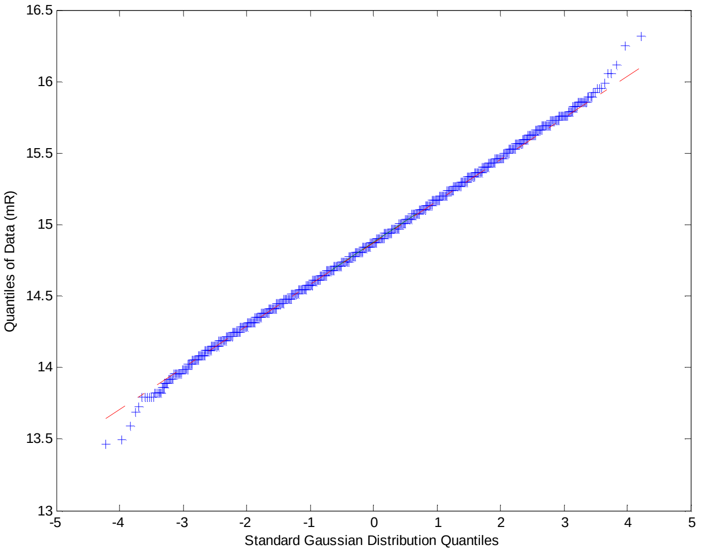

Figure 3.2: The quantile-quantile plot of the same data as in Figure 3.1 with respect to the standard Gaussian distribution with mean of 0 and standard deviation of 1. The data fits well with the Gaussian distribution.

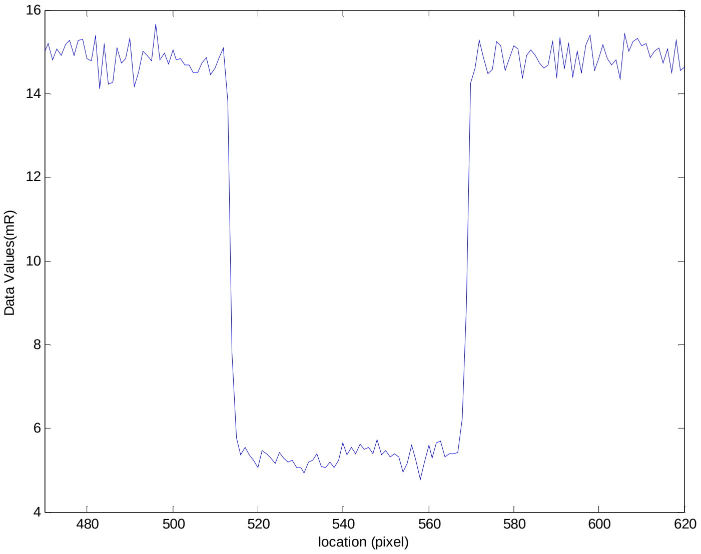

Figure 3.3: One-dimensional profile through the center of a beam stop (or lead disc).

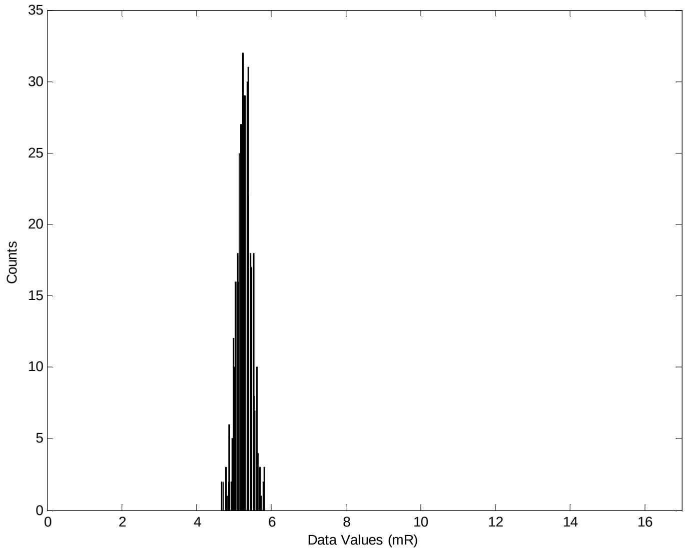

Figure 3.4: The histogram of data from a circular region-of-interest with total of 441 pixels behind a beam stop in an image acquired without an anti-scatter grid. The data is seen to be approximately Gaussian distribution.

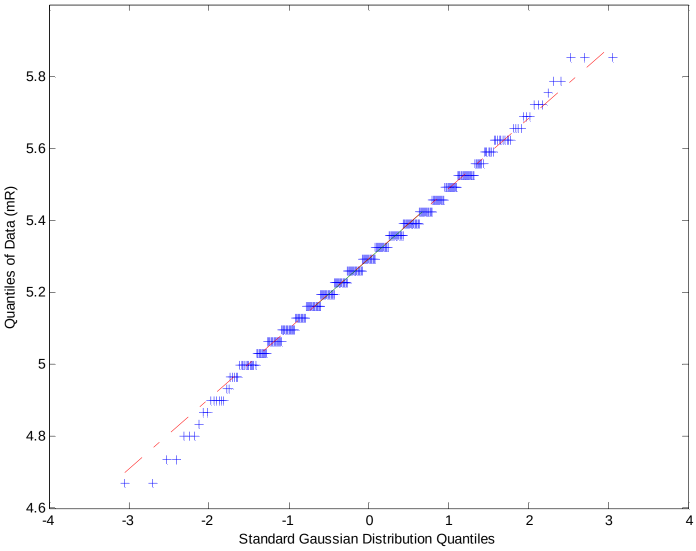

Figure 3.5: The quantile-quantile plot of the same data as in Figure3.4 with respect to the standard Gaussian distribution with mean of 0 and standard deviation of 1.

Except an outlier (data value is about 1.7mR), the rest data fits well with the Gaussian distribution.

3.2 Latent Data Augmentation Scheme for Poisson Model

Assume the exposure or radiation is intrinsically proportional to the number of photons that produce the radiation through a constant C (E), which is dependent on the energies of photons E. For d_i, s_i and y_i, the corresponding number of photons are nd_i, ns_i, and ny_i. The expected number of photons for nd_i is nb_i. The following model is valid:

$$\boxed{\begin{aligned} &nd_i \mid NB \sim Poisson(nb_i) \\ &ns_i \mid NB \sim Poisson((B**P)_i) \\ &ny_i = nd_i + ns_i \mid NB \sim Poisson(nb_i + (NB**P)_i) \end{aligned}}. \tag{3.1}$$

The updating equation for nb_i is the same as equation (2.3):

$$nb_k^{(n+1)} = nb_k{}^{(n)} \cdot \frac{ny_k}{nb_k^{(n)} + (NB^{(n)}**P)_k} . \tag{3.2}$$

If by simplification, assume a single energy independent conversion constant C instead of a set of C(E) exists, then

$$\begin{aligned} b_k &= E(d_k) = C \cdot E(nd_k) = C \cdot nb_k \\ y_k &= C \cdot ny_k \end{aligned}. \tag{3.3}$$

And then,

$$b_k^{(n+1)} = b_k{}^{(n)} \cdot \frac{y_k}{b_k^{(n)} + (B^{(n)}**P)_k} , \tag{3.4}$$

which is the same updating equation for b_k as equation (2.3). In other words, as long as a single conversion constant rather than a set of energy dependent conversion constants C(E) exists between the radiation and the number of photons, The equation (2.3) or (3.3) derived from EM algorithm is scale-invariant regardless of the value of latent data C.

3.3 Comparison between the Poisson and Gaussian Models

Gaussian noise model is sounder than Poisson noise model for the direct modeling of radiations. Poisson model won't give an accurate answer if computation methods which rely heavily on the accuracy of the model such as Gibbs sampling are adopted. However, when EM algorithm is used, the iterating equation obtained based on Poisson assumption can roughly be used to update the expectation of primary radiation. This is based on a simplification that a single conversion factor is valid for all radiation levels, which is not true in reality. By contrast, Gaussian noise model allows for the different conversion factors for different energies.

For the uniform breast phantom, empirical value of W_i (i=1,…,N) in the Gaussian model as shown in equation (2.16) is 0.45. The empirical optimized scatter kernel P has FWHM=80pixels (i.e., 5.6mm) and M=0.52. The images are processed to obtain the MLE estimates from both models. Also the MAP estimates are obtained from both models using the same Gibbs prior with delta of 0.10.

As a convention, in all the figures shown hereafter, the values for iteration 0 are the values measured on the original image without any processing.

Figure 3.6 shows the plots of RSF of MLE and MAP estimates from both models as a function of iteration number. All estimators successfully reduce the scatter radiation in the processed image such that RSF drops with iteration. In addition, they all asymptotically converge to the same value of 0.019 from the original scatter fraction of 0.354. Note that estimators based on Poisson noise model have a slightly faster convergence rate than those based on Gaussian noise model. For example, at iteration 2, the RSF of estimators from Poisson model already drops to 0.019, whereas that from Gaussian model is 0.047.

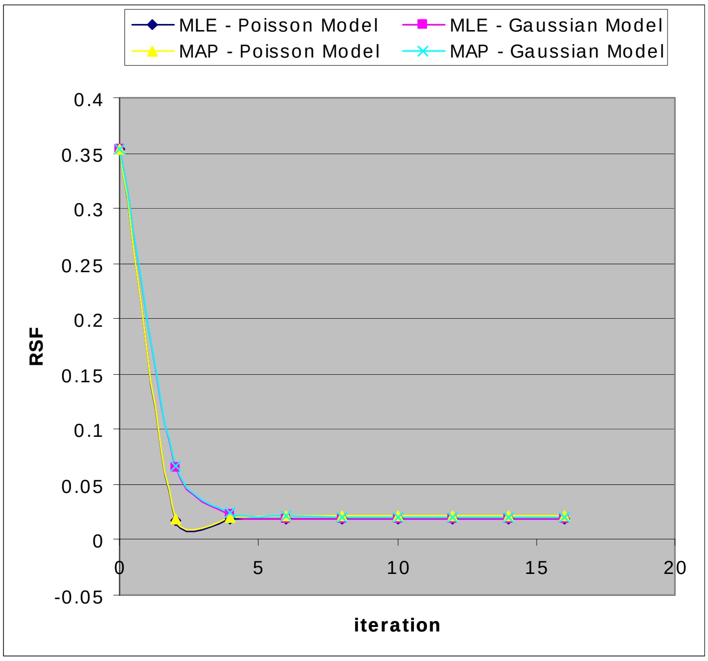

Figure 3.6: RSF vs. iteration plots for MLE and MAP estimator of b from both the Poisson noise model and the Gaussian noise model. The magnitude of scatter kernel is 0.52, which is same as the measured scatter-to-primary ratio (SPR). Therefore, RSF all drops close to zero, meaning almost complete scatter compensation.

Figure 3.7 to Figure 3.9 illustrate how noise, contrast and CNR individually change with iteration numbers. Let’s look at Figure 3.7 first. At iteration 16, the MLE estimators of both Poisson model and Gaussian model increase the noise from the original 0.021 to 0.031, which corresponds to a 47.6% of increase. The MAP estimator from Poisson model keeps the noise at a roughly same level as the original image, whereas the MAP estimator from Gaussian model decreases the noise by 5.6%.

Figure 3.8 show that all four estimators increase the contrast similarly. At iteration 16, they all increase the contrast by 26.8%.

As shown in Figure 3.9, the initial CNR of the lesion is 47.28. After processing by both MLE methods, the CNR of the lesion drops to 39.13, which is equivalent to a 17.2% change. By contrast, the MAP estimators from Poisson and Gaussian models successfully increase CNR by 18.7% and 34.2% respectively.

Table 3.1 shows the resolution results for the MAP estimates from the Poisson noise model and the Gaussian noise model. Both models can retain resolution for initial contrast greater than 2%. Poisson model retains the resolution slightly better than Gaussian model. It is not shown in Table 3.1 that MLE estimates from both models retain the resolution at all initial contrast levels.

In summary, both MLE and MAP estimators work equally well in reducing the scatter radiation, while MAP estimators works better than their MLE counterparts in improving or constraining CNR without general loss of resolution. MAP estimator based on Gaussian model has a better performance in improving or constraining CNR than the MAP estimator based on Poisson model.

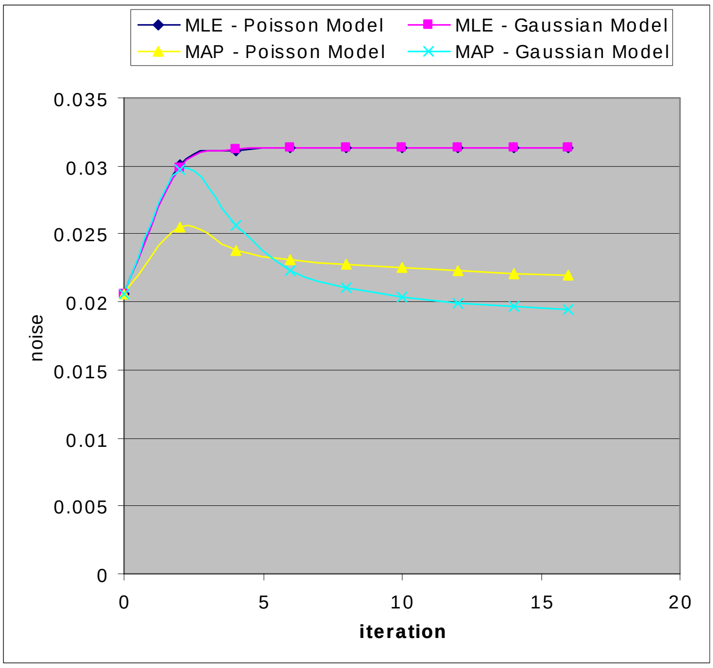

Figure 3.7: The noise vs. iteration plots for MLE and MAP estimator of b from both the Poisson noise model and the Gaussian noise model.

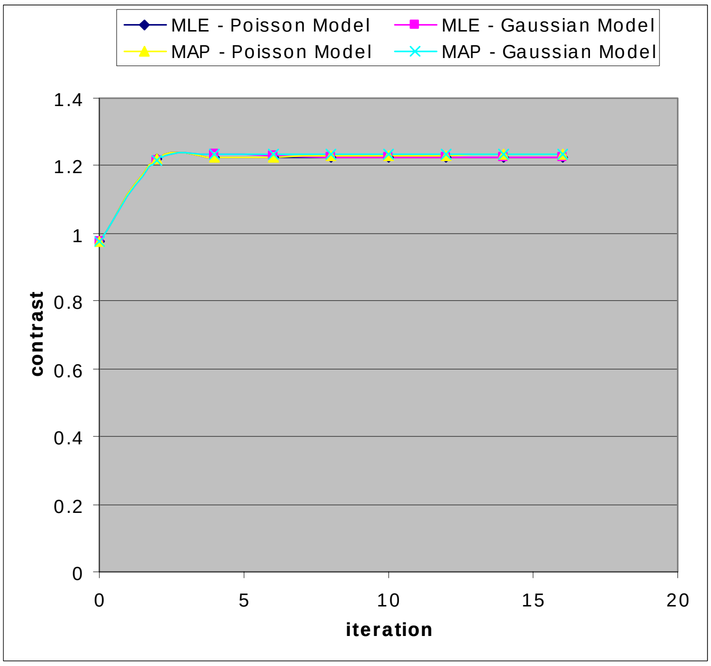

Figure 3.8: The contrast noise vs. iteration plots for MLE and MAP estimator of b from both the Poisson noise model and the Gaussian noise model.

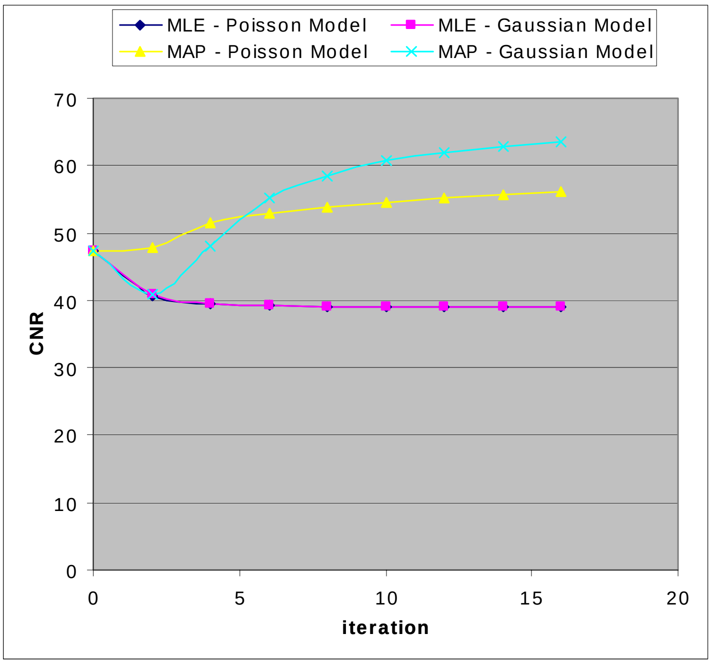

Figure 3.9: The CNR vs. iteration plots for MLE and MAP estimator of b from both the Poisson noise model and the Gaussian noise model.

	Poisson Model	Gaussian Model
Minimum initial contrast that is retainable during processing	1.8%	2.0%

Table 3.1: The resolution results for Poisson model and Gaussian model. The square wave function with Nyquist frequency is used as the test object. For various initial contrasts, the corresponding contrast-improvement-factor (CIF) is computed at iteration 16. CIF no less than 1 is used as the criterion for retaining the spatial resolution. What is reported here is the minimal initial contrast that has CIF no less

than 1.

3.4 Further Evaluation of Gaussian Noise Model

3.3.1 Effect of the Magnitude of the Scatter Kernel

The Magnitude of the Scatter Kernel M, which is the same as the area under the curve, is used to model the scatter-to-primary ratio (SPR). Using the specified technique, the measured SPR for the phantom is 0.52. As is shown in Figure 3.10, when M is specified as 0.52, the RSF drops rapidly from the initial value to a value close to zero, meaning a satisfactory scatter compensation effect. When M is less than 0.52, the scatter radiation is partially compensated. Specifically, when M equals zero, no scatter compensation is made. When M is larger than 0.52, the scatter radiation is over-compensated, i.e., RSF is less than zero.

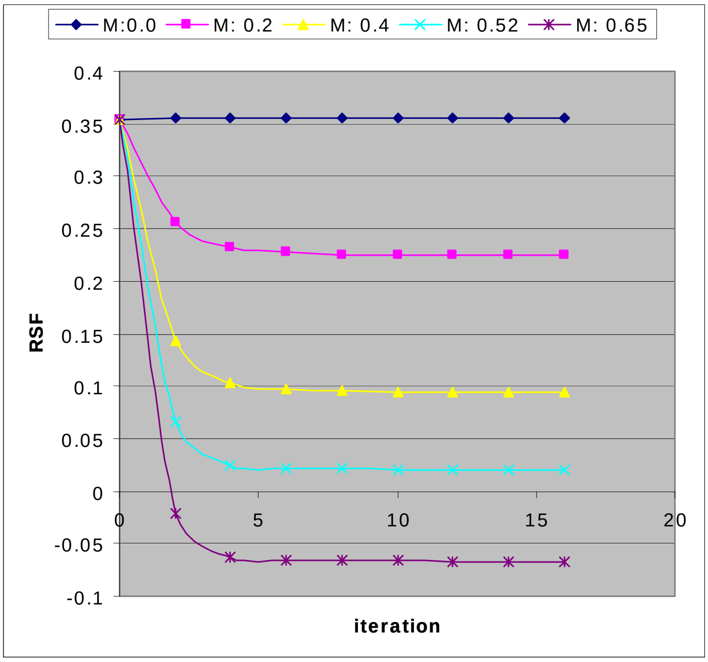

Figure 3.10: The RSF vs. iteration curves for the magnitude (M) of the scatter kernel ranging from 0.0 to 0.65. The measured SPR value using the beam stop technique is 0.52. M of 0.0 represents no scatter compensation. M of 0.20 and 0.40 represents partial scatter compensation. And M of 0.65 overcompensate the scatter radiation in the image.

Figure 3.11 -3.13 illustrate how different magnitude of the scatter kernel affects the noise, contrast and CNR respectively. Overall, these three metrics change monotonically with respect to the magnitude M. More specifically, when M gets larger, both the noise and the contrast become larger, while the CNR gets smaller.

For all the M values investigated, the CNR at iteration 16 is larger than the original value. When M is equal to 0, the CNR improves by as large as 74.7%; even for M of 0.65, CNR improves by 24.3%.

Table 3.2 gives the resolution results for the Gaussian model with various magnitude of scatter kernel. Note that for a magnitude of zero, there will always be resolution loss. For the rest magnitude values, the resolution performances are similar.

If the scatter compensation is the major concern, then the magnitude should be chosen as close to the actual SPR value as possible. The image processed in this setting will improve or constrain CNR without general loss of resolution. If more noise reduction or more CNR improvement is desired, then a smaller magnitude can be selected, at the expense of partial scatter compensation. The magnitude of zero, however, is not a good choice because it reduces the noise and increases the CNR at the expense of all spatial resolution as well as no scatter compensation.

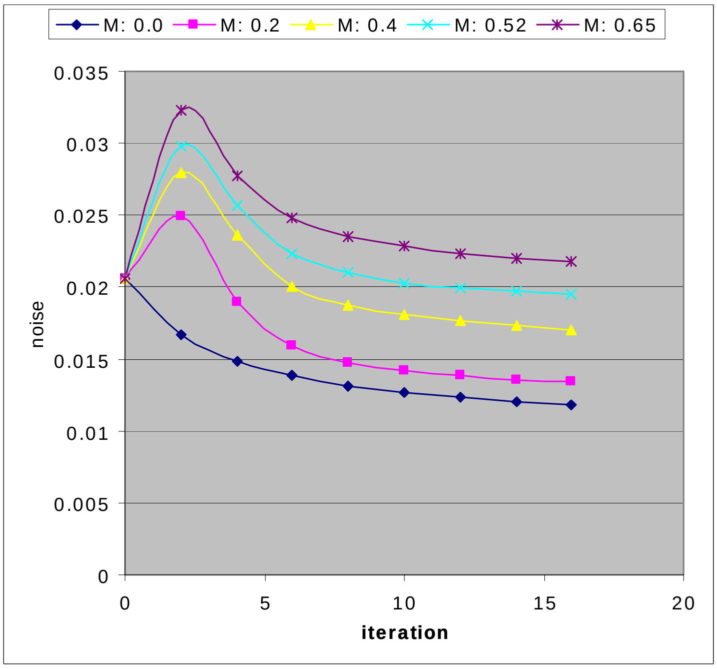

Figure 3.11: The noise vs. iteration curves for M ranging from 0.0 to 0.65. At each M level, the percentage noise reduces asymptotically. The smaller the M value is, the more is the percentage noise reduced from the initial value of 0.021.

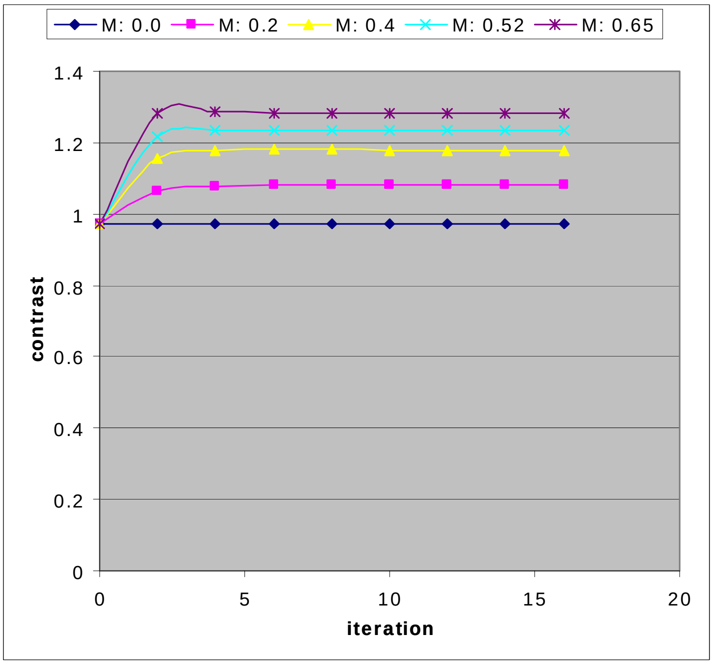

Figure 3.12: The contrast vs. iteration curves for M ranging from 0.0 to 0.65. At each magnitude level, the contrast increases asymptotically. The larger the magnitude is, the more is the contrast increased from the initial value of 0.97.

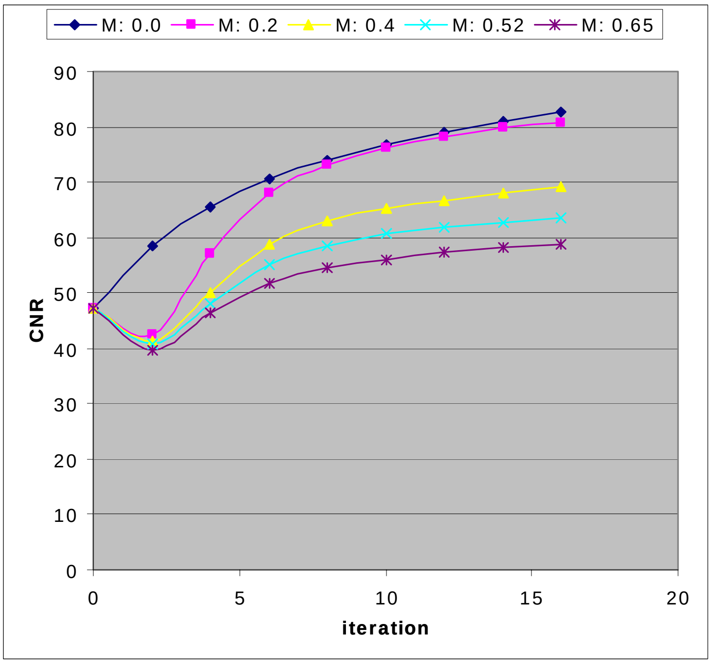

Figure 3.13: The CNR vs. iteration curves for M ranging from 0.0 to 0.65. At each magnitude level, the contrast increases asymptotically. The smaller the magnitude is, the more is the contrast increased.

Magnitude	*0.0*	*0.2*	*0.4*	*0.52*	*0.65*
Minimal initial contrast	---	*2.7%*	*2.2%*	*2.0%*	*2.0%*

Table 3.2: The resolution results for the Gaussian noise model with different magnitude of scatter kernel.

3.3.2 Effect of the Delta in the Gibbs Prior

As mentioned in the subsection 2.4, the delta (δ) in the potential function of the Gibbs prior can be considered as a factor controlling cut off frequency in the processed image. The results shown in the previous sections are for δ=0.10. Now let’s consider δ of 0.2 and 0.05 to see how plots for the image quality metrics change. As expected, different δ values do not change the RSF and the contrast plots, so their plots are not shown. Figure 3.14, Figure 3.15 and Table 3.3 give the noise, CNR plots and the resolution result for delta of 0.2. Figure 3.16, Figure 3.17 and Table 3.4 show the corresponding results for delta of 0.05. By comparing these results to Figure 3.7, Figure 3.9 and Table 3.1 for delta of 0.1, the trend emerges: the larger δ is, the more the image will be smoothed at the expense of slightly more resolution loss. It is understandable since more smoothed the final image is (i.e., less noise in the final image), more likely the details will lose. But still the final image retains a reasonably good spatial resolution (for test bar of smallest possible size (corresponding to Nyquist frequency), all initial contrasts of 3% or larger is retained). When delta is 0.2, CNR in the MAP estimator based on the Gaussian model improves by as large as 120% without general loss of resolution.

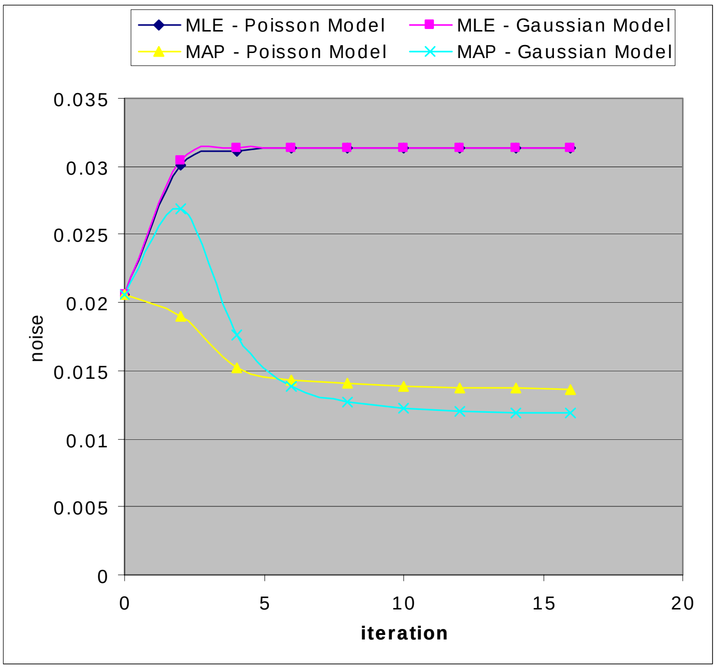

Figure 3.14: The noise vs. iteration plots for MLE and MAP estimators based on delta of 0.2. The MAP estimators decrease the noise more than their counterparts based on delta=0.1 as shown in Figure 3.6.

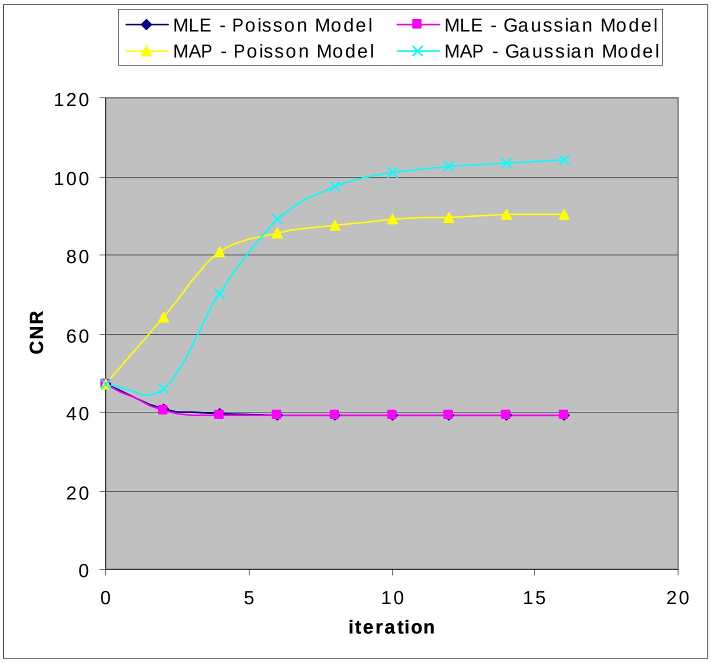

Figure 3.15: The CNR vs. iteration plots for MLE and MAP estimators based on delta of 0.2. The MAP estimators increase the CNR more than their counterparts based on delta=0.1 as shown in Figure 3.8. Also, the MAP estimator from Gaussian model improves CNR more than the one from Poisson model.

	Poisson Model	Gaussian Model
Minimum initial contrast that is retainable during processing	3.0%	3.1%

Table 3.3: The resolution results for Poisson model and Gaussian model when delta=0.2.

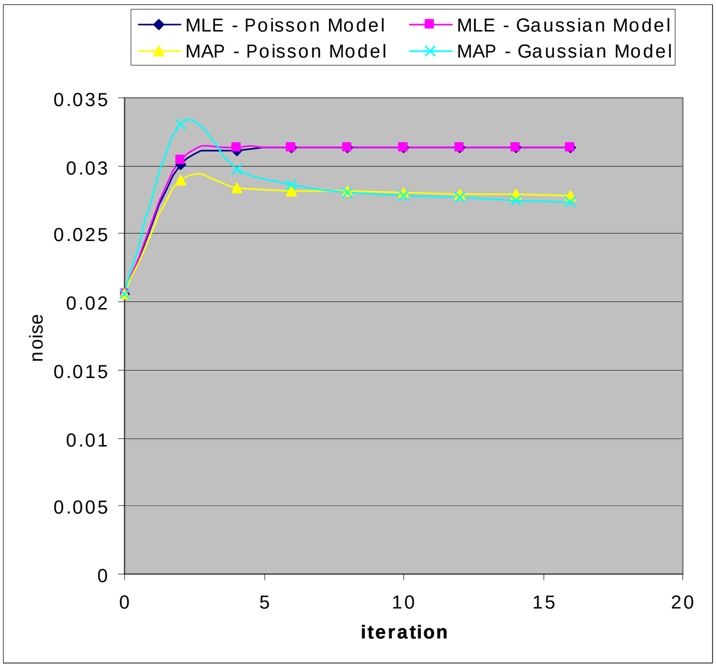

Figure 3.16: The noise vs. iteration plots for MLE and MAP estimators based on delta of 0.05. The MAP estimators decrease the noise less than their counterparts based on delta=0.1 as shown in Figure 3.6.

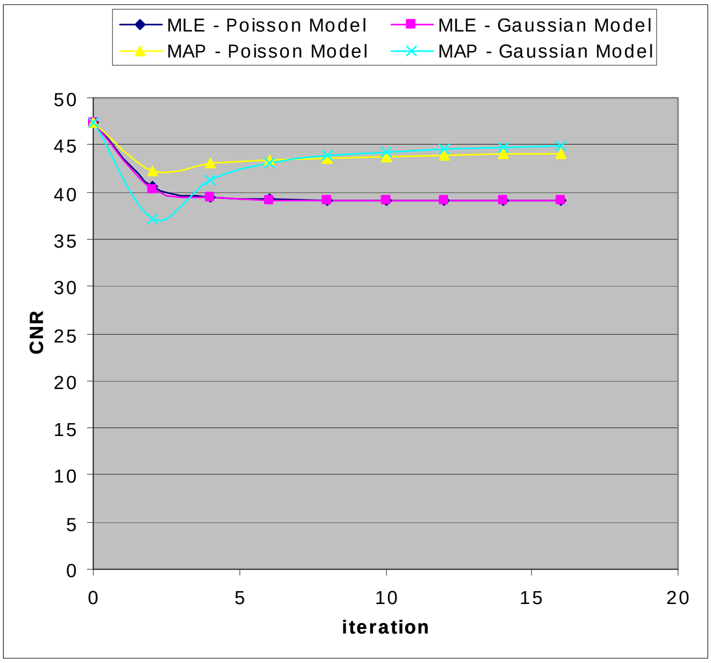

Figure 3.17: The CNR vs. iteration plots for MLE and MAP estimators based on delta of 0.05. In this case, the MAP estimators performs better than the MLE estimators in constraining CNR, but performs worse than their counterparts based on delta=0.1 as shown in Figure 3.8. But the MAP estimator from Gaussian model is still slightly better than the one from Poisson model.

	Poisson Model	Gaussian Model
Minimum initial contrast that is retainable during processing	1.2%	1.6%

Table 3.4: The resolution results for Poisson model and Gaussian model when delta=0.05.

Chapter 4

Conclusion

By checking the experimental data, it was found that the Poisson noise model for scatter compensation in the literature [26] can not account for the radiations (including the primary, scatter and total radiations) directly. It will lead to an erroneous result for the estimation of the expected values of primary radiation if a computation method like Gibbs sampling is used. Luckily, due to the scaling-invariant property of EM algorithm with an approximation that a single factor rather than a set of energy dependent ones exists between the conversion of radiation and the corresponding number of photon, the updating equation derived from the old model can still be useful.

The histograms of radiation data indicate that they might be modeled by a different distribution like Gaussian. The quantile-quantile plots of the data with respect to the standard Gaussian distribution show that Gaussian noise model can be reasonably assumed. The EM algorithm based on this new model is derived and implemented. A MAP algorithm by incorporating a Gibbs prior is also implemented for better CNR in the processed images.

The MLE and MAP estimators from the Gaussian noise model are compared with their counterparts based on the Poisson noise model. Results show that MAP estimators from both models have better CNR performance than MLE ones without a significant loss of resolution. In addition, the MAP estimator from Gaussian model performs better than the one from Poisson model in CNR improvement.

Further evaluation of MAP estimators from Gaussian model shows that both the magnitude of the scatter kernel and the delta in the Gibbs prior can be used to adjust the noise and CNR level in the processed images. The delta in the Gibbs prior acts as a major tuner of CNR without affecting RSF, whereas the magnitude of the scatter kernel acts as a fine tuner of CNR. Changing the magnitude of the scatter kernel will also affect the scatter compensation level. There is a general tradeoff between the CNR improvement and resolution reservation. Fortunately, for the largest CNR improvement (2.2 times the original CNR), the resolution is still reasonably well reserved.

References

[1] Encyclopedia Britannica, Breast Cancer. Encyclopedia Britannica, 2005.

[2] ACS, American Cancer Society: Cancer Facts and Figures 2005. Atlanta, GA: American Cancer Society, 2005.

[3] ML Giger, Computer-aided diagnosis in radiology. *Academic Radiology*, 9: 1-3, 2002.

[4] CE Floyd Jr, JY Lo, and GD Tourassi, Cased-based reasoning computer algorithm that uses mammographic findings for breast biopsy decisions. *American Journal of Roentgenology*, 175: 1347-1352, 2000.

[5] HP Chan, *et al*, Improvement in radiologists' detection of clustered microcalcifications on mammograms: The potential of computer-aided diagnosis. *Investigative Radiology,* 25: 1102-1110, 1990.

[6] ED Pisano, C Gatsonis, E Hendrick, *et al*, Diagnostic performance of digital versus film mammography for breast-cancer screening. *New England Journal of Medicine*, 353 (17): 1773-1783, 2005.

[7] P Skaane, A Skjennald, Young K, *et al*, Follow-up and final results of the Oslo I study comparing screen-film mammography and full-field digital mammography with soft-copy reading. *Acta Radiologica*, 46 (7): 679-689, 2005.

[8] RSNA: Radiological Society of North America website: http://www.rsna.org/rsna/media/pr2005/internet.cfm

[9] JT Dobbins III, DJ Godfrey, Digital x-ray tomosynthesis: current state of the art and clinical potential. *Physics in Medicine and Biology*, 48 (19): R65-R106, 2003.

[10] Y Chen, JT Dobbins III, Impulse response analysis for several digital tomosynthesis mammography reconstruction algorithms. *Proceedings of SPIE Medical Imaging*, 5745, 2005.

[11] JT Bushberg, JA Seibert, EM Leidholdt Jr, and JM Boone, The essential physics of medical imaging (2nd edition). Lippincott Williams and Wilkins, Philadelphia,

PA, 2002.

[12] S Moore, *et al*, Evaluation of scatter compensation methods by their effects on parameter estimation from SPECT projections. *Medical Physics*, 28(2): 278-287, 2001.

[13] H Zaidi, Reconstruction-based estimation of the scatter component in Positron Emission Tomography. *Ann Nucl Med Sci*, 14: 161-172, 2001.

[14] L Niklason, J Sorenson, and J Nelson, Scattered radiation in chest radiography. *Medical Physics*, **8**(5): 677-681, 1981.

[15] AH Baydush, CE Floyd Jr, Improved image quality in digital mammography with image processing. *Medical Physics,* 27 (7): 1503-1508, 2000.

[16] HP Chan, KL Lam, and Y Wu, Studies of performance of antiscatter grids in digital radiography: Effect on signal-to-noise ratio. *Medical Physics*, 17(4): 655-664,1990.

[17] GT Barnes, H Cleare, and IA Brezovich, Reduction of scatter in diagnostic radiology by means of a scanning multiple slit assembly. *Radiology*, 120: 691-694, 1976.

[18] U Neitzel, Grids or air gaps for scatter reduction in digital radiography: a model calculation. *Medical Physics*, 19(2): 475-481, 1992.

[19] JY Lo, CE Floyd Jr, and CE Ravin, Scatter compensation in chest radiography with a single-exposure estimation-subtraction method. *Radiology,* 177(P): 172-173, 1990.

[20] D Bailey and S Meikle, A convolution-subtraction scatter correction method for 3D PET. *Physics in Medicine and Biology*, 39: 411-424, 1994.

[21] JA Seibert and JM Boone, X-ray scatter removal by deconvolution. *Medical Physics*, 15(4): 567-575, 1988.

[22] JY Lo, CE Floyd Jr, and CE Ravin, Spatial-varying scatter compensation for portable chest radiographs using an artificial neural network, in Association of University Radiologists, Chicago, Ill. 1992.

[23] CE Floyd Jr, *et al*, Scatter compensation for digital chest radiography using Maximum Likelihood Expectation Maximization. *Investigative Radiology*, **28**(5): 427-433, 1993.

[24] CE Floyd Jr, *et al*, Bayesian restoration of chest radiographs: Scatter compensation with improved signal to noise ratio. *Investigative Radiology*, **29**(10): 904-910, 1994.

[25] AH Baydush, and CE Floyd Jr, Bayesian image estimation of digital chest radiography – interdependence of noise, resolution and scatter fraction. *Medical Physics*, 22 (8): 1255-1261, 1995.

[26] AH Baydush, JE Bowsher, JK Laading, *et al*, Improved Bayesian image estimation for digital chest radiography. *Medical Physics*, 24 (4): 539-545, 1997.

[27] CE Floyd Jr, *et al*, Measurement of scatter fractions in clinical bedside radiography. *Radiology*, 183: 857-861, 1992.

[28] CE Floyd Jr, *et al*, Posterior beam stop method for scatter fraction measurement in digital radiography. *Investigative Radiology*, 27: 119-123, 1992.

[29] CE Floyd Jr, *et al*, Deconvolution of compton scatter in SPECT. *Journal of Nuclear Medicine*, 26:403-408, 1985.

[30] CE Floyd Jr, *et al*, Scatter compensation in digital chest radiography by fourier deconvolution. *Investigative Radiology*, 24: 30-33, 1989.

[31] B Axelsson, P Msaki and A Israelsson, Subtraction of compton-scattered photons in single-photon emission computerized tomography. *The Journal of Nuclear Medicine*, 25:490-494, 1984.

[32] JM Boone, BA Arnold, and JA Seibert, Characterization of the point spread function and modulation transfer function of scattered radiation using a digital imaging system. *Medical Physics*, 13: 254-256, 1986.

[33] CE Floyd Jr, RJ Jaszczak, CC Harris, *et al*, Energy and spatial-distribution of multiple order Compton scatter in SPECT – a monte carlo investigation. *Physics in Medicine and Biology*, 29 (10): 1217-1230, 1984.

[34] HP Chan and Kunio Doi, Physics characteristics of scattered radiation in diagnostic radiology: Monte Carlo simulation studies. *Medical Physics*, 12:152-165, 1985.

[35] SZ Li, Discontiuity-adaptive MRF prior and robust statistics: A comparative

study. *Image and Vision Computing*,13 (4): 227-233, 1995.

[36] SZ Li, On discontinuity-adaptive smoothness priors in computer vision. *IEEE Transactions on Pattern Analysis and Machine Intelligence*, 17(6):576-586, 1995.

[37] DS Lalush and BMW Tsui, Simulation evaluation of Gibbs prior distributions for use in Maximum a posteriori SPECT reconstruction. *IEEE Transactions on Medical Imaging*, 11:267-275, 1992.

On the Development of a Gaussian Noise Model for Scatter Compensation

Jessie Q. Xia[1,3], Georgia D. Tourassi[1,2], Joseph Y. Lo[1,2,3], and Carey E. Floyd, Jr.[1,2,3]

[1]Duke Advanced Imaging Laboratories, Department of Radiology,
[2]Medical Physics Graduate Program, Department of Radiology,
Duke University Medical Center, Durham, NC 27710;
[3]Department of Biomedical Engineering, Duke University, Durham, NC 27708

ABSTRACT

The underlying mechanism in projection radiography as well as in computed tomography (CT) is the accumulative attenuation of a pencil x-ray beam along a straight line. However, when a portion of photons is deviated from their original path by scattering, it is not valid to assume that these photons are the survival photons along the lines connecting the x-ray source and the individual locations where they are detected. Since these photons do not carry the correct spatial information, the final image is contaminated. Researchers are seeking techniques to reduce scattering, and hence, improve image quality, by scatter compensation. Previously, we presented a post-acquisition scatter compensation technique based on an underlying statistical model. We used the Poisson noise model, which assumed that the signals in the detector individually followed the Poisson process. Since most x-ray detectors are energy integrating rather than photon counting, the Poisson noise model can be improved by taking this property into account. In this study, we developed a Gaussian noise model by the matching-of-the-first-two-moments method. The Maximum Likelihood Estimator of the scatter-free image was derived via the expectation maximization (EM) technique. The maximum a posteriori estimate was also calculated. The Gaussian noise model was preliminarily evaluated on a full-field digital mammography system.

KEYWORDS: Scatter Compensation, Scatter Reduction, Gaussian Noise Model, Expectation Maximization

1. INTRODUCTION

Scattered radiation degrades medical images. A recent Monte Carlo study showed that scattered radiation causes the drop of low-frequency modulation transfer function (MTF), changes the shape of MTF and adds considerable noise to projection images [1]. In computed tomography (CT), scattered radiation leads to cupping artifacts on reconstructed sections. Therefore, removal of scattered radiation from projection images is essential for improved image quality, particularly for the latest advanced imaging radiography techniques including dedicated breast CT and breast tomosynthesis, which typically do not use anti-scatter grids.

There are two categories of scatter compensation techniques: hardware based ones and numerical compensation methods. This study uses a numerical compensation method to develop a statistical scatter reduction technique. Previously, the exposure value of each pixel recorded by a detector was modeled by Poisson distribution [2]. For flat-panel detectors, which belong to the type of energy integrating rather than photon counting, the underlying statistics is a compound Poisson process[3]. It may be well approximated by Gaussian distribution.

In this study, we will propose a Gaussian noise model for scatter reduction, and derive a maximum likelihood expectation maximization (MLE or MLEM) algorithm and a maximum a posteriori (MAP) algorithm. We will then apply the algorithms to radiographs acquired on FFDM for preliminary evaluation.

2. MATERIALS AND METHODS

2.1 Gaussian Noise Model

In the chosen numerical scatter compensation scheme, the projection image is the sum of the primary radiation and scattered radiation. We have modeled scattered radiation as the two-dimensional convolution of primary radiation with a scatter kernel, which is displayed as a double exponential function (Figure 1).

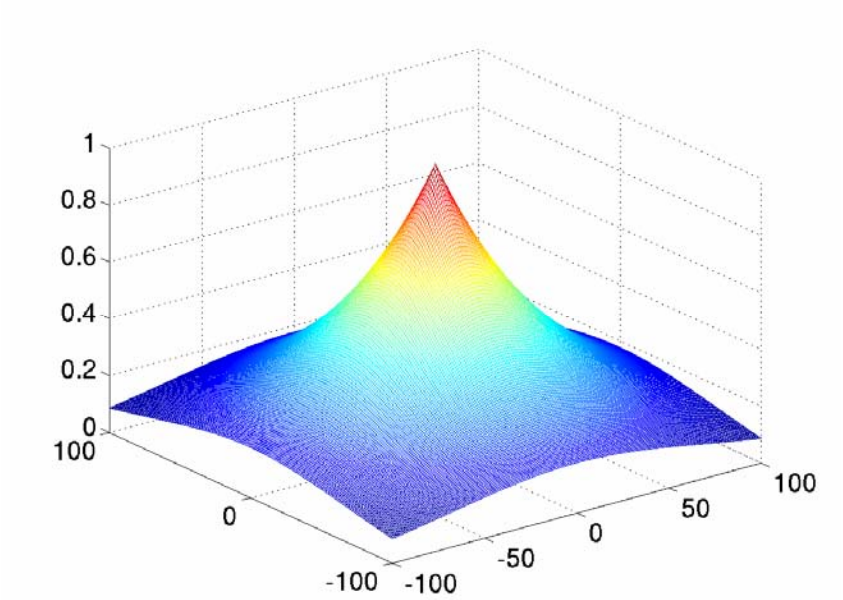

Figure 1: Schematic of a scatter kernel with a radically exponential shape. It has two parameters: full width at half maximum and magnitude).

By the matching-of-the-first-two-moments method, we approximated the energy-integrating signal by using a Gaussian distribution and created a scatter compensation model called the Gaussian noise model.

$$\boxed{\begin{array}{l} d_i \mid B, {\sigma_{i1}}^2 \sim Gaussian(b_i, {\sigma_{i1}}^2) \\ s_i \mid B, {\sigma_{i2}}^2 \sim Gaussian((B**P)_i, {\sigma_{i2}}^2) \\ y_i = d_i + s_i \mid B, {\sigma_{i1}}^2, {\sigma_{i2}}^2 \sim Gaussian(b_i + (B**P)_i, {\sigma_{i1}}^2 + {\sigma_{i2}}^2) \end{array}} \quad (1)$$

where d_i, s_i, and y_i are pixel values at location i corresponding to primary, scattered and total radiation, respectively, b_i is the expectation of d_i, and σ_{i1}^2 and σ_{i2}^2 are the variance of pixel values related to the primary radiation and scattered radiation, respectively.

Using the expectation maximization (EM) algorithm shown in the appendix, the MLE of the ideal scatter-free image was derived with analytical form shown in Equation (2).

$$\begin{aligned} b_k^{(n+1)} &= b_k^{(n)} + w_k \cdot [y_k - (b_k^{(n)} + (B^{(n)} ** P)_k)], \\ w_k &= \sigma_{k1}^2 / (\sigma_{k1}^2 + \sigma_{k2}^2) \end{aligned} \tag{2}$$

MLE estimate is known to increase high frequency image noise. To overcome this, some constraints can be put on the noise level within the estimated B, in other words, prior information about B can be provided. Thus, by Bayes's Rule,

$$p(B \mid Y) \propto p(Y \mid B) p(B), \tag{3}$$

where $p(B|Y)$ is the posterior joint distribution of B, given the measured pixel values $Y = \{y_i; i=1,\ldots,N\}$, $p(Y|B)$ is equal to the likelihood of B, and $p(B)$ is the prior joint distribution of $B = \{b_i; i=1,\ldots,N\}$.

We assumed B is a Markov random process. It therefore follows a Gibbs distribution:

$$p(B) = \frac{1}{K} e^{-U(B)/\beta}, \tag{4}$$

where K is a normalizing factor which is independent of B, $U(B)$ is the energy function, and β is a free parameter adjusting the relative weight of this prior on the maximum *a posteriori* estimator of B. When β approaches infinity, the MAP of B approaches the MLE of B.

The energy function is the sum of the potential function, i.e.,

$$U(B) = \sum_{c \in C} V_c(B), \tag{5}$$

where C is the set comprised of all cliques in the image. In this study, the Gibbs prior is defined over a second-order neighborhood system (for each pixel, its north, south, east, and west neighboring pixels plus its four diagonal neighboring pixels), with each clique comprised of two neighboring pixels. There are many forms of the potential function $V_c(B)$. We chose one that is adaptive to discontinuity [4]:

$$V_c(\{b_i : b_j\}) = \frac{(b_i - b_j)^2}{\delta_c^2 + (b_i - b_j)^2}, \tag{6}$$

where i and j are the neighboring pixels within the clique $i \sim j$ and b_i and b_j represent their respective intensities. δ_c is an adjustable parameter to regulate the cut-off frequency of the noise in the image.

The MAP estimate of $\{b_i\}$ was calculated through the two-step maximization procedure proposed by Hebert and Leahy [5].

2.2 Test Images

Images were acquired with a Siemens prototype digital mammography system (Mammomat Novation ^{DR}; Siemens, Erlangen, Germany) with 70 µm isotropic resolution. Uniform breast phantoms (CIRS, Inc., Norfolk, VA) were imaged (28kVp), with a Mo/Mo target/filter combination. The phantoms were designed to be radiographically equivalent to a 4-cm-thick compressed breast with 50% glandular tissue density. A built-in square-shaped dent in the center of the phantom mimicked a high-contrast lesion in the digital mammography images. All images were acquired without an anti-scatter grid. For the purpose of scatter measurement, all images were repeated with an array of beam stops (lead discs 3 mm in diameter) superimposed on the breast phantoms. Because lead discs absorb all the primary radiation, only scatter radiation can be detected behind them (Figure 2).

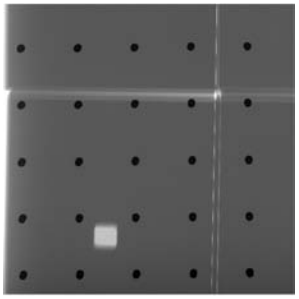

Figure 2: Radiograph of the tissue equivalent slabs. The arrays of black disks are the shadow of beam stops. The CNR values are obtained based on the bright square region of interest.

Images were then be fed into the algorithms for processing. The results were then evaluated through various metrics described in the following subsection.

2.3 Image Evaluation Metrics

Three algorithms were employed to estimate the expected amount of primary radiation. Its effect was measured by the residual scatter fraction (RSF). At the same time, we anticipated that the contrast-to-noise ratio (CNR) would be constrained or even improved after image processing. We implemented a metric to estimate post-contrast CNR. Finally, we monitored with a test bar the effect of the algorithms on the spatial resolution of the images.

2.3.1 Residual Scatter Fraction

Scatter fraction (SF) is defined as the ratio of scatter radiation to total radiation. Residual scatter fraction (RSF) indicates how much of the scatter radiation remains after applying the scatter compensation algorithm.

For our imaging technique, two sets of images of the phantom were obtained: one with, and one without, a beam stop array. The signals behind beam stops (lead discs) comprise the scatter radiation, while the total radiation, which is the sum of primary radiation and scatter radiation, will reach the region without beam stops. We calculated the measured primary radiation ($P_{measured}$) by subtracting the mean radiation of a region-of-interest (ROI) behind a beam stop from the mean of the same ROI location without a beam stop. In the image processed for scatter compensation, the mean of total radiation (T) in the same ROI location ($T_{estimated}$) is the sum of the residual scatter radiation and the primary radiation. Thus,

$$RSF = \frac{T_{estimated} - P_{measured}}{T_{estimated}} . \tag{7}$$

2.3.2 Contrast, Noise and CNR

Contrast was defined as the ratio of the difference between the mean radiation value of the lesion (T_{lesion}) and the background ($T_{background}$) to the mean of the background, that is,

$$Contrast = \frac{T_{lesion} - T_{background}}{T_{background}} . \tag{8}$$

Noise was derived by dividing the standard deviation ($STD_{background}$) by the mean of the background radiation ($T_{background}$):

$$Noise = \frac{STD_{background}}{T_{background}} . \tag{9}$$

CNR is the ratio of the contrast to the noise, i.e.,

$$CNR = \frac{Contrast}{Noise} = \frac{T_{lesion} - T_{background}}{STD_{background}} . \tag{10}$$

2.3.3 Resolution

Due to the nonlinearity of the resolution algorithm, we could not use metrics like MTF, which are designed for a linear system. Instead, a test bar, comprised of alternating bright and dark lines with sizes corresponding to Nyquist frequencies with square wave function, was embedded in the phantom image.

The contrast improvement factor (CIF), defined as the ratio of the contrast after image processing to the initial contrast, was obtained for the test bar with various initial contrast settings. A CIF of 1 or greater was used as the criterion for retaining the spatial resolution. The minimal initial contrast that the test bar can allow with CIF of1 or greater was recorded as an indication of the effect of the image processing on resolution. For the various initial contrasts, the corresponding CIF was computed arbitrarily at iteration 16. We determined the minimal initial contrast value that has a CIF of 1 or greater.

3. RESULTS

3.1 Scatter Compensation Technique -- Tissue Equivalent Slabs

Figure 3 and Table 1 give the RSF, CNR and resolution results for MLE and MAP algorithms based on a Poisson noise model and Gaussian noise model. Both MLE algorithms reduced RSF values to close to zero and decreased CNR values from the original unprocessed value of 47 to slightly below 40. The minimal contrast that is retainable during processing using our Poisson-model-based MAP algorithm was 1.8%. The MAP algorithms were as equally effective as their MLE counterparts in removing scattered radiation from the radiograph; however, they increased the CNR values to 56 and 63, for the Poisson noise model and Gaussian model, respectively. The minimal contrast retainable using the Gaussian model based MAP algorithm was 2.0%, slightly higher than that of Poisson-model-based MAP (1.8%).

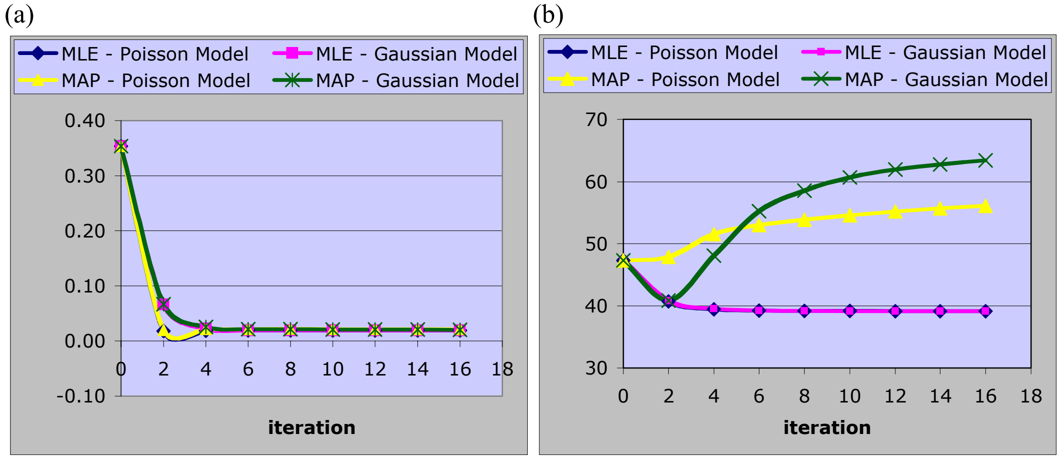

Figure 3: Plots of (a) residual scatter fraction and (b) contrast to noise ratio as the function of iteration numbers between MLE and MAP estimates of scatter free image {bi} based on Poisson and Gaussian noise models. While both techniques were effective at removing scattered radiation, the MAP based on the Gaussian noise model showed greater CNR improvement.

Table 1: Resolution results of MAP estimates based on Poisson noise model and Gaussian noise model with the magnitude of scatter kernel of 0.52. The resolution results from the two models are close to each other.

	Poisson Noise Model	**Gaussian Noise Model**
Minimum initial contrast that is retainable during processing	1.8%	2.0%

How the magnitude of the scatter kernel impacted the MAP algorithm based on the Gaussian noise model was also investigated. Figure 4(a) shows the RSF as a function of iteration for different magnitudes. When the magnitude is zero, there is no scatter reduction effect. As the magnitude increases, the steady-state RSF decreases. When the magnitude is larger than the measured value of 0.52, the scattered radiation is overcompensated such that RSF is less than zero. Figure 4(b) depicts CNR results for the same scatter kernel magnitudes. Overall, the larger the magnitude, the less CNR will increase. In the case of resolution, the smaller the magnitude, the lower the resolution (Table 2). For the magnitude of 0.2, the minimal contrast retainable during processing was 2.7%. For the magnitude of 0, where there was no scatter compensation, no contrast was retainable during processing.

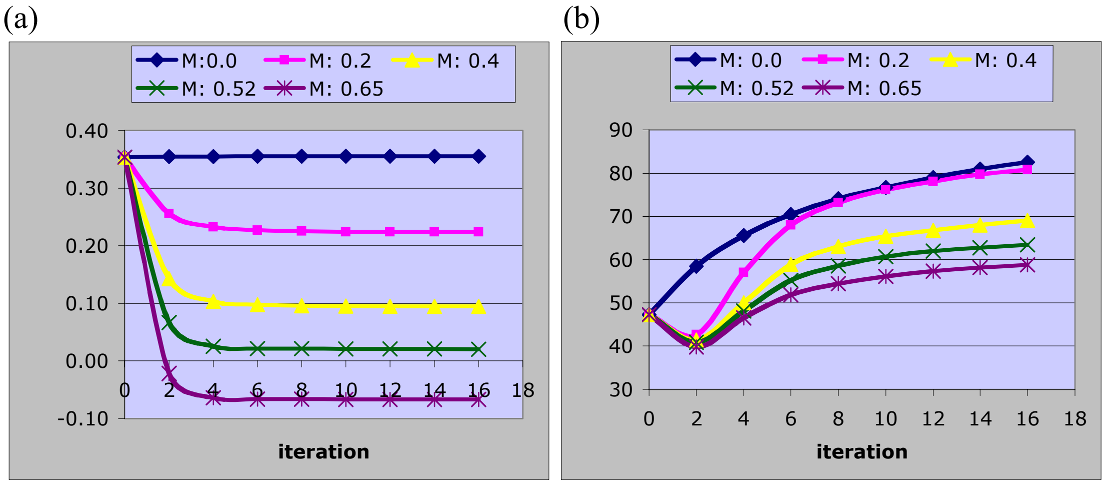

Figure 4: Plots of (a) residual scatter fraction and (b) contrast to noise ratio as the function of iteration numbers were shown for various magnitudes of scatter kernel using MAP estimates of scatter free image {bi} based on the Gaussian noise model. A magnitude of 0.0 corresponds to no scatter removal, whereas a magnitude of 0.65 overcompensates the scattered radiation, resulting in negative residual scatter fraction values. At each magnitude level, the contrast increases asymptotically..

Table 2: Resolution results of the Gaussian noise model based MAP estimates with various magnitudes of scatter kernel. The larger the magnitude of scatter kernel, the sharper the processed image is. For the magnitude of zero, i.e., no scatter removal, the resolution is always degraded.

Magnitude	*0.0*	*0.2*	*0.4*	*0.52*	*0.65*
Minimal initial contrast	---	*2.7%*	*2.2%*	*2.0%*	*2.0%*

3.2 Scatter Compensation Technique -- Anthropomorphic Phantom

The scatter removal procedure reduced SF of the radiograph acquired without a grid from 45% to 10%, the level that an anti-scatter grid achieves (Figure 5, Table 3). At the same time, the procedure improved the CNR to around twice the value on the image acquired with a grid.

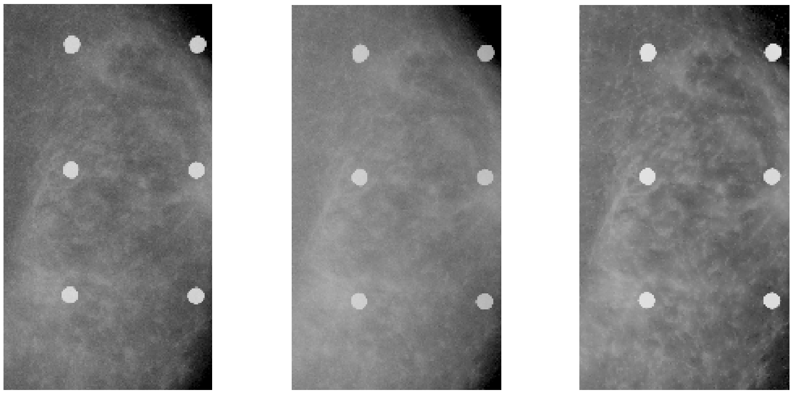

(a) with grid (b) without grid (c) without grid; scatter reduction

Figure 5: Radiographs of the breast anthropomorphic phantom, (a) with an anti-scatter grid, (b) without an anti-scatter grid, and (c) without an anti-scatter grid and with scatter reduction.

Table 3: Corresponding residual scatter fraction and contrast to noise ratio results for the three images shown in Figure 5.

	With grid	**w/o grid**	**w/o grid; scatter reduction**
RSF	11%	45%	10%
CNR	7.04	6.99	15.29

4. DISCUSSION

In this study, both MLE and MAP estimates of the scatter free image were derived based on a novel Gaussian noise model for energy-integrating detectors. The preliminary results were obtained on the two types of phantoms (tissue equivalent slabs and a breast anthropomorphic phantom) obtained on a full-field digital mammography system. Both MLE and MAP techniques were effective in removing the scattered radiation, though MAP outperformed MLE in CNR. For the specific phantom and imaging condition, the MAP of the Gaussian noise model outperformed the MAP of the Poisson noise model.

The next phase of this research will include a comprehensive evaluation of the scatter reduction technique on images acquired on a FFDM system. Also the technique can be applied on dedicated breast CT data for scatter reduction.

5. ACKNOWLEDGMENTS

The authors wish to thank Professor Michael Lavine in Institute of Statistics and Decision Science (ISDS) of Duke University for useful discussions.

This work was partially supported in part by USAMRMC W81XWH-05-1-0278, NIH R01-CA94236, and NIH R01-CA112337.

6. APPENDIX

Derivation of MLE Algorithm based on Gaussian Noise Model

Due to the convolution operation, the estimation of B = {b_i; i=1…N} directly from Y does not have a simple analytic form. The MLE of B is thus derived through the EM algorithm as follows.

Treat the measured Y = {y_i, i=1,…,N} as an incomplete dataset, and unobserved (D,S) = {(d_i,s_i), i=1,…,N} as a complete dataset. The d_i 's and s_i 's given B are mutually independent, therefore the complete data likelihood is

$$p_c(D,S\,|\,B,\{\sigma_{i1}^{\;2},\sigma_{i2}^{\;2};i=1,\ldots,N\})=\prod_{j=1}^{N}[\frac{1}{\sqrt{2\pi\sigma_{j1}^{\;2}}}e^{-(d_j-b_j)^2/2\sigma_{j1}^{\;2}}\cdot\frac{1}{\sqrt{2\pi\sigma_{j2}^{\;2}}}e^{-(s_j-(b**p)_j)^2/2\sigma_{j2}^{\;2}}]. \qquad \text{(A1)}$$

Assuming $\{\sigma_{i1}^2, \sigma_{i2}^2; i=1,\ldots,N\}$ are known, we can obtain the complete data log likelihood by taking the logarithm on both sides,

$$L_c(B \mid D,S) = \sum_{j=1}^{N}[-(d_j - b_j)^2 / 2\sigma_{j1}^2 - (s_j - (b**p)_j)^2 / 2\sigma_{j2}^2 - \log\sqrt{2\pi\sigma_{j1}^2} - \log\sqrt{2\pi\sigma_{j2}^2}]\cdot \qquad \text{(A2)}$$

The EM algorithm is comprised of two steps: one, the E-step, where the expectation of the complete data log likelihood with respect to the present estimate of B is computed, and two, the M-step, where a new estimate of B is obtained which will maximize the computed expectation in the E-step.

First, employ the E-step:

$$\begin{aligned} &Q(B \mid B^{(n)}) \\ &= E[L_c(B \mid D,S) \mid Y, B^{(n)}] \qquad \text{(A3)} \\ &= \sum_{j=1}^{N}\{-(b_j^2 - 2d_j^{(n)} b_j)/2\sigma_{j1}^2 - [(B**P)_j)^2 - 2s_j^{(n)}(B**P)_j]/2\sigma_{j2}^2 \\ &+ terms \cdot independent \cdot of \cdot B\}, \end{aligned}$$

where $d_j^{(n)} = E[d_j \mid Y, B^{(n)}]$. (A4)

$s_j^{(n)} = E[s_j \mid Y, B^{(n)}]$

Second, the M-step to find $B^{(n+1)}$ that will maximize $Q(B|B^{(n)})$:

$$\frac{\partial Q(B \mid B^{(n)})}{\partial b_k} = 0 = -(2b_k - 2d_k^{(n)})/2\sigma_{k1}^2 - \sum_{j=1}^{N}[2(B**P)_j p_{jk} - 2s_j^{(n)} p_{jk}]/2\sigma_{j2}^2 \cdot$$

Solving the above equation for b_k gives

$$b_k^{(n+1)} = d_k^{(n)} - \sigma_{k1}^2 \sum_{j=1}^{N} p_{jk} \cdot [(B^{(n+1)} **P)_j - s_j^{(n)}]/\sigma_{j2}^2. \qquad \text{(A5)}$$

Using $B^{(n)}$ to approximate $B^{(n+1)}$ in the right-hand side yields

$$b_k^{(n+1)} = d_k^{(n)} - \sigma_{k1}^2 \sum_{j=1}^{N} p_{jk} \cdot [(B^{(n)} **P)_j - s_j^{(n)}]/\sigma_{j2}^2. \qquad \text{(A6)}$$

As a good estimate of the primary image is formed, $(B^{(n)} **P)_j - s_j^{(n)} \approx 0$, then,

$$b_k^{(n+1)} \cong d_k^{(n)}. \qquad \text{(A7)}$$

The same apparent form was obtained for Poisson noise model in Reference 2. But due to the different statistical models, the actual forms of $d_k^{(n)}$ are different and so is the iterative formula for b_k.

Equation (A7) combines with equation (A4) to give the following updated equation:

$$b_k^{(n+1)} = b_k^{(n)} + w_k \cdot [y_k - (b_k^{(n)} + (B^{(n)} ** P)_k)], \tag{A8}$$

where

$$w_k = \sigma_{k1}{}^2 / (\sigma_{k1}{}^2 + \sigma_{k2}{}^2). \tag{A9}$$

REFERENCES

[1] R. S. Saunders, Jr. and E. Samei, “A Monte Carlo Investigation on the Impact of Scattered Radiation on Mammographic Resolution and Noise,” Proc. SPIE 6142, 3A1-7 (2006).n

[2] A. H. Baydush, J. E. Bowsher, J. K. Laading, and C. E. Floyd, Jr., ”Improved Bayesian Image Estimation for Digital Chest Radiography," Med. Phys. 24 (4), 539 - 545 (1997).

[3] B. R. Whiting, “Signal Statistics of X-ray Computed Tomography”, Proc. SPIE 4682, 53-60 (2002).

[4] S.Z. Li, “On Discontinuity-Adaptive Smoothness Priors in Computer Vision”, *IEEE Transactions on Pattern Analysis and Machine Intelligence*, 17(6), 576-586 (1995).

[5] T. Hebert and R. Leahy, “A Generalized EM Algorithm for 3D Bayesian Reconstruction from Poisson Data Using Gibbs Priors,” IEEE Trans. Med. Imag. 8, 194 - 202 (1989).

Dedicated breast computed tomography: Volume image denoising via a partial-diffusion equation based technique

Jessie Q. Xia[a)]
Department of Biomedical Engineering, Duke University, Durham, North Carolina 27708 and Duke Advanced Imaging Laboratories, Department of Radiology, Duke University Medical Center, Durham, North Carolina 27705

Joseph Y. Lo
Department of Biomedical Engineering, Duke University, Durham, North Carolina 27708, Duke Advanced Imaging Laboratories, Department of Radiology, Duke University Medical Center, Durham, North Carolina 27705, and Medical Physics Graduate Program, Duke University Medical Center, Durham, North Carolina 27708

Kai Yang
Department of Biomedical Engineering, University of California Davis, Davis, California 95616 and Department of Radiology, University of California Davis Medical Center, Sacramento, California 95817

Carey E. Floyd, Jr.
Department of Biomedical Engineering, Duke University, Durham, North Carolina 27708, Duke Advanced Imaging Laboratories, Department of Radiology, Duke University Medical Center, Durham, North Carolina 27705, and Medical Physics Graduate Program, Duke University Medical Center, Durham, North Carolina 27708

John M. Boone
Department of Biomedical Engineering, University of California Davis, Davis, California 95616 and Department of Radiology, University of California Davis Medical Center, Sacramento, California 95817

(Received 13 February 2007; revised 6 March 2008; accepted for publication 6 March 2008; published 24 April 2008)

Dedicated breast computed tomography (CT) imaging possesses the potential for improved lesion detection over conventional mammograms, especially for women with dense breasts. The breast CT images are acquired with a glandular dose comparable to that of standard two-view mammography for a single breast. Due to dose constraints, the reconstructed volume has a non-negligible quantum noise when thin section CT slices are visualized. It is thus desirable to reduce noise in the reconstructed breast volume without loss of spatial resolution. In this study, partial diffusion equation (PDE) based denoising techniques specifically for breast CT were applied at different steps along the reconstruction process and it was found that denoising performed better when applied to the projection data rather than reconstructed data. Simulation results from the contrast detail phantom show that the PDE technique outperforms Wiener denoising as well as adaptive trimmed mean filter. The PDE technique increases its performance advantage relative to Wiener techniques when the photon fluence is reduced. With the PDE technique, the sensitivity for lesion detection using the contrast detail phantom drops by less than 7% when the dose is cut down to 40% of the two-view mammography. For subjective evaluation, the PDE technique was applied to two human subject breast data sets acquired on a prototype breast CT system. The denoised images had appealing visual characteristics with much lower noise levels and improved tissue textures while maintaining sharpness of the original reconstructed volume. © *2008 American Association of Physicists in Medicine*. [DOI: 10.1118/1.2903436]

Key words: breast imaging, breast CT, PDE, volume noise removal

I. INTRODUCTION

The most common cancer type that affects women globally other than skin cancer is breast cancer.[1] Moreover, breast cancer is a leading cause of cancer-related women mortality, secondary only to lung cancer. It is estimated that the disease will kill about 40 480 U.S. women in 2008.[1] Although mammography is the standard clinical screening technique[2,3] for breast imaging, superimposition of normal anatomical structures may potentially obscure a breast lesion. The situation gets even worse for women with dense breasts,[4] which have more anatomical noise in the projection image. Researchers are developing alternative x-ray breast imaging techniques that may overcome the limitations of mammography, including three-dimensional imaging techniques such as breast tomosynthesis[5,6] and dedicated breast computer tomography (CT).[7–12]

Not long after the CT technique was invented in 1972, a group of researchers showed that using a whole body scanner for breast CT imaging would require a high patient dose to achieve adequate image quality.[13] With the advent of high-resolution flat-panel detectors at the end of the 1990s, breast CT became an active area of research. In particular, a 2001 article[7] showed that dedicated breast CT could achieve quality breast images with dose levels comparable to two-view mammography for the same breast. Other studies have since investigated many aspects of dedicated breast CT.[8–12,14–18]

Preliminary human subject data acquired on our first prototype breast CT system[19] provide exciting new information of the breast that was not available in the past. However, because the relatively low total dose must be split among a large number of projection views (around 500), reconstructed breast CT thin sections contain considerable quantum noise. Thus, it is desirable to reduce noise levels in the reconstructed volume to improve the conspicuity of breast lesions while also retaining spatial resolution. Alternatively, by applying denoising techniques, dose may be reduced while maintaining the image quality.

For low dose CT, some general-purpose sinogram smoothing techniques based on either penalized likelihood[20] or penalized weighted least squares[21] were developed. These techniques can be potentially applied on dedicated breast CT data sets. Zhong *et al.*[22] developed a wavelet-based technique and applied it on phantom breast CT data. Their results showed that with denoising, dose could be potentially reduced by up to 60%.

The partial diffusion equation (PDE) based technique[23,24] is another denoising method which is effective not only in removing noise but also in preserving details. Although computationally intensive, this iterative method can provide more freedom in choosing the desired denoising effect. In this study, we describe several variants of the PDE based denoising technique applicable to different steps along the reconstruction process of breast CT and evaluate it both on simulated and empirically collected human subject data sets.

The image quality of PDE denoised images was compared against that of a Wiener filtering technique as well as two-dimensional (2D) adaptive trimmed mean (ATM) filters. Quantitative comparisons were made using simulated data at various exposure levels, while qualitative comparisons were made using dedicated breast CT scan data from two human subjects.

II. MATERIALS AND METHODS

II.A. Dedicated breast CT system and human subject data sets

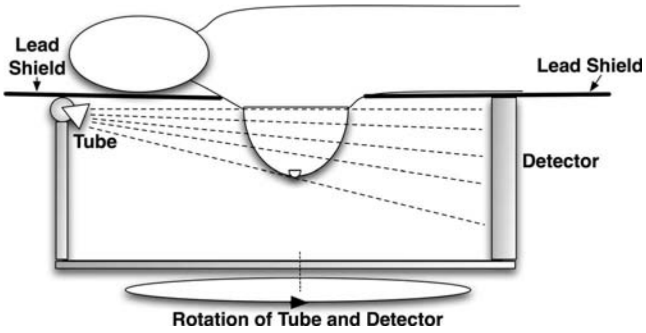

FIG. 1. Illustration of a dedicated breast CT system. The x-ray tube and flat-panel detector rotate together around the breast, which is the only region to be illuminated.

As is illustrated in Fig. 1, dedicated breast CT systems are typically designed as follows: a patient lies prone on a lead-shielded table with one breast hanging through a hole on the table in the pendant geometry. The x-ray tube and the flat-panel detector rotate in the horizontal plane underneath the table. This setup is different from a conventional CT system, where the x-ray tube and detector rotate around the torso of a patient (axial scanning). Since only the breast to be imaged is exposed to the x-ray beam, the dose to the patient can be greatly reduced. A pilot study[7] showed that this type of dedicated breast CT system is able to achieve a satisfactory image quality with dose levels comparable to standard two-view mammography for the same breast.

Using the above system design, a custom-designed breast CT system was fabricated at the University of California Davis Medical Center and is currently accruing patient images. The x-ray tube has a Comet beryllium-windowed, water-cooled tungsten anode and a nominal focal spot with the size of 0.4 mm × 0.4 mm. A Pantak high frequency x-ray generator drives the tube with the voltage ranging from 10 to 160 kV. The CsI-based flat-panel detector (Varian, PaxScan 4030CB) has a field of view of 40 cm × 30 cm. Using 30 frames per second and 2 × 2 pixel binning mode, the detector generates the images each with matrix size of 1024 × 768 and pixel dimension of 0.388 mm × 0.388 mm. A Kollmorgen servo motor was employed to drive the rotation of the tube-detector gantry as well as encode the angular information. The source-to-isocenter distance is 46.9 cm and the source-to-detector distance is 88.4 cm.

For the two human subject data sets presented in this article, the projection images were acquired under 80 kVp using a circular orbit. The mAs values were chosen for each subject such that the mean glandular dose using breast CT was equal to two-view mammography. Each subject is scanned within 17 seconds to get a total of 500 projection images that span slightly over 360 degrees. After dead pixel and flat field corrections, each data set is ready for tomographic reconstruction.

II.B. Simulated breast CT data sets

In this study, simulated breast CT data sets were also generated to aid the analysis. The computer-generated breast is a hemisphere with radius of 7 cm. It has homogeneous breast tissue with a uniform linear attenuation coefficient of 0.17 cm^{-1} and is surrounded by 1 mm thick skin[25] with a linear attenuation coefficient of 0.3 cm^{-1}. Either a contrast detail phantom or a single high-contrast lesion was simulated at the center of the breast. The parameters of the contrast detail phantom are: for each 4 by 4 lesion array, sizes vary vertically (6, 5, 4, and 3 mm); contrasts of the lesions are 15%, 10%, 5%, and 3% from left to right. Five of these arrays were embedded in the shape of a plus sign to cover multiple areas in the central coronal slice in order to detect any regional variations in image quality. Perfect detection would correspond to five sets of 16 lesions or 80 in total. This simulated breast was scanned virtually by a monochromatic x-ray cone beam with infinitely small focal spot and ideal flat-panel detector with 100% detective quantum efficiency. The geometric parameters are the same as the physical breast CT scanner described in the previous subsection.

For each 2D projection image, an analytical line integral image was first obtained based on the aforementioned virtual dedicated breast CT scanning. A noisy raw image was generated according to the measurement model.[26] The model takes into account both photon quantum noise and electronic readout noise. It has the following form:

$$Y_i = G_i\bar{E}\cdot \text{Poisson}(I_0 e^{-l_i}) + \text{Gaussian}(0,\sigma^2), \tag{1}$$

where G_i is the gain factor of the imaging system, $\bar{E}$ is the mean energy level of the polychromatic x-ray beam, and the Gaussian term is for the electronic noise. In our simulation we chose $G_i = 0.0035/\text{keV}$, $\bar{E} = 40\ \text{keV}$, and $\sigma^2 = 10$. The values of G_i and σ^2 were referred to those used in Ref. 26.

Two I_0 values are used. The exposure level affects the noise content of line integral at a fixed location. By varying the exposure levels and plotting the line integrals against those of human subject data, it is found that $I_0 = 2.5e4$ gives a comparable noise level for the same line integral values. Another exposure level is $I_0 = 1e4$, which is 40% of the first exposure level.

II.C. Tomographic reconstruction

Before reconstruction, the raw projection images undergo a preprocessing step. The raw projection image is converted into the line integral via the logarithm operation. On each raw projection image, a region of interest (ROI) is identified which is outside the breast silhouette, and the pixel value without attenuation I_0 is approximated by the mean pixel value within the ROI. Then the line integral image is obtained by $l_{ij} = \log(I_0/I_{ij})$, where I_{ij} is the pixel value at (i,j) position.

Since the data sets have high angular sampling rate, the computationally efficient filtered backprojection[27] (FBP) algorithm was chosen for reconstruction. The Feldkamp type FBP for cone-beam geometry was custom written and a Shepp–Logan filter was used.

II.D. Denoising techniques

Along the reconstruction process, there are four possible steps where a denoising technique can be applied, as illustrated in Fig. 2. However, applying a denoising technique in step 1 will not be very effective due to the nonlinear operation of the preprocessing step. Only steps 2, 3, and 4 are considered. All together five different denoising techniques were implemented for this study. The first three are variants of the partial diffusion equation based denoising technique that were developed for each step. First, the standard 2D PDE technique was applied at step 3. Second, a spatially variant version of the 2D PDE denoted as PDE_{tomo} is used at step 2. Third, the three-dimensional PDE is used at step 4. The last two techniques are Wiener filter and ATM filter, which are also applied to step 2, and which are compared to the PDE_{tomo} technique.

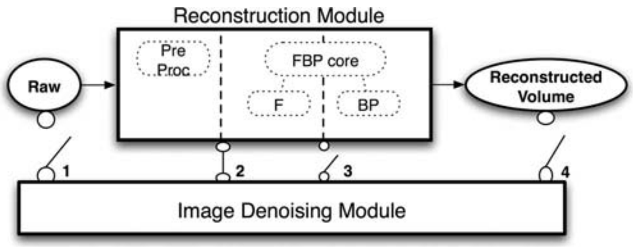

FIG. 2. Illustration of possible steps where image-denoising module may be applied with respect to reconstruction module for dedicated breast CT data. In this study, the denoising techniques are applied at steps 2–4.

II.D.1. PDE_{2D}

An image is processed by a nonlinear PDE technique through

$$\frac{\partial I}{\partial t} = \nabla\cdot\left(p(|\nabla(G_\sigma \otimes I)|)\,\nabla I\right), \tag{2}$$

where ∇I is the gradient of the image I and $\nabla^2 I = \nabla\cdot(\nabla I)$ is the Laplace operation on I over the spatial variables.[28] The function of $p(.)$ is called the diffusivity function, a function of the norm of the gradients in the image $|\nabla I|$. It is used to regulate the local smoothness. In the presence of noise, the gradients can be unbounded. To overcome this problem, a Gaussian kernel G_σ with the standard deviation of σ is applied to the image before gradients are computed as Catte *et al.*[29] suggested. A nonlinear PDE can reduce noise while preserving spatial resolution in the image.

In this study, we chose a diffusivity function proposed by Perona and Malik[23]

$$p(d) = e^{-d^2/\delta_0^2}, \tag{3}$$

where δ_0 is a user-specified parameter. When the image gradient norm is very large at a location region, the diffusivity will be very small, and thus the local image values will be preserved within a small time period whereas another more uniform region will be smoothed out at the same time. The parameter δ_0 acts like a cutoff value; image regions with gradient norm below δ_0 will have more noise removed while regions with a higher gradient norm will stay sharp.

The diffusion equation can be discretized by the finite difference approach using the first-order neighborhood system. Each pixel has four neighbors: the north, south, west, and east neighbor pixels. Assuming $\Delta x = \Delta y = 1$ in the two-dimensional case, the discretized version of Eq. (2) is

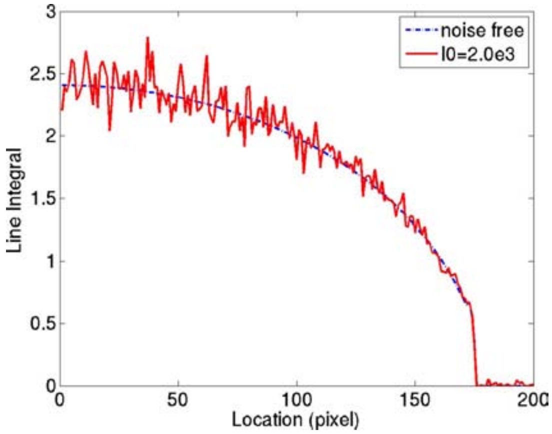

FIG. 3. One-dimensional line integral profiles across the breast on a projection image. The dashed and continuous plots correspond to noise free case and the case with I_0=2.0e3, respectively. The variance of line integral is larger at the center of breast region and gets lower toward the periphery.

$$\frac{I_{(i,j)}^{\langle t+1\rangle} - I_{(i,j)}^{\langle t\rangle}}{\Delta t} = p_{(i-1,j)} \cdot \nabla_{(i-1,j)} I^{\langle t\rangle} + p_{(i+1,j)} \cdot \nabla_{(i+1,j)} I^{\langle t\rangle} + p_{(i,j-1)} \cdot \nabla_{(i,j-1)} I^{\langle t\rangle} + p_{(i,j+1)} \cdot \nabla_{(i,j+1)} I^{\langle t\rangle}, \quad (4)$$

where $\langle t\rangle$ and $\langle t+1\rangle$ represent the iteration step t and $t+1$, respectively; Δt is the discretized time step; $p_{(.,.)}$'s are diffusivity function values at the neighboring pixels of location (i,j); and $\nabla_{(.,.)} I$ is a notation for the difference between $I_{(.,.)}$ and $I_{(i,j)}$ itself. The parameters of PDE$_{2D}$ are Δt, σ, δ, and the number of iterations (denoted by iter_num).

II.D.2. PDE$_{\text{tomo}}$

In the breast CT line integral images, noise is larger toward the chest wall. When the photon fluence is reduced, the phenomenon becomes even more obvious. A line profile is shown in Fig. 3 to help illustrate this point. It can be explained theoretically. Again, a simplifying assumption of monochromatic beam is used. If

$$I_{ij} \sim \text{Poisson}(\lambda_{ij}),$$

$$l_{ij} = \log \frac{I_0}{I_{ij}} = \log I_0 - \log I'_{ij}, \quad (5)$$

where λ_{ij} is the expected number of photons arriving at location (i,j) of the detector, then the variance of the line integral l_{ij} can be approximated by the delta method[30] using the second-order Taylor expansion

$$\text{var}(l_{ij}) = \text{var}(\log I_{ij}) \cong \text{var}(I_{ij}) \cdot [(\log I_{ij})']^2 \cong \lambda_{ij} \cdot \frac{1}{I_{ij}^2} \cong \frac{1}{I_{ij}}. \quad (6)$$

This formalism can be integrated into the PDE denoising technique by adapting the parameter δ in the diffusivity function spatially as

$$\delta_{ij} = k \cdot \sqrt{\text{var}(l_{ij})} = \delta_0 \cdot \sqrt{\frac{1}{\frac{1}{M} \sum_{c \in N(i,j)} e^{l_c}}}, \quad (7)$$

where k is a constant, M is equal to 4, and $N(i,j)$ is the four closest neighbors around pixel (i,j).

The resultant PDE denoising technique is denoted PDE for tomography/tomosynthesis (PDE$_{\text{tomo}}$). The parameters to be considered are Δt, σ, δ_0, and iter_num.

II.D.3. PDE$_{\text{3Dpost}}$

When the PDE denoising is applied on the reconstructed volume instead of the line integral data, its neighborhood system expands to six neighbors along x, y, and z directions. Otherwise this variant of the algorithm, denoted as PDE$_{\text{3Dpost}}$, is implemented in the same way as PDE$_{2D}$. For example, the choice of the parameter in diffusivity function is not spatially adaptive, i.e.,

$$\delta_{ij} = \delta_0. \quad (8)$$

II.D.4. Wiener filter

A Wiener filter is used at step 2 for comparison against the PDE technique investigated in this study. Both techniques are spatially adaptive filters. However, the Wiener filter is a linear technique whereas the PDE technique is nonlinear.

For each pixel, its mean (μ) and variance (σ^2) around a local neighborhood is estimated. Then the Wiener filter updates $l(x,y)$ to the new $l_n(x,y)$ through

$$l_n(x,y) = \mu + \frac{\sigma^2 + \upsilon^2}{\sigma^2}(l(x,y) - \mu), \quad (9)$$

where υ^2 is the average of σ^2 values.

The variable parameter in the Wiener filter is the size of the neighborhood. In this study, 3×3, 5×5, and 7×7 kernels are considered.

II.D.5. ATM filter

Like the PDE filters described in Secs. II D 1 to II D 3, the ATM filter is also a nonlinear spatially adaptive technique. The one-dimensional (1D) ATM filter presented in Ref. 26 is expanded to 2D. The window size, M, and the trimming parameter, α, are adjusted according to the local pixel value

$$M = \frac{2\beta\lambda}{2\lambda + \beta x},$$

$$\alpha = \frac{\alpha_m x}{\lambda}, \quad (10)$$

where x is pixel value on raw projections, and beta and lambda are two parameters of the ATM filter. When x is zero, the window size M obtains its maximal value at beta.

II.E. Quantitative image evaluation in simulation studies

For parameter choice and step comparison using the simulated breast with contrast detail phantoms, the figure of merit was the number of detectible lesions, which was counted automatically by thresholding each lesion's CNR as well as the normalized cross correlation (NCC) of each lesion with its ideal version on the reconstructed coronal slices of the simulated breast.

The CNR is calculated as the ratio of contrast to percentage noise.[31] The contrast of the lesion is defined as the signal difference relative to the mean of background, while the percentage noise is the standard deviation of the background relative to its mean. Since both the contrast and noise are relative to the mean of background, the CNR is reduced to the ratio between the signal difference to the standard deviation of the background.

The NCC is a mathematical operation defined as[32]

$$\mathrm{NCC}(s,t)=\frac{\sum_x\sum_y(f(x,y)-\bar{f}(x,y))(w(x-s,y-t)-\bar{w})}{\{[\sum_x\sum_y(f(x,y)-\bar{f}(x,y))^2]\cdot[\sum_x\sum_y(w(x-s,y-t)-\bar{w}]^2)\}^{1/2}}, \tag{11}$$

where (x,y) and (s,t) are spatial position indices, f and w are an image and a template, respectively, and $\bar{f}$ and $\bar{w}$ are their average values over the space.

The threshold was *ad hoc* set to 1.0 for CNR and 0.28 for NCC.

To compare quantitatively among various denoising techniques, in addition to the above evaluation on the breast with contrast detail phantoms, we also derived plots of percentage noise against resolution.

In order to measure spatial resolution[31] which is a difficult challenge in these nonlinear image processing algorithms, a high intensity sphere was simulated within the breast, projected, and target reconstructed (with an in-plane pixel dimension of 0.2 mm) around the high-intensity sphere. For each specific denoising technique, first the edges of the circular disk within a reconstructed slice were averaged radially. Then, the averaged edge response outside the high-contrast sphere was fitted to a function, which was the convolution of the original edge response without any denoising procedure and a parametric Gaussian function with standard deviation of σ. The best fit Gaussian function was found with the parameter of σ_{best}, and its full width at half maximum, which is equal to $2.35\sigma_{\mathrm{best}}$, was used as the measure of the spatial resolution related to a specific denoising technique. Since the spatial resolution was measured from the indirect Gaussian function fitting method instead of directly measuring from the reconstructed slice, it was reasonable to get values less than a pixel size.

III. RESULTS

III.A. Simulation results

III.A.1. Step comparison

With more iteration steps, more noise will also be removed by using PDE based technique, with the tradeoff of degrading resolution. So there is no global optimization of parameters per se. To compare objectively between the PDE variants applied at various steps in the reconstruction process, the parameters are chosen such that same amount of noise will be removed from the reconstructed volumes of breasts. In other words, if a uniform region in the simulated breast without lesions is selected as the background, its noise level is matched among PDE variants. The number of detectible lesions from the contrast detail phantom is used as the figure of merit to select from a subset of parameters that remove the same amount of background noise in the breast. For the comparable noise removal, a matched group is $\mathrm{PDE}_{\mathrm{tomo}}$ with iter_num=10, $\Delta t=0.1$, $\sigma=1$ and $\delta_0=0.03$,

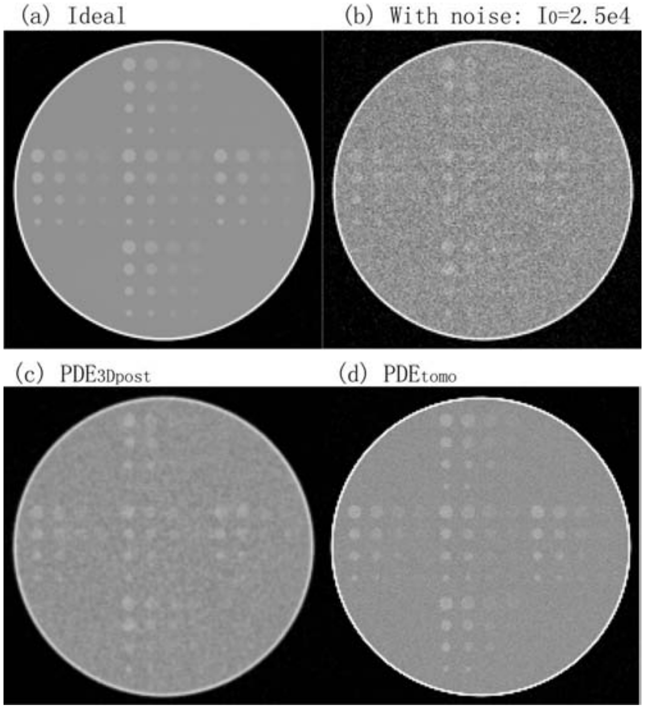

FIG. 4. Step comparison at $I_0=2.5e4$. (a) is a coronal slice of simulated breast with contrast detail phantoms, and (b) shows the same slice with added noise to the projection images. After noise removal, (d) $\mathrm{PDE}_{\mathrm{tomo}}$ applied prior to reconstruction generates better images than (c) $\mathrm{PDE}_{\mathrm{3Dpost}}$ after reconstruction.

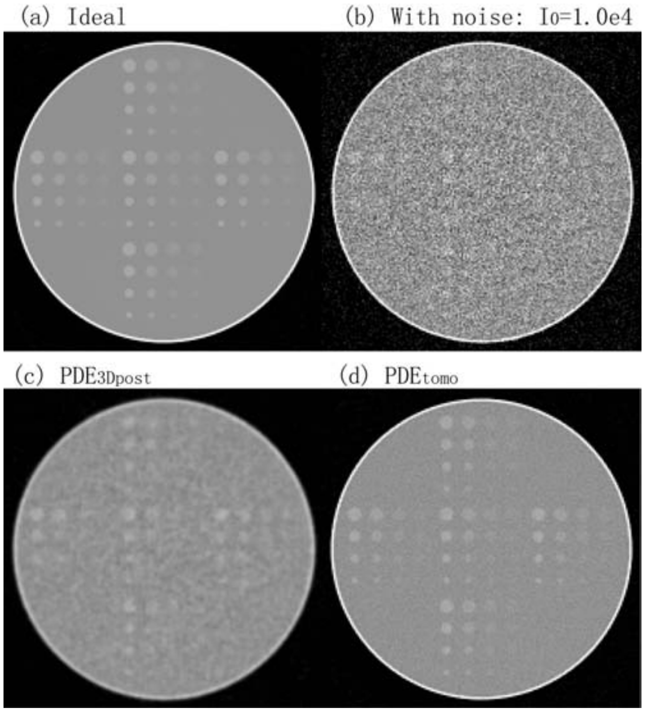

FIG. 5. Step comparison at $I_0=1.0e4$. (b) is noisier than Fig. 4(b). As in Fig. 4: (d) PDE$_{\text{tomo}}$ applied at step 2 is better than (c) PDE$_{\text{3Dpost}}$ applied at step 4.

PDE$_{\text{3Dpost}}$ with iter_num=4, $\Delta t=0.2$, $\sigma=0.15$, and $\delta_0=0.07$, and PDE$_{\text{2D}}$ with iter_num=10, $\Delta t=0.1$, $\sigma=5$, and $\delta_0=0.09$.

Figure 4 shows the reconstructed thin sections of (a) the ideal contrast detail phantom, (b) the image after adding noise corresponding to exposure $I_0=2.5e4$, (c) the image denoised by the PDE$_{\text{3Dpost}}$ algorithm applied at step 4, and (d) the same data denoised by the PDE$_{\text{tomo}}$ algorithm applied at step 2. The reconstructed slice thickness was 0.5 mm and within-plane pixel dimension was 0.4 mm. Figure 5 shows the corresponding results at $I_0=1.0e4$. The noise level is higher in Fig. 5(b) as compared to Fig. 4(b). The sensitivity defined as the ratio of the numbers of detectible lesions to the total number of 80 for each case is shown in Table I. While the CNR and NCC criteria do not give the same number, they provide the same trend: PDE$_{\text{tomo}}$ processed volumes (step 2) have more detectible lesions than PDE$_{\text{3Dpost}}$ processed ones (step 4).

TABLE I. Comparison between denoising applied to reconstruction steps 2 to 4, using CNR and NCC as the criteria. Denoising at step 2 before reconstruction consistently provides a higher number of detectible lesions or a higher ratio of number of detectible lesions to total number of lesions (80 in this study), as does increasing the exposure level.

		Step 2: PDE$_{\text{tomo}}$ (%)	Step 3: PDE$_{\text{2D}}$ (%)	Step 4: PDE$_{\text{3Dpost}}$ (%)
$I_0=1e4$	CNR	55.0	53.8	45.0
	NCC	53.8	53.8	42.5
$I_0=2.5e4$	CNR	61.3	58.8	48.8
	NCC	57.5	53.8	45.0

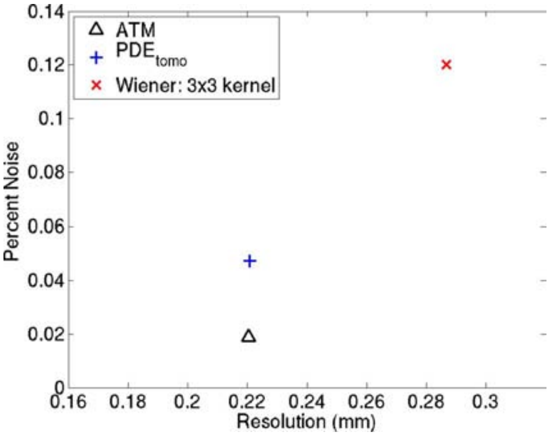

FIG. 6. Noise-resolution plot for PDE$_{\text{tomo}}$, ATM, and Wiener filters at $I_0=2.5e4$. For a high contrast test object, PDE$_{\text{tomo}}$ and ATM have a lower noise level and higher resolution than Wiener filtering. ATM is the best among the three based on the noise-resolution plot.

In addition, both Figs. 4 and 5 show that volumes denoised at step 2 have better visual appearance than those denoised at step 4.

Applying the PDE technique in-between filtering and backprojection steps (step 3) results in reconstructed slices visually similar to Figs. 4(d) and 5(d). However, they have lower sensitivity for detection than PDE$_{\text{tomo}}$ at step 2 but higher than PDE$_{\text{3Dpost}}$ at step 4, as is shown in Table I.

III.A.2. Comparison between denoising techniques

Hereafter, denoising techniques are all applied at step 2. Again, the number of detectible lesions from the contrast detail phantom is used as the figure of merit to select the parameters of ATM filter from within all combinations of beta value ranging from 1 to 20 and lambda from $0.5e4$ to $7.0e4$ with $0.5e4$ as the incremental step. The optimized ATM filter has a beta value of 7 and lambda of $2.0e4$.

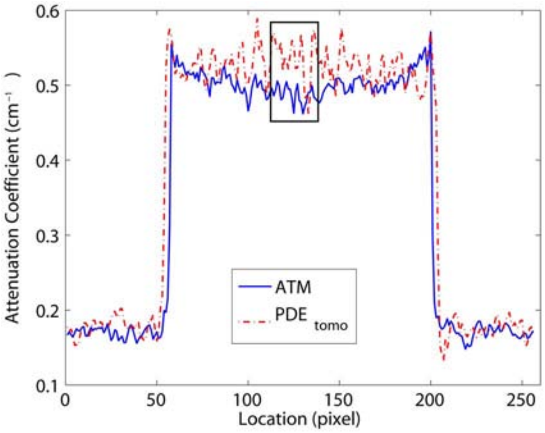

FIG. 7. One-dimensional profiles of the reconstruction through the center of the high contrast object using ATM filter and PDE$_{\text{tomo}}$. It is shown that by using ATM filter there is a cupping effect at the lesion center, which is absent from PDE$_{\text{tomo}}$ and Wiener processed ones. The rectangle is where the noise level is computed for noise-resolution plot.

TABLE II. Technique comparison using contrast detail phantoms. $\mathrm{PDE_{tomo}}$ is the best among three denoising techniques for this task. All images were acquired with the lower exposure of $I_0 = 1.0e4$ counts.

	Wiener (%)	ATM (%)	$\mathrm{PDE_{tomo}}$ (%)
CNR	48.8	51.3	55.0
NCC	42.5	37.5	53.8

The noise-resolution result at the exposure level of $2.5e4$ is given in Fig. 6. It is based on a high-contrast large-size sphere imbedded into the simulated breast. The noise and resolution values are plotted for $\mathrm{PDE_{tomo}}$, Wiener, and ATM techniques. The Wiener filter is applied using a 3×3 kernel. $\mathrm{PDE_{tomo}}$ processing resulted in lower noise than Wiener filtering (4.7% and 12%, respectively). At the same time, $\mathrm{PDE_{tomo}}$ also provided better resolution than Wiener filtering (0.22 versus 0.29 mm, respectively). The ATM filter provided the same 0.22 mm resolution as $\mathrm{PDE_{tomo}}$, while reducing noise to 2.0%. However, the ATM reconstructed image shows a cupping artifact, which is absent in the $\mathrm{PDE_{tomo}}$ processed one. The cupping artifact is evident in the 1D profile through the center of the high-contrast object shown in Fig. 7. Note that the rectangle represents the location where the noise level is measured and does not capture the nonuniformity problem.

To get the number of detectible lesions from the contrast detail phantom or sensitivity comparison, the results from the Wiener 3×3 kernel and 5×5 kernel at exposure level of $1.0e4$ were interpolated to match the background noise with $\mathrm{PDE_{tomo}}$. And the background noise level matched ATM filter has parameters of beta of 7 and lambda=$1.8e4$. The sensitivity results are shown in Table II. $\mathrm{PDE_{tomo}}$ gives the largest number of detectible lesions for the contrast detail phantom, followed by ATM and then the Wiener filter, according to the CNR criterion.

III.B. Human subject results

When applied to the clinical data sets, the parameters of $\mathrm{PDE_{tomo}}$ used are: $\Delta t = 0.1$, $\sigma = 1$, $\delta_0 = 0.03$, and iter_num $= 10$.

Figures 8 and 9 show the coronal reconstructed slices from two human subjects. By visual comparison, the $\mathrm{PDE_{tomo}}$ technique (bottom row) reduces the noise considerably while maintaining the resolution of the original reconstruction (top row).

IV. DISCUSSION

Dedicated breast CT imaging is an exciting new modality that possesses the potential of improving breast cancer diagnosis over conventional mammography. Some preliminary studies[19,33] show that satisfactory images can be acquired using the same dose as standard two-view mammography. When this dose is divided among the potentially hundreds of individual projection images comprising each scan, the high level of quantum noise in the projection data will pass through to the final reconstructed volume. This motivates the development of denoising tools to effectively remove the noise, improve lesion conspicuity, and maintain image resolution.

One important consideration of noise removal in breast CT is where to apply a denoising technique. In this study, five separate techniques were developed for three different steps in the reconstruction process. By optimizing each of them independently within the subsets that result in the same amount of noise removal from the breast, it was found that denoising before reconstruction provides better images than after reconstruction. This is understandable, since some fine details in the volumes can be overwhelmed by the abundant noise during the reconstruction step. Applying denoising afterwards cannot recover that information. By contrast, if a denoising technique is applied before reconstruction, it is possible for the fine details to be preserved.

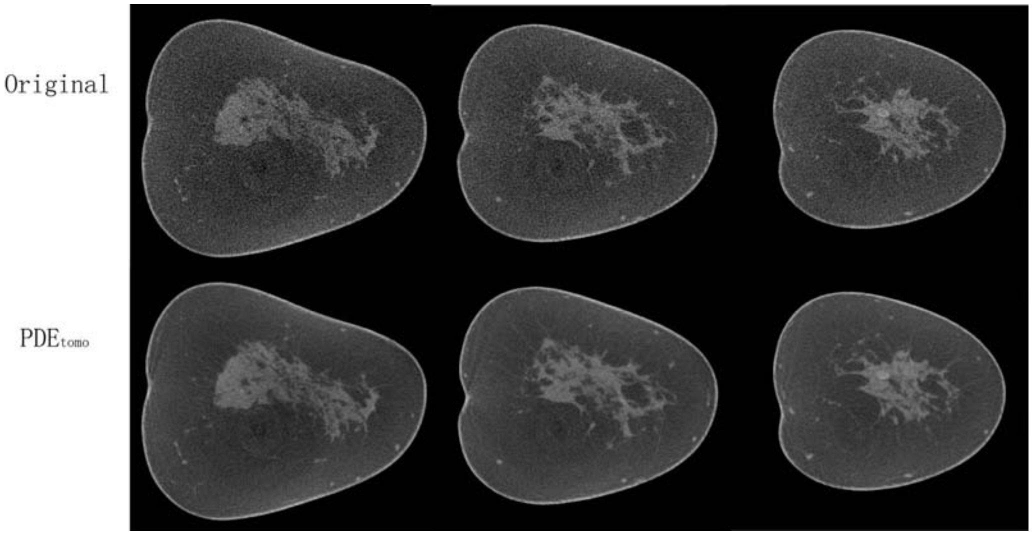

FIG. 8. Human subject result No. 1. Top row shows original reconstruction, coronal slices from normal breast. Bottom row shows same slices with $\mathrm{PDE_{tomo}}$ denoising, resulting in remarkably reduced noise levels.

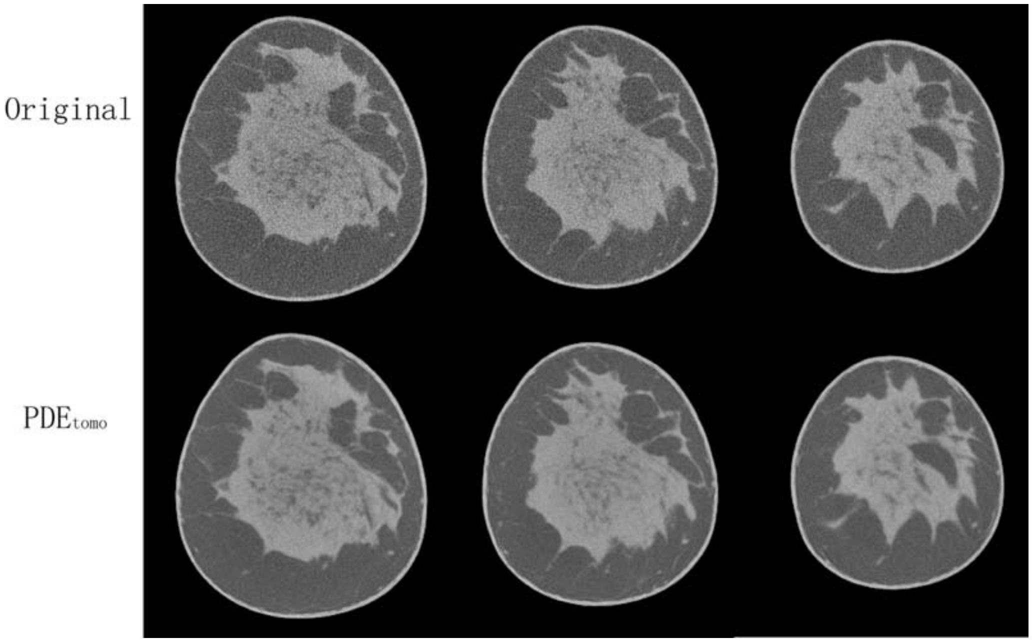

FIG. 9. Human subject result No. 2. Top row shows original reconstruction, coronal slices from normal breast. Bottom row shows same slices with $\mathrm{PDE}_{\mathrm{tomo}}$ denoising, resulting in markedly reduced noise levels.

Both the quantitative results in the simulation study and the visual inspection in human subject data study showed the promise of the $\mathrm{PDE}_{\mathrm{tomo}}$ technique. In the simulation study, it was compared with ATM as well as Wiener techniques, two adaptive denoising techniques. The noise versus resolution results show that $\mathrm{PDE}_{\mathrm{tomo}}$ denoising can achieve lower noise and higher resolution in the reconstructed volume than the Wiener technique. ATM denoising did yield even lower noise, but with cupping artifacts at the center of the breast. In comparison to ATM filtering, $\mathrm{PDE}_{\mathrm{tomo}}$ provided the same high resolution but the noise levels all over the breast region were more uniform. In addition, the detectability of low contrast lesions was assessed with the use of contrast detail phantoms. $\mathrm{PDE}_{\mathrm{tomo}}$ once again proved to be the best overall performer, consistently providing the best sensitivity for lesion detection compared to other techniques. The advantage of $\mathrm{PDE}_{\mathrm{tomo}}$ over other techniques in terms of decreased noise level and improved noise uniformity are both more evident when the dose was lowered to 40% of the original value, which suggests that the $\mathrm{PDE}_{\mathrm{tomo}}$ technique holds more promise for processing data sets acquired at lower dose levels. With $\mathrm{PDE}_{\mathrm{tomo}}$, the sensitivity for lesion detection using the contrast detail phantom drops by less than 7% when the dose is cutoff more than half that of the two-view mammography.

Even though the theoretical description of the noise variance in the projection image due to the quantum noise and the logarithm operation is more approximate for the empirical data, the $\mathrm{PDE}_{\mathrm{tomo}}$ technique still provides good denoised images.

There are some limitations in this study. First, the simulated breast CT data are based on a monochromatic x-ray beam with the kilovolt (kV) value set to be approximately the same as the effective kV value of the x-ray beam used to acquire the empirical data. Second, the parameters in the measurement model used for adding noise to the simulated projection images are all hypothetical, given that presently their empirical values are unknown. Hence, the task of calibrating the dose in the simulation study cannot be fulfilled at this stage. In future work, considerable optimization remains to be performed to calibrate the $\mathrm{PDE}_{\mathrm{tomo}}$ technique using empirical images taken with physical phantoms as well as human subjects. Given the robust trends shown in this study, however, the $\mathrm{PDE}_{\mathrm{tomo}}$ technique should continue to match or outperform the Wiener and possibly ATM technique, especially if dose is further lowered such as to achieve a breast CT scan with equal or less dose than single-view conventional mammograms.

Due to the very low photon fluence on each projection view in dedicated breast CT, the electronic noise is one of the major sources of the overall noise, especially in dense breast regions or if the dose is further reduced. The present version of the $\mathrm{PDE}_{\mathrm{tomo}}$ technique does not consider the effects of additive electronic noise. It will be worthwhile to explore the possibility of taking the characteristics of this type of noise into account in the denoising technique or to combine it with a statistical-modeling approach that explicitly treats the electronic noise.

In conclusion, a partial diffusion equation based denoising technique was developed specifically for sinogram smoothing in dedicated breast CT data. By incorporating into the algorithm the knowledge of the nonuniform distribution of the noise in the projection image after preprocessing but before reconstruction filtering and backprojection, it provides substantially denoised data with sharp edges. The technique may hold even more promise on data sets acquired with lower dose.

ACKNOWLEDGMENTS

This work was supported in part by grants from the National Institutes of Health (R01 CA 94236 and R01 CA 112437) and the U.S. Army Breast Cancer Research Program (W81XWH-05-1-0278). The authors would like to thank the anonymous reviewers for their constructive comments.

[a)] Electronic mail: qing.xia@duke.edu

[1] ACS, *American Cancer Society: Cancer Facts and Figures 2008* (American Cancer Society, Atlanta, Georgia, 2008).

[2] S. W. Fletcher and J. G. Elmore, "Mammographic screening for breast cancer," N. Engl. J. Med. **348**, 1672–1680 (2003).

[3] L. Nystrom, I. Andersson, N. Bjurstam, J. Frisell, B. Nordenskjold, and L. E. Rutqvist, "Long-term effects of mammography screening: Updated overview of the swedish randomised trials," Lancet **359**, 909–919 (2002).

[4] V. P. Jackson, R. E. Hendrick, S. A. Feig, and D. B. Kopans, "Imaging of the radiographically dense breast," Radiology **188**, 297–301 (1993).

[5] L. T. Niklason *et al.*, "Digital tomosynthesis in breast imaging," Radiology **205**, 399–406 (1997).

[6] J. T. Dobbins and D. J. Godfrey, "Digital x-ray tomosynthesis: Current state of the art and clinical potential," Phys. Med. Biol. **48**, R65–R106 (2003).

[7] J. M. Boone, T. R. Nelson, K. K. Lindfors, and J. A. Seibert, "Dedicated breast CT: Radiation dose and image quality evaluation," Radiology **221**, 657–667 (2001).

[8] K. K. Lindfors, J. M. Boone, T. R. Nelson, K. Yang, A. L. C.Kwan, and D. F. Miller, "Dedicated breast CT: Initial clinical experience," Radiology **246**, 725–733 (2008).

[9] X. Gong, A. A. Vedula, and S. J. Glick, "Microcalcification detection using cone-beam CT mammography with a flat-panel imager," Phys. Med. Biol. **49**, 2183–2195 (2004).

[10] C. J. Lai *et al.*, "Effects of radiation dose level on calcification visibility in cone beam breast CT: A preliminary study," Proc. SPIE **6142**, 614233 (2006).

[11] Z. K. Chen and R. Ning, "Why should breast tumor detection go three dimensional?," Phys. Med. Biol. **48**, 2217–2228 (2003).

[12] R. L. McKinley, M. P. Tornai, E. Samei, and M. L. Bradshaw, "Simulation study of a quasi-monochromatic beam for x-ray computed mammotomography," Med. Phys. **31**, 800–813 (2004).

[13] C. H. Chang, J. L. Sibala, S. L. Fritz, J. H. Gallagher, S. J. Dwyer, and A. W. Templeton, "Computed tomographic evaluation of breast," AJR Am. J. Roentgenol. **131**, 459–464 (1978).

[14] R. Ning, X. Tang, and D. Conover, "X-ray scatter correction algorithm for cone beam CT imaging," Med. Phys. **31**, 1195–1202 (2004).

[15] X. Gong, S. J. Glick, B. Liu, A. A. Vedula, and S. Thacker, "A computer simulation study comparing lesion detection accuracy with digital mammography, breast tomosynthesis, and cone-beam CT breast imaging," Med. Phys. **33**, 1041–1052 (2006).

[16] D. J. Crotty, R. L. McKinley, and M. P. Tornai, "Experimental spectral measurements of heavy *K*-edge filtered beams for x-ray computed mammotomography," Phys. Med. Biol. **52**, 603–616 (2007).

[17] K. Yang, A. L. C. Kwan, and J. M. Boone, "Computer modeling of the spatial resolution properties of a dedicated breast CT system," Med. Phys. **34**, 2059–2069 (2007).

[18] S. J. Tu, C. C. Shaw, and L. Y. Chen, "Noise simulation in cone beam CT imaging with parallel computing," Phys. Med. Biol. **51**, 1283–1297 (2006).

[19] J. M. Boone *et al.*, "Performance assessment of a pendant-geometry CT scanner for breast cancer detection," Proc. SPIE **5745**, 319–323 (2005).

[20] P. J. La Riviere, "Penalized-likelihood sinogram smoothing for low-dose CT," Med. Phys. **32**, 1676–1683 (2005).

[21] J. Wang, T. F. Li, H. B. Lu, and Z. R. Liang, "Penalized weighted least-squares approach to sinogram noise reduction and image reconstruction for low-dose x-ray computed tomography," IEEE Trans. Med. Imaging **25**, 1272–1283 (2006).

[22] J. Zhong, R. Ning, and D. Conover, "Image denoising based on multiscale singularity detection for cone beam CT breast imaging," IEEE Trans. Med. Imaging **23**, 696–703 (2004).

[23] P. Perona and J. Malik, "Scale-space and edge detection using anisotropic diffusion," IEEE Trans. Pattern Anal. Mach. Intell. **12**, 629–639 (1990).

[24] J. Weichert, *Anisotropic Diffusion in Image Processing* (Tuebner, Stuttgart, 1998).

[25] T. L. Pope, M. E. Read, T. Medsker, A. J. Buschi, and A. N. Brenbridge, "Breast skin thickness: normal range and causes of thickening shown on film-screen mammography," J. Can. Assoc. Radiol. **35**, 365–368 (1984).

[26] J. Hsieh, "Adaptive streak artifact reduction in computed tomography resulting from excessive x ray photon noise," Med. Phys. **25**, 2139–2147 (1998).

[27] L. A. Feldkamp and J. W. Kress, "Practical cone-beam algorithm," J. Opt. Soc. Am. A **1**, 612–619 (1984).

[28] D. A. McQuarrie, *Mathematical Methods for Scientists and Engineers* (University Science Books, New York, 2003).

[29] F. Catte, P. L. Lions, J. M. Morel, and T. Coll, "Image selective smoothing and edge-detection by nonlinear diffusion," SIAM J. Numer. Anal. **29**, 182–193 (1992).

[30] G. W. Oehlert, "A note on the delta method," Am. Stat. **46**, 27–29 (1992).

[31] J. T. Bushberg, J. A. Seibert, E. M. Leidholdt, Jr., and J. M. Boone, *The Essential Physics of Medical Imaging* (Lippincott Williams & Wilkins, New York, 2001).

[32] R. C. Gonzalez and R. E. Woods, *Digital Image Processing* (Addison-Wesley, New York, 1993).

[33] B. Chen and R. Ning, "Cone-beam volume CT breast imaging: Feasibility study," Med. Phys. **29**, 755–770 (2002).

DEDICATED COMPUTED TOMOGRAPHY OF THE BREAST: IMAGE PROCESSING AND ITS IMPACT ON BREAST MASS DETECTABILITY

by

Qing Xia

Department of Biomedical Engineering
Duke University

Date:_______________________
Approved:

____
Joseph Y. Lo, Ph.D., Supervisor

____
Ehsan Samei, Ph.D.

____
Mary Scott Soo, M.D.

____
Georgia D. Tourassi, Ph.D.

____
Gregg E. Trahey, Ph.D.

Dissertation submitted in partial fulfillment of
the requirements for the degree of Doctor of Philosophy
in the Department of Biomedical Engineering
in the Graduate School
of Duke University

2007

ABSTRACT

DEDICATED COMPUTED TOMOGRAPHY OF THE BREAST: IMAGE PROCESSING AND ITS IMPACT ON BREAST MASS DETECTABILITY

by

Qing Xia

Department of Biomedical Engineering
Duke University

Date:__________________________
Approved:

____
Joseph Y. Lo, Ph.D., Supervisor

____
Ehsan Samei, Ph.D.

____
Mary Scott Soo, M.D.

____
Georgia D. Tourassi, Ph.D.

____
Gregg E. Trahey, Ph.D.

An abstract of a dissertation submitted in partial fulfillment of
the requirements for the degree of Doctor of Philosophy
in the Department of Biomedical Engineering
in the Graduate School
of Duke University

2007

Copyright by
Qing Xia
2007

Abstract

Dedicated breast CT imaging is a novel breast imaging modality. Compared to conventional mammography, breast CT may improve lesion detection while using a comparable radiation dose. As a result of its cone beam geometry, however, breast CT suffers from image degradation due to scatter radiation. Moreover, the breast CT images divide the dose of mammography among hundreds of projection views, resulting in considerable quantum noise. It is therefore desirable to reduce scatter and noise in the reconstructed breast volume without loss of spatial resolution.

Several new image-processing techniques were developed based on the unique physical properties of this modality. Firstly, a Gaussian noise model was proposed for scatter removal, which was a statistical model based post-acquisition scatter compensation technique. Algorithms using maximum likelihood estimation and maximum *a posterior* estimation of scatter-free images were evaluated.

Secondly, several partial diffusion equation (PDE) based denoising technique were developed for dedicated breast CT. The techniques were thoroughly evaluated based on simulation. Specifically two issues were considered: (1) where in the reconstruction process to apply a denoising technique and (2) which of the spatially adaptive techniques is a better choice. The technique was then applied to human subject data.

Finally, the previously described image processing tools were then analyzed for the clinically relevant task of lesion detectability in human subjects, using numerical observers and ROC analysis methodology.

Using images obtained on a full field digital mammography system, the Gaussian noise model demonstrated effective scatter removal. The denoising techniques were also promising. Applying a denoising technique before reconstruction provides better images than after reconstruction. A PDE technique taking into the account the non-uniform distribution of the noise in the projection image after the preprocessing step provides excellent denoised data with sharp edges. It outperforms two other spatially adaptive techniques (Wiener and 2D ATM filters). The preliminary ROC study showed that with a fixed size lesion in real anatomical backgrounds, PDE-denoised images had higher detectability, higher CNR and better qualitative appearance. These promising new techniques for noise and scatter compensation pave the way for future implementations of dedicated breast CT.

Acknowledgments

First and foremost I would like to express my deep gratitude to my previous advisor, Dr. Carey E. Floyd Jr., for the great support during my most difficult time in the graduate school. Without him, I can’t be where I am now.

I would like to thank my present advisor, Dr. Joseph Y. Lo, for the great guidance and encouragement during the last year. His enthusiasm toward science and other people are contagious and always inspires me advancing my projects. Also, I would like to thank my mentor, Dr. Georgia D. Tourassi, for her unique support and encouragement from a female researcher’s perspective.

Thanks are due to other members of my committee: Dr. Loren W. Nolte, Dr. Ehsan Samei, Dr. Mary Scott Soo, and Dr. Gregg E. Trahey. Each one of them has offered their invaluable advice on this project. I thank Dr. John M. Boone and Kai Yang in University of California Davis for providing us the human subject breast CT data.

Thanks are due to all the DAILabers for providing such a nice environment to work in, and to my friends Yong Wang, Hua Guo, Yuting Qi, Dehong Liu, Lihan He, Ya Xue, Jiayu Song and Gang Ye for making the stay in Duke far more interesting.

Finally, I owe a great debt of gratitude to my parents Shenghuai Xia and Jianping Zhu, for providing me precious education opportunities during their difficult time; to my bother Qing Xia, for accompanying the journey of life; to my in-law family members: Gaoxin Zhai, Meizhen Su, Juan Zhai, Jiangqing Guo and Jingyi Guo, for their understanding; and to my husband Liang, my son Ray and my daughter Lily for making my life complete.

Dedication

To my husband Liang, son Ray and daughter Lily!

Table of Contents

Abstract iv

Acknowledgments vi

Dedication vii

List of Tables xii

List of Figures xiii

1 Introduction 1

1.1 Clinical Relevance: Breast Cancer 1

1.2 Limitations of Screening Mammography 2

1.3 Emerging New X-Ray Technologies for Breast Imaging 2

1.3.1 Full Field Digital Mammography 3

1.3.2 Breast Tomosynthesis 4

1.3.3 Dedicated Breast CT 5

1.4 Statement of Work 7

2 Breast CT System and Reconstruction 10

2.1 Feasibility of Breast CT Imaging 10

2.2 Breast CT system in UC Davis 12

2.2.1 Hardware Components of the System 13

2.2.2 System Calibration 13

2.3 Tomographic Reconstruction 14

2.3.1 Reconstruction Technique Categories 14

2.3.2 FBP 18

3 Gaussian Noise Model for Scatter Compensation 21

3.1 Introduction 21

3.2 Gaussian Noise Model 24
3.2.1 Assumption 24
3.2.2 The Model 25
3.2.3 Maximum Likelihood Estimate of Scatter-Free Image 26
3.2.4 Maximum *A Posteriori* Estimate of Scatter-free Image 26
3.3 Materials and Evaluation Methods 27
3.3.1 Test Images 27
3.3.2 Image Evaluation Metrics 28
3.3.2.1 Residual Scatter Fraction 29
3.3.2.2 Contrast, Noise and CNR 29
3.3.2.3 Resolution 30
3.4 Results 31
3.4.1 Scatter Compensation Technique -- Tissue Equivalent Slabs 31
3.4.2 Scatter Compensation Technique -- Anthropomorphic Phantom 34
3.5 Discussion 35
4 Noise Removal in Breast CT: Where to Apply 37
4.1 Introduction 37
4.2 Materials and Methods 38
4.2.1 Simulated Breast CT Datasets 38
4.2.2 PDE Denoising Techniques 40
4.2.2.1 PDE_{2D} 41
4.2.2.2 PDE_{tomo} 43
4.2.2.3 PDE_{3Dpost} 44
4.2.3 Image Evaluation 45
4.3 Results 45

4.3.1 Parameter Choice 45
4.3.2 Step Comparison 46
4.4 Discussion 50
5 Noise Removal in Breast CT: the PDE$_{tomo}$ Technique 53
5.1 Introduction 53
5.2 Materials and Methods 54
5.2.1 Human Subject Datasets 54
5.2.2 Denoising Techniques 54
5.2.2.1 Wiener filter 54
5.2.2.2 Adaptive Trimmed Mean (ATM) filter 55
5.2.3 Image Evaluation 55
5.3 Results 56
5.3.1 Simulation Results: Comparison between denoising techniques 56
5.3.2 Human Subject Results 67
5.4 Discussion 72
6 Breast Mass Detectability Study 75
6.1 Materials and Methods 75
6.1.1 Datasets and Mass Simulation 75
6.1.2 Numerical Observers 76
6.1.2.1 Ideal Observer for SKE/BKE 76
6.1.2.2 Laguerre-Gauss Channelized Hotelling Observer (LG-CHO) 77
6.1.2.3 CNR Observer 78
6.1.3 ROC Analysis 78
6.2 Results 79
6.2.1 Sample ROIs 79

6.2.2 Contrast Detail Phantom Results 85

6.2.3 Human Subject Background Results 88

6.3 Discussion 90

7 Conclusion and Future Work 93

7.1 Summary 93

7.2 Future Direction 95

Appendix Derivation of MLE Algorithm Based on Gaussian Noise Model 97

Bibliography 99

Biography 109

List of Tables

Table 3.1: Resolution results of the Gaussian noise model based MAP estimates with various magnitudes of scatter kernel. The larger the magnitude of scatter 33

kernel, the sharper the processed image is. For the magnitude of zero, i.e., no scatter removal, the resolution is always degraded.. 33

Table 3.2: Corresponding residual scatter fraction and contrast to noise ratio results for the three images shown in Figure 3.8. 35

Table 6.1: AUC values for the three types of numerical observers using real anatomical background from breast CT. 90

List of Figures

Figure 1.1: Picture of a breast tomosynthesis system. The red arrow indicates the arc path that the x-ray tube moves along.. 5

Figure 1.2: Illustration of a dedicated breast CT system. The x-ray tube and flat-panel detector rotate together around the breast, which is the only region to be illuminated. 6

Figure 1.3: Flowchart to show the components of the dissertation. 7

Figure 2.1: Picture of the breast CT system in UC Davis. The table top is removed. Used with permission by John Boone PhD, University of California Davis. 12

Figure 2.2: Example to show the importance of acquiring the accurate geometry of the breast CT system. On the right is the accurate reconstruction. On the left is the one reconstructed with the central ray off by a single pixel... 14

Figure 2.3: When a circular orbit is used, the volume that can be accurately reconstructed is a torus-shaped volume. By contrast, the shadow zone marked by the arrow will have some artifacts.. 15

Figure 2.4: Illustration of the central slice theorem. 16

Figure 2.5: Coordinate systems used in the cone-beam CT reconstruction. (a) 3D view; and (b) 2D view along +Z direction... 18

Figure 3.1: Illustration of possible interactions between x-ray photons and the matter within the diagnostic x-ray energy range. The ellipsoid represents the object to be imaged. Photons can be totally absorbed by the photoelectric effect (ray 1), or be scattered through Compton scattering (ray 2) and Raleigh scattering (a very small portion, thus neglected). The rest will survive the attenuation and are called the primary photons or primary radiation (ray 3). 23

Figure 3.2: An anti-scatter grid can be added on top of the detector to remove scatter radiation. However, as shown by the middle ray, some primary radiation will be blocked as well. To maintain the image quality, the patient dose has to be increased.... 23

Figure 3.3: Schematic of a scatter kernel with a radially exponential shape. It has two parameters: full width at half maximum (FWHM) and magnitude. 25

Figure 3.4: Radiograph of the tissue equivalent slabs. The arrays of white disks are the shadows of beam stops. The CNR values are obtained based on the dark square region of interest. 28

Figure 3.5: Plots of (a) residual scatter fraction and (b) contrast to noise ratio as the function of iteration numbers between MLE and MAP estimates of scatter free image *B* based on Poisson and Gaussian noise models. While both techniques were effective at removing scattered radiation, the MAP based on the Gaussian noise model (green line on right) showed greatest CNR improvement. 31

Figure 3.6: Plots of (a) residual scatter fraction and (b) contrast to noise ratio as a function of iteration numbers were shown for various magnitudes of scatter kernel using MAP estimates of scatter free image *B* based on the Gaussian noise model. A magnitude of 0.0 (blue line) corresponds to no scatter removal, magnitude of 0.52 (green line) corresponds to actual measured values, and a magnitude of 0.65 (purple........................ 32

line) overcompensates the scattered radiation, resulting in negative residual scatter fraction values. At each magnitude level, the contrast increases asymptotically. 32

Figure 3.7: Plots of (a) absolute noise, (b) background mean, (c) absolute signal difference, and (d) contrast as a function of iteration numbers were shown for various magnitudes of scatter kernel using MAP estimates of scatter free image *B* based on the Gaussian noise model. 33

Figure 3.8: Radiographs of the breast anthropomorphic phantom, (a) with an anti-scatter grid, (b) without an anti-scatter grid, and (c) without an anti-scatter grid and with scatter reduction. 34

Figure 4.1 One-dimensional line integral profiles of both simulation and clinical datasets. It's seen that I0=2.5e4 gives a roughly comparable profile to the clinical cases. 39

Figure 4.2: Illustration of possible steps in the reconstruction process that an image denoising module can be applied to in dedicated breast CT. 40

Figure 4.3: Diffusivity function with delta value of 2. 42

Figure 4.4: One-dimensional line integral profiles across the breast on a projection image. The dashed (blue) and continuous (red) plots correspond to noise free case and the case with I_0=2.0e3, respectively. The variance of line integral is larger at the center of breast region, and gets smaller toward the skin. 44

Figure 4.5: Performance from contrast detail phantom as a function of (a) Δt, or (b) δ_0, parameters in the PDE_{tomo} technique, with all other parameters held at their optimal values. 46

Figure 4.6: Step comparison at I_0=2.5e4. To (a) an ideal contrast detail phantom, noise is added to yield (b) the initial image without any denoising. (d) PDE_{tomo} noise removal before the FBP reconstruction is better than (c) after reconstruction. 48

Figure 4.7: Step comparison at I_0=1e4. Figure 4.7 (b) is noisier than Figure 4.6 (b). For subfigures (c) and (d), they come to the same conclusion: (d) PDE_{tomo} applied at step 2 is better than (c) $\text{PDE}_{\text{3Dpost}}$ applied at step4. 49

Figure 4.8: Comparison between denoising applied to reconstruction steps 2, 3 and 4, using CNR and NCC as the criteria. Denoising at step 2 before reconstruction consistently provides higher number of detectable lesions or sensitivity, as does increasing the exposure level... 50

Figure 5.1: Reconstructed slices of original, Wiener (3x3 kernel) and PDE_{tomo} processed datasets in a simulation study with varying photon fluence levels. The lesion is located at the center of each slice... 57

Figure 5.2: Target reconstructed slices of original, Wiener (3x3 kernel) and PDE_{tomo} processed datasets in a simulation study with varying photon fluence levels, corresponding to the data in Figure 5.1.. 58

Figure 5.3: (a) Reconstruction slices without a lesion. Along the horizontal lines marked in (a), standard deviations of local 7x7 ROI are plotted for original, Wiener (3x3 kernel) and PDE_{tomo} processed datasets at I_0 of (b) 2.5e3, (c) 5e3 and (d) 2.5e4......................... 61

Figure 5.4: CNR comparison between the original, Wiener (3x3 kernel) and PDE_{tomo} processed volumes in a simulation study with I_0=2.5e4. 62

Figure 5.5: Comparison of techniques using contrast detail phantoms. All images were acquired with the lower exposure of 1e4 counts. PDE_{tomo} is the best among three denoising techniques for this task. 63

Figure 5.6: (a) Target reconstruction around a high contrast object from original, Wiener processed and PDE_{tomo} processed datasets, and (b) noise-resolution plot at I_0=2.5e4.. 66

Figure 5.7: One-dimensional profile of the reconstruction through the center of the high contrast object using PDE_{tomo} and ATM filter. 66

Figure 5.8: Human subject No.1 slice 60. 67

Figure 5.9: Human subject No.1 slice 80. 68

Figure 5.10: Human subject No.1 slice 80 –smaller ROI corresponding to the rectangle in Figure 5.9. 68

Figure 5.11: Human subject No.1 slice 100... 69

Figure 5.12: Human subject No.1 slice 120... 69

Figure 5.13: Human subject No.2 slice 60. 70

Figure 5.14: Human subject No.2 slice 80. 70

Figure 5.15: Human subject No.2 slice 100... 71

Figure 5.16: Human subject No.2 slice 100 –smaller ROI corresponding to the rectangle in Figure 5.15. 71

Figure 5.17: Human subject No.2 slice 120... 72

Figure 6.1: Sample ROIs No.1 for simulated lesion of 5 mm and 10%: Original ROIs (a) without mass and (b) with a mass, and, PDE denoised ROIs (c) without mass and (d) with a mass. 79

Figure 6.2: Sample ROIs No.2 for simulated lesion of 5 mm and 10%: Original ROIs (a) without mass and (b) with a mass, and, PDE denoised ROIs (c) without mass and (d) with a mass. 80

Figure 6.3: Sample ROIs No.1 for simulated lesion of 5 mm and 3%: Original ROIs (a) without mass and (b) with a mass, and, PDE denoised ROIs (c) without mass and (d) with a mass. 81

Figure 6.4: Sample ROIs No.2 for simulated lesion of 5 mm and 3%: Original ROIs (a) without mass and (b) with a mass, and, PDE denoised ROIs (c) without mass and (d) with a mass. 82

Figure 6.5: Sample ROIs No.1 for simulated lesion of 4 mm and 2%: Original ROIs (a) without mass and (b) with a mass, and, PDE denoised ROIs (c) without mass and (d) with a mass. 83

Figure 6.6: Sample ROIs No.2 for simulated lesion of 4 mm and 2%: Original ROIs (a) without mass and (b) with a mass, and, PDE denoised ROIs (c) without mass and (d) with a mass. 84

Figure 6.7: CNR observer results for contrast detail phantoms embedded in a simulated uniform background. CNR histograms for original and PDE processed ROI databases are shown in (a) and the corresponding ROC curves are shown in (b). The Az value of the PDE processed dataset (0.998 ± 0.005) is statistically higher than the Az value of the original dataset (0.933 ± 0.020). The p value is less than 0.01. 86

Figure 6.8: LG-CHO observer results for contrast detail phantoms embedded in a simulated uniform background. 87

Figure 6.9: CNR observer results for simulated lesions of 4mm and 2% embedded in real anatomical backgrounds. CNR histograms for original and PDE processed ROI databases are shown in (a) and the corresponding ROC curves are shown in (b). The Az value of the PDE processed dataset (0.770 ± 0.023) is statistically higher than the Az value of the original dataset (0.801 ± 0.022). The p value is less than 0.01 89

1 Introduction

1.1 Clinical Relevance: Breast Cancer

Breast cancer is the most common cancer type that affects women globally [1]. In the United States, due to the long life spans, the incidence is even higher: every one woman over eight will develop breast cancer in her lifetime. It was estimated that approximately 178,480 new invasive breast cancer cases would be found in American women in 2007 [2]. Moreover breast cancer is one of the leading causes of cancer-related women mortality, secondary only to lung cancer. It is predicted that the disease will kill about 40,460 US women in 2007 [2].

Presently there is no effective way of preventing the disease. However, detection of the cancer at its early stage has been found to significantly improve survival rates [3-6]. For example, when breast cancer is detected at the localized stage, the five-year relative survival rate is 98% [2]. By contrast, when it is not found until metastasized, the five-year survival rate drops dramatically. In addition, when the cancer is found earlier, more viable treatment options are also available [7-9].

X-ray mammography is presently the primary tool for early detection of breast cancer. The standard screening procedure is to acquire a pair of two-dimensional projection images: mediolateral oblique (MLO) view and cranial-caudal (CC) view. The abnormalities can manifest themselves on a mammogram as masses, clusters of microcalcifications, or architectural distortions. An annual screening program based on mammography is recommended for women older than forty years or younger women with higher risk by National Cancer Institute, American Cancer Society and American College of Radiology. It has been proven to reduce the mortality rate of the breast cancer since its initiation. For example, screening mammography decreases the fifteen year mortality for women in their forties by 20% [10]. Also, it is found that screening is most effective for women older than 55 years old [10, 11].

1.2 Limitations of Screening Mammography

While film-screen X-ray mammography has been proven to be effective, it is not perfect in its detection sensitivity of breast lesions due to several limitations such as two-dimensional (2D) projection data acquisition and restricted range of linear optical response of the detector. With 2D acquisition, the anatomical tissue superimpose with each other such that the anatomical noise may potentially obscure a breast lesion. Overall, it has sensitivity within the range of 63% to 88% depending on the patient's age group, family history [12] and breast density [13]. For women with dense breasts, the sensitivity is lower since on their mammograms the dense appearance of the breast tissue is more likely to obscure any abnormalities and makes the detection of breast cancer even more challenging [14]. In addition, the situation gets complicated by the fact that breast density is also a risk factor by itself, which means that women with dense breasts tend to have higher probability of getting breast cancer.

1.3 Emerging New X-Ray Technologies for Breast Imaging

Other imaging modalities that are explored for breast imaging are: Ultrasound, Magnetic Resonance Imaging (MRI) and nuclear medicine. Ultrasound imaging of the breasts is able to detect some of the lesions that are missed by film-screen mammography. However, using breast ultrasound technique as a screening tool is debatable due to the fact that those lesions are found at the expense of many unnecessary biopsies. For example, in the same study mentioned above [13], ultrasound found 33 cases of breast cancer that were undetected by screening mammography, but it also led to additional 287 false positive cases. Magnetic Resonance Imaging (MRI) is playing an increasing role in breast imaging, such as for screening of high-risk women, local staging of cancers, and monitoring neoadjuvant therapy.

With the advent of flat-panel detector techniques, new approaches to breast imaging using x-rays are emerging. Among them, the three major categories are: Full-Field Digital Mammography (FFDM), breast tomosynthesis and dedicated breast CT.

1.3.1 Full Field Digital Mammography

The major difference between a digital breast-imaging system and a film-screen mammography system is the detector type. The advantages of the digital flat-panel detector over the film-screen detector include excellent linear response and wide latitude, which overcome the underexposure or overexposure problem existing with the film-screen detector. The wide latitude and use of higher quality spectra may also permit dose reduction. It is of great interest to researchers to know whether a FFDM system poses any advantage to the conventional film-screen system in term of lesion detectability [15-23]. Generally the diagnostic accuracies based on the two types of system are comparable. For women within certain categories, the FFDM system even outperforms the film-screen system. For example, Pisano *et al* [18] found that digital mammography has statistically better diagnostic accuracy than film-screen mammography for women less than 50 years old, having dense breasts, or pre-menopausal or peri-menopausal.

Another advanced x-ray technology based on FFDM is the dual-energy digital mammography technique [24, 25]. The breast is imaged twice: one at a low energy level and the other at a high energy level. The resultant images are subtracted to reduce the anatomical noise in the detection of microcalcifications.

Although promising, the FFDM technique and its variant share with the film-screen technique one common limitation: the images acquired are still two-dimensional.

Projecting a three-dimensional object into two-dimensional image inevitably causes the superposition of the breast tissue and sometimes hinders the detection of lesions. Therefore x-ray breast imaging has been moving forward to three-dimensional techniques, which are also made possible by the progress of flat-panel detectors. Among these are breast tomosynthesis [3, 5, 26-31] and dedicated breast Computed Tomography (breast CT) [32-38] techniques which may improve detection of breast lesions among women with dense breasts as well as to reduce unnecessary callbacks of normal fibro-glandular tissue mimicking the appearance of a lesion.

1.3.2 Breast Tomosynthesis

The modern breast tomosynthesis technique belongs to the category of geometric tomography or linear tomography, which was proposed in the early 1930s [39]. Niklason *et al* [31] implemented the tomosynthesis technique with a moving x-ray tube and a stationary detector. The x-ray tube moves along an arc path, which spans a limited angle range, as is shown in Figure 1.1. At each x-ray tube location, a low-dose projection image is acquired. The total number of projections is also limited. This type of tomosynthesis configuration can be easily realized on a FFDM system. Therefore, the progress of the FFDM technique has greatly encouraged the breast tomosynthesis development. A major component of its development is the tomosynthesis reconstruction algorithm. Various methods have been proposed including the iterative reconstruction technique such as maximum likelihood expectation maximization (MLEM) and those based on linear algebra, such as the shift-and-add method [40], Niklason's modified shift-and-add method [31], filtered-back-projection (FBP) [41, 42], and Matrix Inversion Tomosynthesis (MITS) [30]. Some studies [28, 30, 43] were conducted to compare these techniques.

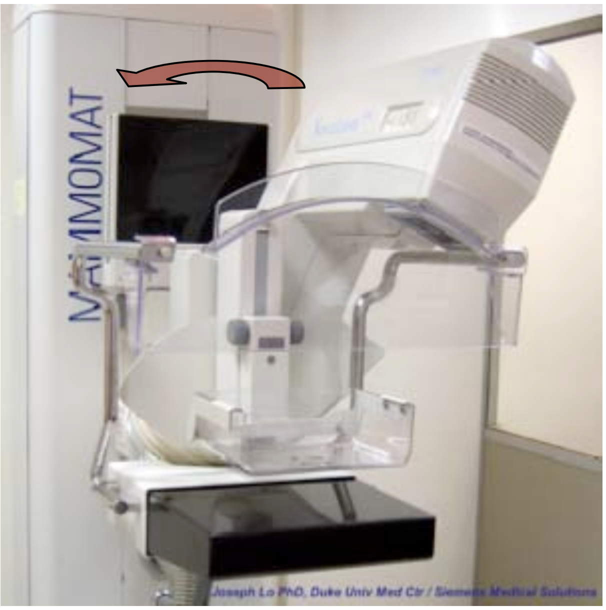

Joseph Lo PhD, Duke Univ Med Ctr / Siemens Medical Solutions

Figure 1.1: Picture of a breast tomosynthesis system. The red arrow indicates the arc path that the x-ray tube moves along.

In the breast tomosynthesis, in order to reduce tissue overlap, patient motion, scatter radiation and dose, the breast is compressed as in conventional mammography. Another limitation is the existence of artifacts and out-of-plane blurring due to the limited angular sampling intrinsic in the technique. By contrast, a dedicated breast CT system acquires the full range of low-dose projections around the uncompressed breast and therefore does not have these problems.

1.3.3 Dedicated Breast CT

Not long after the CT technique was invented in 1972, a group of researchers tried breast CT imaging for the first time [44-48]. They applied the whole-torso-scanning mode and found that a high patient dose was needed to get sufficient image quality.

With the advent of high-resolution flat-panel detectors at the end of the 1990s, breast imaging via a cone-beam CT becomes possible and breast CT regained attention.

Unlike a conventional CT system, where the x-ray tube/ detector move around the torso of a patient, a dedicated breast CT system has a joint x-ray tube/detector move just around a breast. It is set up as is shown in Figure 1.2: a woman patient lies prone on a lead-shielded table with one breast hanging freely through a hole on the table. The x-ray tube and the flat panel detector are installed vertically underneath the table. The tube-detector assembly rotates around the exposed breast of the patient. By this design of the dedicated system, the field of view (FOV) of the detector can be fully employed for breast imaging. What's more, since other tissues do not attenuate the x-ray beam, the effective glandular dose delivered to the patient can be lowered to match the two-view screening mammogram for the same breast, as is demonstrated by Boone *et al* in 2001 [49].

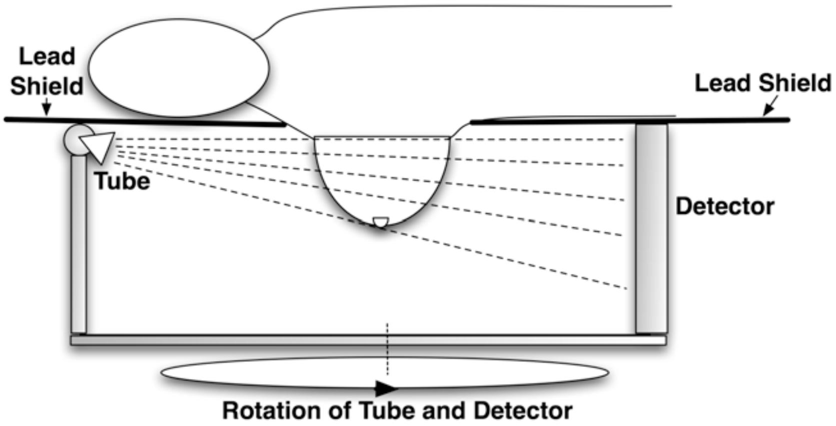

Figure 1.2: Illustration of a dedicated breast CT system. The x-ray tube and flat-panel detector rotate together around the breast, which is the only region to be illuminated.

There are five research groups investigating dedicated breast CT. They are: Dr. Boone *et al* in University of California, Davis [50-53], Glick *et al* in University of Massachusetts [54-56], Ning *et al* in University of Rochester [36, 37, 57, 58], Shaw *et al* in University of Texas M.D. Anderson Cancer Center [59-61], and Tornai *et al* in Duke University [32, 38, 62-64]. In addition, they all have fabricated their own dedicated breast CT systems. These breast CT systems differ in their detailed technical aspects: the choice of x-ray beam, the x-ray source orbit, and the peak voltage and tube current values used.

1.4 Statement of Work

This dissertation has been conducted in close collaboration with Boone's breast CT research group, which provided raw human subject datasets and corresponding geometric calibration results. The components of this dissertation are organized into a flowchart and shown in Figure 1.3.

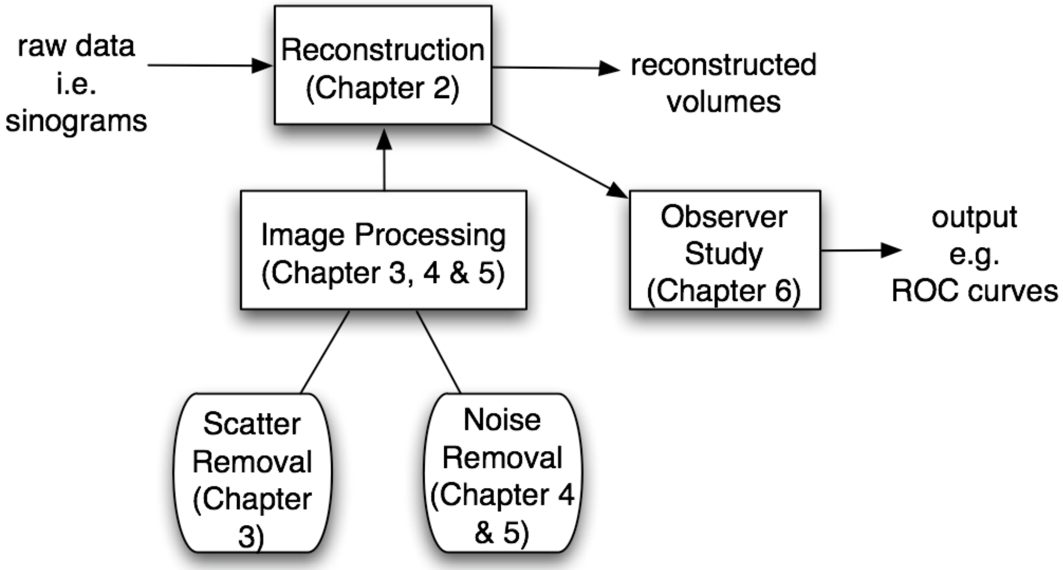
raw data
i.e.
sinograms
Reconstruction
(Chapter 2)
reconstructed
volumes
Image Processing
(Chapter 3, 4 & 5)
Observer
Study
(Chapter 6)
output
e.g.
ROC curves
Scatter
Removal
(Chapter
3)
Noise
Removal
(Chapter 4
& 5)

Figure 1.3: Flowchart to show the components of the dissertation.

As the first basic step, the filtered back-projection algorithm for cone beam was custom-written for tomographic reconstruction. Its technical details will be described in Chapter 2.

Chapter 3 to 5 cover the topic of image processing in dedicated breast CT. There are two major tasks: scatter removal and noise removal. Like many other x-ray imaging modalities, detection of scatter radiation in projection images is a major cause of image degradation. In Chapter 3, a new post-acquisition numerical scatter removal technique based on a statistical model will be introduced. Second, because the breast CT images are acquired at low dose levels (the dose is comparable to that in the two-view screening mammography for each breast) over many projections, each projection image contains a considerable amount of quantum noise as well as electronic noise. Therefore it leaves space for image improvement via post-acquisition image denoising techniques. In this project, we are interested in investigating Partial Diffusion Equation (PDE) based nonlinear denoising technique for cone-beam CT, which is a flexible tool with effective noise removal while maintaining detail. In Chapter 4 and 5, we will focus on different aspects of the image denoising in dedicated breast CT. Chapter 4 is mainly a simulation study. It covers the comparison between different steps in the reconstruction process where a denoising technique can be potentially applied. Chapter 5 first compares the PDE technique investigated in Chapter 4 to other spatially adaptive techniques using simulations. Then, the PDE technique is used on some human subject breast CT datasets for its performance evaluation.

A pilot mass detectability study based on simulation will be given in Chapter 6. Evaluation of the effect of image processing techniques on the reconstructed CT images is a difficult task, especially for those non-linear processing techniques like PDE denoising techniques. Since the ultimate purpose of any medical image is for the detection and diagnosis of tissue abnormalities, the most clinically relevant evaluation criterion is to see how the image processing affects the final diagnosis of diseases. Mathematical or numerical observers will be used and receiver operating characteristic (ROC) analysis will be done in this chapter.

It is hoped to show that: 1) the energy-integrating characteristic of a flat-panel detector can be incorporated into a model for numerical scatter compensation; 2) PDE based denoising techniques are good choice for noise removal in dedicated breast CT; and 3) the noise removal by PDE techniques can translate into the benefit of improved mass detection in dedicated breast CT.

2 Breast CT System and Reconstruction

In this chapter, the feasibility of dedicated breast CT using a dose level comparable to that of a conventional two-view mammography will be firstly described. Then the structure of a prototype breast CT system built in University of California Davis, the first of its kind, will be shown. Finally, the tomographic reconstruction of the CT data will be introduced, which finish the basic process from raw data acquisition to 3D volume reconstruction.

2.1 Feasibility of Breast CT Imaging

This section summarizes some preliminary breast lesion detection studies in breast CT in the literature [49, 59]. Please note that for any of the discussions, the dose in the breast CT is comparable to the two-view mammography for the same breast.

The mechanism of tissue contrast in the reconstructed breast CT images is different from that on a mammogram. In breast CT images, the contrast between tissues is due to their different attenuation coefficients. The linear attenuation coefficients of tissues in a breast decrease when the monochromatic x-ray beam energy is increased [36]. The linear attenuation coefficient of calcification is much higher than that of other tissues including adipose, glandular tissues and carcinoma. The contrast between a carcinoma and other normal breast tissues decreases with a higher photon energy. When a polychromatic x-ray beam is used, the effective linear attenuation coefficient for each type of tissues can be calculated by weighting the ones under monochromatic case and converted to the CT numbers. The CT numbers of breast carcinoma are slightly higher than those of glandular tissue, but much higher than adipose tissue [49].

The detection of a mass depends not only on the contrast of the mass to its surrounding tissue, but also on the noise level in the image. A metric combining these two aspects is contrast-to-noise ratio (CNR). In breast CT, the CNR is independent of the lesion size. The signal-to-noise ratio (SNR) takes into account the lesion size, and is related to the CNR through the following equation:

$$SNR = CNR \times N^{\frac{1}{2}} \tag{2.1}$$

where N is the number of pixels occupied by a lesion [49]. Based on an ideal simulation where a lesion is embedded into uniform glandular tissue (noise level is measured from a cylindrical PMMA phantom with a diameter of 10 cm), the SNR increases linearly with lesion diameter such that a lesion of a diameter of 1mm has the SNR of 5 [49], which is detectable according to the Rose criterion [65]. However, this simulation doesn't take into account the anatomic noise due to the natural appearance of the glandular tissue. With the anatomic noise, the SNR will be lower. But still, according to Boone *et al* [49], it is likely to detect smaller masses on breast CT than on conventional mammography, which by contrast can detect a median sized lesion about 11mm in diameter.

For the detection of microcalcifications, the limiting factor is usually the spatial resolution. It is well known that a film-screen system has excellent spatial resolution. The spatial resolution of breast CT is not as high. But state-of-the-art flat-panel x-ray detectors with a high frame rate can have pixel size of less than 200 μm. For example, most of the breast CT systems adopted the Varian Paxscan 4030CB flat-panel detector, whose pixel size is 194 μm. A human observer study based on experimental data showed that using this pixel size, a microcalcification with a diameter larger than 300 μm could be reliably detected [59].

In summary, the preliminary studies show that a dedicated breast CT system incorporating a high-resolution flat-panel detector has the potential to detect both microcalcifications and masses. The detectable masses based on the breast CT system are likely to be smaller than those can be detected based on a conventional mammography system.

2.2 Breast CT system in UC Davis

The University of California Davis has custom-built a prototype breast CT system, which is the first of its kind for clinical data acquisition [66]. A picture of the system without the table top is shown in Figure 2.1. The x-ray tube and the flat panel detector are installed vertically underneath the table. The tube-detector assembly rotates around the exposed breast of the patient. This setup is different from a conventional CT system, where the x-ray tube and detector move around the torso of a patient. Since only the breast to be imaged is exposed to the x-ray beam, the dose to the patient can be greatly reduced. A pilot study [49] showed that this type of dedicated breast CT system is able to achieve a satisfactory image quality with dose level comparable to standard two-view mammography for the same breast.

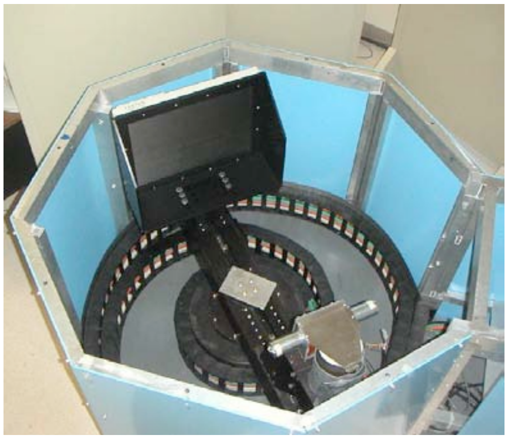

Figure 2.1: Picture of the breast CT system in UC Davis. The table top is removed. Used with permission by John Boone PhD, University of California Davis.

2.2.1 Hardware Components of the System

The dedicated breast CT system has the following hardware components. The x-ray tube has a Comet beryllium-windowed, water-cooled tungsten anode and a nominal focal spot with the size of 0.4 mm x 0.4 mm. A Pantak high frequency x-ray generator drives the tube with the voltage ranging from 10 kV to 110 kV. The CsI-based flat panel detector (Varian, Paxscan 4030CB) has a field of view of 40 mm x 30 mm. Using 30 frames per second and 2 x 2 pixel binning mode, the detector generates the images each with matrix size of 1024 x 768 and pixel dimension of 0.388 mm x 0.388 mm. A Kollmorgen servo motor was employed to drive the rotation of the tube-detector assembly as well as encoding the angles. The source-to-isocenter distance is 46.9 cm and the source-to-detector distance is 88.4 cm. A polychromatic x-ray beam of 80 kVp and circular orbits of x-ray source are used for data acquisition.

2.2.2 System Calibration

There are two components of system calibration in breast CT: geometrical calibration and background calibration. A critical step is the accurate acquisition of geometry of the breast CT system. To illustrate the importance of this, let us look at Figure 2.2. The images are a reconstructed slice of a simulated high-contrast object. The in-plane resolution of reconstruction is 0.2 mm and out-of-plane resolution is 0.5 mm. What's shown on the right is the accurate one, and the one on the left is the result based on one geometry parameter (the projection location of the central ray along horizontal direction) off by a single pixel (on the detector plane, 388 μm). See how different the image sharpness is in these images. An automatic high precision geometric calibration technique based on metal ball bearings array was developed [52]. Background calibration or flat field correction is a step aimed at removing nonuniformity in the background [50].

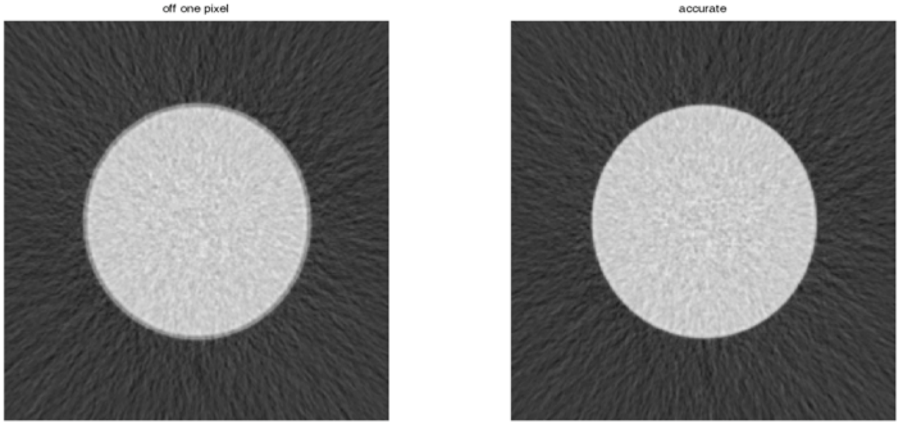

Figure 2.2: Example to show the importance of acquiring the accurate geometry of the breast CT system. On the right is the accurate reconstruction. On the left is the one reconstructed with the central ray off by a single pixel.

2.3 Tomographic Reconstruction

As mentioned in the previous section, the cone-beam geometry of X ray is employed in the dedicated breast CT system. It is made possible by the advancement in the development of flat-panel detectors. The advantage of adopting a cone-beam x-ray illumination of the object is the fast acquisition of true volumetric data, which in turn avoids or reduces the motion artifacts.

2.3.1 Reconstruction Technique Categories

The three-dimensional reconstruction algorithms can be categorized as either exact or approximate. An exact reconstruction algorithm is able to reconstruct the volume to any desired accuracy as long as noise free projections with sufficient view angle sampling and sampling of projection data are provided. The approximate reconstruction algorithm is often developed in the case where an exact reconstruction method is either impossible or less desirable due to the consideration of the computational speed or simplicity.

According to the Tuy-Smith sufficiency condition [67], if all the planes that intersect the object also intersect the orbit of the x-ray source, then there exits an exact reconstruction algorithm. A circular orbit does not satisfy this condition. For example, there exist many planes that are parallel to the orbit (i.e., do not intersect the orbit) and intersect the object. Therefore, no exact reconstruction algorithm is available in this case. Figure 2.3 shows a torus-shaped volume that can be accurately reconstructed via a circular orbit, with a 'shadow zone' indicating the region that cannot be fully sampled. However, as long as the cone angle is not large, the approximately reconstructed volume is of reasonably good quality.

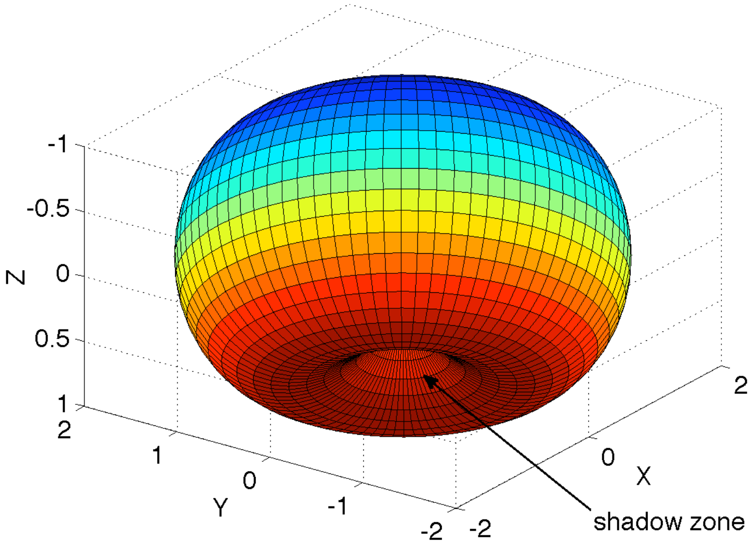

Figure 2.3: When a circular orbit is used, the volume that can be accurately reconstructed is a torus-shaped volume. By contrast, the shadow zone marked by the arrow will have some artifacts.

Many approximate cone-beam reconstruction methods have been proposed [68-70]. Generally, they can be classified into two categories: analytical ones or algebraic ones. The theory behind the analytical reconstruction is the central slice theorem. In a two-dimensional framework, the central slice theorem states that the Fourier transform of the one dimensional projection data is the sampling of the line along the same orientation of the detector in the Fourier transform of the two-dimensional image. An illustration is shown in Figure 2.4.

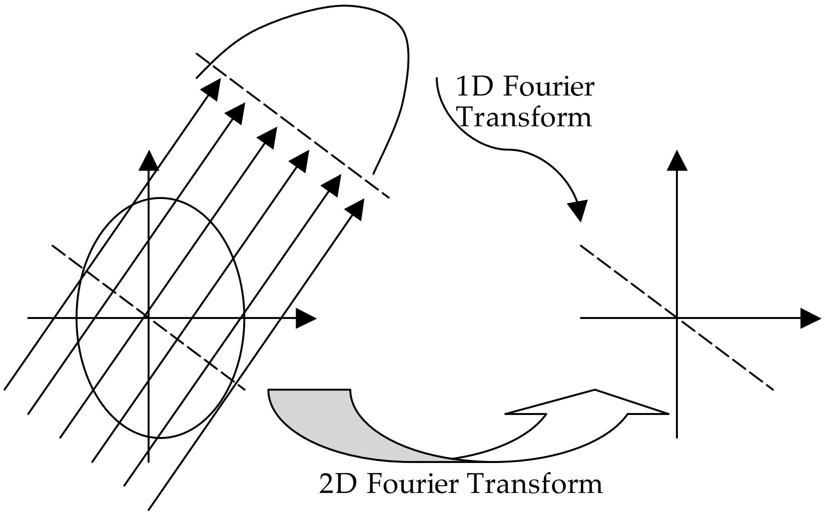

Figure 2.4: Illustration of the central slice theorem.

The central slice theorem provides a direct reconstruction idea through the inverse Fourier transform. This method has several drawbacks: 1) the sampling points in the Fourier domain are not Cartesian; 2) the interpolation in Fourier domain is necessary but susceptible to error; and 3) the error of the interpolation in the Fourier domain will affect the overall appearance of the image in the space domain. Instead of the direct Fourier space based method, another attractive method is the filtered back-projection

(FBP), which is one of the most popular reconstruction algorithms. Not only does it avoid the problems that direct Fourier algorithm has, but it also is computationally more efficient because the data acquisition and reconstruction can be done in parallel.

A different class is iterative reconstruction algorithms that adopt a different strategy. Starting from an initial estimation of the slice or volume to be reconstructed, the forward projections of the estimated slice or volume are obtained and compared to the actual projection data. Then the estimation of the slice or volume to be reconstructed is updated based on the difference. The procedure is repeated until the projections based on the reconstructed data are close to the actual projection data. If the reconstructed data is updated based on the geometry, the iterative algorithm is called the algebraic reconstruction technique (ART); By contrast, if the statistical models are assumed, the iterative algorithm is called a statistical iterative reconstruction. One of the popular ones in this category is the maximum likelihood expectation maximization (MLEM) algorithm.

The iterative reconstruction methods usually are computationally demanding. When the number of projection view angles gets larger, this will be more of the issue. One variation of MLEM is Ordered Subset Expectation Maximization (OSEM) [71]. It has higher computational efficiency than conventional MLEM while maintaining the comparable reconstructed image quality.

On the system in University California Davis, the cone angle for a breast with the mean diameter of 14 cm is less than 10 degrees; therefore an approximate technique will provide reasonably good reconstruction quality. In addition, a total of about 500 projections are obtained over the 360 degrees. Since the datasets have such a high angular sampling rate, the computationally efficient FBP algorithm was chosen for reconstruction. The Feldkamp type FBP [72] for cone-beam geometry was custom written by the author and a Shepp-Logan filter [73] was used.

2.3.2 FBP

Before feeding into the reconstruction core, the raw projection images need to be preprocessed. The simplest preprocessing step is to convert the raw projection image into the line integral via the logarithm operation. On each raw projection image, a region of interest (ROI) is picked up from outside the breast, and the pixel value without attenuation I_0 is approximated by the mean pixel value with the ROI. Then the line integral image is obtained by:

$$l_{ij} = \log(I_0 / I_{ij}), \qquad (2.2)$$

where I_{ij} is the pixel value at (i, j) position.

The details of the FBP core are as follows.

Figure 2.5 shows the three-dimensional coordinate system used in the proposal. The right-hand rule applies.

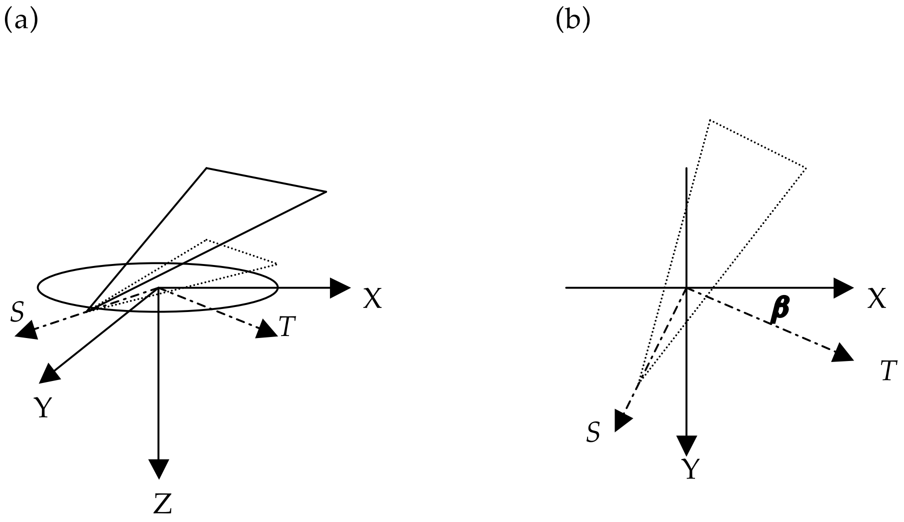

Figure 2.5: Coordinate systems used in the cone-beam CT reconstruction. (a) 3D view; and (b) 2D view along +Z direction.

Other than the fixed coordinate system X-Y-Z, a rotational coordinate system will play an important role in the cone-beam reconstruction. It is denoted by S-T-Z. Figure 2.5 (b) illustrate the X-Y or S-T plane viewed along the +Z direction. The relationship between the two coordinate systems can be easily derived as:

$$\begin{aligned} s &= -x\sin\beta + y\cos\beta \\ t &= x\cos\beta + y\sin\beta \end{aligned}, \qquad (2.3)$$

where β is the view angle shown in Figure 2.5 (b).

The cone-beam geometry can be thought of as ensembles of tilted fan-beams together with an untilted fan-beam. The untilted fan-beam is within the plane of x-ray source trajectory and is the only plane that can be exactly reconstructed. Its reconstruction can be realized by using the Feldkamp fan-beam reconstruction algorithm [74]. The corresponding equation is shown as follows:

$$g(x,y) = \frac{1}{2}\int_0^{2\pi} \frac{\rho^2}{(\rho - s)^2}\int_{-\infty}^{\infty} R_\beta(p) f\left(\frac{\rho}{\rho - s}t - p\right)\frac{\rho}{\sqrt{\rho^2 + p^2}} dp d\beta \qquad (2.4)$$

where $R_\beta(p)$ is the projection with view angle of β, and ρ is the radius of rotation of the x-ray source.

The Feldkamp FBP algorithm for cone-beam geometry [74] is the expansion of the fan-beam reconstruction algorithm. By including the distance of the tilted fan-beams to the untilted one, the generalized FBP algorithm applicable to the cone-beam geometry is as follows:

$$g(x,y,z) = \frac{1}{2}\int_0^{2\pi} \frac{\rho^2}{(\rho - s)^2}\int_{-\infty}^{\infty} R_\beta(p,\zeta) f\left(\frac{\rho}{\rho - s}t - p\right)\frac{\rho}{\sqrt{\rho^2 + p^2 + \zeta^2}} dp d\beta, \qquad (2.5)$$

where ζ is the distance along z direction. The algorithm works in a slice-by-slice manner.

There are generally three steps in FBP:

1) Multiplication of projection data with the pre-weighting factors $\frac{\rho}{\sqrt{\rho^2 + p^2 + \xi^2}}$.

The factors are dependent on the location of each point.

2) Filtering of the weighted projection data by applying a reconstruction kernel in a slice-by-slice manner. In the ideal case where no quantum noise exists, a Lak filter [73] can be used. The Lak filter has the 1/f frequency response. With the real data with noise, however, the Lak filter will amplify the high-frequency noise such that the reconstructed volume is overwhelmed by noise. Therefore, a filter with high-frequency roll-off is preferred. A good option is the Shepp-logan filter. Or a Hamming filter [73] can be utilized, whose cut-off frequency will be adjustable.

3) Back-project the filtered projection data along the cone-beam arrays with different weights $\frac{\rho^2}{(\rho - s)^2}$ depending on their relative distance to the x-ray source. The voxel-driven back projection is used. The available options for interpolation are the nearest neighbor and linear interpolations. For the results shown in the thesis, linear interpolation is used.

To summarize, feasibility and technical details of breast CT imaging are described in this chapter. It is shown that dedicated breast CT has the potential to detect smaller lesions than conventional mammography. Boone *et al* in University of California Davis has custom-built a prototype system and acquired some human subject data. After raw data is calibrated, it is tomographically reconstructed using the Feldkamp FBP algorithm, which was custom-written in our group. From next chapter on, several projects aimed at developing image processing techniques of scatter removal and noise removal in dedicated breast CT will be introduced.

3 Gaussian Noise Model for Scatter Compensation

This chapter and the next two chapters focus on different aspects of image processing in breast CT: scatter removal in this chapter, noise removal in chapter 4 and chapter 5.

3.1 Introduction

Scatter radiation is primarily due to the Compton interaction of photons with atomic electrons in the object being imaged [75]. The photons are deflected from their incident path with a different energy, as is illustrated in Figure 3.1. These photons can either miss the detector or impinge on it. The latter will be inevitably detected due to the fact that the detector typically has broad energy sensitivity and does not effectively reject photons that have lost energy by scattering. The detection of photons in locations that are different from their original path can be considered a component of photon detection noise and degrades medical images. A recent Monte Carlo study in mammography [76] showed that scattered radiation causes the drop of low-frequency modulation transfer function (MTF), changes the shape of MTF and adds considerable noise to projection images. In computed tomography (CT) [77], scattered radiation leads to cupping artifacts on reconstructed sections [58] as well as inaccurate Hounsfield Unit (HU) numbers [78].

Because of its deleterious effect on medical images, scatter radiation needs to be reduced or compensated. There are two general categories of scatter radiation compensation methods: one is hardware compensation such as the application of anti-scatter grids [79], slot scanning systems [80], or air gaps [81]; the other is software compensation via post-acquisition image processing, such as simple estimation-subtraction [82], convolution-subtraction [83], de-convolution [84], artificial neural networks [85], maximum likelihood expectation maximization (MLEM) [86], or Bayesian image estimation [87, 88].

In breast imaging, the scatter radiation is a major concern [89-91]. Various grids have been designed and their performances on film-screen [92] or digital mammography systems [93] have been investigated. An illustration on how a grid prevents scatter radiation from getting detected is shown in Figure 3.2. The effectiveness of grids on scatter radiation reduction for thick breasts has been proven and their application is now a clinically common practice. However, a grid also removes some primary radiation, as shown by the middle ray of Figure 3.2. To maintain the same image quality, the magnitude of the x-ray beam needs to be increased by a factor of 2 or more depending on the x-ray beam and breast thickness [92], which will also increase the total absorbed dose of the patient. Studies find that in some situations using grids will adversely affect the quality of breast images [90, 94].

By contrast, post-acquisition image processing techniques won't change the dose that a patient receives. In addition, some studies [91] [87] show that they can be more effective than an anti-scatter grid in scatter compensation.

The latest advanced imaging radiography techniques including dedicated breast CT and breast tomosynthesis typically do not use anti-scatter grids due to the difficulty of designing a grid that is effective at varying x-ray beam angles. Alternative methods are sought, most of which are simple estimation subtraction techniques [58, 95]. In this project, a statistical model based post-acquisition numerical compensation technique is developed. In this study, we will propose a Gaussian noise model for scatter reduction, and derive a maximum likelihood expectation maximization (MLE or MLEM) algorithm and a maximum a posteriori (MAP) algorithm. We will then apply the algorithms to radiographs acquired on FFDM for preliminary evaluation.

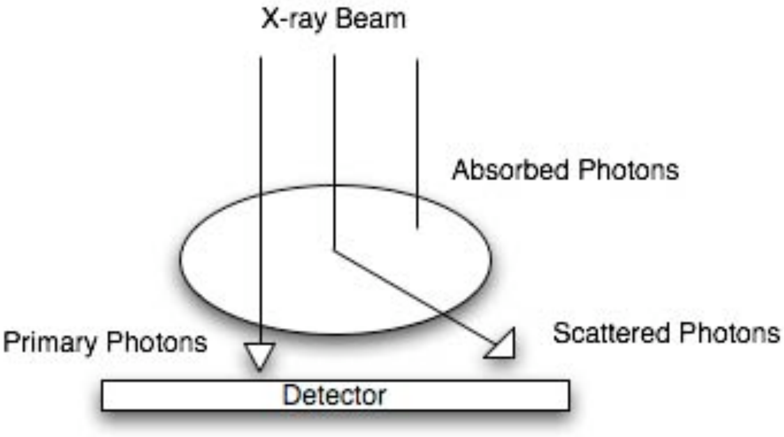
X-ray Beam
Absorbed Photons
Primary Photons
Scattered Photons
Detector

Figure 3.1: Illustration of possible interactions between x-ray photons and the matter within the diagnostic x-ray energy range. The ellipsoid represents the object to be imaged. Photons can be totally absorbed by the photoelectric effect (ray 1), or be scattered through Compton scattering (ray 2) and Raleigh scattering (a very small portion, thus neglected). The rest will survive the attenuation and are called the primary photons or primary radiation (ray 3).

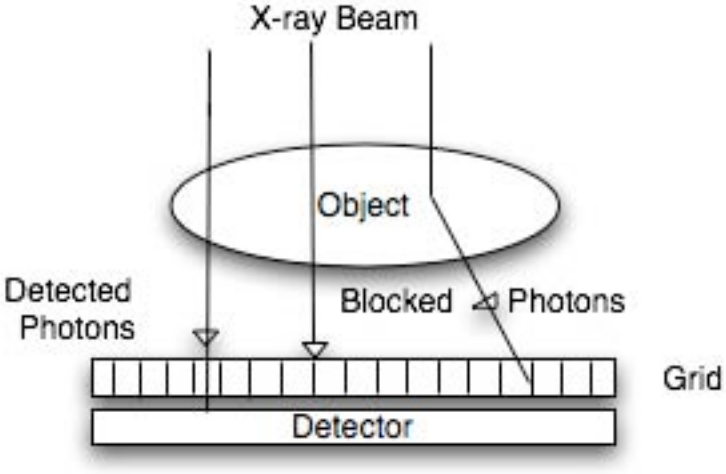
X-ray Beam
Object
Detected Photons
Blocked
Photons
Grid
Detector

Figure 3.2: An anti-scatter grid can be added on top of the detector to remove scatter radiation. However, as shown by the middle ray, some primary radiation will be blocked as well. To maintain the image quality, the patient dose has to be increased.

3.2 Gaussian Noise Model

3.2.1 Assumption

The detected signal on the detector is the sum of the primary radiation and scattered radiation. Scattered radiation can be modeled as the two-dimensional convolution of primary radiation with a scatter kernel, which is assumed to be a double exponential function based on both the empirical measurements [96, 97] and Monte-Carlo simulation studies [98, 99]. A sample scatter kernel is shown in Figure 3.3. On the projection image, if Y is used to represent the two-dimensional matrix of detected total radiation at each pixel, D for the matrix of the primary radiation, S for the matrix of the scatter radiation, and P for the matrix of the scatter kernel, then it holds that:

$$Y = D + S = D + D**P = D**(\delta + P), \tag{3.1}$$

where $**$ is the two-dimensional convolution operator and δ is the Dirac delta function in a matrix form. The task of scatter compensation is equivalent to estimating the unknown D from the measured Y.

One solution is to de-convolve Equation (3.1) [84, 100, 101]. For example, it can be solved via the Fourier Transform (FT), i.e.,

$$D = FT^{-1}\left(\frac{FT(Y)}{FT(\delta + P)}\right). \tag{3.2}$$

Or, statistical models can be formulated to solve the problem. In this context D, S and Y are all multivariate random variables. Previously, they were assumed to follow Poisson distribution [102]. For flat-panel detectors, which belong to the type of energy integrating rather than photon counting, the underlying statistics is a compound Poisson process [103]. It may be well approximated by Gaussian distribution by matching of the first two moments. The resultant statistical scatter compensation technique is denoted in this study as the Gaussian noise model.

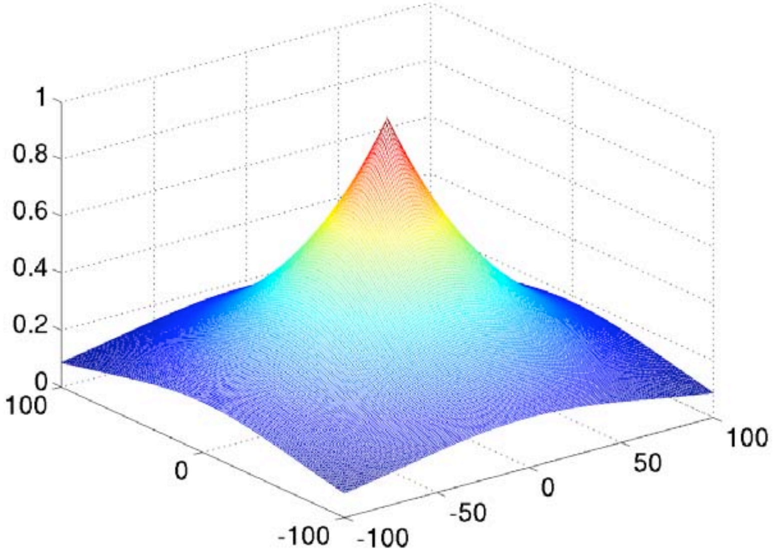

Figure 3.3: Schematic of a scatter kernel with a radially exponential shape. It has two parameters: full width at half maximum (FWHM) and magnitude.

3.2.2 The Model

The Gaussian noise model has following form:

$$\boxed{\begin{aligned} &d_i \mid B, \sigma_{i1}^2 \sim Gaussian(b_i, \sigma_{i1}^2) \\ &s_i \mid B, \sigma_{i2}^2 \sim Gaussian((B**P)_i, \sigma_{i2}^2) \\ &y_i = d_i + s_i \mid B, \sigma_{i1}^2, \sigma_{i2}^2 \sim Gaussian(b_i + (B**P)_i, \sigma_{i1}^2 + \sigma_{i2}^2) \end{aligned}} \tag{3.3}$$

where d_i, s_i, and y_i are pixel values at location i corresponding to primary, scattered and total radiation, respectively, b_i is the expectation of d_i ($B=\{b_i\}$ is its matrix form), and σ_{i1}^2 and σ_{i2}^2 are the variance of pixel values related to the primary radiation and scattered radiation, respectively. The task of scatter compensation here is to estimate B, the scatter-free projection image.

3.2.3 Maximum Likelihood Estimate of Scatter-Free Image

Using the expectation maximization algorithm shown in the appendix, the MLE of the ideal scatter-free image was derived with analytical form shown in Equation (3.4):

$$\begin{aligned} b_k^{(n+1)} &= b_k{}^{(n)} + w_k \cdot [y_k - (b_k{}^{(n)} + (B^{(n)} ** P)_k)]. \\ w_k &= \sigma_{k1}^2 / (\sigma_{k1}^2 + \sigma_{k2}^2) \end{aligned} \qquad \textbf{(3.4)}$$

3.2.4 Maximum *A Posteriori* Estimate of Scatter-free Image

MLE estimate is known to increase high frequency image noise. To overcome this, some constraints can be put on the noise level within the estimated B. Prior information about *B* can be incorporated via Bayes's Rule [104],

$$p(B \mid Y) \propto p(Y \mid B) p(B), \qquad (3.5)$$

where $p(B \mid Y)$ is the posterior joint distribution of *B* given the measured pixel values $Y = \{yi;\ i=1,\ldots,N\}$, $p(Y \mid B)$ is equal to the likelihood of *B*, and $p(B)$ is the prior joint distribution of $B = \{bi;\ i=1,\ldots,N\}$.

We assume that *B* is a Markov random process. It therefore follows a Gibbs distribution:

$$p(B) = \frac{1}{K} e^{-U(B)/\beta}, \qquad (3.6)$$

where *K* is a normalizing factor which is independent of *B*, $U(B)$ is the energy function, and β is a free parameter adjusting the relative weight of this prior on the maximum a posteriori estimator of *B*. When β approaches infinity, the MAP estimate of *B* approaches the MLE estimate of *B*.

The energy function is the sum of the potential function, i.e.,

$$U(B) = \sum_{c \in C} V_c(B), \tag{3.7}$$

where C is the set comprised of all cliques in the image. In this study, the Gibbs prior is defined over a second-order neighborhood system (i.e., for each pixel, its north, south, east, and west neighboring pixels plus its four diagonal neighboring pixels), with each clique comprised of two neighboring pixels. There are many forms of the potential function $V_c(B)$. We chose one that is adaptive to discontinuity [105]:

$$V_c(\{b_i : b_j\}) = \frac{(b_i - b_j)^2}{\delta_c^2 + (b_i - b_j)^2}, \tag{3.8}$$

where i and j are the neighboring pixels within the clique $i{\sim}j$ and b_i and b_j represent their respective intensities. δ_c is an adjustable parameter to regulate the cut-off frequency of the noise in the image.

The MAP estimate of $\{b_i\}$ was calculated through the two-step maximization procedure proposed by Hebert and Leahy [106].

3.3 Materials and Evaluation Methods

3.3.1 Test Images

Images were acquired on a Siemens prototype digital mammography system (Mammomat Novation DR; Siemens, Erlangen, Germany) with 70 μm isotropic resolution. Both tissue equivalent slabs (CIRS, Inc., Norfolk, VA) and an anthropomorphic phantom (model: RMI 165, Gammex Inc., WI) were imaged at 28kVp, with a target/filter combination of Mo/Mo. The tissue equivalent slabs were designed to be radiographically equivalent to breast tissue with various breast densities. In this study, the tissue equivalent slabs used were comparable to a 4-cm-thick compressed breast with 50% glandular tissue density. A built-in square-shaped hole in the center of the phantom mimicked a high-contrast lesion in the digital mammography images. The anthropomorphic breast phantom has an equivalent composition of 50% glandular tissue- 50% adipose tissue and thickness of 5 cm. All images were acquired without an anti-scatter grid. For the purpose of scatter measurement, additional images were acquired with an array of beam stops (lead discs 3 mm in diameter and 3 mm in height) superimposed on the phantoms. A sample radiograph of tissue equivalent slabs together with a beam stop is shown in Figure 3.4. Because lead discs absorb all the primary radiation, only scatter radiation can be detected behind them.

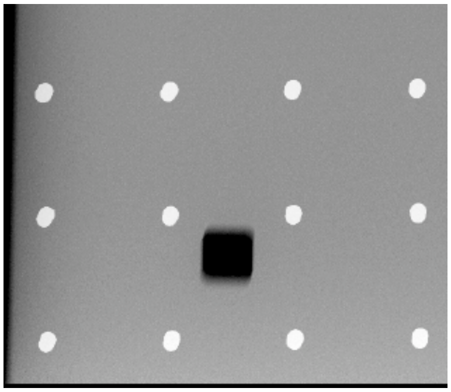

Figure 3.4: Radiograph of the tissue equivalent slabs. The arrays of white disks are the shadows of beam stops. The CNR values are obtained based on the dark square region of interest.

Images were then fed into the scatter compensation algorithms for processing. Both the original and processed images were evaluated through various metrics described in the following subsection.

3.3.2 Image Evaluation Metrics

The effect of scatter reduction was measured by the residual scatter fraction (RSF). At the same time, we anticipated that the contrast-to-noise ratio (CNR) would be constrained or even improved after image processing. We implemented a metric to estimate post-contrast CNR. Finally, we monitored with a line pair pattern the effect of the algorithms on the spatial resolution of the images.

3.3.2.1 Residual Scatter Fraction

Scatter fraction (SF) is defined as the ratio of scatter radiation to total radiation. Residual scatter fraction (RSF) indicates how much of the scatter radiation remains after applying a scatter compensation algorithm.

Using the FFDM imaging technique, two sets of images of phantoms were obtained: one with, and one without, a beam stop array. The signals behind beam stops (lead discs) comprise the scatter radiation, while the total radiation, which is the sum of primary radiation and scatter radiation, will reach those regions without beam stops. We calculated the measured primary radiation ($P_{measured}$) by subtracting the mean radiation of a region-of-interest (ROI) behind a beam stop from the mean of the same ROI location without a beam stop. In the image processed for scatter compensation, the mean of total radiation (T) in the same ROI location ($T_{estimated}$) is the sum of the residual scatter radiation and the primary radiation. Thus,

$$RSF = \frac{T_{estimated} - P_{measured}}{T_{estimated}} \quad . \qquad (3.9)$$

3.3.2.2 Contrast, Noise and CNR

Contrast is defined as the ratio of the difference between the mean radiation value of the lesion (T_{lesion}) and the background ($T_{background}$) to the mean of the background, that is,

$$Contrast = \frac{T_{lesion} - T_{background}}{T_{background}} \quad . \qquad (3.10)$$

Noise, which is the relative noise, is derived by dividing the standard deviation ($STD_{background}$) by the mean of the background radiation ($T_{background}$):

$$Noise = \frac{STD_{background}}{T_{background}} \quad . \tag{3.11}$$

CNR is the ratio of the contrast to the noise, i.e.,

$$CNR = \frac{Contrast}{Noise} = \frac{T_{lesion} - T_{background}}{STD_{background}} \quad . \tag{3.12}$$

CNR by this definition is equivalent to signal difference to noise ratio (SDNR), another term often used in literature.

3.3.2.3 Resolution

Due to the nonlinearity of scatter compensation algorithms, we could not use metric like modulation transfer function, which is designed for a linear system. Instead, a line pair pattern, comprised of alternating bright and dark lines with sizes corresponding to Nyquist frequencies with square wave function, was digitally embedded in the phantom image.

The contrast improvement factor (CIF), defined as the ratio of the contrast after image processing to the initial contrast, was obtained for the line pair pattern with various initial contrast settings. A CIF of 1 or greater was used as the criterion for retaining the spatial resolution. The minimal initial contrast that the line pairs can allow with CIF of 1 or greater was recorded as an indication of the effect of the image processing on resolution. For the various initial contrasts, the corresponding CIF was computed arbitrarily at iteration 16. We determined the minimal initial contrast value that has a CIF of 1 or greater.

3.4 Results

3.4.1 Scatter Compensation Technique -- Tissue Equivalent Slabs

Figure 3.5 gives the RSF and CNR results for MLE and MAP algorithms based on Poisson noise model and Gaussian noise model. In the MAP algorithms, the free parameter β is set at 0.1. Both MLE algorithms reduced RSF values to close to zero and decreased CNR values from the original unprocessed value of 47 to slightly below 40. The minimal contrast that is retainable during processing using our Poisson-model-based MAP algorithm was 1.8%. The MAP algorithms were as equally effective as their MLE counterparts in removing scattered radiation from the radiograph; however, they increased the CNR values to 56 and 63, for the Poisson noise model and Gaussian model, respectively. The minimal contrast retainable using the Gaussian model based MAP algorithm was 2.0%, comparable to that of Poisson-model-based MAP (1.8%).

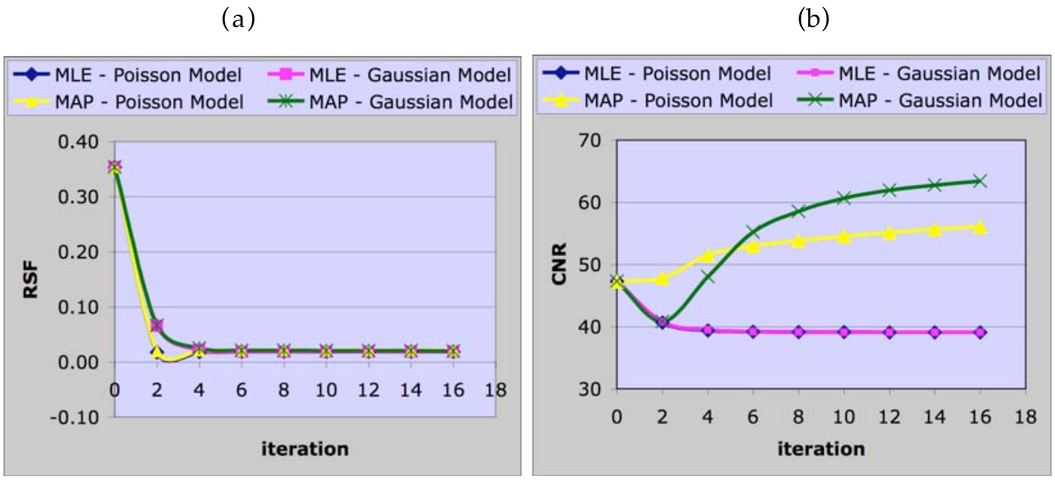

Figure 3.5: Plots of (a) residual scatter fraction and (b) contrast to noise ratio as the function of iteration numbers between MLE and MAP estimates of scatter free image *B* based on Poisson and Gaussian noise models. While both techniques were effective at removing scattered radiation, the MAP based on the Gaussian noise model (green line on right) showed greatest CNR improvement.

How the magnitude of the scatter kernel impacted the MAP algorithm based on the Gaussian noise model was also investigated. Figure 3.6 (a) shows the RSF as a function of iteration for different magnitudes. When the magnitude is zero, there is no scatter reduction effect. As the magnitude increases, the steady-state RSF decreases. When the magnitude is larger than the measured value of 0.52, the scattered radiation is overcompensated such that RSF is less than zero. Figure 3.6 (b) depicts CNR results for the same scatter kernel magnitudes. Overall, the larger the magnitude, the less CNR will increase. The components for CNR calculation including absolute noise, background mean, absolute signal difference and contrast are plotted against iteration numbers in Figure 3.7. The resolution results are shown in Table 3.1: the smaller the magnitude, the lower the resolution. For the magnitude of 0.2, the minimal retainable contrast during processing was 2.7%. For the magnitude of 0, where there was no scatter compensation, no contrast was retainable during processing.

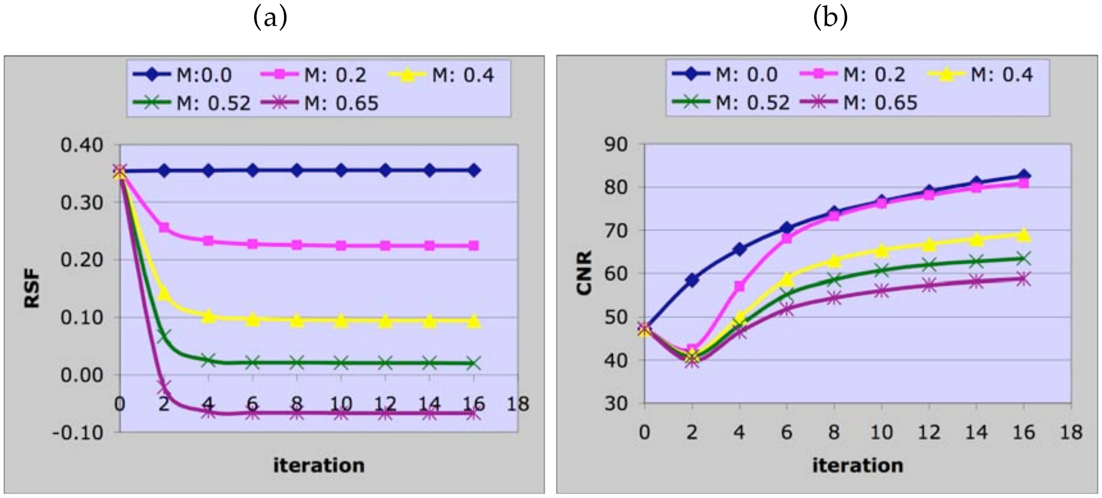

Figure 3.6: Plots of (a) residual scatter fraction and (b) contrast to noise ratio as a function of iteration numbers were shown for various magnitudes of scatter kernel using MAP estimates of scatter free image *B* based on the Gaussian noise model. A magnitude of 0.0 (blue line) corresponds to no scatter removal, magnitude of 0.52 (green line) corresponds to actual measured values, and a magnitude of 0.65 (purple line) overcompensates the scattered radiation, resulting in negative residual scatter fraction values. At each magnitude level, the contrast increases asymptotically.

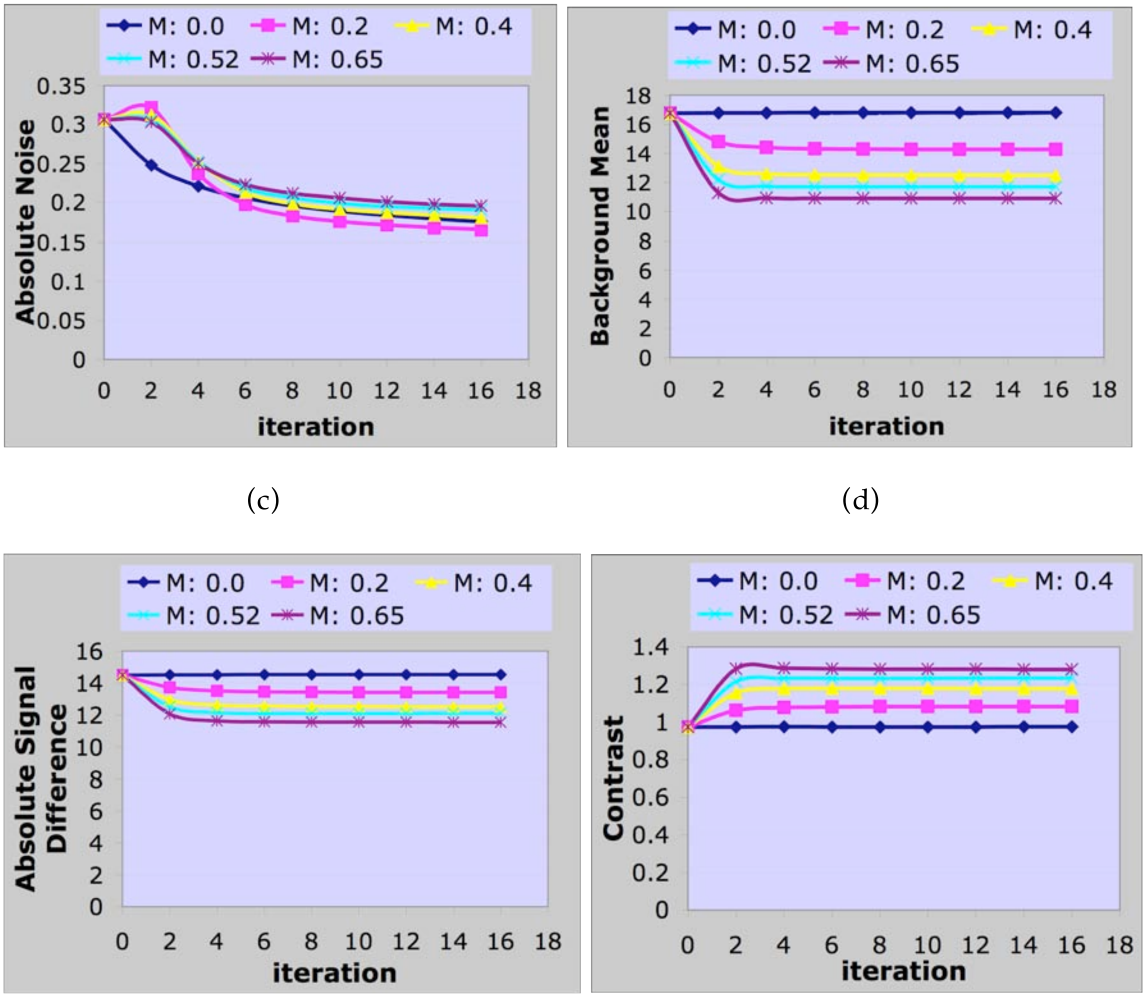
(a) (b) (c) (d)

Figure 3.7: Plots of (a) absolute noise, (b) background mean, (c) absolute signal difference, and (d) contrast as a function of iteration numbers were shown for various magnitudes of scatter kernel using MAP estimates of scatter free image *B* based on the Gaussian noise model.

Table 3.1: Resolution results of the Gaussian noise model based MAP estimates with various magnitudes of scatter kernel. The larger the magnitude of scatter kernel, the sharper the processed image is. For the magnitude of zero, i.e., no scatter removal, the resolution is always degraded.

Magnitude	0.0	0.2	0.4	0.52	0.65
Minimal Contrast	---	2.7%	2.2%	2.0%	2.0%

3.4.2 Scatter Compensation Technique -- Anthropomorphic Phantom

The scatter compensation results of Gaussian noise model are shown in Figure 3.8 and Table 3.2. The scatter removal procedure reduced SF of the radiograph acquired without a grid from 45% to 10%, the level that an anti-scatter grid achieves. At the same time, the procedure improved the CNR to around twice the value on the image acquired with a grid.

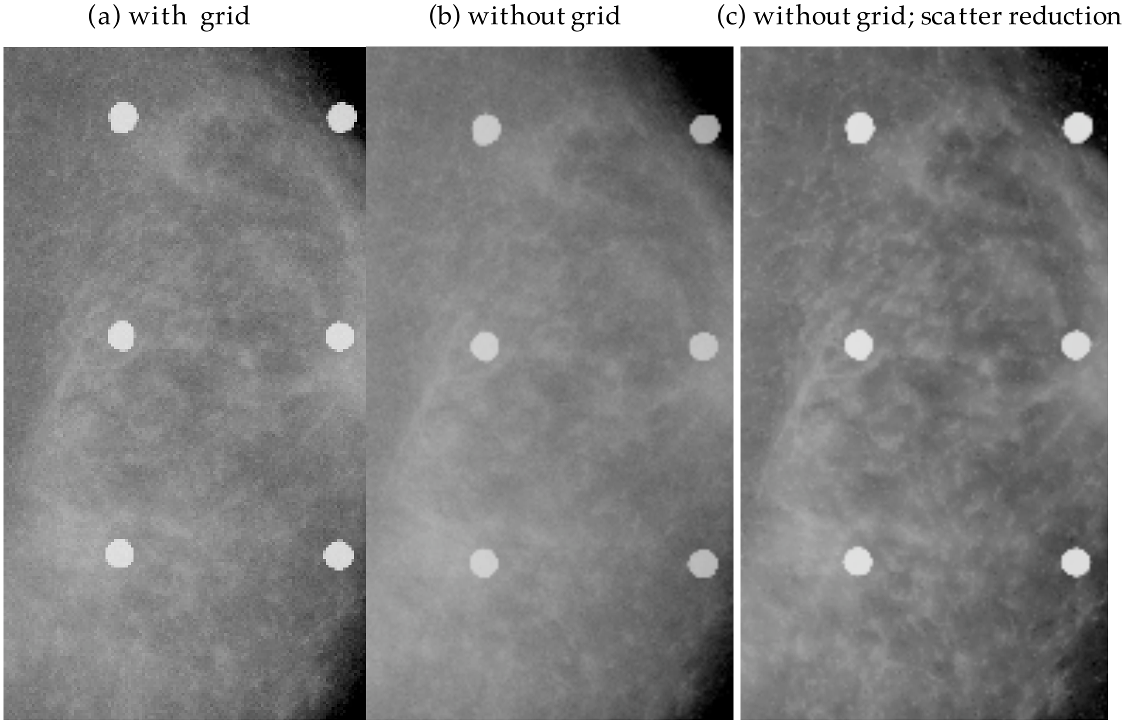

Figure 3.8: Radiographs of the breast anthropomorphic phantom, (a) with an anti-scatter grid, (b) without an anti-scatter grid, and (c) without an anti-scatter grid and with scatter reduction.

Table 3.2: Corresponding residual scatter fraction and contrast to noise ratio results for the three images shown in Figure 3.8.

	With a Grid	W/O a Grid	W/O a Grid; Scatter Reduction
RSF	11%	45%	10%
CNR	7.04	6.99	15.29

3.5 Discussion

Scatter radiation is a physical phenomenon, which together with photoelectric effect is a source of x-ray beam attenuation. The recording of scatter radiation on the detector will degrade the quality of the image and thus adversely affect the medical diagnosis. Therefore, removal of scattered radiation from projection images is essential for improved image quality, particularly for the latest advanced imaging radiography techniques including dedicated breast CT and breast tomosynthesis, which typically do not use anti-scatter grids. Statistical model based scatter compensation technique is a good candidate for dedicated breast CT and breast tomosynthesis imaging.

In this study, novel Gaussian noise model for energy-integrating detectors was proposed, and both MLE and MAP estimates of the scatter free image were derived. Preliminary results were based on the radiographs acquired on a full-field digital mammography system for two types of phantoms (tissue equivalent slabs and a breast anthropomorphic phantom). Both MLE and MAP algorithms were effective in removing the scattered radiation, though MAP outperformed MLE in CNR. For the specific phantom and imaging condition, the MAP of the Gaussian noise model outperformed the MAP of the Poisson noise model.

Additional evaluation of the Gaussian noise model MAP algorithm showed the importance of accurate characterization of the scatter kernel. If the magnitude of the kernel is less than the actual value, the scatter is only partially compensated. On the contrary, if the magnitude of the kernel is larger than the actual value, the scatter is over-compensated, with less CNR improvement. The choice of FWHM of the scatter kernel is also essential. In Gaussian noise model MAP algorithm, another important parameter is β, which regulate the relative importance of the Gibbs prior on scatter-free image B. By varying β value, the CNR improvement will be different. Gaussian noise model MLE algorithm can be considered to be a special case of Gaussian noise model MAP algorithm when β approaches infinity. Therefore, the Gaussian noise model MAP algorithm is a very flexible tool, by varying those parameters we can choose the effect we want on the radiographs acquired without a grid.

The Gaussian noise model techniques can be easily applied to dedicated breast CT datasets. One straightforward strategy is to apply the scatter compensation techniques on individual projection images before reconstruction. However, for reliable results it is critical to have the scatter kernel characterization on the dedicated breast CT system, which is unknown at the current stage. This study has demonstrated initial feasibility for this approach. In the future, the next phase of this research should include a physical measurement of scatter kernel for cone beam and comprehensive evaluation of the scatter reduction technique on images acquired on the breast CT system.

4 Noise Removal in Breast CT: Where to Apply

In this chapter and the next one, we will talk about the projects on noise removal from breast CT data. This chapter focuses on the choice of the step in the reconstruction process where a denoising technique will be applied based on a simulation study. Chapter 5 will focus on a PDE technique we developed for breast CT noise removal, providing both simulation and clinical study results.

4.1 Introduction

Preliminary human subject data acquired on our first prototype breast CT system [66] provide exciting new information of the breast that was not available in the past. Yet, because the relatively low total dose (comparable to the standard two-view mammography for a single breast) must be split among a large number of projection views (around 500), thin slices in reconstructed breast volumes contain considerable noise. Thus it is desirable to be able to remove the noise to improve the conspicuity of breast lesions. At the same time, it is desirable to maintain image resolution. The denoising technique can also be applied in breast CT to reduce the patient dose while maintaining the image quality.

For low dose CT, some general-purpose sinogram smoothing techniques based on either penalized likelihood [107] or penalized weighted least squares [108] have been reported in the literature. These techniques can be potentially applied on dedicated breast CT datasets. Zhong et al [109] developed a wavelet-based technique and applied it on phantom breast CT data. Their results showed that with denoising, dose could be potentially reduced by up to 60%.

Partial Diffusion Equation (PDE) based technique [110, 111] is another denoising method which is effective not only in removing noise but also in preserving details. At the expense of computational cost, this iterative method can provide more freedom in choosing the desired denoising effect. In this study, we developed three variants of PDE based denoising techniques applicable to different steps of the breast CT reconstruction process and compare them against each other to find the best step for noise removal in breast CT.

4.2 Materials and Methods

4.2.1 Simulated Breast CT Datasets

In this study, simulated breast CT datasets were generated for the analysis. The computer-generated breast is a hemisphere with radius of 7cm. It has homogeneous breast tissue with a uniform linear attenuation coefficient of 0.17 cm^{-1} and is surrounded by 1 mm thick skin [112] with linear attenuation coefficient of 0.3 cm^{-1}. A contrast detail phantom was simulated and embedded at the center of the breast. The parameters of the contrast detail phantom are: for each 4 by 4 lesion array, sizes vary vertically (6, 5, 4, and 3 mm); contrasts of the lesions are 15%, 10%, 5% and 3% from left to right. Five of these arrays were embedded in the shape of a plus sign to cover multiple areas in the central coronal slice in order to detect any regional variations in image quality. Perfect detection would correspond to five sets of sixteen lesions or eighty in total. This simulated breast together with lesions was scanned virtually by a monochromatic x-ray cone beam with infinitely small focal spot and ideal flat-panel detector with 100% detective quantum efficiency. The geometric parameters are the same as the physical breast CT scanner described in Chapter 2.

For each 2D projection image, an analytical line integral image was first obtained based on the aforementioned virtual dedicated breast CT scanning. A noisy raw image was generated according to the measurement model [113]. The model takes into account both photon quantum noise and electronic read-out noise. It has the following form:

$$Y_i = G_i \overline{E} \cdot Poisson(I_0 e^{-l_i}) + Gaussian(0, \sigma^2), \qquad (4.1)$$

where G_i is the gain factor of the imaging system, $\overline{E}$ is the mean energy level of the polychromatic x-ray beam, and the Gaussian term is for the electronic noise. In our simulation we chose G_i=0.0035 /keV, $\overline{E}$=40 keV, and σ^2=10. The values of G_i and σ^2 were referred to those used in a previous publication [113].

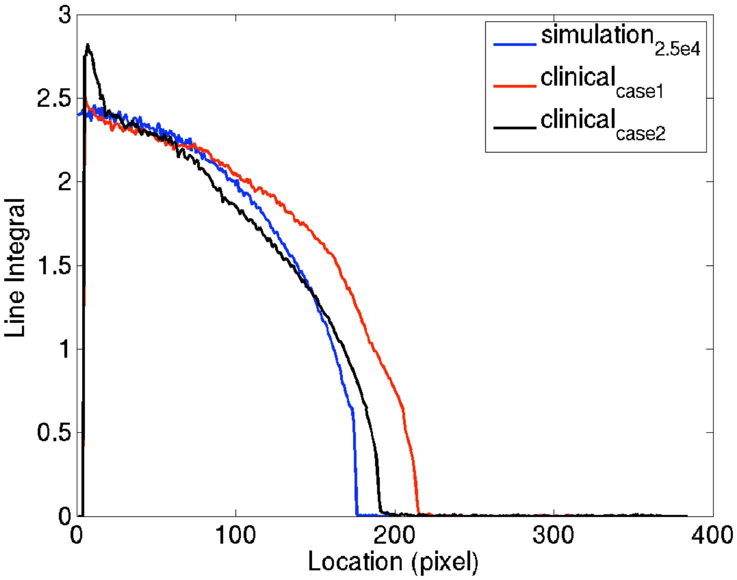

Figure 4.1 One-dimensional line integral profiles of both simulation and clinical datasets. It's seen that I0=2.5e4 gives a roughly comparable profile to the clinical cases.

Two I_0 values are used. The exposure level affects the noise content of line integral at a fixed location. By varying the exposure levels and plotting the line integrals against those of human subject data, it is found that I_0=2.5e4 gives a comparable noise level for the same line integral values, as is shown in Figure 4.1. Clinical case 1 and case 2 have a breast radius of 7.4 cm and 7 cm (same as the simulation data) in coronal view respectively. The first 5 pixels are set zero due to the bad pixels of the detector. The peak of clinical case 2 is due to the superposition of some tissue outside of the breast. The second exposure level used is I_0=1e4,which is 40% of the first exposure level [109].

4.2.2 PDE Denoising Techniques

Along the reconstruction process, there are four possible steps where a denoising technique can be applied, as illustrated in Figure 4.2. However, applying a denoising technique in step 1 won't be very effective due to the nonlinear operation of the preprocessing step. Only step 2, 3 and 4 are considered. All together three variants of the Partial Diffusion Equation based denoising techniques were implemented for this study, corresponding to the three steps considered. First, the standard 2D PDE technique was applied at step 3. Second, a spatially variant version of 2D PDE denoted as PDE_{tomo} is used at step 2. Third, a 3D PDE is used at step 4. The technical details of them are described as follows.

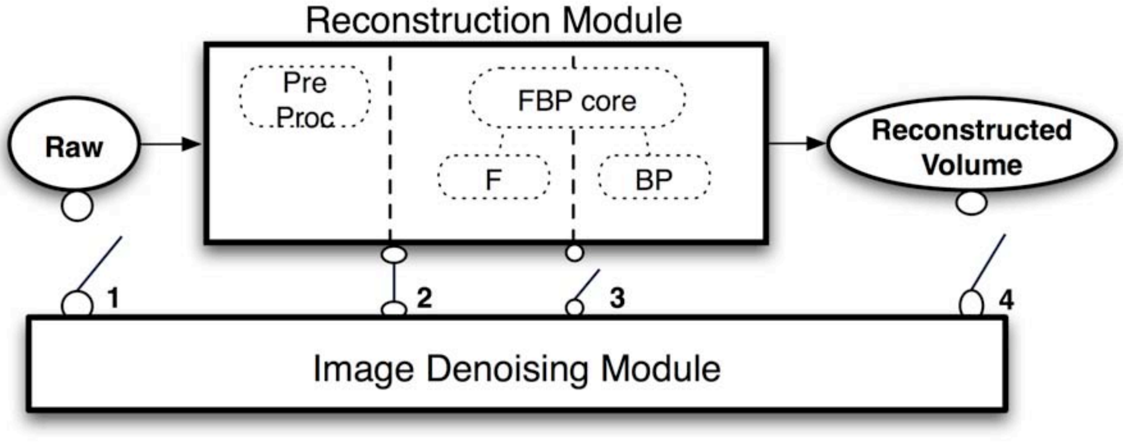

Figure 4.2: Illustration of possible steps in the reconstruction process that an image denoising module can be applied to in dedicated breast CT.

4.2.2.1 PDE$_{2D}$

The PDE denoising strategy was inspired by the heat equation, which regulates the spatial temperature distribution at a certain time. When the time period is very long, the temperatures tend to be uniform in space, i.e., the temperature map is smoothed over time. Therefore, if any image needs to be denoised, it can be treated as a temperature image and fed into the heat equation for smoothing. The simplest case will be the heat propagation in a homogenous media, or equivalently, smoothing equally all over the space. The heat equation in this case will be:

$$\frac{\partial I}{\partial t} = k\nabla^2 I = \nabla \cdot (k\nabla I), \tag{4.2}$$

where k is a scalar diffusivity constant of the homogeneous media, ∇I is the gradient of the image I and $\nabla^2 I = \nabla \cdot (\nabla I)$ is the Laplace operation on image I over the spatial variables [114].

This simplest case will smooth out both the noise and the details such as the edges in the image. Instead, a nonlinear PDE not only removes the noise but also preserves the details in the image:

$$\frac{\partial I}{\partial t} = \nabla \cdot (p(|\nabla(G_\sigma \otimes I)|)\nabla I). \tag{4.3}$$

The function of $p(.)$ is called the diffusivity function, a function of the norm of the gradients in the image $|\nabla I|$. It is used to regulate the local smoothness. In the presence of noise, the gradients can be unbounded. To overcome this problem, a Gaussian kernel G_σ with the standard deviation of sigma σ is applied to the image before gradients are computed as Catte *et al* [115] suggested.

In this study, we chose a diffusivity function proposed by Perona and Malik [110]:

$$p(d) = e^{-\frac{d^2}{\delta^2}}, \tag{4.4}$$

where delta δ is a user-specified parameter. A sample diffusivity function with delta value of 2 is shown in Figure 4.3. When the image gradient norm (or in the discrete case, the pixel value difference) is very large at a location region, the diffusivity will be very small, and thus the local image values will be preserved within a small time period whereas another more uniform region will be smoothed out at the same time. The parameter δ acts like a cut-off value; image regions with gradient norm below δ will have more noise removed while regions with a higher gradient norm will stay sharp.

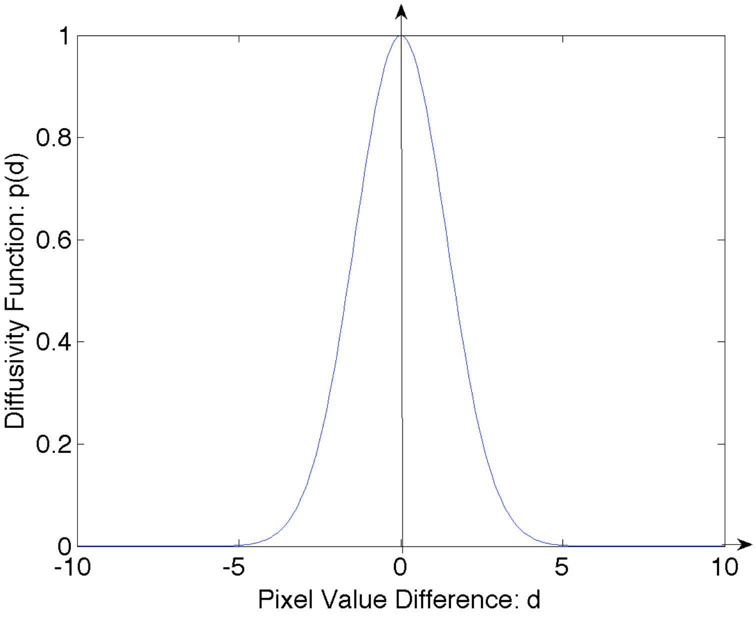

Figure 4.3: Diffusivity function with delta value of 2.

The diffusion equation can be discretized by the finite difference approach using the first-order neighborhood system. Each pixel has four neighbors: the north, south, west and east neighbor pixels. Assuming $\Delta x = \Delta y = 1$ in the two-dimensional case, the discretized version of Equation (4.3) is

$$\frac{I_{(i,j)}^{<t+1>} - I_{(i,j)}^{<t>}}{\Delta t} = p_{(i-1,j)} \cdot \nabla_{(i-1,j)} I^{<t>} + p_{(i+1,j)} \cdot \nabla_{(i+1,j)} I^{<t>} + p_{(i,j-1)} \cdot \nabla_{(i,j-1)} I^{<t>} + p_{(i,j+1)} \cdot \nabla_{(i,j+1)} I^{<t>} \quad (4.5)$$

where *<t>* and *<t+1>* represent the iteration step t and t+1 respectively; Δt is the discretized time step; *p(.,.)'s* are diffusivity function values at the neighboring pixels of location (i,j); and *∇(.,.)I* is a notation for the difference between $I_{(\cdot,\cdot)}$ and $I_{(i,j)}$ itself. The parameters of PDE2D are: *Δt*, *σ*, *δ*, and the number of iterations (denoted by *iter_num*).

4.2.2.2 PDE$_{\text{tomo}}$

In the breast CT line integral images, noise is larger toward the chest wall. When the photon fluence is reduced, the phenomenon becomes even more obvious. A line profile with I_0=2.0e3 is shown in Figure 4.4 to help illustrate this point. It can be explained theoretically. Again, a simplifying assumption of monochromatic beam is used. If

$$\begin{aligned} &I_{ij} \sim Poisson(\lambda_{ij}) \\ &l_{ij} = \log \frac{I_0}{I_{ij}} = \log I_0 - \log I_{ij} \end{aligned} , \quad (4.6)$$

where λ_{ij} is the expected number of photons arriving at location (i, j) of the detector, then the variance of the line integral l_{ij} can be approximated by the delta method [116] using the second-order Taylor expansion:

$$\mathrm{var}(l_{ij}) = \mathrm{var}(\log I_{ij}) \cong \mathrm{var}(I_{ij}) \bullet [(\log I_{ij})']^2 \cong \lambda_{ij} \bullet \frac{1}{I_{ij}{}^2} \cong \frac{1}{I_{ij}}. \quad (4.7)$$

This formalism can be integrated into the PDE denoising technique by adapting the parameter δ in the diffusivity function spatially as:

$$\delta_{ij} = k \cdot \sqrt{\mathrm{var}(l_{ij})} = \delta_0 \cdot \sqrt{\frac{1}{\frac{1}{M} \sum_{c \in N(i,j)} e^{l_c}}}, \quad (4.8)$$

where *M* equals to 4, and *N (i, j)* is the four closest neighbors around pixel (i, j).

The resultant PDE denoising technique is denoted PDE for Tomography/Tomosynthesis ($\mathrm{PDE}_{\mathrm{tomo}}$). The parameters to be considered are: Δt, σ, δ_0, and *iter_num*.

4.2.2.3 $\mathbf{PDE}_{\mathbf{3Dpost}}$

When the PDE denoising is applied on the reconstructed volume at step 4 as shown previously in Figure 4.2 instead of the line integral data, its neighborhood system expands to six neighbors along x, y and z directions. Otherwise this variant of the algorithm, denoted as PDE_{3Dpost}, is implemented in the same way as before.

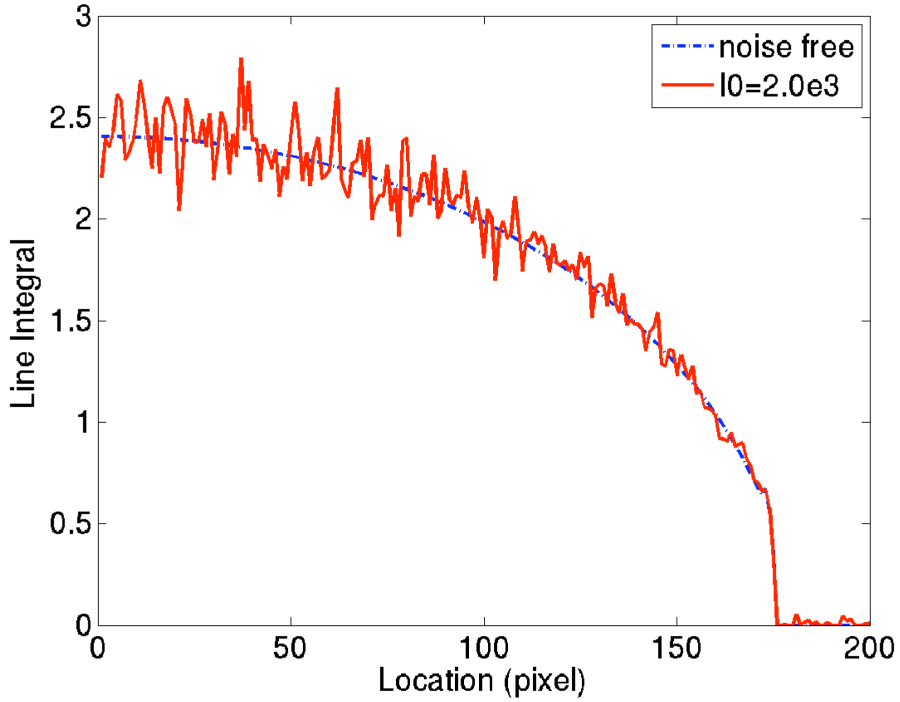

Figure 4.4: One-dimensional line integral profiles across the breast on a projection image. The dashed (blue) and continuous (red) plots correspond to noise free case and the case with $\mathbf{I_0}$=2.0e3, respectively. The variance of line integral is larger at the center of breast region, and gets smaller toward the skin.

4.2.3 Image Evaluation

The metrics for quantitative evaluation of the denoising technique are calculated based on the reconstructed slices of the simulated breast.

The contrast of the lesion is defined as the relative difference between the average pixel values within the lesion and those outside the lesion. The noise level is characterized by the percentage noise, that is, the standard deviation of the pixel values within a uniform ROI relative to the mean value. The CNR measure is the ratio of contrast of the lesion to the percentage noise.

The normalized cross correlation (NCC) is a mathematical operation defined as [117]:

$$NCC(s,t) = \frac{\sum_x \sum_y (f(x,y) - \bar{f}(x,y))(w(x-s,y-t) - \overline{w})}{\{[\sum_x \sum_y (f(x,y) - \bar{f}(x,y))^2] \cdot [\sum_x \sum_y (w(x-s,y-t) - \overline{w}]^2)\}^{\frac{1}{2}}} \quad , \tag{4.9}$$

where (x,y) and (s,t) are spatial position indices, f and w are an image and a template respectively, and, $\bar{f}$ and $\overline{w}$ are their average values over the space .

For a simulated breast with contrast detail phantoms, the figure of merit was the number of detectible lesions, which was counted automatically by thresholding each lesion's CNR as well as NCC of each lesion with its ideal version. The threshold was set to 1.0 for CNR and 0.28 for NCC.

4.3 Results

4.3.1 Parameter Choice

The number of detectible lesions from the contrast detail phantom is used as the figure of merit (FOM). For each technique, the parameters are multi-dimensionally grid-searched for the best combinations. The best parameters for PDE_{tomo} with *iter_num*=10 are: Δt=0.1, σ=1 and δ_0=0.03. Figure 4.5 shows how the FOM varies as a function of Δt or δ_0 when other parameters are kept at optimized values. Matching the background noise level with $\mathrm{PDE}_{\mathrm{tomo}}$, $\mathrm{PDE}_{\mathrm{3Dpost}}$ has the best parameter set as: *iter_num*=4, Δt=0.2, σ=0.15, and δ_0=0.07.

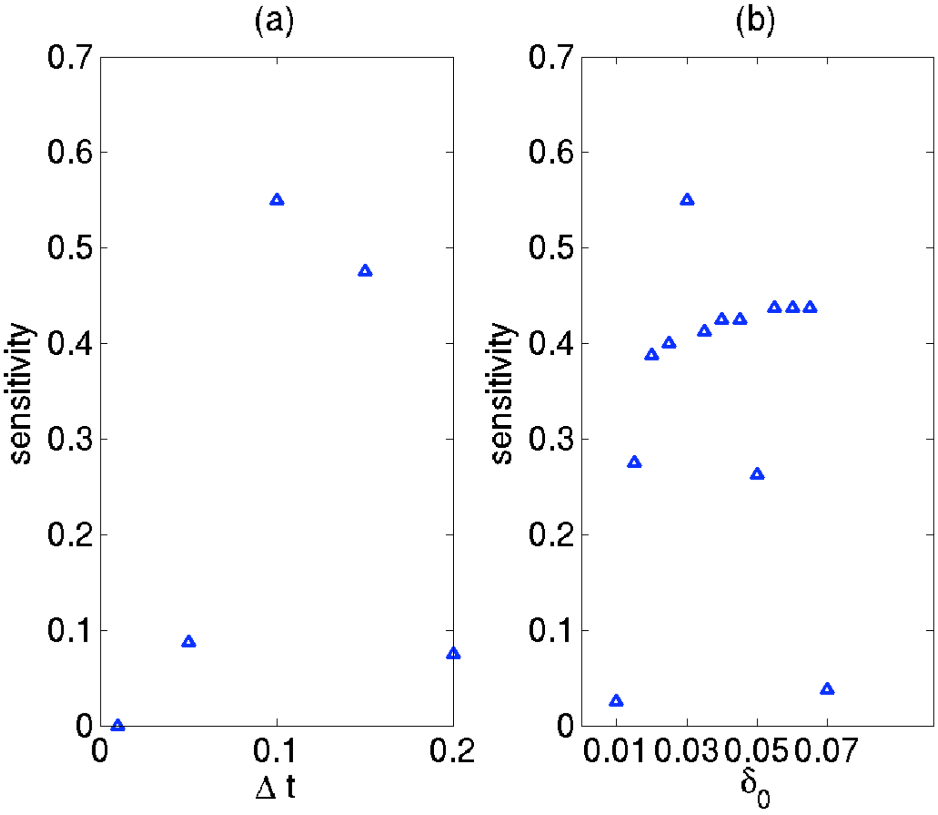

Figure 4.5: Performance from contrast detail phantom as a function of (a) Δt, or (b) δ_0, parameters in the $\mathrm{PDE}_{\mathrm{tomo}}$ technique, with all other parameters held at their optimal values.

4.3.2 Step Comparison

Figure 4.6 shows the reconstructed thin sections of a) the ideal contrast detail phantom, b) the image after adding noise corresponding to exposure I_0=2.5e4, c) the image denoised by $\mathrm{PDE}_{\mathrm{3Dpost}}$ algorithm applied at step 4 and d) the same image denoised by $\mathrm{PDE}_{\mathrm{tomo}}$ algorithm applied at step2, matching the background noise with the one in Figure 4.6 (c). The reconstructed slice thickness was 0.5 mm and within-plane pixel dimension was 0.8 mm. Figure 4.7 shows the corresponding results at I_0=1e4. The noise level is higher in Figure 4.7 (b) as compared to Figure 4.6 (b). The background noise in the processed volumes in Figure 4.7 (c) and (d) is comparable to those in Figure 4.6 (c) and (d). The sensitivity defined as the ratio of the numbers of detectible lesions to the total number of 80 for each case is shown in Figure 4.8.

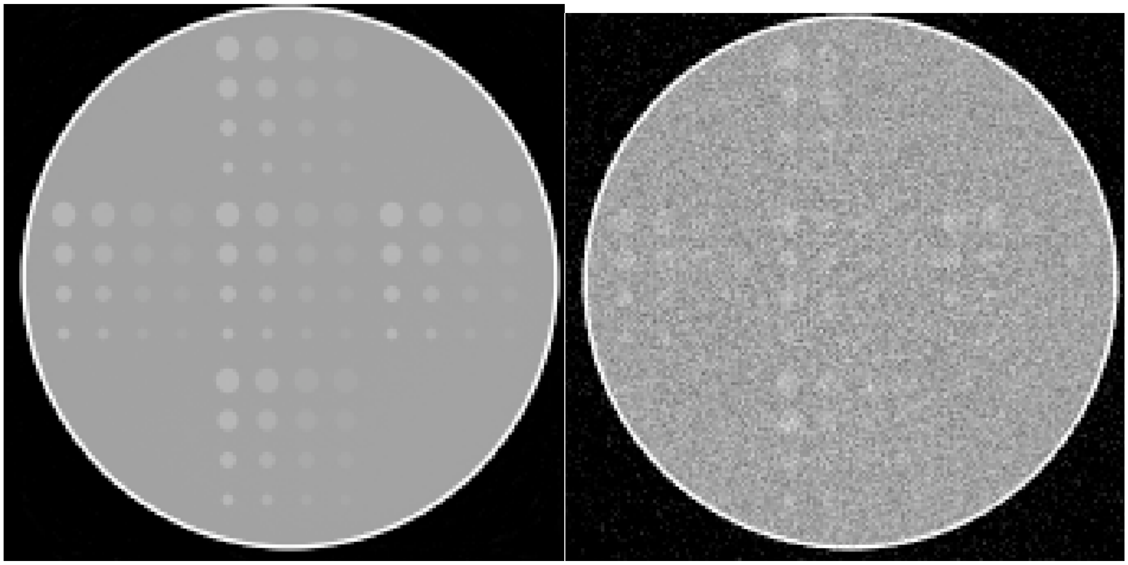

(a) Ideal

(b) With Noise: I_0=2.5e4

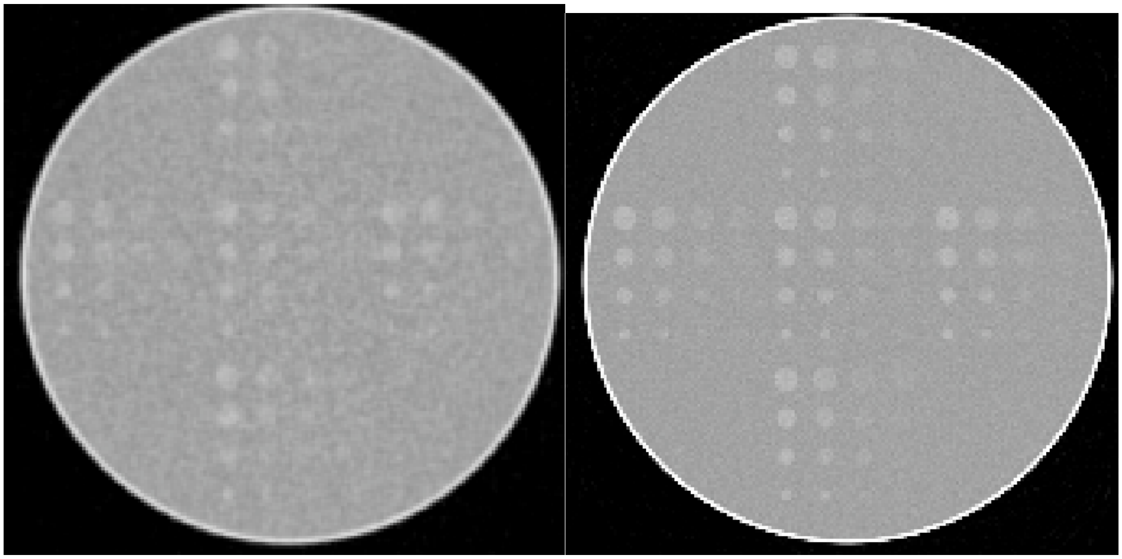

(c) PDE_{3Dpost}

(d) PDE_{tomo}

Figure 4.6: Step comparison at I_0=2.5e4. To (a) an ideal contrast detail phantom, noise is added to yield (b) the initial image without any denoising. (d) PDE_{tomo} noise removal before the FBP reconstruction is better than (c) after reconstruction.

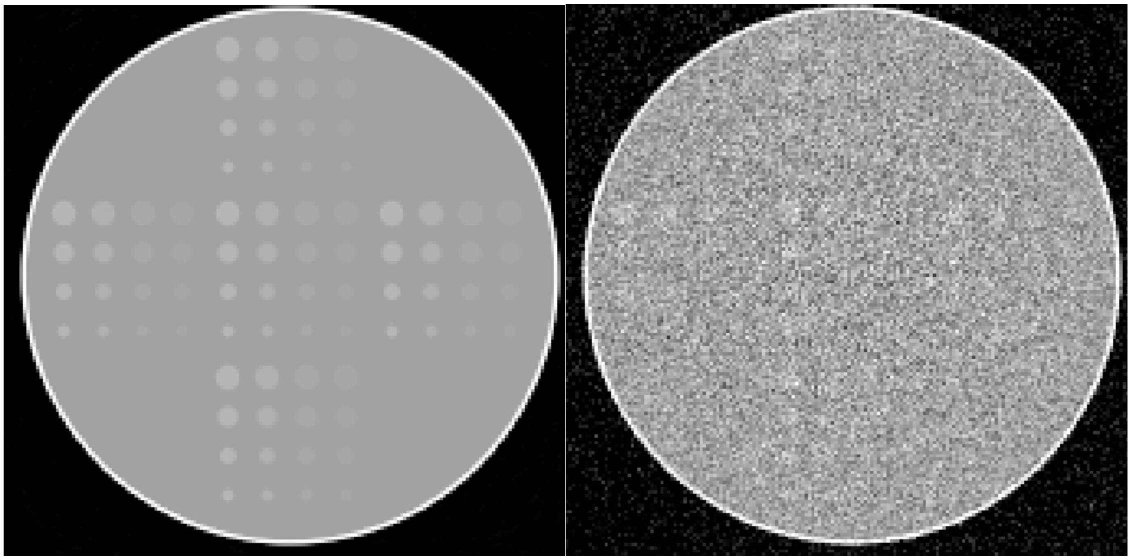

(a) Ideal

(b) With Noise: I_0=2.5e4

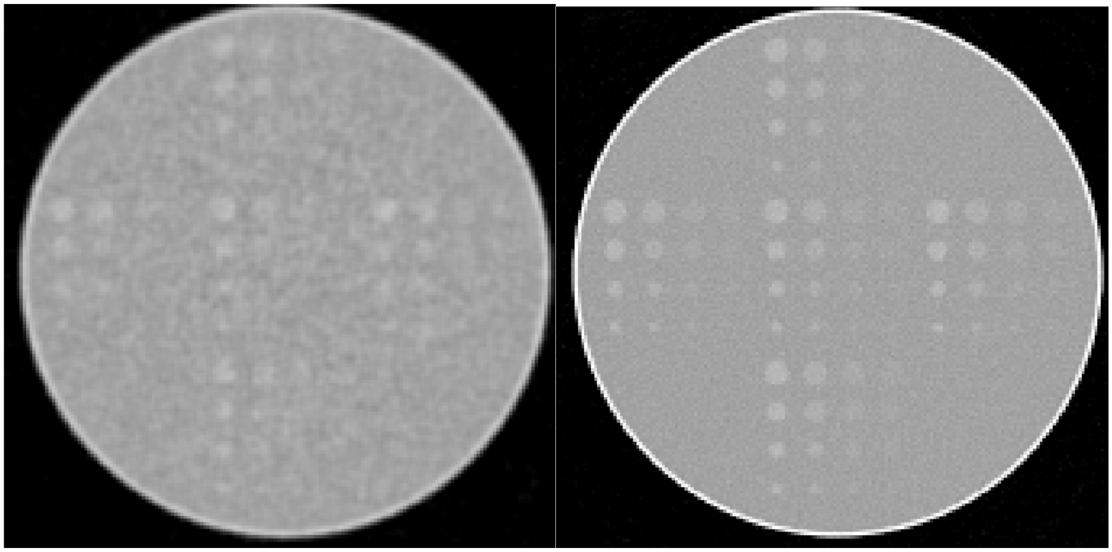

(c) $\text{PDE}_{3\text{Dpost}}$

(d) PDE_{tomo}

Figure 4.7: Step comparison at I_0=1e4. Figure 4.7 (b) is noisier than Figure 4.6 (b). For subfigures (c) and (d), they come to the same conclusion: (d) PDE_{tomo} applied at step 2 is better than (c) $\text{PDE}_{3\text{Dpost}}$ applied at step4.

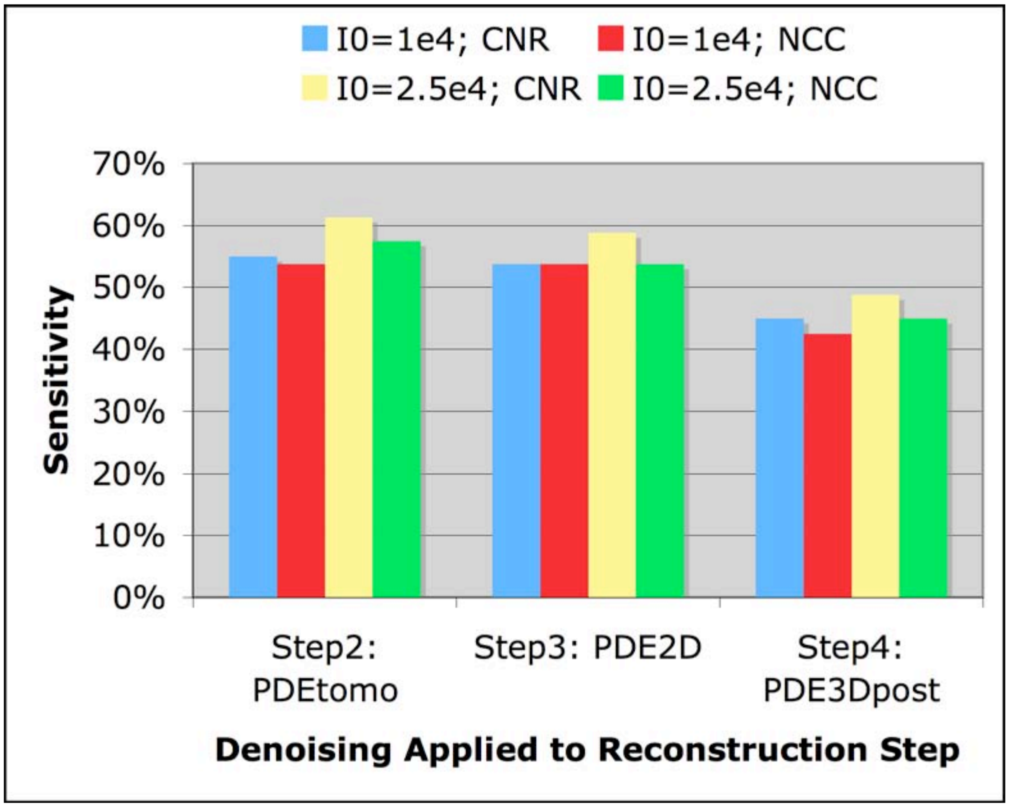

Figure 4.8: Comparison between denoising applied to reconstruction steps 2, 3 and 4, using CNR and NCC as the criteria. Denoising at step 2 before reconstruction consistently provides higher number of detectible lesions or sensitivity, as does increasing the exposure level.

4.4 ***Discussion***

Dedicated breast CT imaging possesses the potential for improved lesion detection over conventional mammograms, especially for women with dense breasts. The breast CT images are acquired with a glandular dose comparable to that of standard two-view mammography for a single breast. Hence the reconstructed volume has a substantial amount of noise when very thin coronal-view slices are viewed. It is thus desirable to remove the noise in the reconstructed breast volume without losing the resolution.

Along the breast CT reconstruction process, there are three feasible steps for a denoising technique. Thus the aim of this study is to investigate which step will give the best result. The comparison between step 2 and step 4 is especially interesting, because noise can be better characterized in step 2 whereas the PDE technique works better for the underlying data structure in step 4, which is piecewise constant data with sharp edges. For the comparison study, a contrast detail phantom is used, which represents the clinically important task of detecting small, low contrast lesions.

Visual comparison between PDE_{tomo} and $\text{PDE}_{\text{3Dpost}}$ processed volumes show that PDE_{tomo} results in superior denoised volume than $\text{PDE}_{\text{3Dpost}}$. Even though the background noise are matched for two volumes, as is shown in Figure 4.6 and Figure 4.7, $\text{PDE}_{\text{3Dpost}}$ processed volume exhibits some unpleasant mottle, which is especially true in Figure 4.7 (c). The noise mottle is due to the FBP reconstruction process, which correlates the independent quantum noise in the projection views. By contrast, PDE_{tomo} processed volumes are exempt from this effect. Applying PDE technique between filtering and back-projection steps (step 3) results in reconstructed slices visually similar to Figure 4.6 (d) and Figure 4.7 (d).

Quantitative results based on the lesion detection sensitivity of the contrast detail phantom agree with the qualitative evaluation. While the CNR and NCC criteria don't give the same number, they are very close to each other and provide the same trend: PDE_{tomo} processed volumes (step 2) have more detectible lesions than processed ones by PDE_{2D} (step 3) and $\text{PDE}_{\text{3Dpost}}$ (step 4). Moreover, given that the background noise is matched, when the exposure level is higher, the lesion detection sensitivity is higher for all three variants of PDE technique according to the CNR criterion.

To summarize, three separate techniques were developed for three different steps in the reconstruction process. By optimizing each of them independently, it was found that denoising before reconstruction provides better images than after reconstruction.

This is understandable, since some fine details in the volumes can be overwhelmed by the abundant noise during the reconstruction step. Applying denoising afterwards cannot recover that information. By contrast, if a denoising technique is applied before reconstruction, it is possible for the fine details to be preserved. As far as we know, this is the first time that anybody has studied the effect of where to apply denoising in dedicated breast CT. In the next chapter, the best technique here - PDE_{tomo} technique - will be compared with other techniques that are also applied at step 2 for further evaluation.

5 Noise Removal in Breast CT: the PDE$_{tomo}$ Technique

As a continuation of the theme in previous chapter about the noise removal in breast CT, this one introduces more simulation studies on the PDE$_{tomo}$ technique for its comparison to two other spatially adaptive denoising techniques. The PDE$_{tomo}$ is also applied to the clinical datasets.

5.1 Introduction

Dedicated breast CT imaging is designed at present stage to acquire images using a glandular dose level same as that of standard two-view mammography. Hence the reconstructed volume has a non-negligible quantum noise when thin section CT slices are visualized. It is thus desirable to remove the noise in the reconstructed breast volume without losing the resolution.

A good candidate denoising technique should have the following property: removing noise while maintaining the spatial resolution. In the literature, many techniques satisfying this requirement have been developed. Among them are level set methods [118], multi-resolution denoising techniques [119-124], and Partial Diffusion Equation (PDE) based techniques [110, 111]. Some modeling based denoising techniques are also developed [107].

In this study, besides the PDE$_{tomo}$ technique described in section 4.2.2.2 of Chapter 4, two more spatially adaptive denoising techniques are implemented, applied on the projection data with preprocessing (step 2 shown in Figure 4.2), and compared to PDE$_{tomo}$. Of them, Wiener filter [125] is a linear spatially adaptive technique whereas Adaptive Trimmed Mean (ATM) filter [113, 126] is a nonlinear spatially adaptive technique. As is noted from Chapter 4, PDE$_{tomo}$ technique is also a nonlinear spatially adaptive technique.

Quantitative comparisons are made using simulated data at various exposure levels. First, the detailed comparison between the PDE_{tomo} and Wiener filter based on a single low-contrast lesion is given. Second, the ATM is added into the comparison using the contrast detail phantoms. Third, the noise-resolution tradeoff plots of three techniques are compared to each other using a single high-contrast lesion. Moreover, the PDE_{tomo} technique is applied to dedicated breast CT scan data from several human subjects for qualitative evaluation of its denoising performance.

5.2 Materials and Methods

5.2.1 Human Subject Datasets

Volunteer human subjects were recruited in the University of California Davis Medical Center consistent with an IRB protocol and their breast CT datasets were acquired on the custom-built dedicated breast CT system (described in section 2.2). For each human subject dataset, the projection images were obtained under 80 kVp using a circular orbit. The mAs values are chosen for each subject in such a way that the mean glandular dose using breast CT is equal to two-view mammography. Each subject is scanned within 20 seconds to get a total of 530 projection images that span slightly over 360 degrees. After bad pixel and flat field correction (described in section 2.2.3), each dataset is ready for tomographic reconstruction (described in section 2.3).

5.2.2 Denoising Techniques

5.2.2.1 Wiener filter

A Wiener filter is used at step 2 for comparison against the PDE technique investigated in this study. Both techniques are spatially adaptive filters. However, the Wiener filter is a linear technique whereas the PDE technique is nonlinear.

For each pixel, its mean (μ) and variance (σ^2) around a local neighborhood is estimated. Then the Wiener filter updates $l(x,y)$ to the new $l_n(x,y)$ through:

$$l_n(x,y) = \mu + \frac{\sigma^2 - \upsilon^2}{\sigma^2}(l(x,y) - \mu) \qquad (5.1)$$

where υ^2 is the average of σ^2 values.

The variable parameter in the Wiener filter is the size of the neighborhood. In this study, 3x3, 5x5 and 7x7 kernels are considered.

5.2.2.2 Adaptive Trimmed Mean (ATM) filter

Like the PDE filters described in Chapter 4, the ATM filter is also a nonlinear spatially adaptive technique. The one-dimensional ATM filter presented in reference [113] is expanded to two-dimensional. The window size M and the trimming parameter α are adjusted according to the local pixel value:

$$M = \frac{2\beta\lambda}{2\lambda + \beta x}, \quad \alpha = \frac{\alpha_m x}{\lambda} \qquad (5.2)$$

where x is pixel value on raw projections, and beta and lambda are two parameters of the ATM filter. When x is zero, the window size M obtains its maximal value at beta.

5.2.3 Image Evaluation

The metrics of contrast of the lesion, noise level, and contrast-to-noise ratio (CNR) [73] described in section 4.2.3 are utilized in this study. Again, these metrics are calculated based on the reconstructed slices of the simulated breast. In addition, the NCC is also calculated for contrast detail phantoms for technique comparison.

Moreover, the spatial resolution [73] is quantified based on high-contrast lesions. The corresponding volumes are target reconstructed (in-plane resolution is 0.2 mm) around the high-intensity sphere. If a specified denoising technique is to be evaluated, it is applied to the projection images before they are sent to the FBP reconstruction core for the targeted reconstruction. Then the edges of the circular disc within a reconstructed slice are averaged radially. For each specific denoising technique, a Gaussian function is fitted to the edge with standard deviation of σ_0, and the full width at half maximum (FWHM) of that function is measured as:

$$FWHM = \sqrt{8 \cdot \log 2} \times \sigma_0 = 2.3548\sigma_0. \quad (5.3)$$

5.3 Results

5.3.1 Simulation Results: Comparison between denoising techniques

In Figure 5.1, the three columns correspond to the reconstructed slices of the simulated breast CT data without denoising, with Wiener denoising (kernel 3x3) and with the $\mathrm{PDE}_{\mathrm{tomo}}$ denoising, respectively. The four rows show the results using varying photon fluences using I_0=2.5e3, 5e3, 7.5e3 and 2.5e4 correspondingly from the top to the bottom. The noise level is appreciably lower for each successive row. The reconstructed slice thickness is 0.5 mm and within-plane pixel dimension is 0.8 mm. These slices contain a lesion at the center, which is only barely visible for the highest fluence level (bottom panel) with the original dataset. With Wiener processing, the lesion is visible for the higher two fluence levels. With $\mathrm{PDE}_{\mathrm{tomo}}$ processing, the lesion is visible for the higher three fluence levels.

As a counterpart of Figure 5.1, Figure 5.2 shows a magnified view of the periphery of the breast, using targeted reconstruction with the same slice thickness and a reduced within-plane pixel size of 0.2 mm. The sharpness of the image is manifest in the skin line. The trends are similar to the lesion detection task above, such that higher exposures (going down the rows) greatly improve the noise level and sharpness of the skin line. Similarly, improvements in noise were apparent going from left to right for original, Wiener, and PDE$_{tomo}$ filtering techniques, respectively.

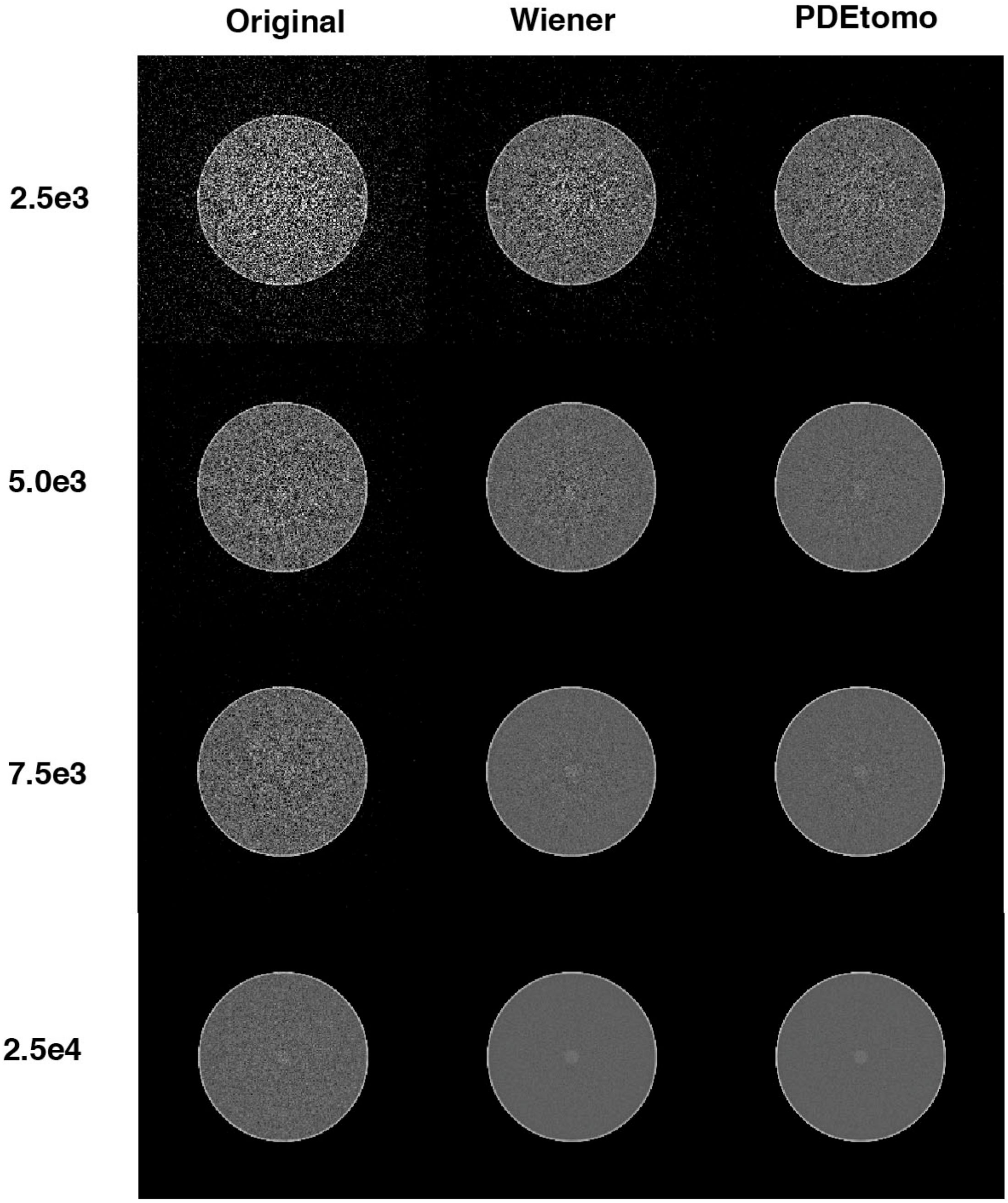
Original
Wiener
PDEtomo
2.5e3
5.0e3
7.5e3
2.5e4

Figure 5.1: Reconstructed slices of original, Wiener (3x3 kernel) and PDE$_{tomo}$ processed datasets in a simulation study with varying photon fluence levels. The lesion is located at the center of each slice.

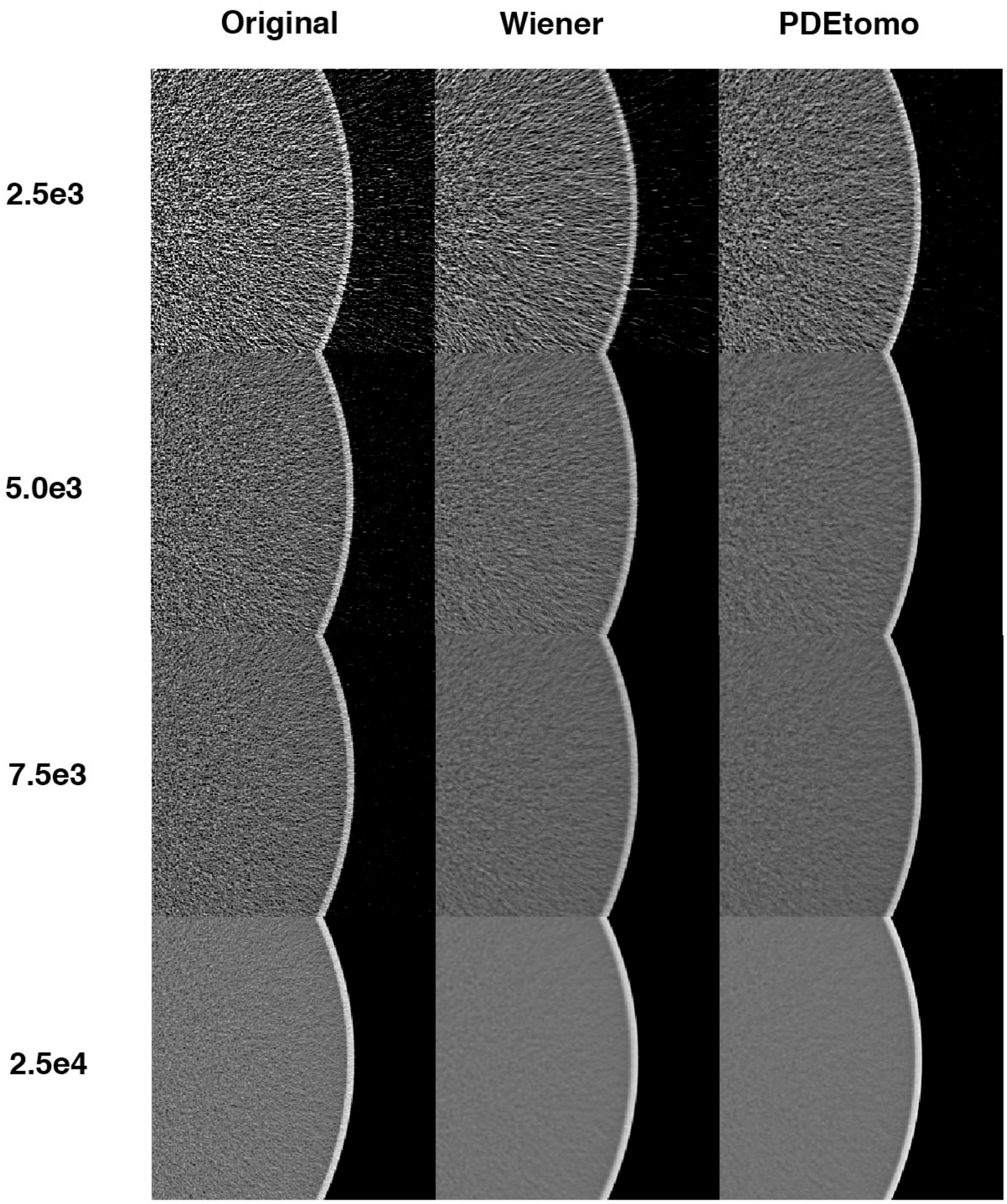
Original
Wiener
PDEtomo
2.5e3
5.0e3
7.5e3
2.5e4

Figure 5.2: Target reconstructed slices of original, Wiener (3x3 kernel) and PDE_{tomo} processed datasets in a simulation study with varying photon fluence levels, corresponding to the data in Figure 5.1.

To demonstrate the effect of denoising on the uniformity of the noise level across the image, another reconstructed coronal view slice containing only homogeneous breast tissue is shown in Figure 5.3 (a). For the horizontal centerline, the standard deviation of a local 7x7 ROI centered at each pixel on that horizontal line is plotted in Figure 5.3 (b) to (d) for photon fluence of 2.5e3, 5e3 and 2.5e4.

In all three cases, the original plots present a non-uniform level of noise such that the interior section has higher standard deviation values, that is, higher noise levels than the periphery. Wiener processing reduces the overall noise level, but the non-uniform trend remains in Figure 5.3 (b) and (c) corresponding to lower photon fluences. The PDE_{tomo} processed images reduce not only the noise level but also the uniformity of the plot for all three fluence levels. Only at the highest fluence level did Wiener filtering converge towards the performance of the PDE_{tomo} technique.

The simulation of noise in projection images using the measurement model shown in Equation (4.1) was repeated 10 times. Each one was reconstructed without denoising (original datasets) or after denoising (Wiener or PDE_{tomo} processed). The CNR values for the single low-contrast lesion are summarized with mean and standard deviation. The results are plotted in Figure 5.4.

(a) Reconstructed Slices Without a Lesion

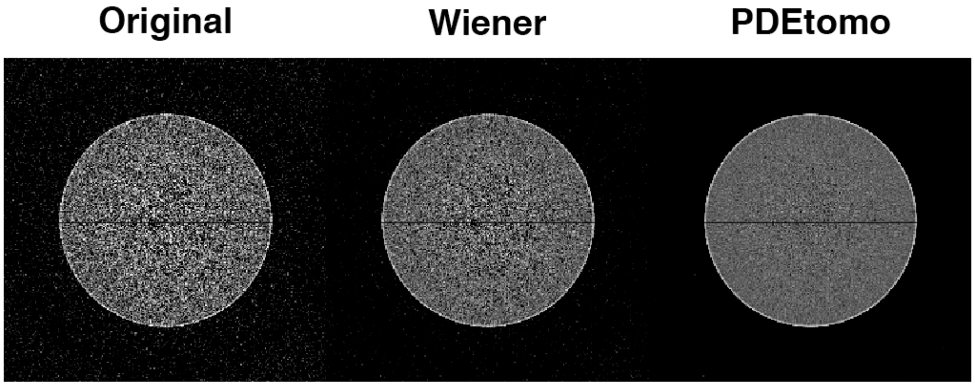
Original
Wiener
PDEtomo

(b) I_0=2.5e3

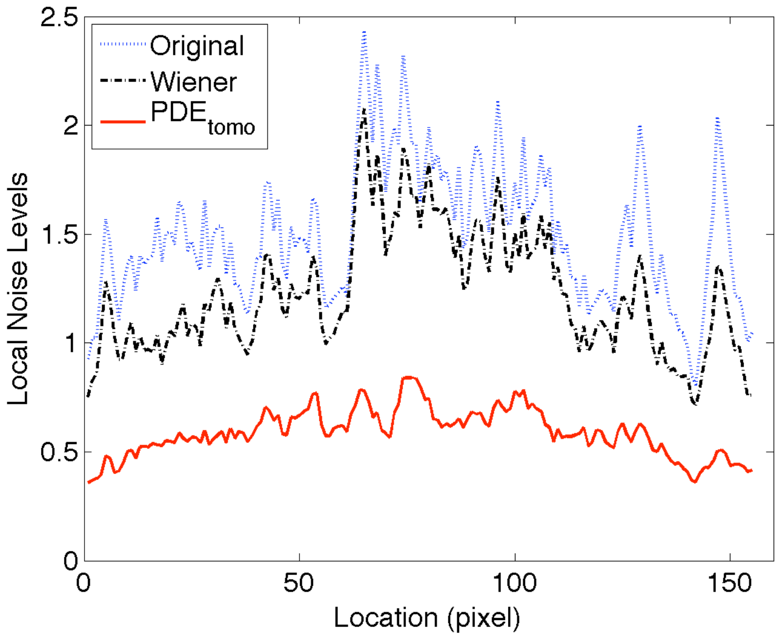

(c) I_0=5.0e3

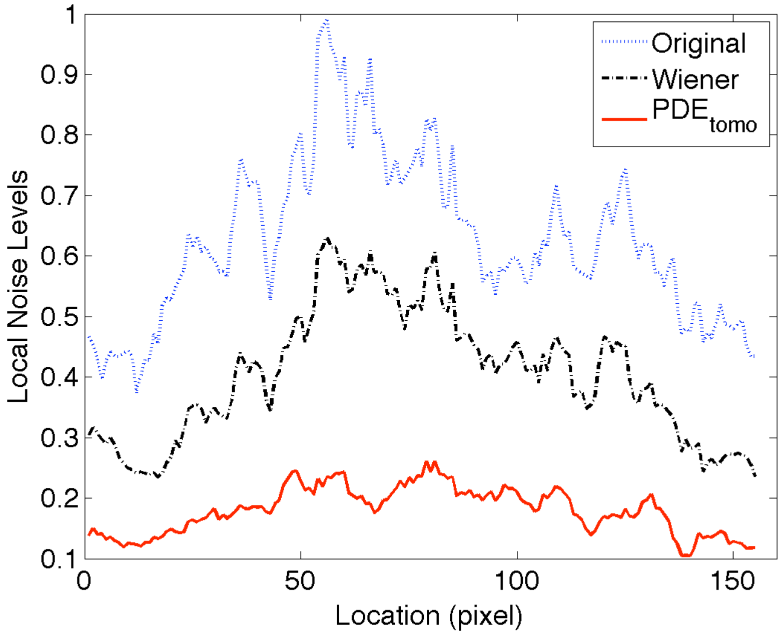

(d) I_0=2.5e4

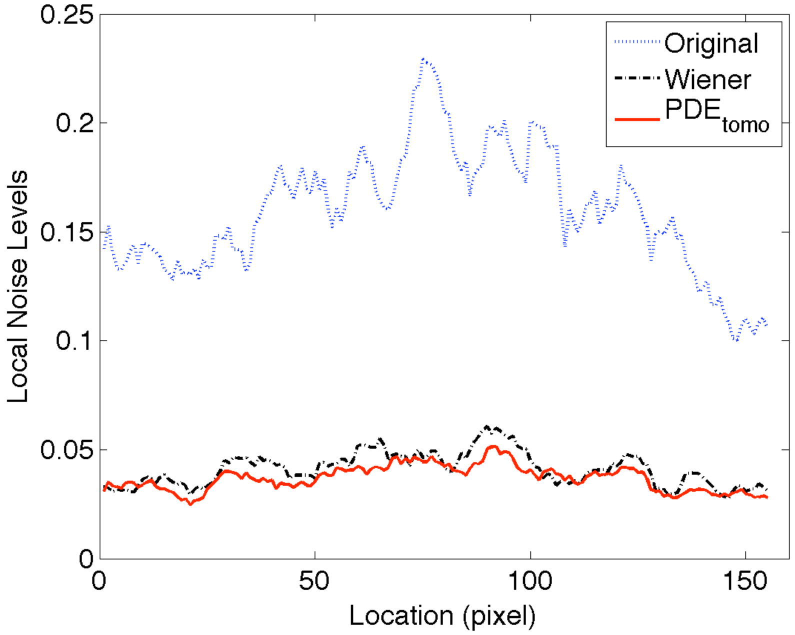

Figure 5.3: (a) Reconstruction slices without a lesion. Along the horizontal lines marked in (a), standard deviations of local 7x7 ROI are plotted for original, Wiener (3x3 kernel) and PDE$_{tomo}$ processed datasets at I_0 of (b) 2.5e3, (c) 5e3 and (d) 2.5e4.

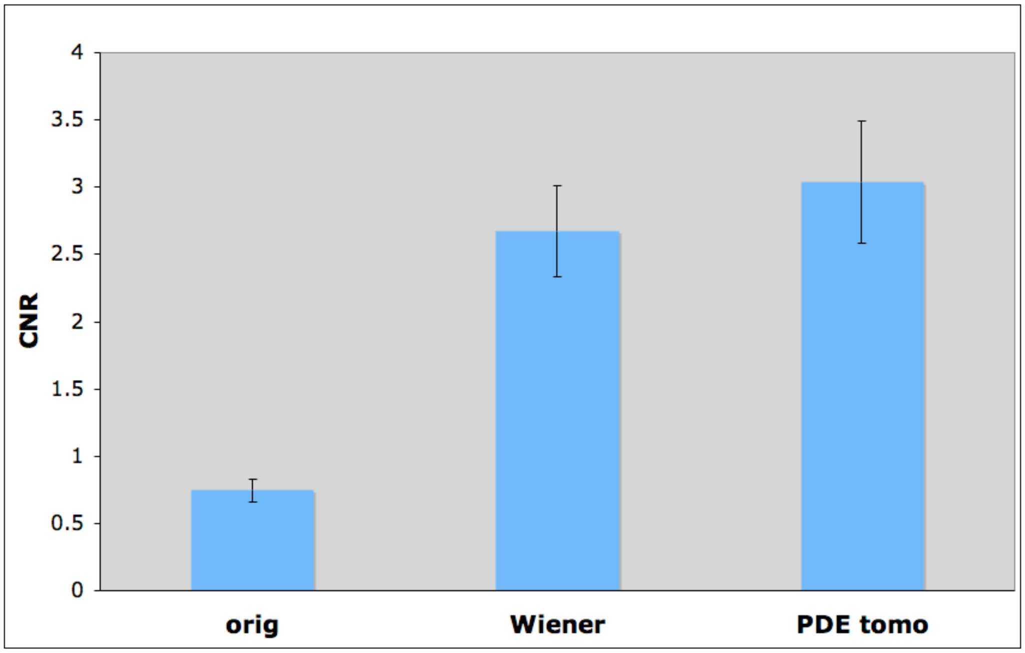

Figure 5.4: CNR comparison between the original, Wiener (3x3 kernel) and PDE$_{tomo}$ processed volumes in a simulation study with I_0=2.5e4.

At the highest fluence of 2.5e4, mean CNR values of the Wiener and PDE$_{tomo}$ processed images are 3.59 and 4.08 times that of the original one, respectively. The PDE$_{tomo}$ has consistently higher CNR values than Wiener filter for the same data. The paired two-tailed Student t test gives a p-value of 0.0036, which indicate the difference between the CNR values of PDE$_{tomo}$ and Wiener filter are statistically significant. Similar trends were observed at the lower fluence levels.

The comparison of PDE$_{tomo}$ against Wiener and ATM filters based on contrast detail phantoms is shown in Figure 5.5. PDE$_{tomo}$ gives the largest number of detectible lesions for the contrast detail phantom, followed by ATM and then Wiener filter, according to the CNR criterion.

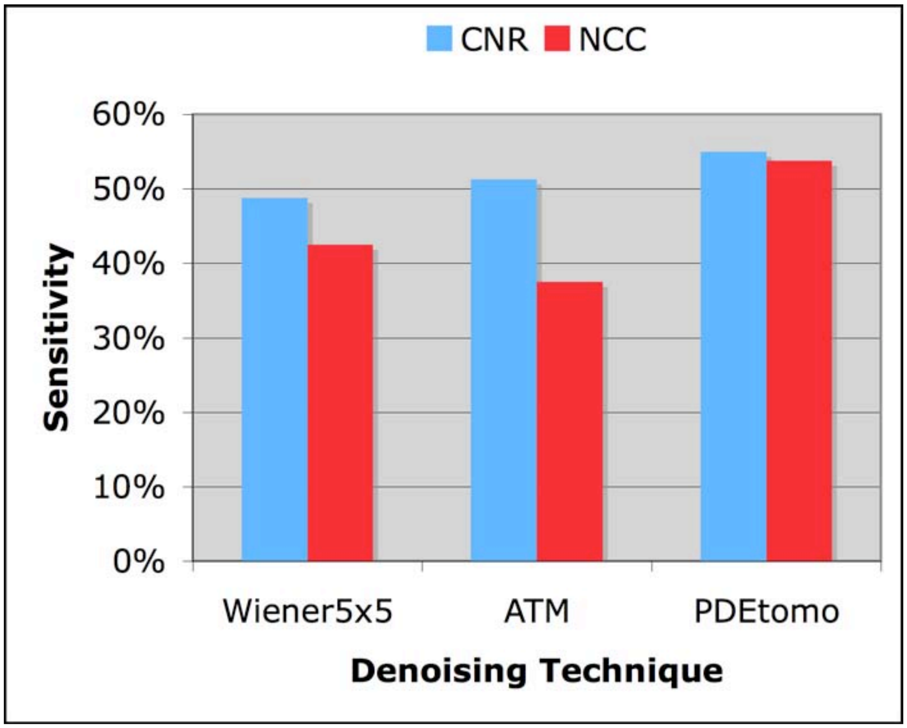

Figure 5.5: Comparison of techniques using contrast detail phantoms. All images were acquired with the lower exposure of 1e4 counts. PDE$_{tomo}$ is the best among three denoising techniques for this task.

In addition, the noise-resolution result is given in Figure 5.6. In Figure 5.6 (a), the first image shows the full view reconstructed slice with a high-intensity sphere embedded into the center of the breast tissue. The ROI for targeted reconstruction is marked on the slice. The original target reconstructed ROI as well as the wiener denoised one are to the right of the first row. In the second row of Figure 5.6 (a), the PDE$_{tomo}$ denoised result is shown in the middle. To its left, a Gaussian kernel is directly applied to the original target-reconstructed slice and its resultant blurred slice obtains the same noise level as the PDE$_{tomo}$ result. To its right, a corresponding Gaussian blurred one obtains the same resolution level. As a comparison, the PDE$_{tomo}$ achieves a low noise level and the high resolution simultaneously.

The noise and resolution values are plotted in Figure 5.6 (b) for PDE_{tomo}, Wiener and ATM techniques. The Wiener filter is applied using a 3x3 kernel. PDE_{tomo} processing resulted in lower noise than Wiener filtering (4.7% and 12%, respectively). At the same time, PDE_{tomo} also provided better resolution than Wiener filtering (0.22 vs. 0.29 mm, respectively). The ATM filter provided the same 0.22 mm resolution as PDE_{tomo}, while reducing noise to 2.0%. However, the ATM reconstructed image shows a cupping artifact, which is absent in the PDE_{tomo} processed images. The cupping artifact is evident in the one-dimensional profile through the center of the high-contrast object, as shown in Figure 5.7. Note that the rectangle represents the location where the noise level is measured, and does not capture the non-uniformity problem.

(a) Reconstructed Slices

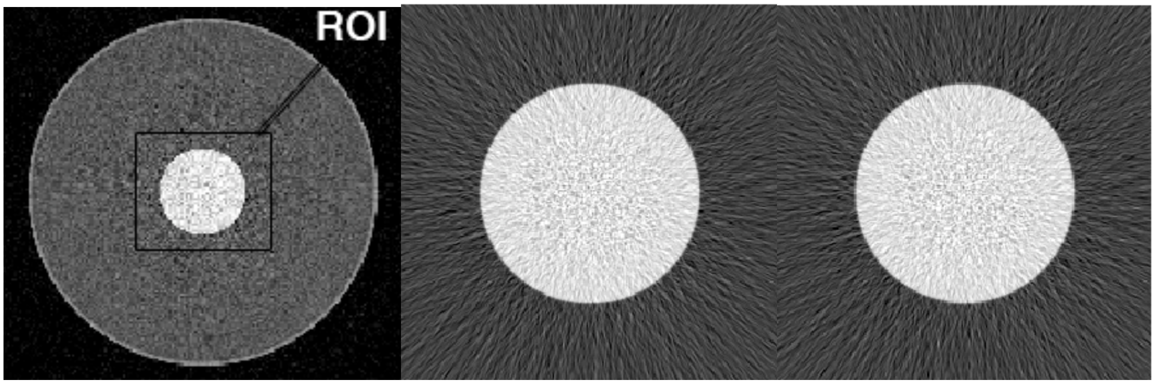

Full View – Original ROI-Target Recon - Orig ROI-Target Recon – Wiener

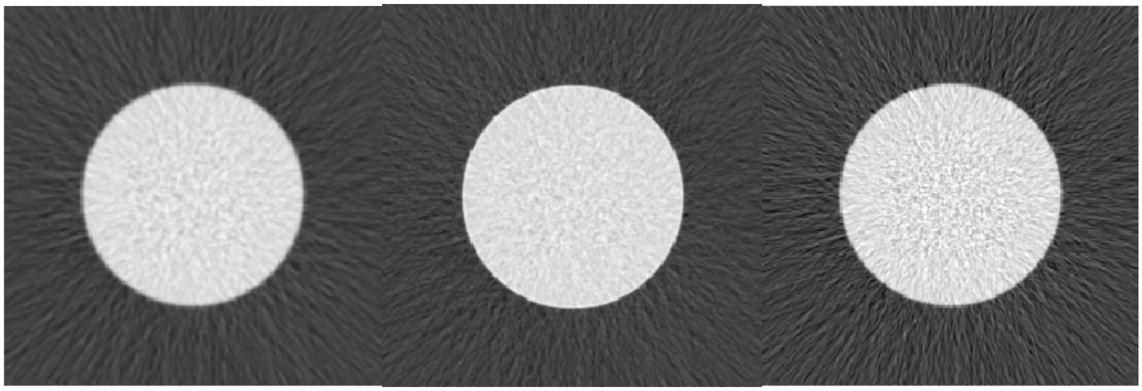

ROI-Gaussian – Match Noise ROI-Target Recon – PDE_{tomo} ROI-Gaussian – Match Res

(b) Noise Resolution Plot

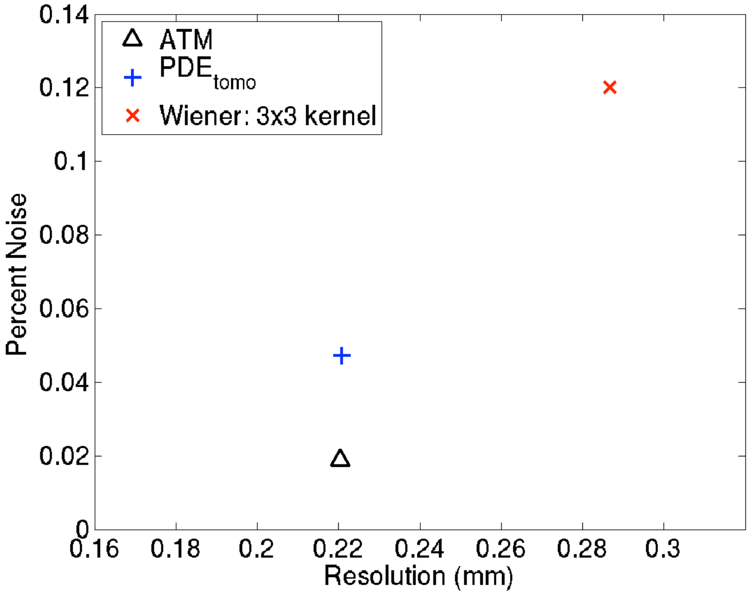

Figure 5.6: (a) Target reconstruction around a high contrast object from original, Wiener processed and PDE_{tomo} processed datasets, and (b) noise-resolution plot at I_0=2.5e4.

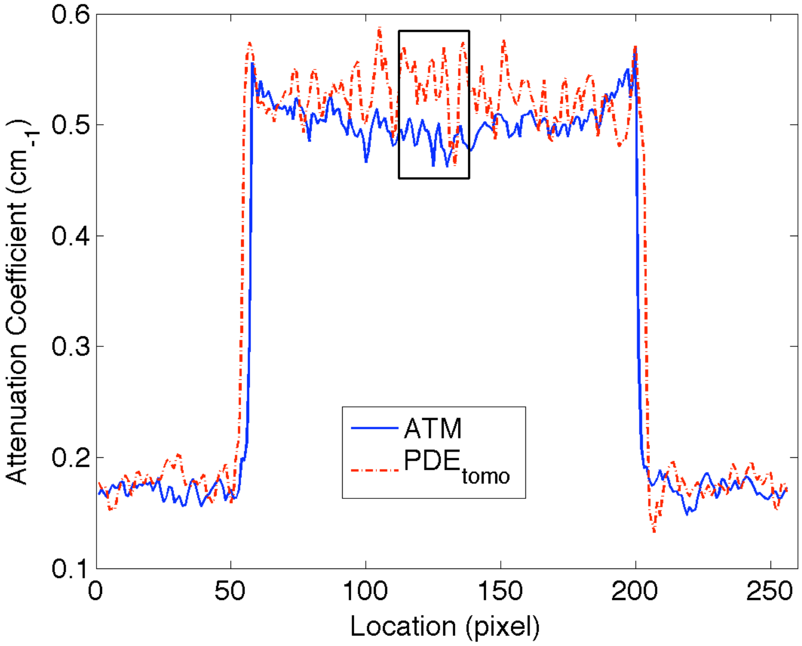

Figure 5.7: One-dimensional profile of the reconstruction through the center of the high contrast object using PDE_{tomo} and ATM filter.

5.3.2 Human Subject Results

When applied to the clinical datasets, the parameters of $\mathrm{PDE}_{\mathrm{tomo}}$ used are: Δt=0.1, σ=1, δ_0=0.03 and *iter_num*=10.

Figure 5.8 to Figure 5.12 show the coronal reconstructed slices from human subject 1 with and without the $\mathrm{PDE}_{\mathrm{tomo}}$ technique. The slice thickness is 0.5 mm. The small region marked in Figure 5.9 is zoomed in and shown in Figure 5.10.

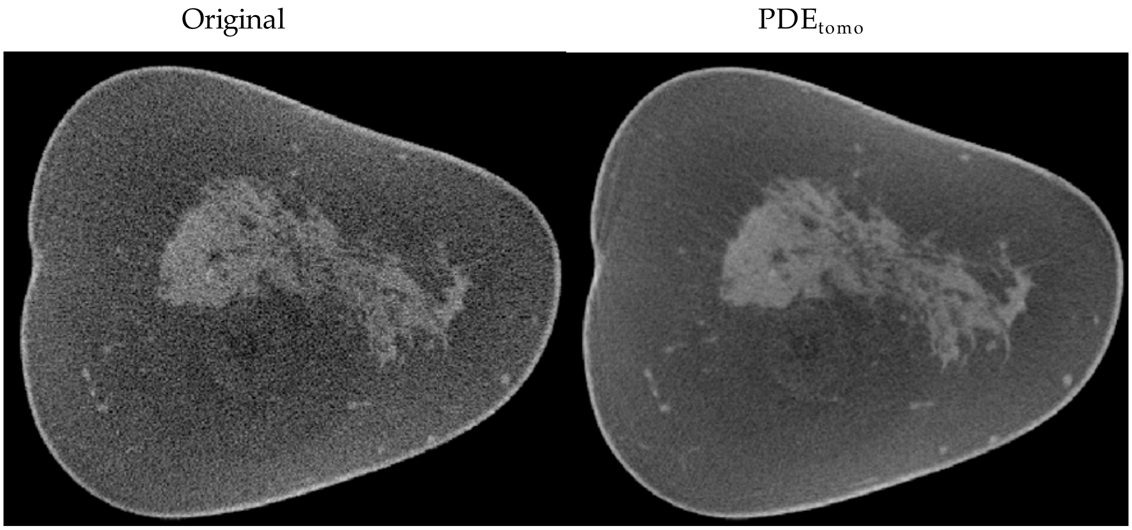

Figure 5.8: Human subject No.1 slice 60.

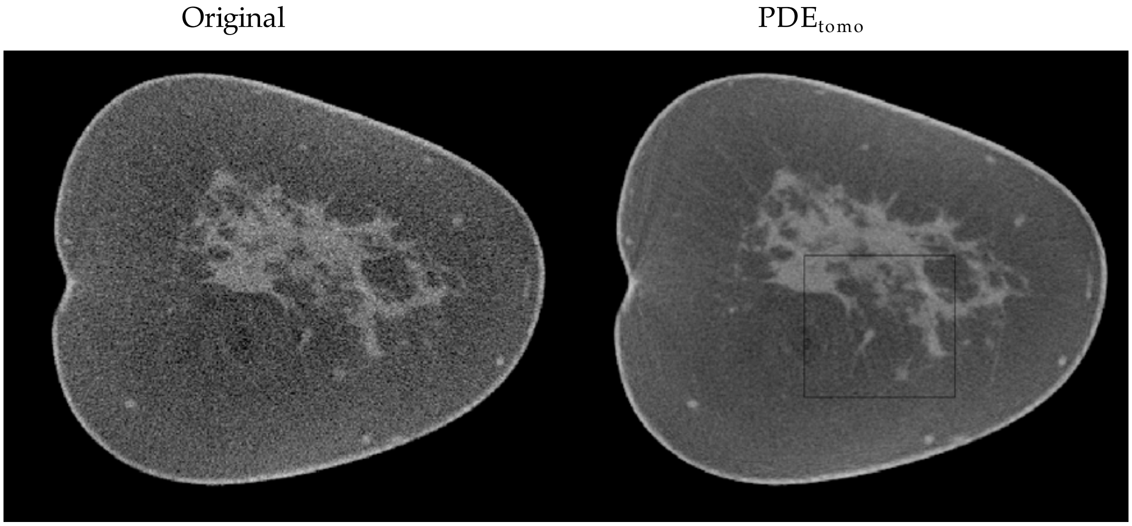
Original
PDE$_{tomo}$

Figure 5.9: Human subject No.1 slice 80.

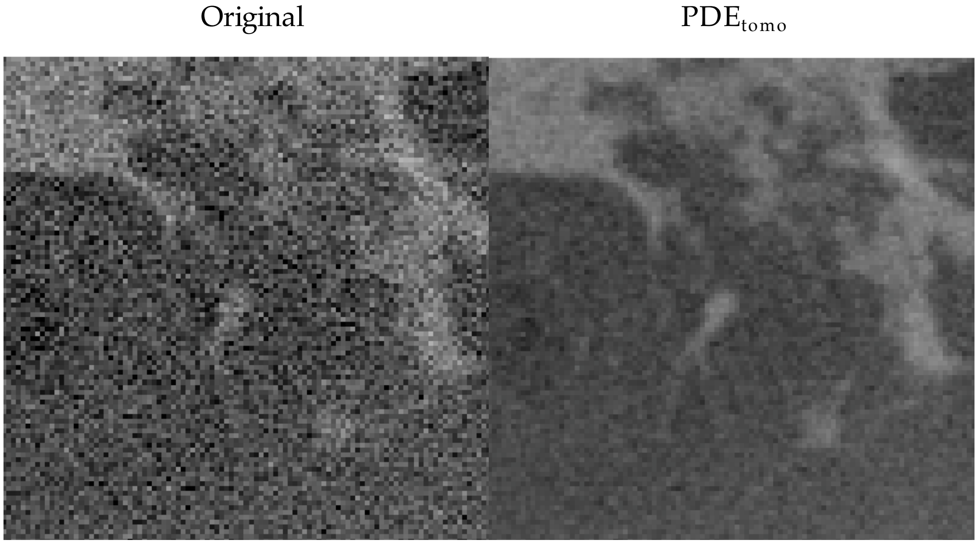
Original
PDE$_{tomo}$

Figure 5.10: Human subject No.1 slice 80 –smaller ROI corresponding to the rectangle in Figure 5.9.

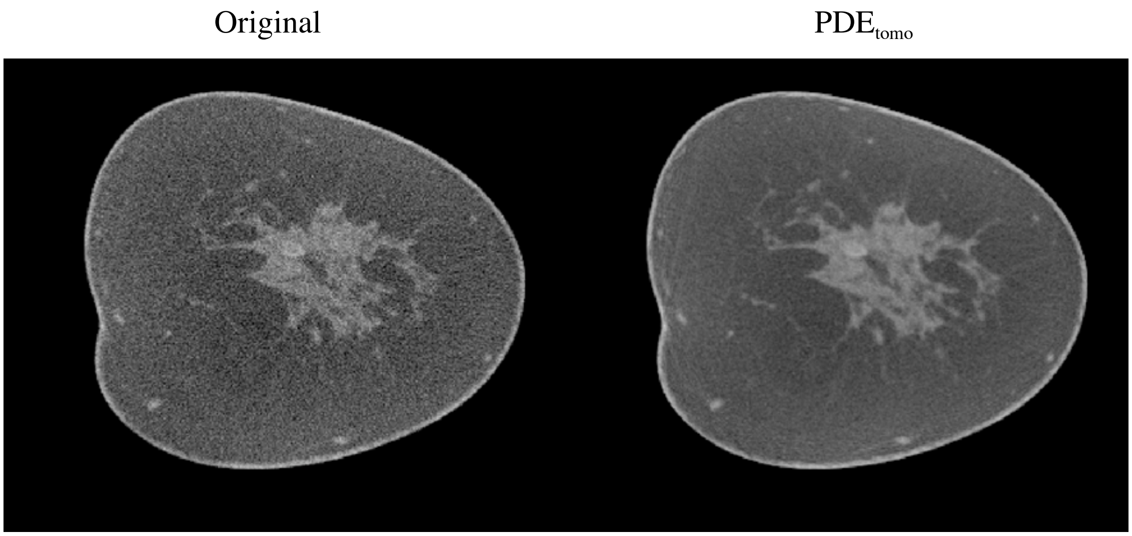

Original

$\mathrm{PDE}_{\mathrm{tomo}}$

Figure 5.11: Human subject No.1 slice 100.

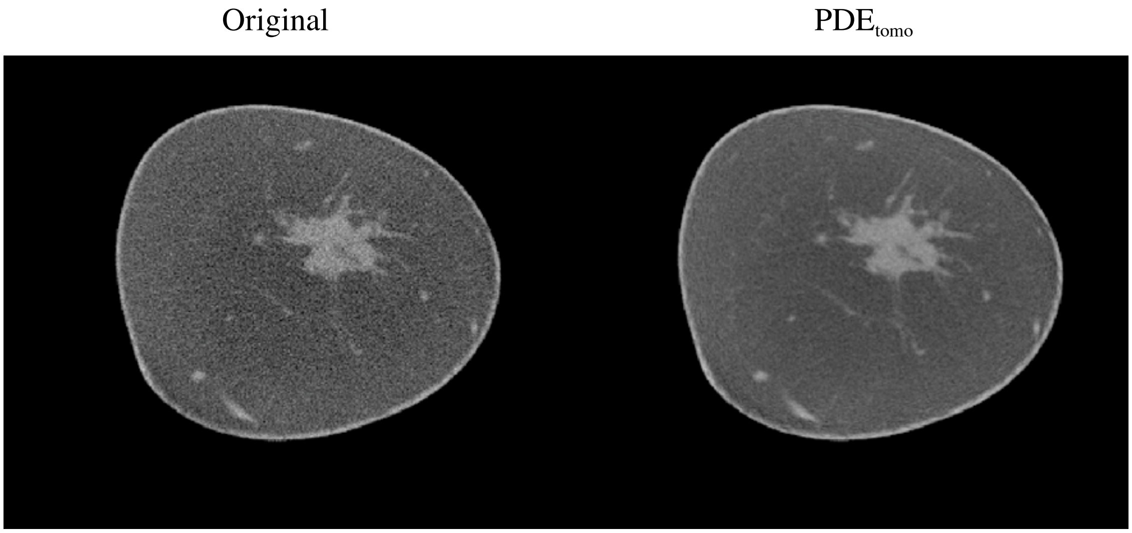

Original

$\mathrm{PDE}_{\mathrm{tomo}}$

Figure 5.12: Human subject No.1 slice 120.

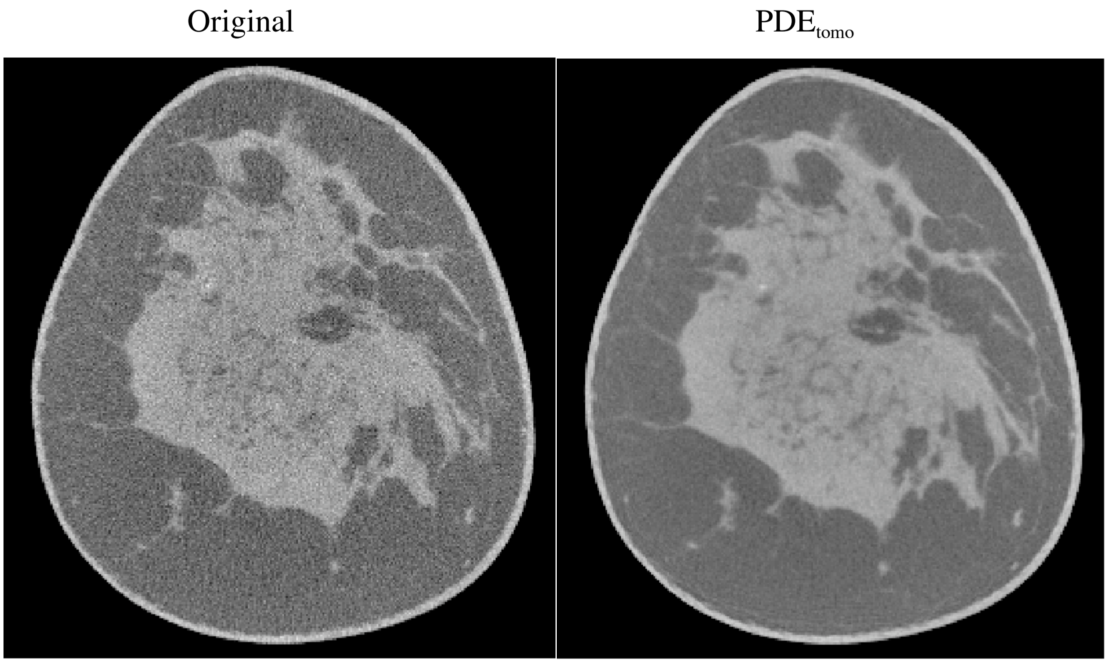
Original
PDE_{tomo}

Figure 5.13: Human subject No.2 slice 60.

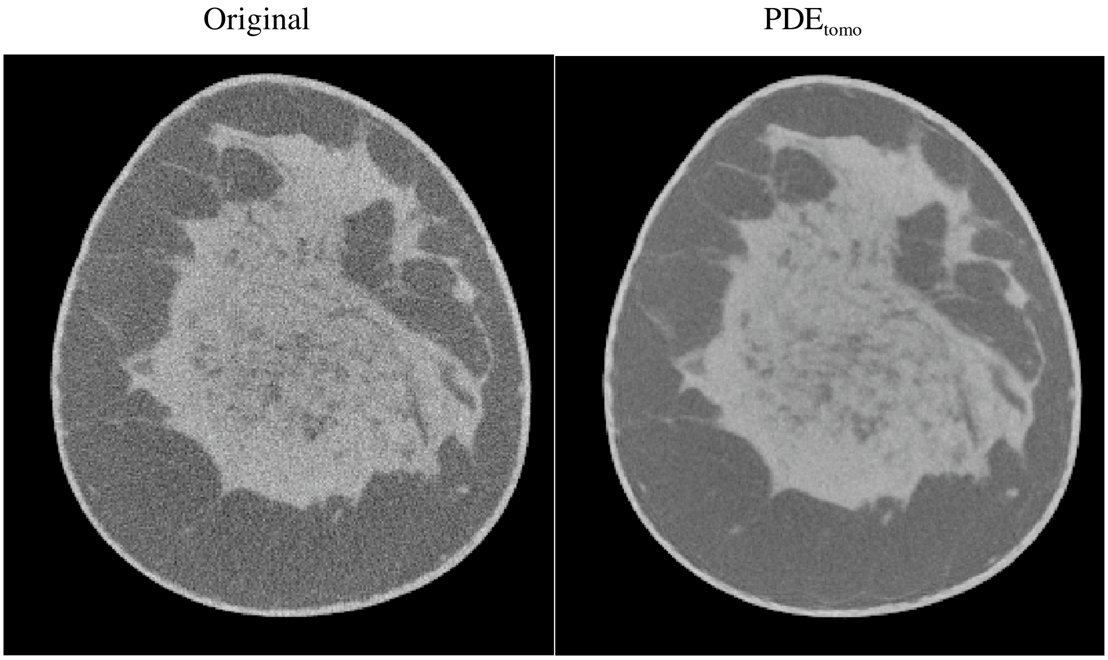
Original
PDE_{tomo}

Figure 5.14: Human subject No.2 slice 80.

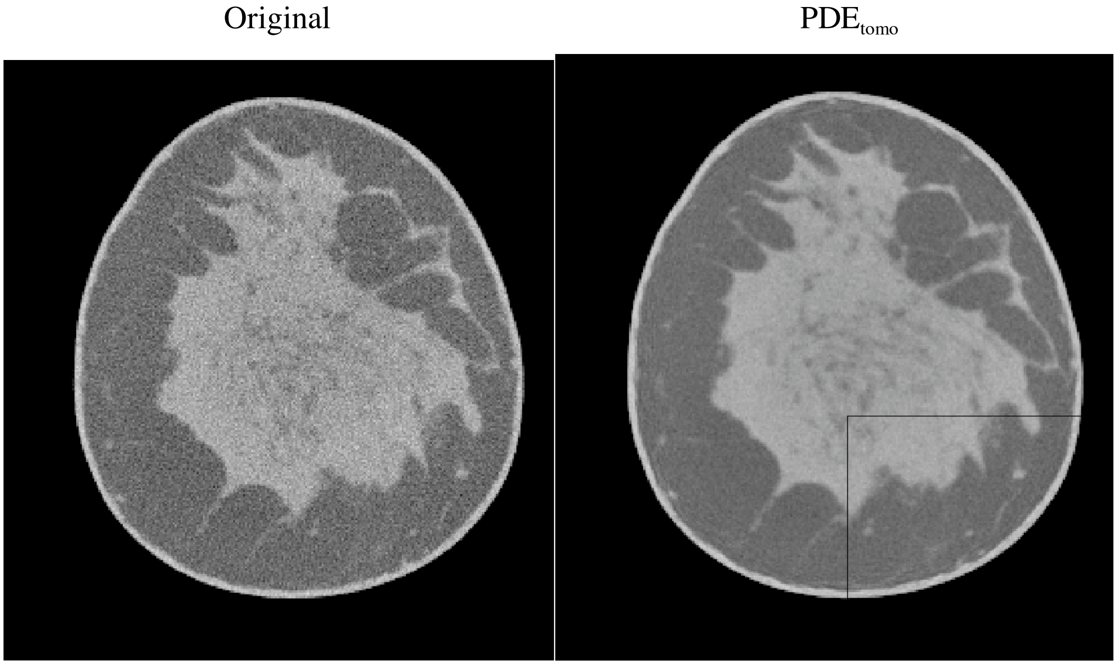

Original

PDE$_{tomo}$

Figure 5.15: Human subject No.2 slice 100.

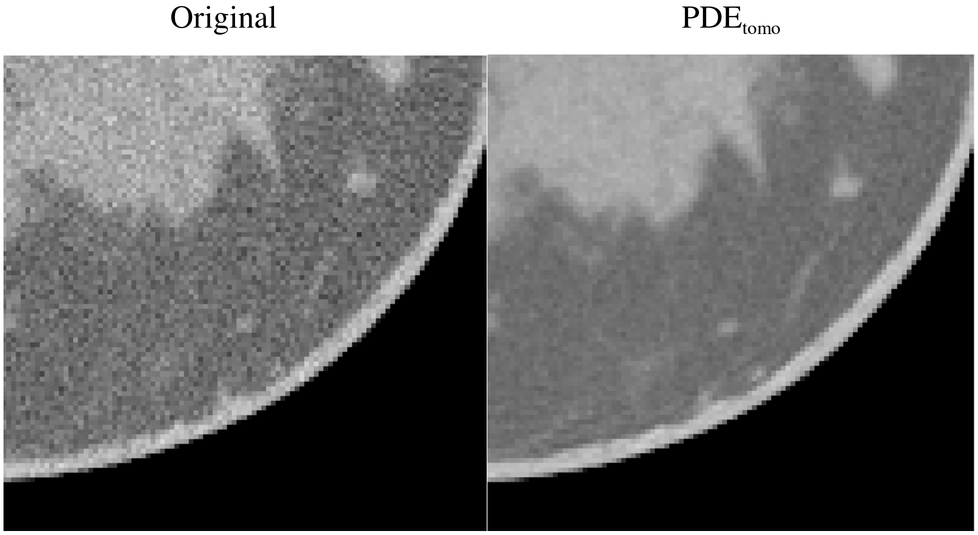

Original

PDE$_{tomo}$

Figure 5.16: Human subject No.2 slice 100 –smaller ROI corresponding to the rectangle in Figure 5.15.

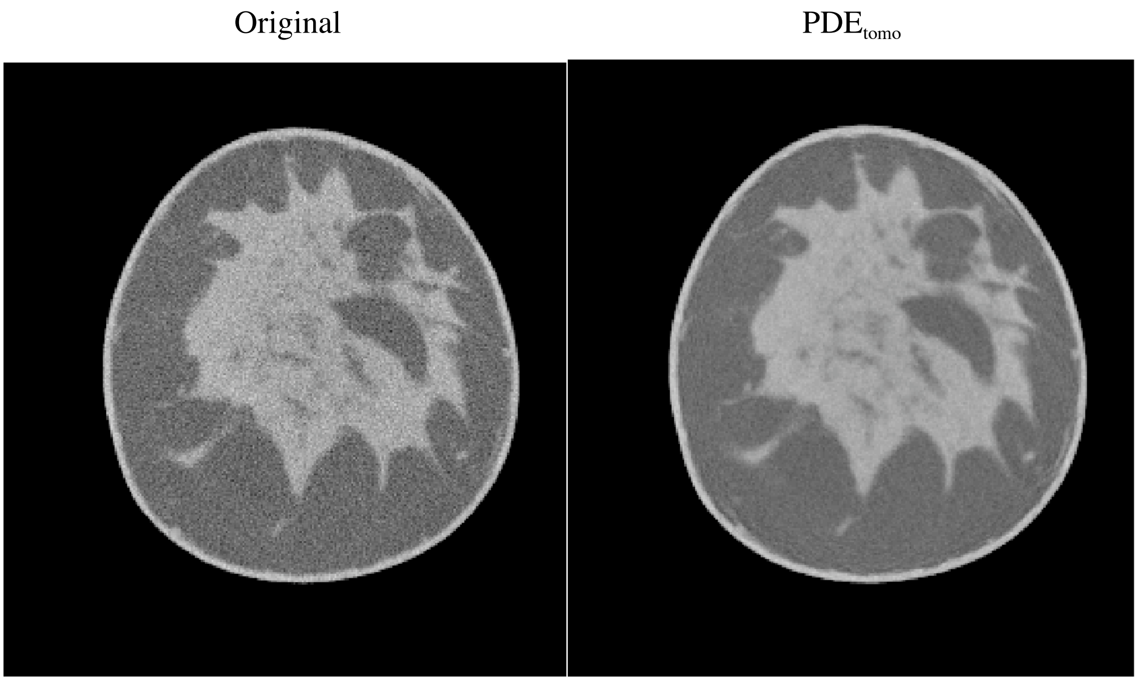

Figure 5.17: Human subject No.2 slice 120.

Similarly, the results of human subject 2 are shown in Figure 5.13 to Figure 5.17. The small region marked in Figure 5.15 is zoomed in and shown in Figure 5.16. By visual comparison, $\mathrm{PDE}_{\mathrm{tomo}}$ technique (right column) reduces the noise considerably while maintaining the resolution of the original reconstruction (left column).

5.4 Discussion

A partial diffusion equation (PDE) based denoising technique was specifically developed for processing breast tomography data. This $\mathrm{PDE}_{\mathrm{tomo}}$ technique takes into account the noise distribution characteristic in the projection image after converting to the line integrals via the nonlinear logarithm operation. From the contrast detail phantom study in the previous chapter, $\mathrm{PDE}_{\mathrm{tomo}}$ is able to generate good reconstructed images with reduced noise and maintained details. That previous study focuses on the comparison between the steps where a denoising technique can be applied along the breast CT reconstruction process. This study continues on the investigation of $\mathrm{PDE}_{\mathrm{tomo}}$ as a good candidate for breast CT denoising. Specifically, it is compared with two other spatially adaptive techniques imaging: Wiener and ATM filters.

Both the quantitative results in the simulation study and the visual inspection in human subject data study showed the promise of this new $\mathrm{PDE}_{\mathrm{tomo}}$ technique. In the simulation study, it was compared with the Wiener technique, an adaptive technique that is accepted as a competitive denoising tool. The results show that the new denoising technique can achieve lower noise level in the reconstructed volume with higher resolution than Wiener technique. The low contrast lesion put in the center of the simulated breast can be better detected on the $\mathrm{PDE}_{\mathrm{tomo}}$ processed datasets than on the Wiener processed datasets, as is shown in Figure 5.1. Not only is the noise in the reconstructed slices filtered by PDEtomo lower than those by Wiener filtering, but the noise levels all over the breast region tend to be more uniform as well. This is shown in Figure 5.3. The advantage of PDEtomo over Wiener filtering in terms of decreased noise level and improved noise uniformity are both more evident for lower dose cases, which indicates that the $\mathrm{PDE}_{\mathrm{tomo}}$ technique holds promise for processing datasets acquired at lower dose levels. $\mathrm{PDE}_{\mathrm{tomo}}$ processed results have lower and more uniform local noise levels than Wiener results. The difference is more manifest at lower fluence level.

Even though the theoretical description of the noise variance in the projection image due to the quantum noise and the logarithm operation is more approximate for the empirical data, the $\mathrm{PDE}_{\mathrm{tomo}}$ technique still provides good denoised images.

There are some limitations in this study. Firstly, the simulated breast CT data are based on a monochromatic x-ray beam with the kV value set to be approximately the same as the mean kV value of the x-ray beam used to acquire the empirical data. Secondly, the parameters in the measurement model used for adding noise to the simulated projection images are all hypothetical, given that presently their empirical values are unknown. Hence, the task of calibrating the dose in the simulation study cannot be fulfilled at this stage. In future work, considerable optimization remains to be performed to calibrate the $\mathrm{PDE}_{\mathrm{tomo}}$ technique using empirical images taken with physical phantoms as well as human subjects. Given the robust trends shown in this study, however, the $\mathrm{PDE}_{\mathrm{tomo}}$ technique should continue to match or outperform the Wiener and ATM techniques, especially if dose is further lowered such as to achieve a breast CT scan with equal or less dose than a single conventional mammogram.

Due to the very low photon fluence on each projection view in dedicated breast CT, the electronic noise is one of the major sources of the overall noise, especially in dense breast regions or if the dose is further reduced. The present version of the $\mathrm{PDE}_{\mathrm{tomo}}$ technique does not consider the effects of additive electronic noise. It will be worthwhile to explore the possibility of taking the characteristics of this type of noise into account in the denoising technique or to combine it with a statistical-modeling approach that explicitly treats the electronic noise.

In conclusion, a Partial Diffusion Equation based denoising technique was developed specifically for dedicated breast CT data. By incorporating into the algorithm the knowledge of the non-uniform distribution of the noise in the projection image after the preprocessing step, it provides excellent denoised data with sharp edges. The technique shows the most promise on datasets acquired with lower dose.

6 Breast Mass Detectibility Study

In Chapters 3 to 5, various image-processing techniques for scatter removal and noise removal were introduced. In particular, chapters 4 and 5 relied upon uniform, simulated backgrounds to facilitate algorithm evaluation. Since medical images are acquired to aid doctors for abnormality diagnosis, it will be very useful to analyze how the previously described image processing tools affect the lesion detectibility. Particularly, we are interested in breast mass detectibility in actual human subject data from dedicated breast CT imaging. This chapter gives preliminary results on the topic. In the study, numerical observers and ROC analysis are used.

6.1 Materials and Methods

6.1.1 Datasets and Mass Simulation

At this time, very few groups are conducting clinical trials with dedicated breast CT. We were very fortunate to have secured from Boone *et al* at University of California Davis 20 human subject datasets to be used for the breast mass detectibility study. As these are prospectively collected cases, the ground truth of these 20 volumes is unknown. In present study, we will assume that there is no lesion in the volumes. And all the lesions of interest will be simulated.

The procedure of simulating a mass is as follows:

1. For a given human subject dataset, the reconstructed volume is used as the reference. The location of 10 masses that will be embedded into the volume is randomly chosen.
2. Spherical masses with fixed size and contrast are put at the locations selected in step 1, and projected onto a virtual 100% DQE detector using a virtual

monochromatic cone-beam projector, which has the same system geometry, projection angles and reconstruction parameters as the individual human subject dataset. These projection images of masses will be added to the original projection images of human subjects to get the synthetic projection sets.

3. The synthetic projection sets either go through the denoising technique followed by FBP reconstruction or directly go for FBP reconstruction.
4. The three-dimensional region of interest (ROIs) can then be retrieved from the reconstructed volumes. In the present study, instead of using 3D ROIs, only the x-y plane section containing the mass (i.e., 2D ROIs) is retrieved for numerical observer study.

Using the 80 ROIs containing contrast detail mass phantoms in simulated, uniform backgrounds, a PDE denoising technique was optimized. This technique was then applied to the human subject ROI dataset, which is comprised of a total of 400 ROIs, 200 with and 200 without simulated masses.

6.1.2 Numerical Observers

6.1.2.1 Ideal Observer for SKE/BKE

The task of an observer is to detect these masses from background tissues. It can also be formulated as the following hypothesis testing:

$$\begin{aligned} H_0 &: x = n \\ H_1 &: x = n + s \end{aligned} \quad . \tag{6.1}$$

The null hypothesis represents the mass absent case, whereas the alternative hypothesis represents the mass present case. If treated as signal known exactly (SKE) case, according to signal detection theory [127], the optimal detector is a likelihood ratio detector. Assuming the background noise n follows a Gaussian distribution with a covariance matrix of Σ, the log likelihood ratio has the following form:

$$\ln(\lambda(x)) = s^T \Sigma^{-1} x . \tag{6.2}$$

If the background noise follows independent and identical distributed (i.i.d.) Gaussian, i.e., the covariance matrix Σ is an identity matrix, then Equation (6.2) can be further simplified to:

$$\ln(\lambda(x)) = s^T x / \sigma^2 . \tag{6.3}$$

Usually real breast tissue background does not satisfy the i.i.d. condition, so the ideal observer shown in Equation (6.3) will perform sub-optimally on the real breast tissue background case.

6.1.2.2 Laguerre-Gauss Channelized Hotelling Observer (LG-CHO)

When the covariance matrix Σ is not an identity matrix, the likelihood ratio observer shown in Equation (6.2) is equivalent to a Hotelling observer [128]. The estimation of the covariance matrix Σ requires a large number of training cases, which is presently not available in breast CT. Alternatively, Laguerre-Gauss channelized hotelling observer (LG-CHO) [128, 129] can be used for this purpose.

The nth order Laguerre function has the following form:

$$L_n(x) = \sum_{m=0}^{n} (-1)^m \binom{n}{m} \frac{x^m}{m!} . \tag{6.4}$$

The LG-CHO has nth order template with the form of:

$$LG_n(r) = \exp(-\frac{\pi r^2}{a^2}) \cdot L_m(\frac{2\pi r^2}{a^2}), \tag{6.5}$$

where a is a free parameter proportional to the standard deviation of the Gaussian kernel through

$$a = \sqrt{2\pi}\sigma. \tag{6.6}$$

6.1.2.3 CNR Observer

Finally, the contrast to noise ratio for each ROI is calculated and used as the decision variable. Given the uncertainties associated with any model observer study, it is desirable to be able to compare all results against such a simple, well-understood technique.

6.1.3 ROC Analysis

The receiver operating characteristic (ROC) analysis is a comprehensive tool for performance measure of the numerical observers. The horizontal axis represents False Positive Fraction (FPF), which equals to (1- specificity), and the vertical axis represents True Positive Fraction (TPF), which equals to sensitivity. They both range from 0 to 1. A ROC curve can be summarized by its area under the curve (AUC). The larger AUC value, the better the performance is, while AUC of 0.5 corresponds to random guessing. The area can also be calculated via semi-parametric fitting resulting in an area index denoted as Az [130].

6.2 Results

6.2.1 Sample ROIs

Figure 6.1 to Figure 6.6 give sample ROIs with real anatomical background structure on reconstructed breast CT slices. The first pair of images is for 5 mm and 10% simulated masses. The second pair is for 5 mm and 3% simulated masses. The third pair is for 4 mm and 2% simulated masses. On each of these figures, (a) and (b) are the original ROIs without and with a simulated mass at the center; whereas (c) and (d) are the ROIs from a PDE denoised volume without and with a simulated mass.

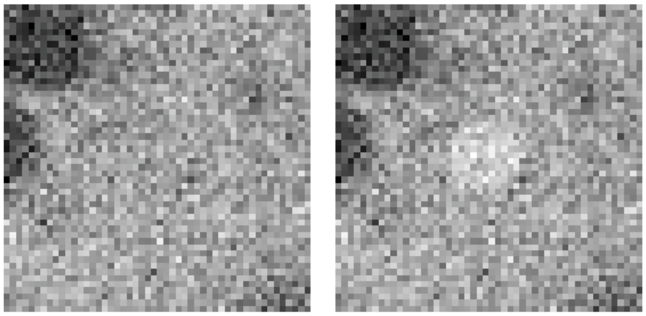

(a) Orig; nomass (b) Orig; mass

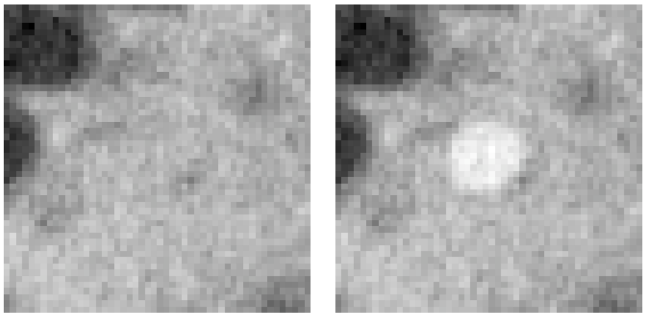

(c) PDE; nomass (d) PDE; mass

Figure 6.1: Sample ROIs No.1 for simulated lesion of 5 mm and 10%: Original ROIs (a) without mass and (b) with a mass, and, PDE denoised ROIs (c) without mass and (d) with a mass.

(a) Orig; nomass (b) Orig; mass

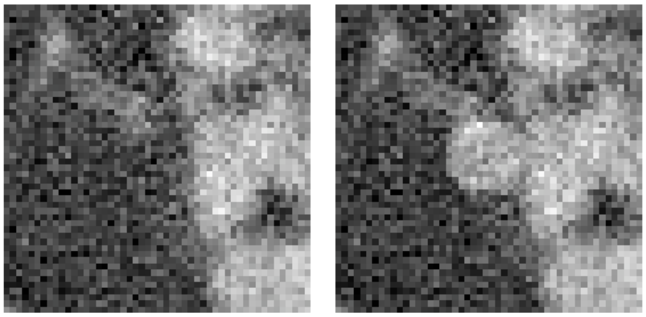

(c) PDE; nomass (d) PDE; mass

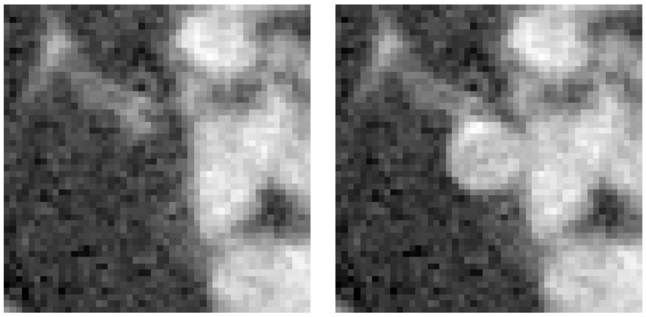

Figure 6.2: Sample ROIs No.2 for simulated lesion of 5 mm and 10%: Original ROIs (a) without mass and (b) with a mass, and, PDE denoised ROIs (c) without mass and (d) with a mass.

(a) Orig; nomass (b) Orig; mass

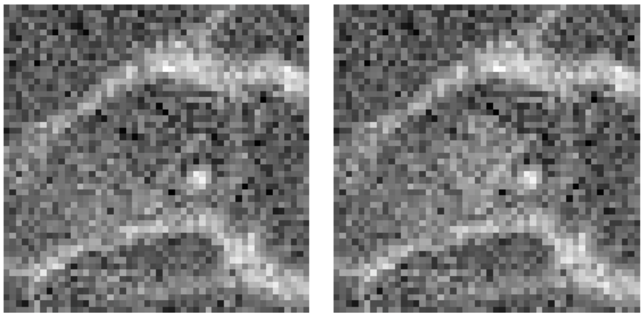

(c) PDE; nomass (d) PDE; mass

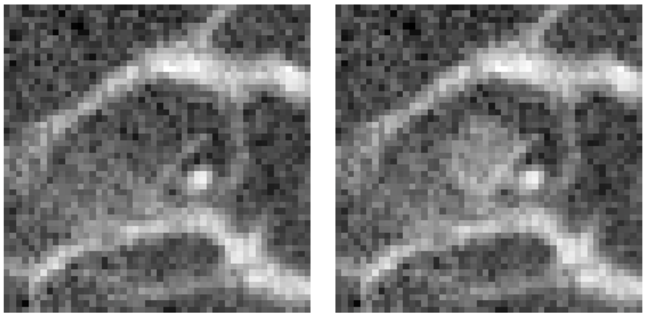

Figure 6.3: Sample ROIs No.1 for simulated lesion of 5 mm and 3%: Original ROIs (a) without mass and (b) with a mass, and, PDE denoised ROIs (c) without mass and (d) with a mass.

(a) Orig; nomass (b) Orig; mass

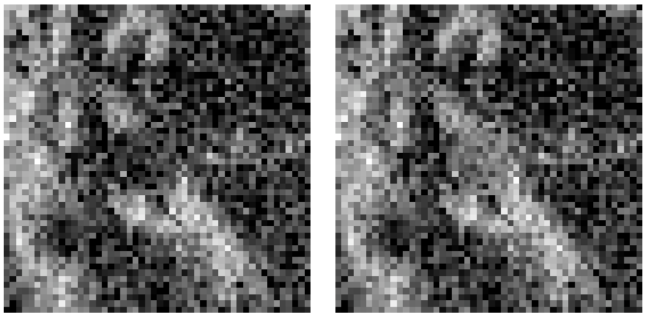

(c) PDE; nomass (d) PDE; mass

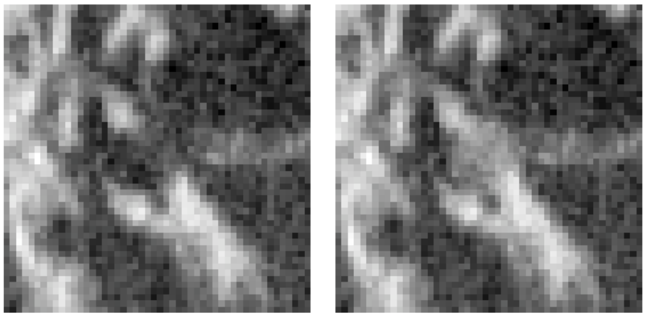

Figure 6.4: Sample ROIs No.2 for simulated lesion of 5 mm and 3%: Original ROIs (a) without mass and (b) with a mass, and, PDE denoised ROIs (c) without mass and (d) with a mass.

(a) Orig; nomass (b) Orig; mass

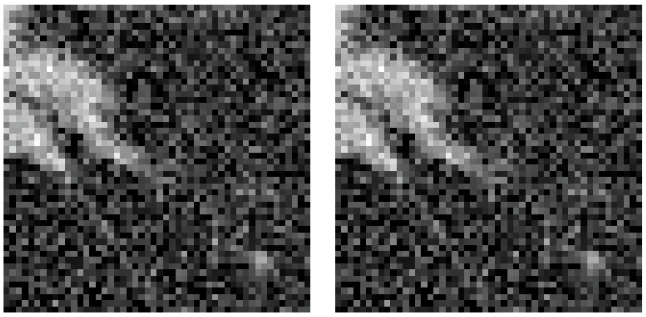

(c) PDE; nomass (d) PDE; mass

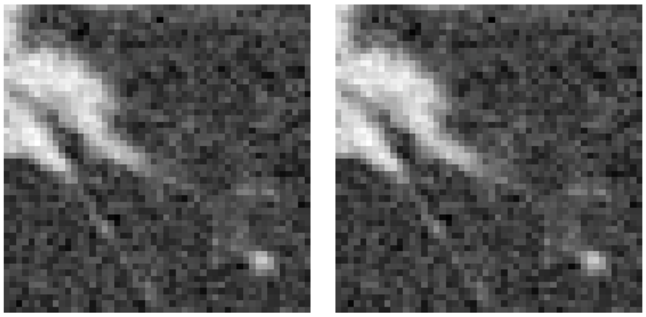

Figure 6.5: Sample ROIs No.1 for simulated lesion of 4 mm and 2%: Original ROIs (a) without mass and (b) with a mass, and, PDE denoised ROIs (c) without mass and (d) with a mass.

(a) Orig; nomass (b) Orig; mass

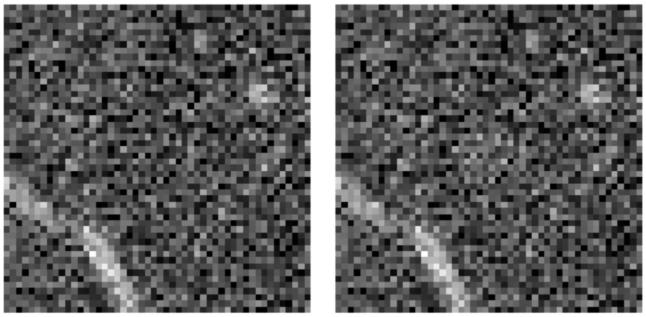

(c) PDE; nomass (d) PDE; mass

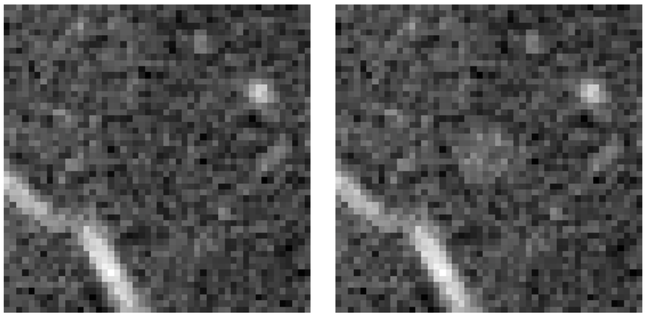

Figure 6.6: Sample ROIs No.2 for simulated lesion of 4 mm and 2%: Original ROIs (a) without mass and (b) with a mass, and, PDE denoised ROIs (c) without mass and (d) with a mass.

6.2.2 Contrast Detail Phantom Results

CNR observer and LG-CHO observer results are shown in Figure 6.7 and Figure 6.8 respectively for the contrast detail phantom embedded in a uniform background.

In Figure 6.7 (a), the histograms of CNR for original and PDE processed ROIs with and without simulated masses are plotted. It is obvious that PDE processed ROIs with simulated masses have higher CNR values than original ROIs with masses. The Az values were obtained using the software package ROCKIT (Charles Metz, University of Chicago). For original dataset, the Az is 0.933 ± 0.020; and for PDE processed dataset, the Az is 0.998 ± 0.005. The corresponding two-tailed p-value is 0.0009, indicating that Az of PDE processed dataset is statistically higher than Az of the original dataset. The ROC curves are shown in Figure 6.7 (b).

Figure 6.8 (a) plots the AUC values with 1st order LG template with varying *a* value, which is equivalent to a Difference of Gaussian (DoG) filter [131]. It is shown that when *a* value is greater than 14 AUC values are close to 1. LG template is then fixed at a=18 with various orders, whose AUC values are shown in Figure 6.8 (b). The 1st order LG template gives the highest AUC value.

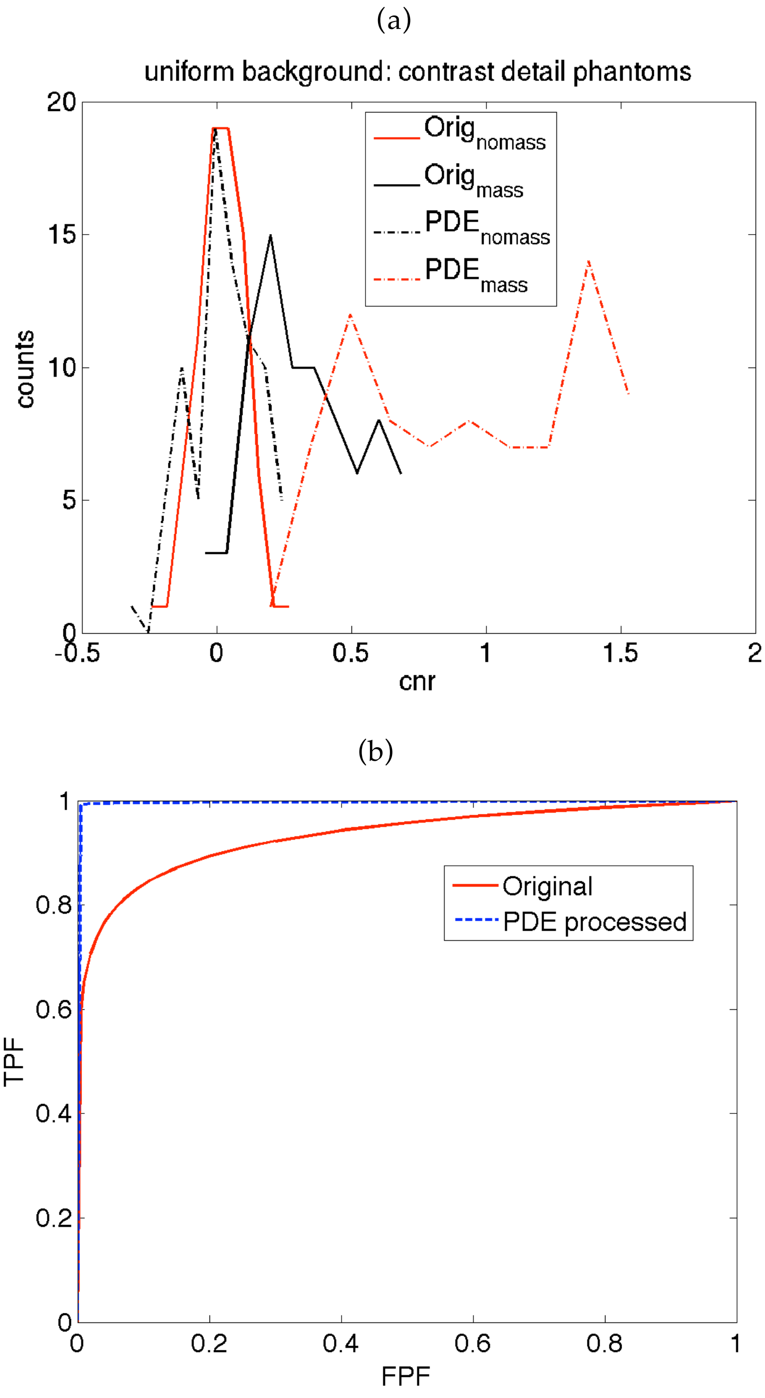

Figure 6.7: CNR observer results for contrast detail phantoms embedded in a simulated uniform background. CNR histograms for original and PDE processed ROI databases are shown in (a) and the corresponding ROC curves are shown in (b). The Az value of the PDE processed dataset (0.998 ± 0.005) is statistically higher than the Az value of the original dataset (0.933 ± 0.020). The p value is less than 0.01.

(a)

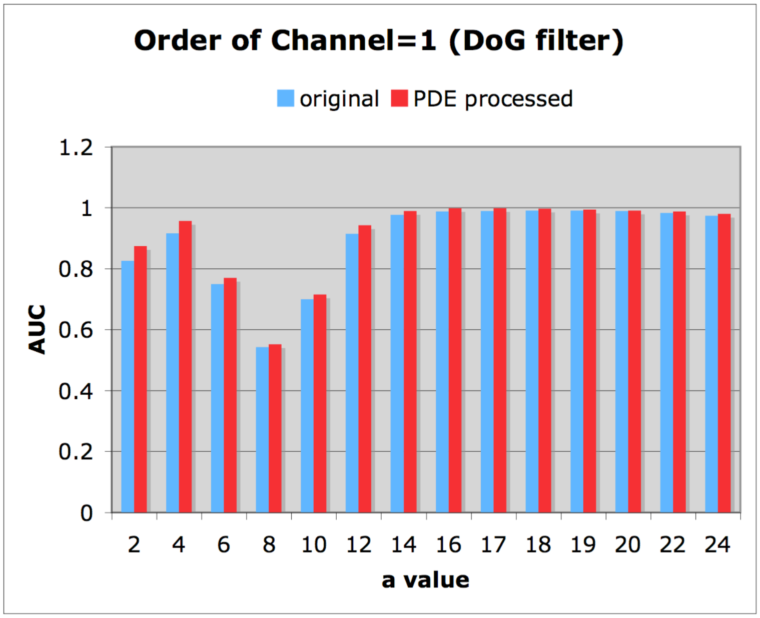

(b)

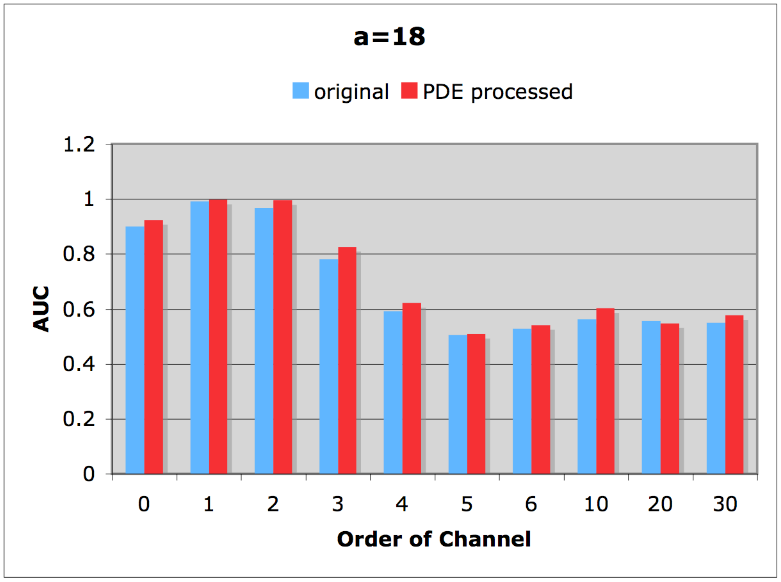

Figure 6.8: LG-CHO observer results for contrast detail phantoms embedded in a simulated uniform background.

6.2.3 Human Subject Background Results

The human subject background ROC analysis based on CNR observer is shown in Figure 6.9 for simulated mass of 4 mm and 2%. The histograms of CNR for original and PDE processed datasets with and without simulated masses are shown in Figure 6.9 (a). The corresponding ROC curves are plotted in Figure 6.9 (b). The Az value of the PDE processed dataset (0.770 ± 0.023) is higher than the Az value of the original dataset (0.801 ± 0.022). The p value is less than 0.009, indicating that the difference is statistically significant. AUC values of the three types of numerical observers using real anatomical background from breast CT are shown in Table 6.1 for lesions of 5 mm and 10%, 5 mm and 3%, and 4 mm and 2%, respectively. For all the cases, the CNR observer gives the highest AUC values, followed by 1st order LG template, and the ideal observer gives the lowest AUC values. For masses with 4 mm diameter and 2% contrast, the ROC performance of ideal observer reduces to the chance curve.

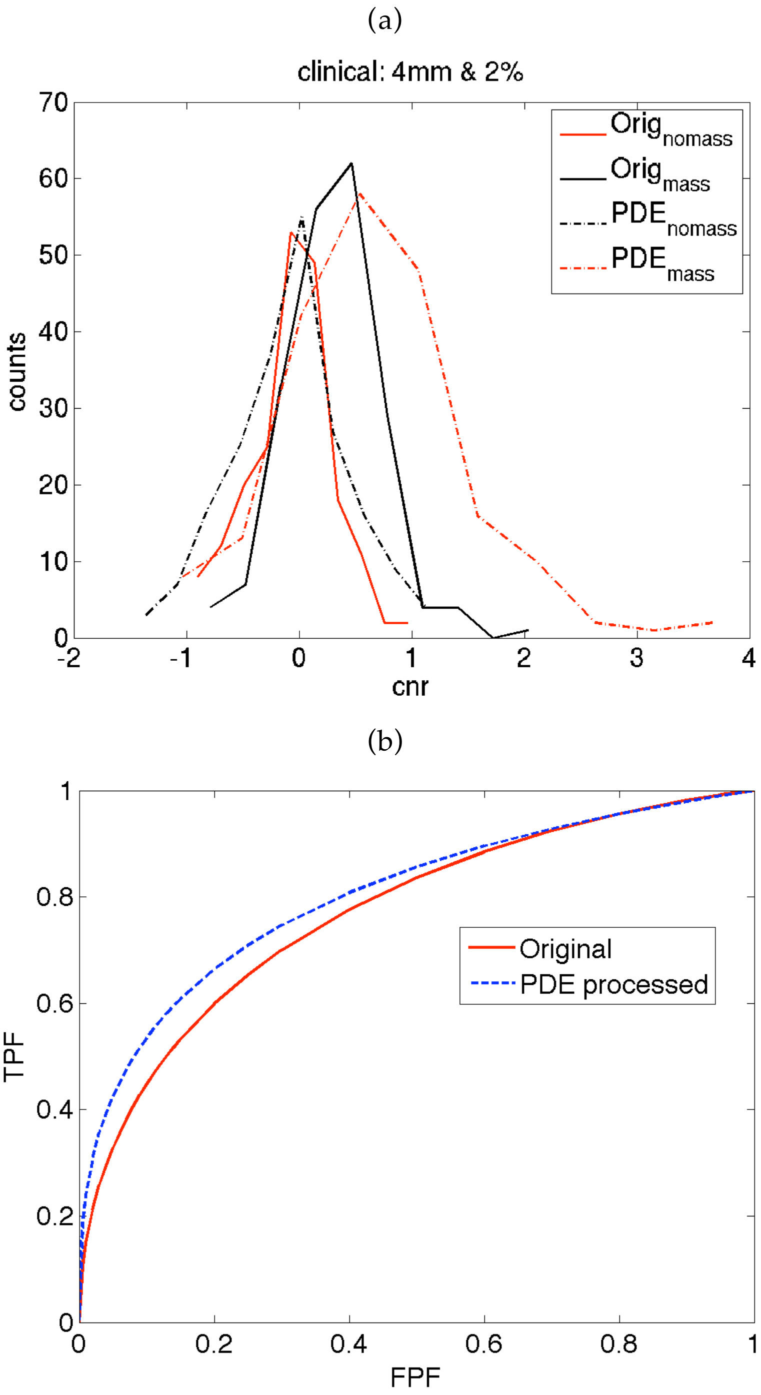

Figure 6.9: CNR observer results for simulated lesions of 4mm and 2% embedded in real anatomical backgrounds. CNR histograms for original and PDE processed ROI databases are shown in (a) and the corresponding ROC curves are shown in (b). The Az value of the PDE processed dataset (0.770 ± 0.023) is statistically higher than the Az value of the original dataset (0.801 ± 0.022). The p value is less than 0.01.

Table 6.1: AUC values for the three types of numerical observers using real anatomical background from breast CT.

Lesion	CNR observer		LG-CHO observer (a=22 & n=1)		Ideal observer	
	Original	PDE processed	Original	PDE processed	Original	PDE processed
5mm & 10%	0.999	0.997	0.999	0.999	0.896	0.904
5mm & 3%	0.877	0.883	0.850	0.853	0.690	0.700
4mm & 2%	0.770	0.801	0.703	0.702	0.446	0.443

6.3 Discussion

Some studies [132-136] have shown that numerical observers can be good candidates for lesion detection tasks without the tremendously time consuming and tedious process of human observer studies. In this study, a SKE ideal observer, n^{th} order LG-CHO templates, and CNR observers are used for detecting the simulated masses in the anatomical background. As expected, SKE ideal observer worked sub-optimally whereas LG-CHO worked much better than SKE case. The CNR observer as a simple one works the best.

For the contrast detail phantoms in a simulated uniform breast background, the initial AUC based on CNR observer is 0.933 ± 0.020. After PDE denoising, the AUC improves to 0.998 ± 0.005, which is close to the perfect performance. The improvement is statistically significant with two-tailed $p<0.001$.

For the ROIs with real anatomical backgrounds, the ROC curves vary with respect to the mass size and contrast. For masses with 5 mm and 10%, it is very easy to detect them, whereas for masses with 4 mm and 2%, the detection task is extremely challenging. Even in such conditions, PDE denoising always provided statistically significant improvements in performance, as well as higher CNR values and better visual appearance.

There are some limitations in this study. First, the simulated masses are perfect spheres, which are rare in the real situation. A more realistic mass simulation may render more advantages toward evaluating nonlinear image processing techniques such as $\mathrm{PDE}_{\mathrm{tomo}}$. Second, the ROIs are two dimensional due to the limited number of human subject datasets available. In the future, when more human subject datasets are collected, three-dimensional ROIs can be used instead. Third, in this study, individual LG-CHO channels are used for ROC analysis. An ensemble LG-CHO is often used with the form:

$$w = \sum_{m=0}^{n} \alpha_m LG_m(r), \qquad (6.7)$$

where the parameters (α_1, α_2, α_3,….) are determined by Hotelling Observer.

A common problem shared by all the observers is the tendency to perform too well due to the fixed, single type of lesion. Even for the subtlest lesions that were virtually impossible to see by the human eye, the observers routinely performed quite well with ROC areas approaching 0.8. As such, such model observer performances should not be construed as what would be typical of clinical performance by radiologists. Instead, these studies offer valuable insight in terms of comparing one technique against another in a fair (or equally unfair) fashion. The best techniques from such a study may then be validated in human observer studies in the future.

In summary, several numerical observers are used to analyze the mass detectibility in breast CT using simulated uniform background and real anatomical background. With simulated uniform background and contrast detail phantoms, the PDE denoised datasets give the better results than the original datasets using CNR observer. The performances are similar when LG-CHO templates are used. With real anatomical background with fixed size lesion, PDE denoised images have higher detectability, higher CNR and better qualitative appearance.

7 Conclusion and Future Work

7.1 Summary

This dissertation described some image processing techniques in dedicated breast CT imaging. Specifically, it explored the techniques for scatter removal and noise removal. The noise removal technique is then evaluated further by the simulated mass detectibility study utilizing mathematical observers.

The first chapter introduced the background of this dissertation: breast cancer and the motivation of developing dedicated breast CT imaging modality.

The second chapter first introduced the feasibility of dedicated breast CT imaging for mass and micro-calcification detections. It then gave some technical description of the prototype dedicated breast CT system fabricated in University California Davis, which is the source of the data presented in this dissertation. Finally, the custom-written FBP reconstruction algorithm for the cone-beam geometry was described.

Chapter 3 focused on the first aspect of image processing in breast CT: scatter removal. The model based mathematical scatter compensation scheme was followed. A new Gaussian noise model was proposed. The corresponding MLE and MAP estimates of scatter-free image were derived and some preliminary results on the FFDM system was obtained. It was compared with the previously developed Poisson noise model and the connection was extracted. In model x-ray breast imaging techniques, such as FFDM, breast tomosynthesis and breast CT, flat-panel detectors are the detectors of the choice due to its many attractive characteristics. The Gaussian noise model successfully grasped the energy integrating property of a flat-panel detector.

In Chapter 4 and 5, the second aspect of image processing in breast CT was explored: noise removal. When a denoising technique is used for dedicated breast CT, there are four possible steps in the reconstruction process where it can be incorporated. Chapter 4 focused on the evaluation and comparison between these steps to find the best location for application of denoising techniques. Three variants of partial diffusion equation based denoising techniques were developed for three different steps, optimized individually and compared against each other based on a simulated breast with contrast detail phantoms. It was found that denoising before reconstruction provided better sensitivity of mass detection as well as better visual appearance of the processed volumes. Especially, the PDE_{tomo} technique applied at step 2 after pre-processing but before reconstruction gave the best results among all.

In Chapter 5, further evaluation of the PDE_{tomo} technique described in Chapter 4 was investigated. It took account of the knowledge of the non-uniform distribution of the noise in the projection image after the preprocessing step. Both Wiener filter and a two-dimensional adaptive trimmed mean (ATM) filter were developed and applied to step2. All these techniques are spatially adaptive techniques for noise removal. Yet, Wiener filter is a linear technique, whereas ATM and PDE_{tomo} are nonlinear techniques. They were compared to each other based on a simulated, uniform breast with a single low-contrast lesion, contrast detail phantoms, or a single high-contrast object. The PDE_{tomo} technique was an overall winner of all cases. Its advantage was even more obvious when the dose level is lowered, which may have substantial clinical implications for future tomosynthesis or tomography applications. The PDE_{tomo} technique was then applied to the human subject breast CT data. Qualitatively, it provided pleasant denoised volumes with much lowered noise and maintained details.

Chapter 6 focused on the simulated mass detectibility study using the clinical data as the background and mathematical observers. To the best of our knowledge, this was the first ever such study conducted on human subject breast CT data. The PDE denoised datasets improved mass detectibility performance statistically significantly over a wide range of lesion sizes and contrasts, and also improved CNR and visual appearance of the reconstructed volumes.

7.2 Future Direction

There are several future directions to extend the study in this dissertation.

The Gaussian noise model is presently only evaluated on the projection images from FFDM system. It will be of natural interest to apply it to the dedicated breast CT datasets. In order to do so, the physical measurement on the system of the scatter kernel parameters is a critical first step. The technique can then be evaluated first on some physical phantoms, such as PMMA phantoms. And it can then be evaluated on the human subject datasets where the true scatter radiation measurement is often not well characterized due to the dose constraints.

The preliminary results of $\mathrm{PDE}_{\mathrm{tomo}}$ technique on human subject datasets already showed its promise for the application. Yet, the technique is optimized based on the simulation study. As pointed out at the end of Chapter 5, the connection between simulation and clinical studies is unknown. Therefore, the parameter choice for $\mathrm{PDE}_{\mathrm{tomo}}$ used in clinical situation might be sub-optimal. Only when this connection is truly established, can we optimize the technique for the clinical application.

At the end of Chapter 5, some further development of $\mathrm{PDE}_{\mathrm{tomo}}$ technique was briefly described. For example, the technique can be extended to explicitly consider the electronic noise. In addition, it can be extended to a tensor-based 3D denoising technique applied to the data after pre-processing but before reconstruction by including the neighboring projection information.

Finally, more work can be done for the simulated mass study in Chapter 6. Rather than a perfect sphere, more realistic 3D masses can be simulated. Moreover, noises can be added to the breast CT datasets to simulate various reduced dose levels. As suggested by the results with low dose data in Chapter 5, with lower dose levels, it will be more advantageous to use $\mathrm{PDE}_{\mathrm{tomo}}$ for noise removal.

In conclusion, this dissertation has demonstrated promising progress towards several state of the art algorithms to compensate for scatter and noise in tomographic imaging. Several new image processing techniques were proposed based on the unique physical properties of this modality. An exhaustive series of phantom simulation studies were conducted to validate the proposed techniques, which were then applied for the first time to human subject data. These are the first steps towards the eventual goal of optimizing image quality and thus diagnostic utility for the novel modality of dedicated breast CT imaging.

Appendix Derivation of MLE Algorithm Based on Gaussian Noise Model

Due to the convolution operation, the estimation of $B = \{b_i; i=1\ldots N\}$ directly from Y does not have a simple analytic form. The MLE of B is thus derived through the EM algorithm as follows.

Treat the measured $Y = \{y_i, i=1,\ldots,N\}$ as an incomplete dataset, and unobserved $(D,S) = \{(d_i,s_i), i=1,\ldots,N\}$ as a complete dataset. The d_i 's and s_i 's given B are mutually independent, therefore the complete data likelihood is

$$p_c(D,S \mid B,\{\sigma_{i1}{}^2,\sigma_{i2}{}^2;i=1,\ldots,N\}) = \prod_{j=1}^{N}[\frac{1}{\sqrt{2\pi\sigma_{j1}{}^2}}e^{-(d_j-b_j)^2/2\sigma_{j1}{}^2}\cdot\frac{1}{\sqrt{2\pi\sigma_{j2}{}^2}}e^{-(s_j-(b^{**}p)_j)^2/2\sigma_{j2}{}^2}]. \qquad \textbf{(A1)}$$

Assuming $\{\sigma_{i1}{}^2, \sigma_{i2}{}^2 ; i=1,\ldots,N\}$ are known, we can obtain the complete data log likelihood by taking the logarithm on both sides,

$$L_c(B \mid D,S) = \sum_{j=1}^{N}[-(d_j-b_j)^2/2\sigma_{j1}{}^2-(s_j-(b**p)_j)^2/2\sigma_{j2}{}^2-\log\sqrt{2\pi\sigma_{j1}{}^2}-\log\sqrt{2\pi\sigma_{j2}{}^2}]. \qquad \textbf{(A2)}$$

The EM algorithm is comprised of two steps: one, the E-step, where the expectation of the complete data log likelihood with respect to the present estimate of B is computed, and two, the M-step, where a new estimate of B is obtained which will maximize the computed expectation in the E-step.

First, employ the E-step:

$$\begin{aligned}&Q(B \mid B^{(n)})\\&= E[L_c(B \mid D,S) \mid Y,B^{(n)}]\\&= \sum_{j=1}^{N}\{-(b_j{}^2-2d_j{}^{(n)}b_j)/2\sigma_{j1}{}^2-[((B**P)_j)^2-2s_j{}^{(n)}(B**P)_j]/2\sigma_{j2}{}^2\\&+ terms\cdot independent\cdot of\cdot B\},\end{aligned} \qquad \textbf{(A3)}$$

where
$$\begin{aligned}d_j{}^{(n)} &= E[d_j \mid Y,B^{(n)}]\\ s_j{}^{(n)} &= E[s_j \mid Y,B^{(n)}]\end{aligned}. \qquad \textbf{(A4)}$$

Second, the M-step to find $B^{(n+1)}$ that will maximize $Q(B \mid B^{(n)})$:

$$\frac{\partial Q(B \mid B^{(n)})}{\partial b_k} = 0 = -(2b_k - 2d_k^{(n)})/2\sigma_{k1}^2 - \sum_{j=1}^{N}[2(B**P)_j p_{jk} - 2s_j^{(n)} p_{jk}]/2\sigma_{j2}^2 \cdot \tag{A5}$$

Solving the above equation for b_k gives

$$b_k^{(n+1)} = d_k^{(n)} - \sigma_{k1}^2 \sum_{j=1}^{N} p_{jk} \cdot [(B^{(n+1)}**P)_j - s_j^{(n)}]/\sigma_{j2}^2. \tag{A6}$$

Using $B^{(n)}$ to approximate $B^{(n+1)}$ in the right-hand side yields

$$b_k^{(n+1)} = d_k^{(n)} - \sigma_{k1}^2 \sum_{j=1}^{N} p_{jk} \cdot [(B^{(n)}**P)_j - s_j^{(n)}]/\sigma_{j2}^2. \tag{A7}$$

As a good estimate of the primary image is formed, $(B^{(n)}**P)_j - s_j^{(n)} \approx 0$, then,

$$b_k^{(n+1)} \cong d_k^{(n)}. \tag{A8}$$

The same apparent form was obtained for Poisson noise model in the Reference [137]. But due to the different statistical models, the actual forms of $d_k^{(n)}$ are different and so is the iterative formula for b_k.

Equation (A7) combines with equation (A4) to give the following updated equation:

$$b_k^{(n+1)} = b_k^{(n)} + w_k \cdot [y_k - (b_k^{(n)} + (B^{(n)}**P)_k)], \tag{A9}$$

where

$$w_k = \sigma_{k1}^2/(\sigma_{k1}^2 + \sigma_{k2}^2). \tag{A10}$$

Bibliography

[1] "Breast cancer," Encyclopedia Britannica (2004).

[2] ACS, "American cancer society: Cancer facts and figures 2007," Atlanta, Ga: American Cancer Society (2007).

[3] I. Reiser, R.M. Nishikawa, M.L. Giger, *et al.*, "Computerized detection of mass lesions in digital breast tomosynthesis images using two- and three dimensional radial gradient index segmentation," Technology in Cancer Research & Treatment 3, 437-441 (2004).

[4] C.E. Floyd, Jr, J.Y. Lo and G.D. Tourassi, "Cased-based reasoning computer algorithm that uses mammographic findings for breast biopsy decisions," AJR. American Journal of Roentgenology 175, 1347-1352 (2000).

[5] H.P. Chan, J. Wei, B. Sahiner, *et al.*, "Computer-aided detection system for breast masses on digital tomosynthesis mammograms: Preliminary experience," Radiology 238, 1075-1080 (2006).

[6] V.L. Ernster, J. Barclay, K. Kerlikowske, *et al.*, "Mortality among women with ductal carcinoma in situ of the breast in the population-based surveillance, epidemiology and end results program," Archives of Internal Medicine 160, 953-958 (2000).

[7] G. Dave, H. Cosmatos, T. Do, *et al.*, "Metaplastic carcinoma of the breast: A retrospective review," International Journal of Radiation Oncology Biology Physics 64, 771-775 (2006).

[8] S. Sahoo, W.M. Recant, N. Jacskowiak, *et al.*, "Defining negative margins in dcis patients treated with breast conservation therapy: The university of chicago experience," Breast Journal 11, 242-247 (2005).

[9] S.A. Joslyn, "Ductal carcinoma in situ: Trends in geographic, temporal, and demographic patterns of care and survival," Breast Journal 12, 20-27 (2006).

[10] S.W. Fletcher and J.G. Elmore, "Mammographic screening for breast cancer," New England Journal of Medicine 348, 1672-1680 (2003).

[11] L. Nystrom, I. Andersson, N. Bjurstam, *et al.*, "Long-term effects of mammography screening: Updated overview of the swedish randomised trials," Lancet 359, 909-919 (2002).

[12] K. Kerlikowske, P.A. Carney, B. Geller, *et al.*, "Performance of screening mammography among women with and without a first-degree relative with breast cancer," Annals of Internal Medicine 133, 855-863 (2000).

[13] T.M. Kolb, J. Lichy and J.H. Newhouse, "Comparison of the performance of screening mammography, physical examination, and breast us and evaluation of factors that influence them: An analysis of 27,825 patient evaluations," Radiology 225, 165-175 (2002).

[14] V.P. Jackson, R.E. Hendrick, S.A. Feig, *et al.*, "Imaging of the radiographically dense breast," Radiology 188, 297-301 (1993).

[15] E. Cole, E.D. Pisano, M. Brown, *et al.*, "Diagnostic accuracy of fischer senoscan digital mammography versus screen-film mammography in a diagnostic mammography population," Academic Radiology 11, 879-886 (2004).

[16] J.M. Lewin, C.J. D'Orsi, R.E. Hendrick, *et al.*, "Clinical comparison of full-field digital mammography and screen-film mammography of breast cancer," American Journal of Roentgenology 179, (2002).

[17] P. Skaane and A. Skjennald, "Screen-film mammography versus full-field digital mammography with soft-copy reading: Randomized trial in a population-based screening program - the oslo ii study," Radiology 232, 197-204 (2004).

[18] E.D. Pisano, C. Gatsonis, E. Hendrick, *et al.*, "Diagnostic performance of digital versus film mammography for breast-cancer screening," New England Journal of Medicine 353, 1773-1783 (2005).

[19] P. Skaane, A. Skjennald, K. Young, *et al.*, "Follow-up and final results of the oslo i study comparing screen-film mammography and full-field digital mammography with soft-copy reading," Acta Radiologica 46, 679-689 (2005).

[20] P. Skaane, C. Balleyguier, F. Diekmann, *et al.*, "Breast lesion detection and classification: Comparison of screen-film mammography and full-held digital mammography with soft-copy reading - observer performance study," Radiology 237, 37-44 (2005).

[21] P. Crystal and S. Strano, "Digital and film mammography," New England Journal of Medicine 354, 765-766 (2006).

[22] D.D. Dershaw, "Film or digital mammographic screening?," New England Journal of Medicine 353, 1846-1847 (2005).

[23] R. Schulz-Wendtland, K.P. Hermann and W. Bautz, "Digital mammography. Results of clinical studies," Radiologe 45, 255-263 (2005).

[24] M.R. Lemacks, S.C. Kappadath, C.C. Shaw, *et al.*, "A dual-energy subtraction technique for microcalcification imaging in digital mammography - a signal-to-noise analysis," Medical Physics 29, 1739-1751 (2002).

[25] S.C. Kappadath and C.C. Shaw, "Dual-energy digital mammography for calcification imaging: Scatter and nonuniformity corrections," Medical Physics 32, 3395-3408 (2005).

[26] T. Wu, A. Stewart, M. Stanton, *et al.*, "Tomographic mammography using a limited number of low-dose cone-beam projection images," Medical Physics 30, 365-380 (2003).

[27] J.Y. Kim and J.S. Yoon, *Image distortion compensation by using a polynomial model in an x-ray digital tomosynthesis system*, in *Advances in fracture and strength, pts 1-4*. 2005. p. 2034-2039.

[28] T. Wu, R.H. Moore, E.A. Rafferty, *et al.*, "A comparison of reconstruction algorithms for breast tomosynthesis," Medical Physics 31, 2636-2647 (2004).

[29] J.T. Dobbins and D.J. Godfrey, "Digital x-ray tomosynthesis: Current state of the art and clinical potential," Physics in Medicine and Biology 48, R65-R106 (2003).

[30] Y. Chen, J.Y. Lo and J.T. Dobbins, 3rd, "Impulse response analysis for several digital tomosynthesis mammography reconstruction algorithms," in Proceedings of SPIE Medical Imaging 2005: Image Processing (2005).

[31] L.T. Niklason, B.T. Christian, L.E. Niklason, *et al.*, "Digital tomosynthesis in breast imaging," Radiology 205, 399-406 (1997).

[32] R.L. McKinley, M.P. Tornai, E. Samei, *et al.*, "Initial study of quasi-monochromatic x-ray beam performance for x-ray computed mammotomography," Ieee Transactions on Nuclear Science 52, 1243-1250 (2005).

[33] J.M. Boone, N. Shah and T.R. Nelson, "A comprehensive analysis of dgn(ct) coefficients for pendant-geometry cone-beam breast computed tomography," Medical Physics 31, 226-235 (2004).

[34] J.M. Boone, A.L.C. Kwan, J.A. Seibert, *et al.*, "Technique factors and their relationship to radiation dose in pendant geometry breast ct," Medical Physics 32, 3767-3776 (2005).

[35] A.L.C. Kwan, J.M. Boone and N. Shah, "Evaluation of x-ray scatter properties in a dedicated cone-beam breast ct scanner," Medical Physics 32, 2967-2975 (2005).

[36] B. Chen and R.L. Ning, "Cone-beam volume ct breast imaging: Feasibility study," Medical Physics 29, 755-770 (2002).

[37] R.L. Ning, D. Conover, B. Chen, *et al.*, "Flat panel detector-based cone beam volume ct breast imaging: Phantom and specimen study," Proceedings of SPIE 4682, 218–27 (2002).

[38] R.L. McKinley, M.P. Tornai, E. Samei, *et al.*, "Development of an optimal x-ray beam for dual-mode emission and transmission mammotomography," Nucl Instrum Methods Phys Res A 527, 102-109 (2004).

[39] B.G. Ziedses des Plantes, "Eine neue methode zur differenzierung in der roentgenographie (planigraphie)," Acta Radiologica 13, 182-192 (1932).

[40] D.G. Grant, "Tomosynthesis: A three-dimensional radiographic imaging technique.," IEEE Transactions on Biomedical Engineering 19, 20-28 (1972).

[41] G. Lauritsch and W.H. Harer, "A theoretical framework for filtered backprojection in tomosynthesis," in Proceedings of Proceedings of SPIE, 1127-1137 (1998).

[42] T. Mertelmeier, J. Orman, W. Haerer, *et al.*, "A theoretical framework for filtered back-projection in tomosynthesis," Proceedings of SPIE 6142, 6142F1-12 (2006).

[43] Y. Chen, J.Y. Lo and J.T. Dobbins, "Noise power spectrum analysis for several digital breast tomosynthesis reconstruction algorithms," Proceedings of SPIE 6142, 614259-1:12 (2006).

[44] C.H. Chang, J.L. Sibala, F. Lin, *et al.*, "Preoperative diagnosis of potentially pre-cancerous breast lesions by computed tomography breast scanner - preliminary study," Radiology 129, 209-210 (1978).

[45] R.A. McLeod, J.J. Gisvold, D.H. Stephens, *et al.*, "Computed tomography of soft-tissues and breast," Seminars in Roentgenology 13, 267-275 (1978).

[46] J.J. Gisvold, D.F. Reese and P.R. Karsell, "Computed tomographic mammography (ctm)," American Journal of Roentgenology 133, 1143-1149 (1979).

[47] C.H.J. Chang, J.L. Sibala, S.L. Fritz, *et al.*, "Specific value of computed tomographic breast scanner (ct-m) in diagnosis of breast diseases," Radiology 132, 647-652 (1979).

[48] C.H. Chang, J.L. Sibala, S.L. Fritz, *et al.*, "Computed tomographic evaluation of breast," American Journal of Roentgenology 131, 459-464 (1978).

[49] J.M. Boone, T.R. Nelson, K.K. Lindfors, *et al.*, "Dedicated breast ct: Radiation dose and image quality evaluation," Radiology 221, 657-667 (2001).

[50] A.L.C. Kwan, J.A. Seibert and J.M. Boone, "An improved method for flat-field correction of flat panel x-ray detector," Medical Physics 33, 391-393 (2006).

[51] A.L.C. Kwan, J.M. Boone, K. Yang, *et al.*, "Evaluation of the spatial resolution characteristics of a cone-beam breast ct scanner," Medical Physics 34, 275-281 (2007).

[52] K. Yang, A.L.C. Kwan, D.F. Miller, *et al.*, "A geometric calibration method for cone beam ct systems," Medical Physics 33, 1695-1706 (2006).

[53] K. Yang, A.L.C. Kwan and J.M. Boone, "Computer modeling of the spatial resolution properties of a dedicated breast ct system," Medical Physics 34, 2059-2069 (2007).

[54] X. Gong, A.A. Vedula and S.J. Glick, "Microcalcification detection using cone-beam ct mammography with a flat-panel imager," Physics in Medicine and Biology 49, 2183-2195 (2004).

[55] S.C. Thacker and S.J. Glick, "Normalized glandular dose (dgn) coefficients for flat-panel ct breast imaging," Physics in Medicine and Biology 49, 5433-5444 (2004).

[56] X. Gong, S.J. Glick, B. Liu, *et al.*, "A computer simulation study comparing lesion detection accuracy with digital mammography, breast tomosynthesis, and cone-beam ct breast imaging," Medical Physics 33, 1041-1052 (2006).

[57] R. Ning, "Flat panel detector-based cone beam volume ct imaging," MED PHYS 30, 1370-1370 (2003).

[58] R.L. Ning, X.Y. Tang and D. Conover, "X-ray scatter correction algorithm for cone beam ct imaging," Medical Physics 31, 1195-1202 (2004).

[59] C.J. Lai, C.C. Shaw, M.C. Altunbas, *et al.*, "Effects of radiation dose level on calcification visibility in cone beam breast ct: A preliminary study," Proceedings of SPIE 6142, 614233-1:8 (2006).

[60] L.Y. Chen, C.C. Shaw, C.J. Lai, *et al.*, "Comparison of full-scan and half-scan for cone beam breast ct imaging," Proceedings of SPIE 1642, (2006).

[61] S.J. Tu, C.C. Shaw and L.Y. Chen, "Noise simulation in cone beam ct imaging with parallel computing," Physics In Medicine and Biology 51, 1283-1297 (2006).

[62] M.P. Tornai, J.E. Bowsher and C.N. Archer, "Feasibility of application specific emission & transmission tomography (asett) of the breast," Journal of Nuclear Medicine 43, 39 (2002).

[63] R.L. McKinley, M.P. Tornai, E. Samei, *et al.*, "Simulation study of a quasi-monochromatic beam for x-ray computed mammotomography," Med Phy 31, 800-813 (2004).

[64] D.J. Crotty, R.L. McKinley and M.P. Tornai, "Experimental spectral measurements of heavy k-edge filtered beams for x-ray computed mammotomography," Physics in Medicine and Biology 52, 603-616 (2007).

[65] A. Rose, Vision: Human and electronic (New York: Plenum, 1974).

[66] J.M. Boone, "Performance assessment of a pendant-geometry ct scanner for breast cancer detection," Proceedings of SPIE (2005).

[67] H.K. Tuy, "An inversion-formula for cone-beam reconstruction," Siam Journal on Applied Mathematics 43, 546-552 (1983).

[68] G. Wang, T.H. Lin, P.C. Cheng, *et al.*, A general cone-beam reconstruction algorithm 1993).

[69] S.H. Manglos, G.M. Gagne, A. Krol, *et al.*, "Transmission maximum-likelihood reconstruction with ordered subsets for cone-beam ct," Physics in Medicine and Biology 40, 1225-1241 (1995).

[70] K. Lange and R. Carson, "Em reconstruction algorithms for emission and transmission tomography," J Comput Assist Tomogr 8, 306-316 (1984).

[71] H.M. Hudson and R.S. Larkin, "Accelerated image reconstruction using ordered subsets of projection data," IEEE Transactions on Medical Imaging 13, 601-609 (1994).

[72] L.A. Feldcamp, L.C. Davis and J.W. Kress, "Pratical cone-beam algorithm," Journal of Optical Society of America A 1, 612-619 (1984).

[73] J.T. Bushberg, J.A. Seibert, E.M.L. Jr., *et al.*, The essential physics of medical imaging (Lippincott Williams & Wilkins, 2001).

[74] A.C. Kak and M. Slaney, Principles of computerized tomographic imaging (New York: IEEE Press, 1999).

[75] T.S. Curry, III, J.E. Dowdey and R.C. Murry, Jr, Christensen's introduction to the physics of diagnostic radiology (Lea & Febiger, Philadelphia, 1990).

[76] R.S. Saunders Jr and E. Samei, "A monte carlo investigation on the impact of scattered radiation on mammographic resolution and noise," Proceedings of SPIE 6142, 3A1-7 (2006).

[77] J. Hsieh, Computed tomography: Principles, design, artifacts, and recent advances (SPIE Press, 2003).

[78] J.H. Siewerdsen and D.A. Jaffray, "Cone-beam computed tomography with a flat-panel imager: Magnitude and effects of x-ray scatter," Medical Physics 28, 220-231 (2001).

[79] H.-P. Chan, K.L. Lam and Y. Wu, "Studies of performance of antiscatter grids in digital radiography: Effect on signal-to-noise ratio," Medical Physics 17, 655-664 (1990).

[80] G.T. Barnes, H.M. Cleare and I.A. Brezovich, "Reduction of scatter in diagnostic radiology by means of a scanning multiple slit assembly," Radiology 120, 691-694 (1976).

[81] U. Neitzel, "Grids or air gaps for scatter reduction in digital radiography: A model calculation," Medical Physics 19, 475-481 (1992).

[82] J.Y. Lo, C.E. Floyd Jr and C.E. Ravin, "Scatter compensation in chest radiography with a single-exposure estimation-subtraction method," Radiology 177(P), 172-173 (1990).

[83] D.L. Bailey and S.R. Meikle, "A convolution-subtraction scatter correction method for 3d pet," Physics in Medicine and Biology 39, 411-424 (1994).

[84] J.A. Seibert and J.M. Boone, "X-ray scatter removal by deconvolution," Medical Physics 15, 567-575 (1988).

[85] J.Y. Lo, C.E. Floyd, Jr and C.E. Ravin, "Spatial-varying scatter compensation for portable chest radiographs using an artificial neural network," in Proceedings of Association of University Radiologists (1992).

[86] C.E. Floyd, Jr, A.H. Baydush, J.Y. Lo, *et al.*, "Scatter compensation for digital chest radiography using maximum likelihood expectation maximization," Investigative Radiology 28, 427-433 (1993).

[87] C.E. Floyd, Jr, A.H. Baydush, J.Y. Lo, *et al.*, "Bayesian restoration of chest radiographs: Scatter compensation with improved signal to noise ratio," Investigative Radiology 29, 904-910 (1994).

[88] A.H. Baydush, J.E. Bowsher and C.E. Floyd, Jr, "Improved scatter compensation with a bayesian image-estimation technique," Radiology 197(P), 223 (1995).

[89] A. Krol, D.A. Bassano, C.C. Chamberlain, *et al.*, "Scatter reduction in mammography with air gap," Medical Physics 23, 1263-1270 (1996).

[90] W.J.H. Veldkamp, M.A.O. Thijssen and N. Karssemeijer, "The value of scatter removal by a grid in full field digital mammography," Medical Physics 30, 1712-1718 (2003).

[91] A.H. Baydush and C.E. Floyd, Jr, "Improved image quality in digital mammography with image processing," Medical Physics 27, 1503-1508 (2000).

[92] P.S. Rezentes, A. de Almeida and G.T. Barnes, "Mammography grid performance," Radiology 210, 227-232 (1999).

[93] R. Fahrig, J.G. Mainprize, N. Robert, *et al.*, "Performance of glass fiber antiscatter devices at mammographic energies," Medical Physics 21, 1277-1282 (1994).

[94] D.P. Chakraborty, "The effect of the antiscatter grid on full-field digital mammography phantom images," Journal of Digital Imaging 12, 12-22 (1999).

[95] J.H. Siewerdsen, M.J. Daly, B. Bakhtiar, *et al.*, "A simple, direct method for x-ray scatter estimation and correction in digital radiography and cone-beam ct," Medical Physics 33, 187-197 (2006).

[96] B. Axelsson, P. Msaki and A. Israelsson, "Subtraction of compton-scattered photons in single-photon emission computerized tomography.," Journal of Nuclear Medicine 25, (1984).

[97] J.M. Boone, B.A. Arnold and J.A. Seibert, "Characterization of the point spread function and modulation transfer function of scattered radiation using a digital imaging system," Medical Physics 13, 254-256 (1986).

[98] C.E. Floyd, Jr, R.J. Jaszczak, C.C. Harris, *et al.*, "Energy and spatial distribution of multiple order compton scatter in spect: A monte carlo investigation," Physics in Medicine and Biology 29, 1217-1230 (1984).

[99] H.P. Chan and K. Doi, "Physical characteristics of scattered radiation in diagnostic radiology: Monte carlo simulation studies," Medical Physics 12, 152-165 (1985).

[100] C.E. Floyd, Jr, P.T. Beatty and C.E. Ravin, "Scatter compensation in digital chest radiography by fourier deconvolution," Investigative Radiology 24, 30-33 (1989).

[101] C.E. Floyd, Jr, R.J. Jaszczak, K.L. Greer, *et al.*, "Deconvolution of compton scatter in spect," Journal of Nuclear Medicine 26, 403-408 (1985).

[102] A.H. Baydush, C.E. Floyd, Jr, J.Y. Lo, *et al.*, "Scatter reduction in portable digital chest radiography by bayesian image estimation," Radiology 185(P), 305 (1992).

[103] B.R. Whiting, "Signal statistics of x-ray computed tomography," Proceedings of SPIE 4682, 53-60 (2002).

[104] G. Casella and R.L. Berger, Statistical inference (Thomson Learning, 2001).

[105] S.Z. Li, "On discontinuity-adaptive smoothness priors in computer vision," Ieee Transactions on Pattern Analysis and Machine Intelligence 17, 576-586 (1995).

[106] T. Hebert and R. Leahy, "A generalized em algorithm for 3-d bayesian reconstruction from poisson data using gibbs priors," IEEE Transactions on Medical Imaging 8, 194-202 (1989).

[107] P.J. La Riviere, "Penalized-likelihood sinogram smoothing for low-dose ct," Medical Physics 32, 1676-1683 (2005).

[108] J. Wang, T.F. Li, H.B. Lu, *et al.*, "Penalized weighted least-squares approach to sinogram noise reduction and image reconstruction for low-dose x-ray computed tomography," IEEE Transactions on Medical Imaging 25, 1272-1283 (2006).

[109] J.M. Zhong, R.L. Ning and D. Conover, "Image denoising based on multiscale singularity detection for cone beam ct breast imaging," IEEE Transactions on Medical Imaging 23, 696-703 (2004).

[110] P. Perona and J. Malik, "Scale-space and edge detection using anisotropic diffusion," IEEE Transactions on Pattern Analysis and Machine Intelligence 12, 629-639 (1990).

[111] J. Weichert, Anisotropic diffusion in image processing (Tuebner: Stuttgart, 1998).

[112] T.L. Pope, M.E. Read, T. Medsker, *et al.*, "Breast skin thickness - normal range and causes of thickening shown on film-screen mammography," Journal Of The Canadian Association Of Radiologists-Journal De L Association Canadienne Des Radiologistes 35, 365-368 (1984).

[113] J. Hsieh, "Adaptive streak artifact reduction in computed tomography resulting from excessive x ray photon noise," Medical Physics 25, 2139-2147 (1998).

[114] D.A. McQuarrie, Mathematical methods for scientists and engineers (University Science Books, 2003).

[115] F. Catte, P.L. Lions, J.M. Morel, *et al.*, "Image selective smoothing and edge-detection by nonlinear diffusion," SIAM Journal on Numerical Analysis 29, 182-193 (1992).

[116] G.W. Oehlert, "A note on the delta method," The American Statistician 46, 27-29 (1992).

[117] R.C. Gonzalez and R.E. Woods, Digital image processing (New York: Addison-Wesley, 1993).

[118] G. Chung and L.A. Vese, *Energy minimization based segmentation and denoising using a multilayer level set approach*, in *Energy minimization methods in computer vision and pattern recognition, proceedings*. 2005. p. 439-455.

[119] S.G. Mallat, "Multifrequency channel decompositions of images and wavelet models," IEEE Transactions on Acoustics, Speech, and Signal Processing 37, 2091-2110 (1989).

[120] S. Mallat and S. Zhong, "Characterization of signals from multiscale edges," Ieee Transactions on Pattern Analysis and Machine Intelligence 14, 710-732 (1992).

[121] Z.H. Cai, T.H. Cheng, C. Lu, *et al.*, "Efficient wavelet-based image denoising algorithm," Electronics Letters 37, 683-685 (2001).

[122] T.C. Hsung, D.P.K. Lun and W.C. Siu, "Denoising by singularity detection," Ieee Transactions on Signal Processing 47, 3139-3144 (1999).

[123] G.Y. Chen and B. Kegl, "Image denoising with complex ridgelets," Pattern Recognition 40, 578-585 (2007).

[124] S. Tan and L.C. Jiao, "Image denoising using the ridgelet bi-frame," Journal of the Optical Society of America a-Optics Image Science and Vision 23, 2449-2461 (2006).

[125] J.S. Lim, *Two-dimensional signal and image processing*. 1990, Englewood Cliffs, NJ: Prentice Hall.

[126] A. Restrepo and A.C. Bovik, "Adaptive trimmed mean filters for image-restoration," Ieee Transactions on Acoustics Speech and Signal Processing 36, 1326-1337 (1988).

[127] S.M. Kay, Fundamentals of statistical signal processing: Detection theory (Prentice Hall, 1998).

[128] H.H. Barrett, C.K. Abbey and B. Gallas, "Stabilized estimates of hotelling-observer detection performance in patient-structured noise," Proceedings of SPIE 3340, 27-43 (1998).

[129] A.H. Baydush, D.M. Catarious and C.E. Floyd, Jr, "Computer aided detection of masses in mammography using a laguerre-gauss channelized hotelling observer," Proceedings of SPIE 5034, 71-76 (2003).

[130] C.E. Metz, B.A. Herman and J.H. Shen, "Maximum likelihood estimation of receiver operating characteristic (roc) curves from continuously-distributed data," Statistics in Medicine 17, 1033-1053 (1998).

[131] D.M. Catarious, "A computer-aided detection system for mammographic masses," Duke University Ph.D. (2004).

[132] H.H. Barrett, J. Yao, J.P. Rolland, *et al.*, "Model observers for assessment of image quality," Proceedings of the National Academy of Sciences of the United States of America 90, 9758-9765 (1993).

[133] M.P. Eckstein, C.K. Abbey and J.S. Whiting, "Human vs. Model observers in anatomic backgrounds," Proceedings of SPIE 3340, 16-26 (1998).

[134] M.P. Eckstein, C.K. Abbey, F.O. Bochud, *et al.*, "The effect of image compression in model and human performance," Proceedings of IEEE 3663, 243-252 (1999).

[135] Y. Zhang, B.T. Pham and M.P. Eckstein, "Task-based model/human observer evaluation of spiht wavelet compression with human visual system-based quantization," Academic Radiology 12, 324-336 (2005).

[136] J. Yao and H.H. Barrett, "Predicting human performance by a channelized hotelling observer model," Proceedings of SPIE 1768, 161-168 (1992).

[137] A.H. Baydush, J.E. Bowsher, J.K. Laading, et al., "Improved bayesian image estimation for digital chest radiography," Medical Physics 24, 539-545 (1997).

Biography

Name	Qing Xia
Date of Birth	December 26, 1977
Place of Birth	Nantong, Jiangsu Province, China

EDUCATION:

Duke University, Durham, NC September 2007
Ph.D. in Biomedical Engineering

Duke University, Durham, NC May 2006
M.S. in Statistics and Decision Science

Tsinghua University, Beijing, China July 2000
B.E. in Biomedical Engineering

HONORS AND AWARDS:

Pre-doctoral Trainingship Award, Department of Defense Breast Cancer Research Program, USAMRMC W81XWH-05-1-0278, *2005-2008*

Graduate Fellowship, Department of BME, Duke University, *2001-2004*

1st Place in PhD-Level Research Paper Presentation, the Twenty First Southern Biomedical Engineering Conference, Washington DC, *2002*

University Scholarship, Tsinghua University, *1995-1998*

PUBLICATIONS:

Refereed Papers

1. **Jessie Q. Xia**, John M. Boone, Carey E. Floyd Jr., Joseph Y. Lo, Improved Lesion Detection in Breast CT via a Volume Image Denoising Technique *(in preparation)*.

2. **Jessie Q. Xia**, Joseph Y. Lo, Kai Yang, Carey E. Floyd Jr., John M. Boone, Dedicated Breast CT: Volume Image Denoising via a Partial Diffusion Equation Based Technique. *Medical Physics (in review)*.

3. Carey E. Floyd, Anuj J. Kapadia, Janelle E. Bender, Amy C. Sharma, **Jessie Q. Xia**, Brian Harrawood, Georgia D. Tourassi, Joseph Y. Lo, Corwell, AS, Kiser, MR, Howell, CR. Neutron Stimulated Emission Computed Tomography of a Multi-element Phantom. *IEEE Transactions on Medical Imaging (submitted Sept 2006).*

4. **Jessie Q. Xia**, Joseph Y. Lo, Carey E. Floyd Jr., Scatter Measurement on a Full Field Digital Mammography System. *Academic Radiology (in revision).*

5. Carey E. Floyd Jr., Janelle E. Bender, Amy C. Sharma, Anuj Kapadia, **Jessie Q Xia**, Brian Harrawood, Georgia D. Tourassi, Joseph Y. Lo, Matthew R Kiser, Robert A. macri, Ronald S. Pedroni, Shigeyuki Tajima, Alexander S. Crowell, Calvin R. Howell, Neutron stimulated Emission Computed Tomography: Background Correction. *Nuclear Instruments and Methods in Physics Research Section B 254:329-336, 2007.*

6. Carey E. Floyd Jr., Janelle E. Bender, Amy C. Sharma, Anuj Kapadia, **Jessie Q Xia**, Brian Harrawood, Georgia D. Tourassi, Joseph Y. Lo, Alexander S. Crowell, Calvin R. Howell, Introduction to Neutron Stimulated Emission Computed Tomography. *Physics in Medicine and Biology 51: 3375-3390, 2006.*

7. Mary Scott Soo, Eric L. Rosen, **Jessie Q. Xia**, Sujata V. Ghate, Jay A. Baker, Computer-aided Detection of Amorphous Calcification. *American Journal of Roentgenology 184: 887-892, 2005.*

8. Christopher L. Gilchrist, **Jessie Q. Xia**, Lori A. Setton, Edward W. Hsu, High-Resolution Determination of Soft Tissue Deformations Using MRI and First-Order Texture Correlation. *IEEE Transactions on Medical Imaging 23(5): 546-553, 2004.*

9. Wang Feng, Ding Haishu, Tian Fenghua, Zhao Jun, **Xia Qing** and Tang Xianwu, Influence of Overlying Tissue and Probe Geometry On the Sensitivity of a Near-Infrared Tissue Oximeter. *Physiological Measurement 22: 201-208, 2001.*

Conference Proceedings

1. **Jessie Q. Xia**, Georgia D. Tourassi, Joseph Y. Lo, Carey E. Floyd Jr., On the Development of Gaussian Noise Model for Scatter Compensation. *Proceedings of SPIE 6510-93:1-10, 2007.*

2. Amy Sharma, Georgia D Tourassi, Anuj Kapadia, Janelle Bender, **Jessie Q. Xia**, Brian Harrawood, Crowell, AS, Kiser, MR, Howell, CR, Carey E Floyd Jr. Development of a High-Energy Gamma Camera for use with NSECT Imaging of the Breast. *Proceedings of the 2006 IEEE NSS-MIC, San Diego, CA Nov. 2006.*

3. **Jessie Q. Xia**, Joseph Y. Lo, Carey E. Floyd Jr., Characterization of scatter radiation of a breast phantom on Siemens prototype FFDM with and without an anti-scatter grid. *Proceedings of SPIE 5145: 1096-1102, 2005.*

4. Jonathan L. Jesneck, Robert S. Saunders, Jr., Ehsan Samei, **Jessie Q. Xia**, Joseph Y. Lo, Detector Evaluation of A Prototype Amorphous Selenium-based Full Field Digital Mammography System. *Proceedings of SPIE 5745: 478-485, 2005.*

5. Carey Floyd, Calvin Howell, Anuj Kapadia, **Jessie Xia**, Brian Harrawood, Ronald Pedroni, Alexander Crowell, Robert Macri, Mathew Kiser, Richard Walter,Werner

Tornow, Neutron Stimulated Emission Computed Tomography of Stable Isotopes. *Proceedings of SPIE 5368: 248-254, 2004.*

6. **Jessie Q. Xia**, Christopher L. Gilchrist, Lori A. Setton, Edward W. Hsu, MRI Measurement of Strain in Materials Subject to Non-Periodic Motion. *Proceedings of the Twenty-First Southern Biomedical Engineering Conference, Washington DC: 207-208, 2002.*

Scientific Presentations

1. Carey E. Floyd, Jr., Calvin Howell, Anuj J. Kapadia, Brian Harrawood, **Jessie Q. Xia**, Georgia D. Tourassi, Experimental Implementation of Spectroscopic Imaging By Neutron Stimulated Emission Computed Tomography. *SPIE Medical Imaging Conference 2005, San Diego, CA.*

2. **Jessie Q. Xia**, Carey Floyd, Joseph Lo, Brian Harrawood, Improved SNR In FFDM By Replacing the Anti-scatter Grid With Non-linear Image Processing. *RSNA 2004, Chicago,IL.*

3. Carey Floyd, Calvin Howell, Anuj Kapadia, Brian Harrawood, **Jessie Xia**, Georgia Tourassi, Cancer Diagnosis Using Neutron Scattering Analysis of Elemental Composition. *AAPM annual meeting 2004, Pittsburgh, PA.*

Improved Mass Detectability in Dedicated Breast CT by Applying Novel Volume Noise Removal Techniques

Jessie Q. Xia and Joseph Y. Lo

Department of Biomedical Engineering, Duke University, Durham, NC 27708

Duke Advanced Imaging Laboratories, Duke University Medical Center, Durham, NC 27710

Dedicated breast CT imaging is a novel breast imaging modality, which may improve lesion detection while using the same radiation dose as compared against conventional mammography. However, since the breast CT images divide the dose of mammography among hundreds of projection views, resulting in considerable quantum noise, it is therefore desirable to reduce noise in the reconstructed breast volume without loss of spatial resolution.

Several partial diffusion equation (PDE) based denoising techniques were developed for dedicated breast CT. The techniques were thoroughly evaluated based on simulation. It was found that applying a denoising technique before reconstruction provided better images than after reconstruction. In addition, a spatially adaptive PDE technique denoted by PDE_{tomo} (which takes into the account the non-uniform distribution of the noise in the projection images after the preprocessing step) outperformed other techniques. The PDE_{tomo} tool was analyzed for the clinically relevant task of lesion detectability in human subjects, using numerical observers and ROC analysis methodology.

The preliminary ROC study showed that with a fixed size lesion in real anatomical backgrounds, PDE-denoised images had higher detectability (statistically significant), higher CNR and better qualitative appearance. The promising new

techniques for volume noise removal pave the way for future implementations of dedicated breast CT.

Mass Detectability in Dedicated Breast CT: A Simulation Study with the Application of Volume Noise Removal

Jessie Q. Xia*, ***Member, IEEE*** **and Joseph Y. Lo**

***Abstract*—Dedicated breast CT is an emerging new technique for breast cancer imaging. It was found that low dose levels comparable to those used in the conventional two-view mammography could be used for breast CT data acquisition. Since the dose is equally split into the hundreds of projection views, each projection image contains non-ignorable quantum noise and/or electronic noise. This study is aimed at investigating how volume noise removal affects the mass detectability in breast CT. Both simulated and real breast CT data were considered in the study. For the simulated breast volumes, contrast detail phantoms of masses with varying sizes and contrasts were simulated and embedded. For the real human subject breast CT volumes, spherical masses with fixed size and contrast were simulated and embedded. A Partial Diffusion Eqn (PDE) based denoising technique applied before reconstruction was tested. Using a mathematical observer based on CNR values of masses, it is found that PDE denoising technique improves the mass detectability in a statistical significant sense. In addition, the results of LG-CHO observer and ideal observer on the human subject breast CT data are also presented.**

***Index Terms*—breast cancer, tomography, noise, breast CT, lesion detection, observer study**

I. INTRODUCTION

The advance of flat panel detector technology made it possible to develop some three dimensional breast cancer imaging techniques, such as breast tomosynthesis[1] and dedicated breast CT[2]. Breast tomsynthesis acquires high-resolution projection images over a limited angle range. Its tomographic reconstruction is complicated by incomplete sampling and therefore is the focus of many research endeavors[3-6]. Intrinsically, reconstructed breast tomosynthesis volumes have high within-plane resolution and low cross-plane resolution. By contrast, dedicated breast CT acquires projection images over the full 360-degree angle span; whose tomographic reconstruction is conventional and can generate isotropic resolution both within plane and cross-plane. Due to the practical consideration, the flat-panel detector in breast CT system has lower spatial resolution than the one used in breast tomosynthesis system. Thus, the resolution in the reconstructed volume of breast CT is in-between the within-plane and cross-plane resolutions of breast tomosynthesis volumes.

Another image quality metric is noise level. Currently, dedicated breast CT techniques use the same dose as the one of conventional two-view mammography[7], which is split among hundreds of projection images. Due to the Poisson process of the projection views, the quantum noise is higher than the noise on mammograms. These noisy projection images are then combined by a reconstruction algorithm to generate the reconstructed volume, whose noise level is particularly affected by the noisiest projection channel. In a separate study[8], we found that applying a noise removal module before reconstruction is much better than applying after reconstruction.

The motivation for the work presented in this paper is to investigate the effectiveness of a noise removal module in terms of mass detectability in breast CT. Consistent with our paper[8], we will use the partial diffusion Eqn (PDE) based denoising technique applied on the line integral projection images.

II. METHODS

A. Dedicated Breast CT System

A dedicated breast CT system is set up differently from the conventional CT system. Rather than illuminating the whole torso, it only illuminates a breast of the patient. Figure 1 is an illustration of the major components of a typical breast CT system. The lead-shielded bed on which the patient lies prone was not shown in this illustration. The x-ray tube and the vertically standing flat panel detector rotate concurrently for a span of 360 degrees.

B. Datasets and Mass Simulation

There are two types of breast CT data used in this study: the ones acquired virtually for a simulated breast with simulated contrast detail phantoms in the middle of the breast; and the

This work was supported in part by NIH grant (R01 CA 94236 and R01 CA 112437) and the U.S. Army Breast Cancer Research Program (W81XWH-05-1-0278). We thank Professor John Boone and his group in UC Davis for providing us the human subject breast CT datasets.

*Jessie Q. Xia was with the Department of Biomedical Engineering and the DAILabs of the Department of Radiology, Duke University, Durham, NC, 27710 USA. She is now with the Department of Statistical Science, Duke University, Durham, NC 27708 USA and National Institute of Statistical Sciences, RTP, NC 27709 USA (email: qing.xia@duke.edu).

J. Y. Lo is with the Department of Biomedical Engineering and the DAILabs of the Department of Radiology, Duke University, Durham, NC, 27710 USA (email: joseph.lo@ duke.edu).

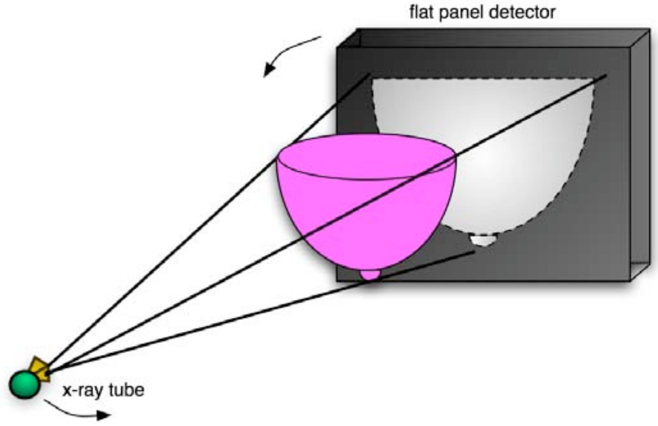

Figure 1: In a dedicated breast CT system, the x-ray tube and flat-panel detector rotate simultaneously around the breast.

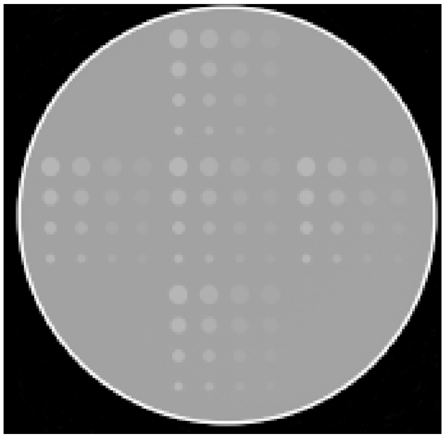

Figure 2: Coronal view of a simulated breast and contrast detail phantoms.

human-subject breast CT data from Dr. Boone's lab at University of California Davis.

Figure 2 shows the cross-section of the simulated breast with contrast detail phantoms. Each of the five 4x4 arrays in contrast detail phantoms has masses with sizes varying vertically (6, 5, 4 and 3 mm) and contrasts varying horizontally (15%, 10%, 5% and 3%). Square regions containing all 80 masses form the 2D ROIs for numerical observer study.

As the 20 human subject datasets used for the breast mass detectability study were prospectively collected cases, the ground truth of their volumes is unknown. In present study, we will assume that there is no lesion in the volumes. And all the lesions of interest will be simulated.

The procedure of simulating a mass in human subject breast CT data is as follows:

Step1: For a given human subject dataset, the reconstructed volume is used as the reference. The locations of 10 masses that will be embedded into the volume are randomly chosen.

Step2: Spherical masses with fixed size and contrast are put at the locations selected in Step 1, and projected onto a virtual 100% DQE detector using a virtual monochromatic cone-beam projector, which has the same system geometry, projection angles and reconstruction parameters as the individual human subject dataset. These projection images of masses will be added to the original projection images of human subjects to get the synthetic projection sets.

Step3: The synthetic projection sets either go through a denoising module followed by FBP reconstruction or directly go for FBP reconstruction.

Step4: The three-dimensional region of interest (ROIs) can then be retrieved from the reconstructed volumes. In the present study, instead of using 3D ROIs, only coronal region of interest containing the center of masses (i.e., 2D ROIs) are retrieved for numerical observer study.

Using the 80 ROIs containing contrast detail mass phantoms in simulated, uniform backgrounds, a PDE denoising technique was optimized. This technique was then applied to the human subject ROI dataset, which is comprised of a total of 400 ROIs, 200 with and 200 without simulated masses.

C. Volume Noise Removal

The $\mathrm{PDE}_{\mathrm{tomo}}$ technique[8] for volume noise removal in breast CT is used in this study. Details of the technique can be found in Ref. xx. A brief description of the technique is as follows.

The image to be denoised is denoted as *I*. A nonlinear partial diffusion Eqn on *I* will be:

$$\frac{\partial I}{\partial t} = \nabla \cdot (p(|\nabla(G_\sigma \otimes I)|)\nabla I), \qquad (1)$$

where ∇I is the gradient of the image *I* and $\nabla \cdot (*)$ is the divergence operator on image *I* over the spatial variables. By carefully selecting the appropriate *p(*),* the diffusivity function, the image can be processed in such a way that not only noise is reduced but also the details in the image will be preserved. To bound the gradient values in the presence of noise, a Gaussian kernel G_σ with the standard deviation of sigma σ is convoluted with the image before gradients are computed as Catte *et al* [9] suggested.

In this study, we chose a diffusivity function with the form of

$$p(d) = e^{-\frac{d^2}{\delta^2}}, \qquad (2)$$

where delta δ is a user-specified parameter. The parameter δ acts like a cut-off value; image regions with gradient norm below δ will have more noise removed while regions with a higher gradient norm will stay sharp. We used a spatially adaptive type of the parameter δ as:

$$\delta_{ij} = \delta_0 \cdot \sqrt{\frac{1}{\frac{1}{M}\sum_{c\in N(i,j)} e^{I_c}}}, \qquad (3)$$

where *M* equals to 4, and *N (i, j)* is the four closest neighbors around pixel (i, j) of image *I*.

Eqn (1) can be discretized by the finite difference approach using the first-order neighborhood system. Each pixel has four neighbors: the north, south, west and east neighbor pixels.

Assuming $\Delta x = \Delta y = 1$ in the two-dimensional case, the discretized version of Eqn (1) is

$$\frac{I_{(i,j)}^{<t+1>} - I_{(i,j)}^{<t>}}{\Delta t} = p_{(i-1,j)} \cdot \nabla_{(i-1,j)} I^{<t>} + p_{(i+1,j)} \cdot \nabla_{(i+1,j)} I^{<t>} \quad , \qquad (4)$$
$$+ p_{(i,j-1)} \cdot \nabla_{(i,j-1)} I^{<t>} + p_{(i,j+1)} \cdot \nabla_{(i,j+1)} I^{<t>}$$

where <t> and <t+1> represent the iteration step t and t+1 respectively; Δt is the discretized time step; $p_{(.,.)}$'s are diffusivity function values at the neighboring pixels of location (i,j); and ∇(.,.)I is a notation for the difference between $I_{(\cdot,\cdot)}$ and $I_{(i,j)}$. The parameters used in this study are: Δt=0.1, σ=1, δ_0=0.03, and the number of iterations = 10.

D. Numerical Observers

D.1. Ideal Observer

The task of an observer is to detect these masses from background tissues. It can also be formulated as the following hypothesis testing:

$$H_0 : x = n$$
$$H_1 : x = n + s \quad . \qquad (5)$$

The null hypothesis represents the mass absent case, whereas the alternative hypothesis represents the mass present case. If treated as signal known exactly (SKE) case, according to signal detection theory[10], the optimal detector is a likelihood ratio detector. Assuming the background noise n follows a Gaussian distribution with a covariance matrix of Σ, the log likelihood ratio has the following form:

$$\ln(\lambda(x)) = s^T \Sigma^{-1} x \quad . \qquad (6)$$

If the background noise follows independent and identical distributed (i.i.d.) Gaussian, i.e., the covariance matrix Σ is an identity matrix, then Eqn (6) can be further simplified to:

$$\ln(\lambda(x)) = s^T x / \sigma^2 \quad . \qquad (7)$$

This is the ideal observer. Usually real breast tissue background does not satisfy the i.i.d. condition, so the ideal observer shown in Eqn (7) will perform sub-optimally on the real breast tissue background case.

D.2. Laguerre-Gauss Channelized Hotelling Observer (LG-CHO)

When the covariance matrix Σ is not an identity matrix, the likelihood ratio observer shown in Eqn (6) is equivalent to a Hotelling observer [11]. The estimation of the covariance matrix Σ requires a large number of training cases, which is presently not available in breast CT. Alternatively, Laguerre-Gauss channelized hotelling observer (LG-CHO) [11, 12] can be used for this purpose.

The nth order Laguerre function has the following form:

$$L_n(x) = \sum_{m=0}^{n} (-1)^m \binom{n}{m} \frac{x^m}{m!}. \qquad (8)$$

The LG-CHO has nth order template with the form of:

$$LG_n(r) = \exp(-\frac{\pi r^2}{a^2}) \cdot L_m(\frac{2\pi r^2}{a^2}), \qquad (9)$$

where *a* is a free parameter proportional to the standard deviation of the Gaussian kernel through

$$a = \sqrt{2\pi}\sigma. \qquad (10)$$

D.3. CNR Observer

Traditionally, one would like to use Rose model of statistical detection for a simple lesion detectability study based on x-ray projection images. However Rose model does not directly apply to the breast CT reconstructed slices in this study since the physical measurement on these reconstructed slices is linear attenuation coefficients. Instead, the contrast to noise ratio for each ROI is calculated and used as the decision variable. Given the uncertainties associated with any model observer study, it is desirable to be able to compare all results against such a simple, well-understood technique.

E. ROC Analysis

The receiver operating characteristic (ROC) analysis is a comprehensive tool for performance measure of the numerical observers. Of the two axes on ROC plots, the horizontal axis represents False Positive Fraction (FPF), which equals to the value of one minus the specificity; and the vertical axis denotes True Positive Fraction (TPF), which equals to the sensitivity. FPF and TPF both range from 0 to 1. A metric of ROC curve is the area under the curve (AUC). The larger AUC value, the better the performance is, while AUC of 0.5 corresponds to random guessing. The area can also be calculated via semi-parametric fitting resulting in an area index denoted as Az[13].

III. RESULTS

Results are presented hereafter for two cases: contrast detail phantoms in simulated breast CT background, and masses with fixed size and contrast in human subject background. First we present in Figure 3 and Figure 4 two sample ROIs for simulated masses embedded in the anatomical background. The top row showed the ROIs derived from the original dataset, whereas the bottom row showed the ROIs from the processed dataset with volume noise removal. The left column showed the ROIs without masses, while the right column showed the ROIs containing the simulated masses following Step1 to Step 4 in Methods section B.

A. Contrast Detail Phantom Results

CNR observer result is shown in Figure 5 for the contrast detail phantom embedded in a uniform background.

In Figure 5 (a), the histograms of CNR for original and PDE processed ROIs with and without simulated masses are plotted. It is obvious that PDE processed ROIs with simulated masses have higher CNR values than original ROIs with

(a) Orig; nomass (b) Orig; mass

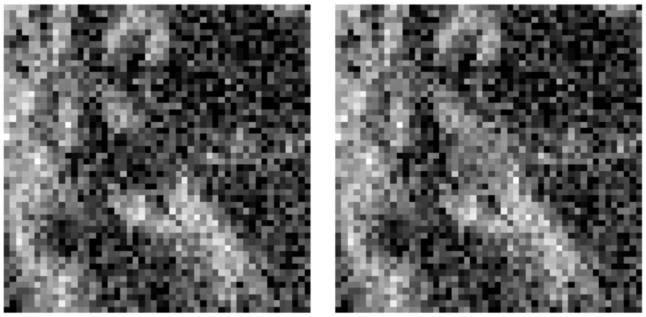

(c) PDE; nomass (d) PDE; mass

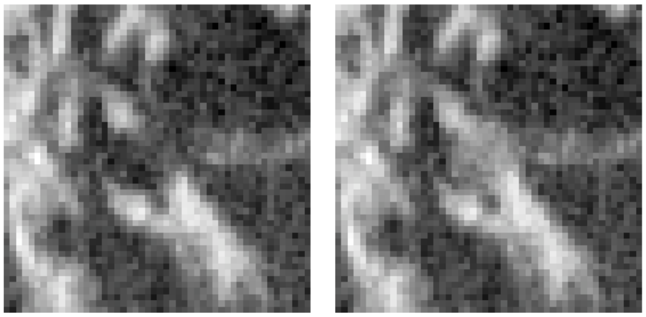

Figure 3: Sample ROIs No.1 for simulated lesion of 5 mm and 3%: Original ROIs (a) without mass and (b) with a mass, and, PDE denoised ROIs (c) without mass and (d) with a mass.

(a) Orig; nomass (b) Orig; mass

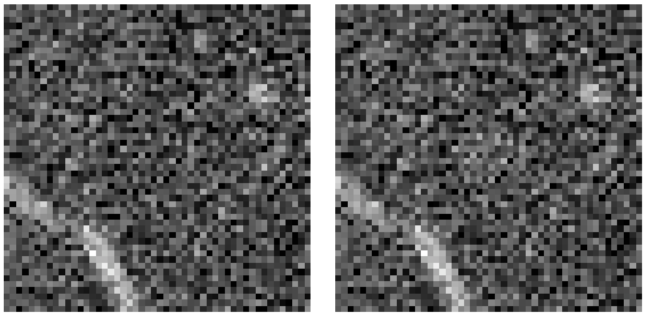

(c) PDE; nomass (d) PDE; mass

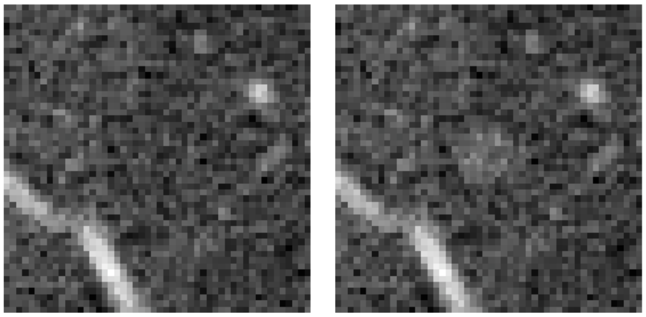

Figure 4: Sample ROIs No.2 for simulated lesion of 4 mm and 2%: Original ROIs (a) without mass and (b) with a mass, and, PDE denoised ROIs (c) without mass and (d) with a mass.

(a)

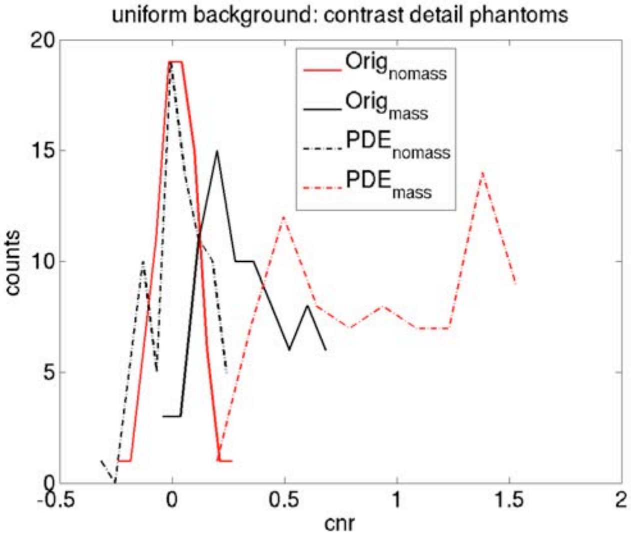

(b)

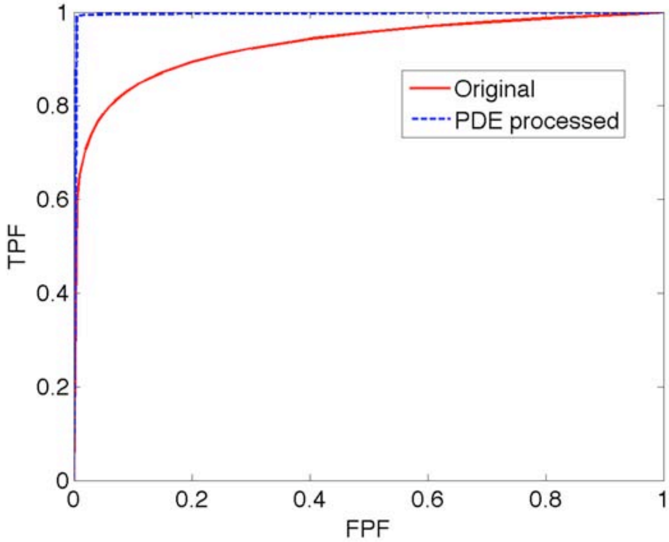

Figure 5: CNR observer results for contrast detail phantoms embedded in a simulated uniform background. CNR histograms for original and PDE processed ROI databases are shown in (a) and the corresponding ROC curves are shown in (b). The Az value of the PDE processed dataset (0.998 ± 0.005) is statistically higher than the Az value of the original dataset (0.933 ± 0.020). The p value is less than 0.01.

masses. The Az values were obtained using the software package ROCKIT (Charles Metz, University of Chicago). For original dataset, the Az is 0.933 ± 0.020; and for PDE processed dataset, the Az is 0.998 ± 0.005. The corresponding two-tailed p-value is 0.0009, indicating that Az of PDE processed dataset is statistically higher than Az of the original dataset. The ROC curves are shown in Figure 5 (b).

B. *Human Subject Background Results*

The human subject background ROC analysis based on CNR observer is shown in Figure 6 for simulated mass of 4 mm and 2%. The histograms of CNR for original and PDE processed datasets with and without simulated masses are shown in Figure 6(a). The corresponding ROC curves are plotted in Figure 6(b). The Az value of the PDE processed dataset (0.801 ± 0.022) is higher than the Az value of the original dataset (0.770 ± 0.023). The p value is less than 0.009, indicating that the difference is statistically significant.

(a)

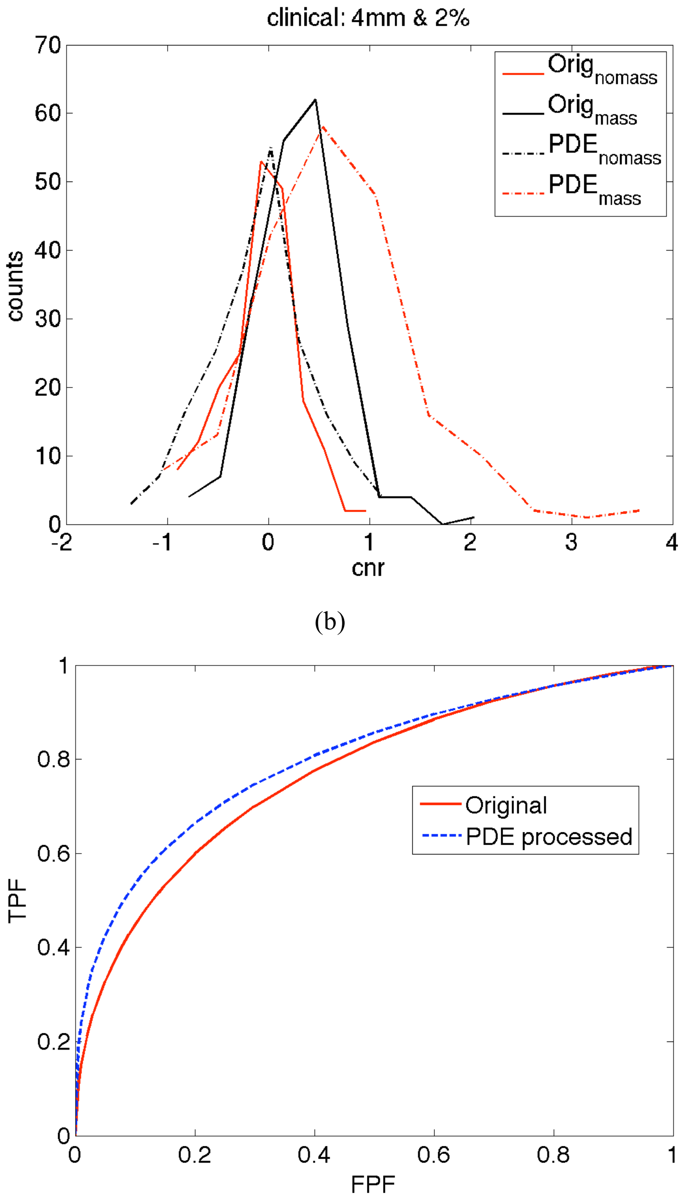

(b)

Figure 6: CNR observer results for simulated lesions of 4mm and 2% embedded in real anatomical backgrounds. CNR histograms for original and PDE processed ROI databases are shown in (a) and the corresponding ROC curves are shown in (b). The Az value of the PDE processed dataset (0.801 ± 0.022) is statistically higher than the Az value of the original dataset (0.770 ± 0.023). The p value is less than 0.01.

AUC values of the three types of numerical observers using real anatomical background from breast CT are shown in Table 1 for lesions of 5 mm and 10%, 5 mm and 3%, and 4 mm and 2%, respectively. For all the cases, the CNR observer gives the highest AUC values, followed by 1st order LG template, and the ideal observer gives the lowest AUC values. For masses with 4 mm diameter and 2% contrast, the ROC performance of ideal observer reduces to the chance curve.

IV. DISCUSSION

Some studies [14-18] have shown that numerical observers can be good candidates for lesion detection tasks.

As compared to human observers, numerical observers posses several advantages, such as higher repeatability, and better tolerance of tedious process of observer studies. In this study, detectability of simulated masses in both simulated breast CT background and the real anatomical background were investigated. CNR observers were used in both cases. In addition, a SKE ideal observer and nth order LG-CHO observers were used for detecting the simulated masses in the anatomical background. As expected, SKE ideal observer worked sub-optimally whereas LG-CHO worked much better than SKE case. The CNR observer as a simple one worked the best, as is evident in Table 1.

For the contrast detail phantoms in a simulated uniform breast background, shown in Figure 5, the initial AUC based on CNR observer is 0.933 ± 0.020. After PDE denoising, the AUC improves to 0.998 ± 0.005, which is close to the perfect performance. The improvement is statistically significant with two-tailed $p<0.001$.

With real anatomical backgrounds, masses with a single combination of size and contrast was embedded. And the resultant ROC curves are a function of both the mass size and contrast. It is very easy to detect large masses (e.g., 5 mm in diameter and 10% in contrast), whereas the detection task is extremely challenging for subtle masses (e.g., 4 mm in diameter and 2% in contrast). Using a CNR observer in the latter condition showed that PDE denoising provided statistically significant improvements in performance, as well as higher CNR values and better visual appearance.

There are some limitations in this study. First, the simulated masses are perfect spheres, which are rare in the real situation. A more realistic mass simulation may render more advantages toward evaluating nonlinear image processing techniques such as PDE$_{tomo}$. Second, the ROIs are two dimensional due to the limited number of human subject datasets available. In the future, when more human subject datasets are collected, three-dimensional ROIs can be used instead. Third, in this study, individual LG-CHO channels are used for ROC analysis. An ensemble LG-CHO is often used with the form:

Table 1: Numerical observer AUC values for simulated masses in real anatomical background of breast CT.

Lesion		5mm & 10%	5mm & 3%	4mm & 2%
CNR Observer	Original	0.999	0.877	0.770
	PDE processed	0.997	0.883	0.801
LG-CHO Observer	Original	0.999	0.850	0.703
	PDE processed	0.999	0.853	0.702
Ideal Observer	Original	0.896	0.690	0.446
	PDE processed	0.904	0.700	0.443

$$w = \sum_{m=0}^{n} \alpha_m LG_m(r), \qquad (11)$$

where the parameters (α_1, α_2, α_3,….) are determined by Hotelling Observer.

A common problem shared by the observers is the tendency to perform too well due to the fixed, single type of lesion. Even for the subtlest lesions (masses with 4mm in diameter and 2% in contrast in this study) that were virtually impossible to see by the human eye, the observers routinely performed quite well with ROC areas around 0.7 to 0.8. As such, such mathematical observer performances should not be construed as what would be typical of clinical performance by radiologists. Instead, these studies offer valuable insight in terms of comparing one technique against another in a fair (or equally unfair) fashion. The best techniques from such a study may then be validated in human observer studies in the future.

In summary, several numerical observers are used to analyze the mass detectability in breast CT using simulated uniform background and real anatomical background. With simulated uniform background and contrast detail phantoms, the PDE denoised datasets give the better results than the original datasets using CNR observer. The performances are similar when LG-CHO templates are used. With real anatomical background with fixed size lesion, PDE denoised images have higher detectability, higher CNR and better qualitative appearance.

V. Conclusion

This manuscript has presented ROC study using simulated masses and mathematical observers. With either simulated background or the real anatomical breast CT background, volume noise removal of breast CT dataset improves significantly the detectability of masses.

References

[1] J. T. Dobbins, III and D. J. Godfrey, "Digital x-ray tomosynthesis: current state of the art and clinical potential," *Physics in Medicine and Biology,* vol. 48, pp. R65-R106, 2003.

[2] S. J. Glick, "Breast CT," *Annual Review of Biomedical Engineering,* vol. 9, pp. 501-526, 2007.

[3] T. Wu, R. H. Moore, E. A. Rafferty, and D. B. Kopans, "A Comparison of Reconstruction Algorithms for Breast Tomosynthesis," *Medical Physics,* vol. 31, pp. 2636-2647, 2004.

[4] G. Lauritsch and W. H. Harer, "A theoretical framework for filtered backprojection in tomosynthesis," *Proceedings of SPIE,* vol. 3338, pp. 1127-1137, 1998.

[5] T. Mertelmeier, J. Orman, W. Haerer, and M. K. Dudam, "A theoretical framework for filtered back-projection in tomosynthesis," *Proceedings of SPIE,* vol. 6142, pp. 6142F1-12, 2006.

[6] Y. Chen, J. Y. Lo, and J. T. Dobbins, 3rd, "Impulse response analysis for several digital tomosynthesis mammography reconstruction algorithms," *Proceedings of SPIE,* vol. 5745, pp. 541-549, 2005.

[7] J. M. Boone, "Performance Assessment of a Pendant-geometry CT Scanner for Breast Cancer Detection," *Proceedings of SPIE,* vol. 5745, pp. 319-323, 2005.

[8] J. Q. Xia, J. Y. Lo, K. Yang, C. E. Floyd Jr, and J. M. Boone, "Dedicated breast computed tomography: Volume image denoising via a partial-diffusion equation based technique," *Medical Physics,* vol. 35, pp. 1950-1958, 2008.

[9] F. Catte, P. L. Lions, J. M. Morel, and T. Coll, "Image Selective Smoothing and Edge-detection by Nonlinear Diffusion," *SIAM Journal on Numerical Analysis,* vol. 29, pp. 182-193, 1992.

[10] S. M. Kay, *Fundamentals of Statistical Signal Processing: Detection Theory*: Prentice Hall, 1998.

[11] H. H. Barrett, C. K. Abbey, and B. Gallas, "Stabilized estimates of Hotelling-observer detection performance in patient-structured noise," *Proceedings of SPIE,* vol. 3340, pp. 27-43, 1998.

[12] A. H. Baydush, D. M. Catarious, and C. E. Floyd, Jr, "Computer aided detection of masses in mammography using a Laguerre-Gauss channelized Hotelling observer," *Proceedings of SPIE,* vol. 5034, pp. 71-76, 2003.

[13] C. E. Metz, B. A. Herman, and J. H. Shen, "Maximum likelihood estimation of receiver operating characteristic (ROC) curves from continuously-distributed data," *Statistics in Medicine,* vol. 17, pp. 1033-1053, May 1998.

[14] H. H. Barrett, J. Yao, J. P. Rolland, and K. J. Myers, "Model Observers For Assessment of Image Quality," *Proceedings of the National Academy of Sciences of the United States of America,* vol. 90, pp. 9758-9765, 1993.

[15] M. P. Eckstein, C. K. Abbey, and J. S. Whiting, "Human vs. model observers in anatomic backgrounds," *Proceedings of SPIE* vol. 3340, pp. 16-26, 1998.

[16] M. P. Eckstein, C. K. Abbey, F. O. Bochud, J. L. Bartroff, and J. S. Whiting, "The effect of image compression in model and human performance," *Proceedings of IEEE,* vol. 3663, pp. 243-252, 1999.

[17] Y. Zhang, B. T. Pham, and M. P. Eckstein, "Task-based model/human observer evaluation of SPIHT wavelet compression with human visual system-based quantization," *Academic Radiology,* vol. 12, pp. 324-336, Mar 2005.

[18] J. Yao and H. H. Barrett, "Predicting human performance by a channelized hotelling observer model," *Proceedings of SPIE,* vol. 1768, pp. 161-168, 1992.